High pressure experimental study of natural antigorite dehydration reactions

Juliette Maurice

UNIVERSITE BLAISE PASCAL
U.F.R Sciences et Technologies

ECOLE DOCTORALE DES SCIENCES FONDAMENTALES

THESE

Présentée pour obtenir le grade de
DOCTEUR D'UNIVERSITE

Spécialité : Pétrologie

Par
Juliette MAURICE
Titulaire du Master 2 Recherche :
« Magmas et Volcans »

Étude expérimentale des réactions de déshydratation de l'antigorite naturelle à haute pression

Soutenue publiquement le 17 mars 2017 devant la commission d'examen composée de:

Jörg Hermann	Professeur, Universität Bern	Rapporteur
Bruno Reynard	Directeur de Recherches, ENS Lyon	Rapporteur
Patrizia Fumagalli	Professeur, Università Degli Studi di Milano	Examinateur
Damien Guillaume	Professeur, LMV Saint-Etienne	Examinateur
Nathalie Bolfan-Casanova	Directrice de Recherches, LMV	Directeur de thèse
Tahar Hammouda	Maître de Conférence, LMV	Directeur de thèse

Contents

Remerciements

Je tiens tout d'abord à remercier mes directeurs de thèse Nathalie Bolfan-Casanova et Tahar Hammouda. Merci Nathalie de m'avoir permis de travailler sur des sujets si passionnants, de m'avoir ouvert les portes du monde de la pétrologie expérimentale et en particulier de la multi-enclumes. Merci de m'avoir éclairée de ton intérêt et de tes ressources intarissables durant ces années, ce qui a contribué à la richesse de cette thèse ainsi qu'à celle de l'expérience que j'en ai vécue. Tahar, merci pour tes conseils avisés et ton implication dans ma thèse, en particulier pour ton aide concernant les analyses de Schreinemakers et tes remarques qui m'ont guidées pour mener à terme le second article sur les DHMS.

Merci aux membres du Jury, Jôrg Hermann, Bruno Reynard, Patrizia Fumagalli et Damien Guillaume d'avoir accepté de vous déplacer et d'évaluer mon travail. Merci pour les discussions qui ont enrichi ce travail, et en particulier les deux articles inscrit dans ce manuscrit de thèse.

Un grand Merci à José-Alberto Padrón-Navarta, pour m'avoir accueillie dans les locaux de Géosciences Montpellier et collaboré à une version de l'article sur les phases hydratées post-antigorite. J'ai beaucoup appris et l'article en a été enrichi. Merci pour tout le temps que tu as consacré à nos multiples échanges de diagrammes de phase divers et variés ! Merci aussi à Sylvie Demouchy, à l'origine avec Nathalie du prototype de mon sujet de thèse et des premières expériences qui m'ont introduites à la pétrologie expérimentale. Merci pour ton aide précieuse sur l'article et merci de m'avoir accueillie chez toi à Montpellier ! Je remercie Geeth Manthilake (j'aurais pu écrire en anglais pour toi Geeth, mais je sais que tu comprends le français, haha!) de m'avoir « coachée », aussi bien en ce qui concerne l'optimisation de mes expériences mais également par le biais de discussions scientifiques et moins scientifiques qui m'ont beaucoup appris et guidé. Merci à Federica Schiavi pour ta disponibilité et ton investissement personnel pour m'aider à mener des analyses Raman de super qualité. Merci Fédé pour ta bonne humeur et ta gentillesse ! Merci à Christian Nicollet et Pierre Bouilhol de vous être penchés sur la complexité des relations de phases associées à mes expériences et de m'avoir conseillée dans la première approche de ce système chimique. Merci à Baptiste Debret, mon copain de serpentine pour les discussions de (pas que) serpentine qui m'ont bien éclairée sur ce sujet. Merci pour toute ton aide, tes commentaires et idées pour l'article de déshydratation

de l'antigorite à 3 GPa. Merci à Denis Andrault, de m'avoir permis d'approfondir mes travaux à l'issue de ma thèse.

Bien que la totalité de l'étude concernant le XANES sur les expériences de fusion partielle en conditions hydratées ne figure pas dans ce manuscrit, beaucoup de temps et d'efforts y ont été consacrés et je tiens à remercier ceux qui m'ont aidé à parvenir au meilleur protocole expérimental possible et à mieux comprendre les analyses et données obtenues au synchrotron. Merci à Pierre Condamine et Davide Novella. Vous m'avez donné des conseils basés sur votre propre expérience de ce genre d'expériences hydratées tumultueuses qui m'ont été très utiles. Merci Amrei Baasner de m'avoir guidée dans ma quête de composition initiale pour des expériences optimales, et merci pour tes expériences de piston cylindre. Merci aussi à Muriel Laubier, pour les chouettes discussions au cours des temps de faisceau et pour ton aide lors du traitement de données. Merci pour tes conseils et ta bienveillance tout au long de ma thèse.

Merci à Jean-Luc Devidal, pour toutes ces heures de calibration et de diagnostique « minéraux non identifiés » à la microsonde. Merci aussi pour les discussions sympas entre deux points d'analyse, c'est un plaisir de travailler avec toi ! Merci de m'avoir sacré manipulatrice officielle de métaliseur. Merci à Jean-Marc Hénot d'avoir tellement de fois changé le filament après mes passages intensifs de maltraitance du MEB, la malédiction est levée ! Merci de m'avoir formée à être autonome pour mes nombreuses cartographies et merci pour ton implication pour l'EBSD. Merci Mahmmed Benbakkar pour la composition en roche totale de la serpentine que j'ai utilisée dans mes expériences et ton sourire. Merci Franck Pointud pour tes interventions d'urgence sur la presse 1000 tonnes, même au milieu de ta semaine de court-métrage/vacances. Merci aussi Antoine Mathieu pour ta disponibilité et ton expertise sur la presse 1500 tonnes. Merci Claire Fonquernie pour ton aide dans le broyage de la serpentine, et merci à Jean-Luc Fruquière et Cyrille Guillot pour les préparations des pièces d'assemblage de multi enclume. Merci à Chistophe Constantin pour la préparation de l'unique et très importante lame mince que j'ai côtoyée pendant des années. Merci à Chantal Bosq d'avoir accepté de passer quelques creusets à l'HF pour moi.

Merci à Sandrine Sicard, Cécile Sergère, Marie-Christine Auzolle, Audrey Chazal et Véronique Gimenez pour votre aide dans les démarches administratives. Merci à Thierry Hamel pour les salvatrices interventions informatiques diverses et variées !

Merci à tous les thésards et les post docs avec qui j'ai pu partager de super moments. Merci aux copains de début de thèse, Lola, Marina, Angélie, Corentin, Baptiste, Vincent, Nina,

Cotto, Julien et Julien, Asmaa, Giacomo, Camille, Oscar, Amélie, Simon, Yannick, Baptiste, Elodie, Gareth, Engielle, Grace, Lydie, Nico, Mathias. Merci à Marine. Vous m'avez tellement fait rigoler ! C'est une période dont je me souviens avec un grand sourire. Merci aux autres copains de milieu et fin de thèse, en particulier à la team Valentins (je sais que vous êtes deux personnes distinctes, mais la synergie était parfaite). Vous avez rendu la rédaction presque marrante. Non, ce n'est pas vrai mais c'était un plaisir de partager le bureau avec vous et j'ai adoré votre capacité à me rebooster avec les pires blagues pourries et inavouables qui soient. Et puis merci à ceux qui ont aussi contribué à détendre l'ambiance de fin de thèse, Pierre, Marie-Anne, Mélo, Marion, toujours de très chouettes moments avec vous. Merci aux pétroguys de dernière génération, Damien, Lois et Nathan pour les discussions qui n'ont aucun sens (pas uniquement, mais celles-là comptent particulièrement !).

Merci à mes super copines de toujours pour votre soutien, votre patience devant ma disparition de la circulation pendant quelques années, Coralie, Véro, Lucie, Noémie et Lucie, vous étiez (bien trop loin), mais vous étiez là quand même !

Merci à Taya pour avoir été une coloc, amie et collègue géniale. Taya, merci pour tous ces moments, un peu partout et un peu tout le temps. Ces moments de joie, de rigolade, de calme aussi, d'échange et d'apprentissage beaucoup, et parfois même de tristesse, qui m'ont permis de découvrir malgré le chaos de la thèse (porté au carré) une personne profondément honnête, gentille et forte. C'était formidable de partager ce temps avec toi, je m'en sens grandie et reconnaissante !

Merci à Dominique Faure, sans votre soutien, cette thèse n'existerait tout simplement pas.

Finalement, merci à ma famille ! Merci à mes parents de m'avoir soutenue tout ce temps. Merci d'avoir été patients et réconfortants quand je doutais, d'être pleins de compassion dans mes aventures. Merci maman de t'être toujours préoccupée que je conduise avec les deux mains sur le volant, et pas en sens interdit, ça aurait pu mal se passer. Merci papa d'avoir fait du sauvetage de fichier word, et ce, même au détriment de la sieste sacrée. Un énorme merci pour toutes les super choses trop bonnes dont vous vous êtes occupés pour mon pot de soutenance, c'était génial ! Merci Quentin pour ton soutien métaphysique, mais aussi de t'être bien assuré que je mangeais assez de graines au gluten. Merci à ma petite sœur la meilleure du monde ! Merci d'avoir été tellement tellement une bouffée d'air pour moi pendant ma thèse. Tu m'as beaucoup soutenue et tu m'as fait mourir de rire, on a partagé plein de moments géniaux, et de

situations à la tuche ensemble, et on sait que c'est ça la vraie vie. D'ailleurs, merci Mamie Suz' pour la Suze ! Et aussi pour ta gentillesse et tes encouragements !

Mes excuses aux personnes qui de près ou de loin ont participé à rendre cette thèse possible et ce qu'elle est, et que j'aurais oublié de mentionner dans ces quelques paragraphes.

Résumé

Les serpentinites sont les roches produites par l'hydratation de la péridotite au niveau du plancher océanique. L'antigorite est la phase de haute température et haute pression appartenant au groupe minéral des serpentines, pouvant contenir dans sa structure jusqu'à 13 wt% H_2O, et permet ainsi le transfert de quantités considérables d'eau dans le manteau, à travers les processus de subduction. Sa déstabilisation est fonction du chemin thermique emprunté par la plaque plongeante. Durant cette thèse nous avons étudié deux cas de figure pour la déshydratation de l'antigorite menant soit à la libération des fluides dans le coin mantellique et à la production des magmas d'arc, soit au transfert de l'eau à plus grandes profondeurs).

Dans un premier temps, des expériences de déshydratation d'antigorite naturelle ont été conduites sur la presse multi-enclumes à 3 GPa et entre 600 et 900°C. Les conditions oxydantes ou bien réductrices ont été contrôlées par le dispositif expérimental (four en graphite ou en chromite de lanthane). Cette étude a permis de caractériser les produits de déshydratation de l'antigorite dans un système chimique représentatif des systèmes naturels ainsi que de contraindre l'état redox des réactions associées. En effet, les résultats mis en avant par cette étude montrent une fO_2 équivalente au tampon Quartz-Magnétite-Fayalite (QFM) +5. Un tel potentiel oxydant des fluides issus de la déshydratation de l'antigorite soutient l'hypothèse de l'oxydation de la source mantellique des magmas d'arcs, présentant des rapports Fe^{3+}/Fe_{total} plus élevés que les basaltes de ride médio-océanique par exemple.

Dans un second temps, nous nous sommes intéressés aux modalités de transfert de l'eau dans le manteau profond. L'antigorite naturelle a cette fois été déstabilisée à de plus fortes pressions allant de 6.5 à 10 GPa pour des températures comprises entre 500 et 850°C. Ces résultats expérimentaux, ainsi qu'une analyse géométrique des relations de phases dans le

system FMASH selon la méthode de Shreinemaker, ont mis en avant des modifications dans le diagramme de phase pour un système ultramafique hydraté en comparaison des études précédentes. En effet, la phase A est communément décrite comme le produit de déstabilisation de l'antigorite à haute pression, tandis que la phase E n'apparait qu'à des profondeurs plus importantes. Nos résultats suggèrent, dans le système naturel enrichi en aluminium et en fer, une stabilité continue des phases hydratées, suivant la transition antigorite > phase E > phase A pour des températures inférieures à 750°C. Cette étude a également permis d'affiner les estimations des quantités d'eau pouvant être stockées dans les assemblages de minéraux hydratés stables dans la lithosphère plongeante (slab). Dans le cas des plaques plongeantes relativement froides (<750°C à 8-10 GPa) le transport de l'eau par le biais des « Dense Hydrous Magnesium Silicates » (DHMS) phase A et phase E soutient l'hypothèse de l'hydratation de la zone de transition dans le manteau.

Mots clés

Antigorite
Fluides issus du slab
Fluides oxydants
Transport de l'eau
DHMS – phase A – phase E - balangeroite
Équilibre de phases hydratées
Presse multi enclumes

Abstract

From the Mid-Oceanic-Ridge to the subduction trench, hydration of peridotite minerals in the upper part of the oceanic lithosphere produces hydrous phases such as serpentine. Because of its high-water content (13 wt% H_2O) this mineral family is of particular interest for water fluxes. Depending on the thermal path followed by the lithosphere while sinking into the mantle, antigorite destabilization can either lead to fluid release in the mantle wedge or water transfer to deeper levels. During this thesis we conducted experimental investigations of antigorite dehydration in the framework of these two scenarios.

First, we investigated antigorite dehydration under conditions relevant to slab water release, known to trigger partial melting and to generate arc magmatism. Multi-anvil experiments were conducted on a natural serpentinite sample, at 3 GPa and between 600 and 900°C under different redox conditions. We were able to constrain phase assemblages produced by antigorite dehydration as well as the fO_2 of such reactions to 5 units above the FMQ (Fayalite-Magnetite-Quartz buffer). These results support the oxidizing character of slab released fluids, that could explain the oxidized character of arc magmas compared to Mid-Oceanic-Ridge basalts or Oceanic-Island basalts.

The second experimental work conducted during this thesis allowed to refine phase equilibria involving antigorite and the Dense Hydrous Magnesium Silicates (DHMS) phase A and phase E, in a realistic chemical composition for hydrated ultramafic system. Antigorite destabilization was performed between 6.5 and 10 GPa, for temperatures in the range <500-850°C. Our experimental results, together with a Shreinemaker's analysis in the FMASH system led to establish a modified phase diagram compared to those presented in previous studies. While phase A has been described as the high-pressure product of antigorite breakdown in the literature, followed by phase E stability at higher pressure, we propose the transition

antigorite>phase E>phase A for the aluminous and iron-rich hydrated peridotite system. This study allowed the refinement of water budgets that can be stored in relatively cold slabs (<750°C at 8-10 GPa), supporting the hypothesis of water survival down to the transition zone.

Key words

Antigorite

Slab derived fluids

Oxidizing fluids

Water transfer

DHMS – phase A – phase E - balangeroite

Hydrous phase equilibria

Multi-anvil apparatus

Résumé détaillé

Contexte

Les processus de subduction permettent le recyclage de l'eau à l'échelle de la Terre globale. À mesure que la lithosphère océanique nouvellement créée s'éloigne de la dorsale océanique, ses minéraux incorporent progressivement de l'eau, qu'ils composent les sédiments, les lithologies crustales ou encore ultramafiques. Sous l'effet d'une plus forte densité, ainsi que de son refroidissement, la lithosphère océanique plonge dans le coin mantellique, sous une autre plaque lithosphérique plus chaude et/ou moins dense. Tandis que cette plaque plongeante, également appelée « slab » s'enfonce, ses minéraux subissent une augmentation importante de température et de pression, aboutissant à leur déshydratation. Ce phénomène engendre la libération de fluides dans le coin mantellique, à l'origine de sa fusion partielle et du magmatisme d'arc. Il a été observé que les magmas d'arc possèdent des rapports $Fe^{3+}/\Sigma Fe$ plus élevés que les MORBs (Mid-Oceanic-Ridge-Basalts) avec des valeurs variant entre 0.18 et 0.32 (Kelley and Cottrell, 2009) versus 0.13 à 0.17 respectivement (Bézos and Humler, 2005; Cottrell and Kelley, 2011). Ce rapport exprimant la quantité de fer ferrique par rapport au fer total dans la composition d'un liquide est reflet de son degré d'oxydation. En effet plus le magma est oxydé, plus il contient de fer ferrique, par rapport au fer total (addition de fer ferrique et fer ferreux). Deux hypothèses sont avancées pour expliquer une apparente plus forte oxydation des magmas d'arcs en comparaison aux MORBs. Dans un premier temps, cela pourrait être expliqué par des processus tardifs dans l'évolution des magmas, comme par exemple des phénomènes d'assimilation, de cristallisation fractionnée, ou encore de dégazage. Cette hypothèse suggère que la source de ces magmas d'arcs ne serait donc pas plus oxydée que celle des MORBs (Lee et al., 2005; Mallmann and O'Neill, 2009). Cependant, les xénolites associés aux zones de supra-subduction témoignent de fugacité d'oxygène élevée pour la source

des magmas d'arc, jusqu'au niveau du tampon FMQ+2 (Fayalite-Magnétite-Quartz) (Brandon and Draper, 1996; Carmichael, 1991; Parkinson and Arculus, 1999). La seconde hypothèse est plutôt en faveur d'une oxydation de la source de ces magmas, et il est envisagé qu'une telle oxydation puisse être imposée par l'oxydation du slab, et en particulier par les fluides qui en sont libérés (Evans, 2012; Kelley and Cottrell, 2012; Frezzotti et al., 2011; Tumiati et al., 2015).

Bien qu'une grande partie de l'eau incorporée par le slab soit libérée au cours de la subduction et dégazée au niveau des volcans d'arc, des minéraux hydratés de haute pression permettent une conservation partielle d'eau à plus grande profondeur dans le manteau. La convection mantellique permet de répartir ces fluides à l'échelle globale, comme un témoigne le dégazage au niveau des dorsales et des arcs océaniques. Néanmoins, des estimations de flux globaux on permit de mettre en évidence que la totalité de l'eau enfouie avec le slab n'était pas retournée en surface et qu'une partie de cette eau pourrait rester stockée en profondeur dans le manteau.

Dans le cadre de la compréhension des flux d'eau associés aux zones de subduction, les serpentinites présentent un intérêt particulier. Ces roches sont formées par l'altération de la péridotite au niveau du plancher océanique, notamment au niveau des fractures et failles. L'antigorite est le minéral appartenant à la famille des serpentines, stable à haute pression et haute température. Ce minéral contient jusqu'à 13 pourcents de son poids (wt%) d'eau dans sa structure. De part cette teneur en eau élevée et son abondance dans la lithosphère océanique, l'antigorite est considérée comme le principal transporteur d'eau et joue ainsi un rôle majeur dans la libération de fluides à mesure que le slab plonge dans le coin mantellique et se réchauffe (Ulmer and Trommsdorff, 1995). Les conditions de pression et température suivant lesquelles la déshydratation de l'antigorite est effective sont critiques en ce qui concerne le devenir de l'eau qu'elle contient. Il va de même pour les conditions de stabilité des minéraux hydratés présents au-delà de la stabilité de l'antigorite, à des conditions de pression intermédiaires

(clinohumite, phase 10Å, chondrodite, Mg-Sursassite...) et à haute pression (phases denses silicatées et magnésiennes hydratées, ou Dense Hydrous Magnesium Silicates – DHMS). La répartition relative dans l'espace pression-température des champs de stabilité de ces différents minéraux hydratés (la façon dont ils sont connectés ou non) définit la possibilité d'un transfert éventuel de l'eau contenue initialement dans le slab, ou bien sa libération dans le coin mantellique. Après la déstabilisation de l'antigorite, à haute pression et basse température, se forme la phase A. À plus haute pression encore, la déstabilisation de la phase A produit la phase E. Les conditions de stabilité de ces « phases alphabet » sont plus ou moins connues grâce aux apports de la pétrologie expérimentale, notamment grâce aux expériences menées dans le système chimique MgO-SiO_2-H_2O (MSH). Cependant, l'effet stabilisant thermique de l'aluminium sur quelques phases hydratées a été mis en avant pas des études expérimentales menées dans des systèmes alumineux, en particulier dans le cas de l'antigorite (Bromiley and Pawley, 2003), la chlorite, ou encore la phase hydratée de haute pression nommée phase D. De plus l'ajout d'aluminium modifie les relations de phases en ajoutant de nouveaux minéraux aux assemblages existant dans le système MSH, comme par exemple le pyroxène alumineux ou Hydrous Al-bearing Pyroxene (HAPY phase) la phase 11.5Å et la phase 23.5Å.

Objectifs de la thèse

Le centre d'intérêt principal de cette thèse s'articule autour des réactions de déstabilisation de l'antigorite naturelle, afin de mieux comprendre les flux de fluides associés à phénomènes de subduction. Cette thèse s'attache en particulier à contraindre les conditions redox associées à la libération de fluides dans le cas de la déshydratation de l'antigorite à basse pression (3 GPa, chemin bleu sur la figure 1) ainsi que les modalités de transfert d'eau à haute pression (6.5-11 GPa) au-delà de la stabilité de l'antigorite (chemin jaune).

Afin de mieux comprendre si l'hypothèse d'un coin mantellique oxydé par les fluides issus de la subduction (dans le cas présent, issus de la déshydratation de l'antigorite) est envisageable, nous nous sommes intéressés aux produits de déshydratation de l'antigorite à 3 GPa, c'est à dire environ 100 km de profondeur, ce qui correspond à la profondeur de la fusion du coin mantellique, source des magmas d'arc.

Le deuxième centre d'intérêt de cette thèse concerne le potentiel de transfert d'eau en profondeur par les minéraux hydratés de haute pression, par exemple la phase A et la phase E. Nous nous sommes particulièrement intéressés au rôle de l'aluminium sur le diagramme de phase pour un système proche de la péridotite hydratée, ainsi qu'au rôle du fer. Nous avons pour cela conduit des expériences de déstabilisation d'antigorite naturelle et observé les assemblages minéralogiques formés entre 6.5 et 11 GPa, pour des températures variant entre 500 et 850°C.

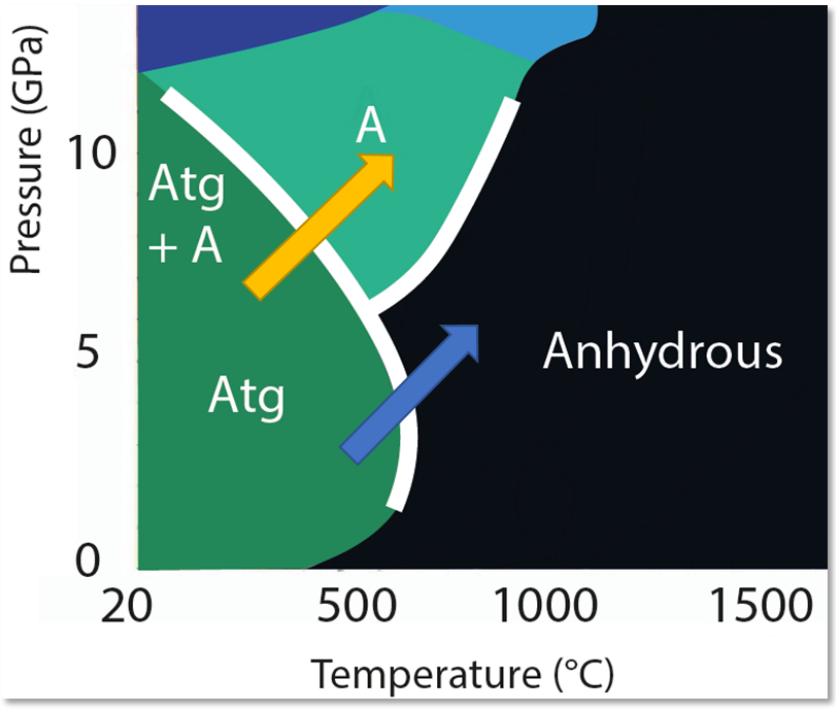

Figure 0-1. Diagramme de phase simplifié représentant les domaines de stabilité de l'antigorite, de la phase A et des minéraux nominalement anhydres (en noir). Les deux principales zones d'investigation expérimentales examinées au cours de cette thèse sont représentées par les deux flèches.

Organisation du manuscrit

Cette thèse s'articule autour de 7 chapitres. Le premier chapitre est consacré à une revue de la littérature concernant le recyclage de l'eau en lien avec les processus de subduction. Le second chapitre présente les différents minéraux hydratés d'intérêt pour la lithosphère océanique subduite, et en particulier l'antigorite, ainsi que les DHMS tels que la phase A et la phase E. Le chapitre 3 présente les différents aspects méthodologiques de cette thèse. Le choix de l'échantillon de départ d'antigoritite naturel y est expliqué, ainsi que les techniques expérimentales utilisées (multi enclumes) puis les différentes techniques d'analyse du matériel de départ ainsi que des produits expérimentaux sont exposés. Le quatrième chapitre est présenté sous forme d'un article soumis à publication. Il concerne les conditions redox associées à la déstabilisation de l'antigorite à 3 GPa. Le chapitre 5 correspond à une description détaillée de l'approche méthodologique utilisée afin de contraindre les relations de phases post antigorite complexes associées au système naturel (riche en fer et aluminium). Le chapitre 6 correspond à la version de cette étude soumise à publication. Cet article s'attache plus particulièrement à un bilan de la composition chimique de chaque phase minérale produite, ainsi qu'au rôle de la magnétite (comme source de fer, ferreux et ferrique) et de l'aluminium dans la nature des assemblages minéralogiques formés à haute pression, suite à la déshydratation de l'antigorite. Finalement, le chapitre 7 est une discussion s'attachant à mettre en évidences les limites des expériences conduites en systèmes synthétique et simplifiés, en comparaison à la complexité des relations de phases ayant lieu dans la nature. L'importance d'acquérir de nouvelles données thermodynamiques en accord avec la composition naturelle des minéraux hydratés est ici soulignée, afin de pouvoir utiliser à profit le pouvoir des simulations thermodynamiques (entre autres via le logiciel Perplex) et de mieux contraindre les équilibres de phases pertinents dans le cas de la lithosphère hydratée subduite.

Méthodes expérimentales et analytiques

Dans le but de rester aussi proche que possible des conditions naturelles, nous avons choisi un échantillon de serpentinite naturel. Cet échantillon est composé d'antigorite à environ 95 % et de 5 % de magnétite (et en minorité d'oxydes métalliques appartenant à la famille des spinels : Al-spinel et chromite). En effet, bien que les mélanges d'oxydes synthétiques offrent la possibilité d'établir les relations de phases nécessaires à une compréhension de premier ordre des équilibres de minéraux représentatifs de la lithosphère océanique hydratée, ils ne permettent pas de comprendre de tels équilibres pertinents pour un système chimique naturel. L'utilisation d'antigoritite naturelle permet de préserver la complexité chimique de roche telle qu'elle existe dans de réelles conditions de subduction. En particulier, l'antigorite possède une structure spécifique, affectant ses conditions de stabilité en fonction de la pression et de la température. L'utilisation d'un échantillon naturel permet notamment de préserver son caractère oxydé, comme en témoignent les rapports $Fe^{3+}/\Sigma fe$ élevés (0.5-0.7) (Andreani et al., 2013; Debret et al., 2015; Marcaillou et al., 2011). De plus, cet échantillon contient environ 5 % de son poids de magnétite, permettant de reproduire les conditions de déshydratation naturelles ayant lieu dans la subduction de serpentinites, qui elles-mêmes sont composées de magnétite jusqu'à 7% (Debret et al., 2015, 2014, Padrón-Navarta et al., 2013, 2011; Schwartz et al., 2013). Reproduire un tel minéral par synthèse à base de poudres d'oxydes ou de gel est difficile. Le choix de ne pas broyer le matériel de départ afin de l'utiliser sous forme de poudre permet également d'éviter la contamination en CO_2, associée à l'utilisation d'éthanol. Une telle contamination pourrait en effet affecter les équilibres de phases, comme certains auteurs ont pu le constater lors d'ajout de carbonates dans leurs compositions (Luth, 1995). Le choix d'un matériel naturel représente cependant un certain inconvénient par rapports aux produits synthétiques, l'atteinte de l'équilibre réactionnel étant plus long. Nous avons cependant pu attester de l'équilibre des réactions lors de nos expériences, de par la croissance de minéraux

homogènes, la mise en évidence de systématiques dans le partitionnement des éléments ainsi que par les bilans de masses.

L'échantillon utilisé provient de serpentine naturelle de la région Iron Mountain des Cascades du nord dans l'état de Washington aux Etats-Unis, il nous a généreusement été fourni par David Mainprice (Géosciences Montpellier). Il est composé d'une matrice d'antigorite, dont la composition suit la formule $Mg_{2.7}Fe_{0.1}Al_{0.09}Si_{2.02}O_5(OH)_4$. L'observation au microscope optique d'une lame mince à révéler la présence de d'oxydes métalliques (de fer) répartis en agrégats et veines. Les analyses à la microsonde électronique ont permis de mettre en évidence trois principales catégories de minéraux pour ces oxydes métalliques, appartenant à la famille des spinels. Il s'agit de spinel $(Mg,Fe)Al_2O_4$, de chromite $(Mg,Fe)Cr_2O_4$ et de magnétite $(Mg,Fe)_3O_4$, hérités du protolithe péridotitique (Bliss and MacLean, 1975). Les agrégats de spinel (jusqu'à 900 µm de largeur) présentent une double couronne de chromite riche en fer et de magnétite. La magnétite se retrouve également sous forme de grains d'environ 100 µm de largeur formant des veines (3 mm de longueur maximum). L'antigorite contient environ 12.04 wt% d'eau, et la roche totale environ 11.4 wt%. Afin d'attester de l'homogénéité de la répartition de la magnétite au sein des cylindres de matériel utilisé pour les expériences, 5 fragments de roche ont été sélectionnés. Ils ont été broyés séparément puis analysés par Inductively Coupled Plasma Atomic Emission Spectroscopy (ICP-AES). Les résultats suggérèrent bien une homogénéité de composition chimique avec de faibles déviations standards sur les éléments majeurs 40.04 ± 0.3 wt% SiO_2, 1.63 ± 0.11 wt% Al_2O_3, 7.79 ± 0.48 wt% FeO, and 38.94 ± 0.40 wt% MgO. Les cylindres forés dans l'échantillon mesurent 3 mm de diamètre pour les expériences à 3 GPa, et 2mm pour les expériences entre 6.5 et 11 GPa. Les expériences ont été réalisées à l'aide des deux presses multi enclumes de type Kawai du Laboratoire Magmas et Volcans. Il s'agit de système hydraulique permettant de générer des conditions de pression (jusqu'à 25 GPa – 750 km de profondeur) et de température

représentative du manteau terrestre. Le premier niveau d'enclumes forme une cavité cubique ou vient se loger le second niveau d'enclumes en carbure de tungstène. Ce deuxième niveau produit une cavité octaédrique, dans laquelle est positionné un octaèdre composé de matériau transmetteur de pression (MgO + 5% Cr_2O_3), lui-même contenant l'échantillon. Différentes tailles d'octaèdre permettent d'accéder à différentes gammes de pression. La calibration en pression de la presse a été effectuée en observant les transitions de phases Bi(I)-Bi(II) à 2.55 GPa et Bi(III)-Bi(V) à 7.7 GPa.

Le cylindre de serpentinite est placé dans un tube composé d'un alliage d'or et de palladium, soudé de part et d'autre et formant la capsule métallique. Cet alliage est particulièrement intéressant pour les expériences sur des échantillons contenant du fer car il limite les alliages fer/métal en comparaison au platine couramment utilisées en pétrologie expérimentale. L'échantillon est porté à haute température grâce à un four à trois étages, dont la partie centrale est plus épaisse, en vue de limiter les gradients thermiques au sein de la capsule. Deux matériaux sont utilisés, le graphite et la chromite de lanthane pour leurs différentes capacités résistives. Le graphite est plus particulièrement utilisé à basse pression (en dessous de 10 GPa, avant la transition graphite/diamant) mais nous avons également utilisé le four en chromite de lanthane à 3 GPa, dans le but de modifier les conditions redox environnantes au cours de la déshydratation de la serpentinite. Un courant électrique est produit par un générateur externe, et la chaleur est ainsi produite par effet Joule associé aux propriétés du four cylindrique. La température est contrôlée grâce à un thermocouple placé à l'intérieur de l'assemblage, au contact de la paroi supérieure de la capsule métallique.

Les échantillons sont ainsi portés à haute pression dans un premier temps. Ce stade de compression est progressif, sur environ 3 à 4 heures pour les pressions ici atteintes. Une fois le pallier de pression visée atteint, l'échantillon est porté à la température souhaitée, pour des durées variables. Les échantillons sont récupérés à la fin de la décompression (au moins 9

heures, pour éviter provoquer la fracture des enclumes de carbure de tungstène). La capsule métallique est sortie à la main de l'assemblage puis placée dans une résine d'« époxy ». La capsule est amenée à l'affleurement du plot de résine en polissant grossièrement sa surface. Dès que la capsule est percée sur le flanc, elle est plongée dans de l'éthanol, ce qui permet de vérifier l'échappement de petites bulles, attestant de la saturation en eau de l'expérience de déshydratation. La capsule est ensuite polie plus finement, jusqu'à pouvoir observer l'échantillon sur toute la coupe latérale de la capsule cylindrique. Une fine couche de carbone est finalement déposée sur la surface de l'échantillon, afin d'améliorer la conductivité durant les diverses analyses aux microscopes électroniques.

Étude expérimentale de déshydratation de l'antigorite naturelle à 3 GPa : Implications pour les conditions de fugacité d'oxygène lors de la déshydratation du slab

Les expériences de déshydratation de la serpentinite à 3 GPa visent à reproduire les réactions ayant lieu dans des conditions naturelles de subduction, notamment en préservant le caractère intrinsèque des conditions d'oxydation accompagnant ce processus. Ces expériences ont été conduites entre 600 et 900°C en presse multi-enclumes dans un environnement redox le plus neutre possible, c'est-à-dire en utilisant un four en chromite de lanthane, au caractère oxydant. Ce dernier est en accord avec le fort degré d'oxydation des serpentinites naturelles, contrairement au four en graphite plus traditionnellement utilisé dans les techniques de pétrologie expérimentales à de telles pressions. En effet le four graphite possède quant à lui un caractère réducteur, qui altérerait la nature de l'échantillon de départ. Afin de mettre en avant l'importance de cet environnement, deux expériences ont été menées avec un four en graphite.

Quatre différents assemblages minéralogiques ont ainsi été obtenus après déstabilisation de la serpentinite, et correspondent à quatre étapes de déshydratation. L'antigorite initiale se

déstabilise dans un premier temps seulement partiellement (à 580°C), et produit un assemblage composé d'antigorite secondaire et d'un fluide (H_2O). Avec l'augmentation de la température (680-690°C), l'antigorite continue de se déstabiliser et produit un assemblage contenant de l'antigorite secondaire, de la chlorite, de l'olivine, de l'enstatite et du fluide (700-800°C). Après déstabilisation totale, l'antigorite s'est décomposée en chlorite + olivine + enstatite + H_2O, et finalement l'étape finale de déshydratation est observée avec l'assemblage olivine + enstatite + H_2O (900°C). Concernant l'évolution chimique des minéraux observés, une augmentation de la teneur en fer dans l'antigorite secondaire a été notée. Cette évolution du fer est en accord avec les observations dans le cas des roches naturelles (Debret et al., 2014), suggérant la dissolution de la magnétite simultanément à la déshydratation de l'antigorite. L'aluminium quant à lui diminue dans l'antigorite secondaire, par rapport à l'antigorite initiale. Ceci est expliqué par la cristallisation de chlorite riche en aluminium. Une augmentation de la teneur en fer dans l'olivine et l'enstatite après la déstabilisation complète de l'antigorite et de la chlorite est observée, de façon similaire à l'évolution des minéraux secondaires dans les serpentinites naturelles. De plus, la déshydratation de l'antigorite s'accompagne de la formation de lamelles d'hématite, au sein de la magnétite préexistante, également observé dans les échantillons naturels (Debret et al., 2015). La présence d'hématite dans les produits expérimentaux prouve que sa cristallisation dans les roches naturelles n'est pas un artéfact rétrograde. L'antigorite est riche en Fe^{3+}, qui est partiellement redistribué parmi les produits de sa déstabilisation. Cependant, la chlorite n'incorpore pas autant de Fe^{3+} que la quantité initialement contenue dans l'antigorite, et l'enstatite dans des quantités moindres (maximum 10% du fer total) et l'olivine ne présente que du Fe^{2+}. La déshydratation de la serpentine correspond en effet à une réduction du fer ferrique, en fer ferreux dans ces minéraux secondaires. Cela implique une remobilisation du caractère oxydé de la serpentinite initiale. La mobilité du fer est réduite dans les fluides aqueux, et s'effectue principalement par le biais d'espèces Fe(II)-SO_4^{2-}. La déstabilisation

d'antigorite et la dissolution de magnétite simultanée ne peuvent alors être associées qu'avec une réaction libérant de l'oxygène. Cet élément est cependant très peu mobile dans les fluides. La présence d'hématite au sein de nos expériences, ainsi que dans le cas des échantillons naturels, témoigne de la consommation d'oxygène excessif libéré lors de la déshydratation de la serpentinite. Cela permet de plus de contraindre la fugacité d'oxygène associé à cette réaction de déshydratation au niveau du tampon magnétite-hématite, c'est-à-dire entre 10^{-4} to 5.10^{-2} bars. En revanche, l'hématite n'apparait pas dans les produits de déshydratation d'antigorite pour les expériences conduites avec un four en graphite. L'absence d'hématite est également notée dans le cas des expériences similaires conduites en piston-cylindre avec un four en graphite présentées dans Merkulova et al. (2016, 2017). Un dispositif incluant un four en graphite induit en effet un transfert d'hydrogène en direction de l'échantillon, qui impose des conditions réductrices n'existant pas dans les réactions naturelles, et empêchent donc l'oxydation de la magnétite en hématite. L'oxygène n'étant pas mobile dans les fluides, différents mécanismes de transfert de l'oxydation des serpentinites au coin mantellique sont envisagés dans la littérature récente. Un tel transfert est vraisemblablement possible via des espèces $SO_4^{2-}{}_{(aq)}$, quant à elles mobiles dans les fluides, et pouvant potentiellement oxyder le coin mantellique, source des magmas d'arc (Debret et Sverjensky, 2017).

Stabilité des phases hydratées au-delà de la déstabilisation de serpentine naturelle contenant de la magnétite entre 6.5 et 11 GPa

À l'opposition de la libération de fluides issus de la déshydratation de l'antigorite dans le cas d'un slab relativement chaud, une conservation partielle de l'eau initialement contenue dans l'antigorite est possible dans le cas des slabs plus froids. La déstabilisation de l'antigorite à haute pression (supérieure à 5 GPa) et à des températures relativement faibles permet la formation de la phase A contenant également de l'eau dans sa structure. Cette réaction est traditionnellement présentée comme la possibilité de transférer de l'eau en profondeur dans le

manteau. La réaction de déstabilisation de la phase A produisant de l'olivine et une phase fluide est quant à elle considéré comme la réaction limitant cette possibilité de transfert, et a été désignée comme la « water line » (Liu, 1987). Elle permet de délimiter la zone de stabilité de minéraux hydratés du côté des faibles températures, de la zone de stabilité de minéraux nominalement anhydres tels que l'olivine, le pyroxène et de phase fluide libre du côté des plus fortes températures. Cette région du diagramme de phase est relativement bien contrainte grâce aux études expérimentales concernant la stabilité des phases dans le système $MgO\text{-}SiO_2\text{-}H_2O$. Le point triple impliquant les stabilités de l'antigorite et la phase A est suggéré aux alentours de 5 GPa et 550°C (Komabayashi et al., 2005). Cependant, il n'existe pas d'étude dans le cas de serpentine naturelle, présentant une composition chimique plus complexe. Connaitre les relations de phases post antigorite à haute pression et dans le cadre d'une composition naturelle est pourtant cruciale afin de mieux comprendre les modalités de transfert d'eau en profondeur dans le manteau via la lithosphère hydratée. En effet, il a été démontré que l'aluminium possédant un effet stabilisant thermique sur certains minéraux hydratés tels que l'antigorite, la chlorite ou encore la phase D ou la phase H à des conditions extrêmes. En addition de modifier les domaines de stabilités des minéraux hydratés, l'ajout d'aluminium introduit de nouvelles espèces minérales dans les assemblages, et modifie ainsi le diagramme de phase de la péridotite hydratée. De la même façon, l'effet de l'ajout de fer au simple système MSH peut modifier les relations de phases.

Nous avons donc examiné la déstabilisation d'antigorite naturelle contenant aluminium et fer, entre 6.5 et 11 GPa, pour des températures variant entre 400 et 850°C à l'aide d'expériences conduites en presse multi-enclumes. La complexité du système chimique investigué produit à des assemblages minéralogiques présentant plusieurs phases. Le système ici étudié est composé d'antigorite, Mg-sursassite, balangeroite, phase A, phase E, brucite, enstatite, olivine, grenat et d'une phase fluide. L'approche géométrique associée à l'analyse de

Schreinemaker permet d'établir le réseau de réactions uni-variantes connectées aux points invariants impliquant les différents minéraux observés dans nos expériences. Cette méthode est basée sur la règle des phases (Gibbs, 1961), selon laquelle le nombre de phases en présence dans un assemblage (P) est lié on nombre de composant chimiques (C) et associé à une grandeur appelée degré de liberté (F) : P+F=C+2. Dans notre cas le nombre de phases correspond aux 9 minéraux observés dans les produits expérimentaux ainsi que la phase fluide, c'est à dire 10. Le système chimique étudié comprend les 10 éléments suivants : SiO_2, TiO_2, Al_2O_3, Cr_2O_3, FeO, NiO, MnO, MgO, CaO et H_2O. Dans le but de simplifier au maximum le nombre de combinaisons possible d'assemblages minéralogiques ainsi que de réactions, nous avons choisi de faire quelques hypothèses en amont de l'analyse de Schreinemakers. Le système a été réduit aux composants MgO-Al_2O_3-SiO_2-H_2O, en négligeant dans un premier temps les oxydes présents en quantités négligeables, tels que TiO_2, NiO, MnO et CaO (0.03, 0.25, 0.09, 0.02 wt%). Dans un deuxième temps, nous avons regroupé les éléments occupant les mêmes sites structuraux dans les minéraux observés. Cela consiste à reporter la quantité de chrome sur celle de l'aluminium, et de même, comptabiliser le fer avec le magnésium. De la même façon, nous avons réduit le nombre de phases considérées dans le système. Par exemple, la brucite n'entre pas dans l'analyse, car elle est certainement liée à une précipitation de fluide riche en magnésium, comme sa présence uniquement en bordure de capsule et en faible quantité le suggère. De plus, la Mg-sursassite n'a été observée que dans une seule expérience et semble reliée à la déstabilisation du grenat et n'a donc pas été prise en compte.

L'antigorite reste stable jusqu'à 8 GPa et 400°C, aucune réaction n'étant observée après le chauffage de l'expérience pendant 8 heures. Les différents assemblages observés dans les expériences de déshydratation et compatibles avec la théorie (règle des phases) sont les suivants : olivine, enstatite, grenat ; olivine, enstatite, Mg-sursassite, phase E, enstatite, olivine ; phase E, enstatite, balangeroite et phase A, phase E, enstatite. La Mg-sursassite est observée à

8 GPa et 550°C, la phase A (cristaux d'environ 20 à 150 µm) apparait avec la phase E entre 550 et 730°C et à 9 et 10 GPa. La phase E se présente sous forme de cristaux petits (<5µm) mélangés dans une matrice contenant également de l'enstatite (même taille de cristaux). À 8 GPa, 700°C et 8.5 GPa, 650°C l'assemblage présente un silicate ferromagnésien hydraté identifié en tant que balangeroite $(Mg,Fe)_{42}Si_{16}O_{54}(OH)_{40}$ (Deriu et al., 1994). La balangeroite se présente dans une matrice fine (taille de grains < 10 µm) d'enstatite et de phase. Ce minéral se retrouve dans deux de nos expériences avec des textures aciculaires (jusqu'à 150 µm de long), similaire aux descriptions texturales dans le cas d'échantillons naturels (Bonaccorsi et al., 2012), ainsi que sous la forme de primes sub-idiomorphiques. À 8 GPa, 650°C et 750°C ainsi qu'à 8.5 GPa, 700°C, le seul minéral hydraté subsistant est la phase E. Elle se déstabilise finalement à plus haute température, et produit l'assemblage anhydre contenant olivine, enstatite et grenat (6.5 GPa, 700°C ; 8 GPa, 800°C and 850°C). Les grenats observés sont de texture poikilitique, et de tailles variées (20 µm à 100 µm). Ils contiennent de nombreuses inclusions d'olivine et parfois d'enstatite et apparaissent préférentiellement en bordure d'échantillon.

Concernant la composition chimique de ces produits de déstabilisation d'antigorite, nous avons pu noter un coefficient de partage du fer entre l'olivine et l'enstatite proche de 1, avec $Kd_{Fe\text{-}Mg}^{\varphi 1/\varphi 2} = (X_{Fe}^{\varphi 1}. X_{Mg}^{\varphi 2}) / (X_{Mg}^{\varphi 1}. X_{Fe}^{\varphi 2})$ où X est la concentration de fer ou magnésium dans la phase φ1 ou φ2. Ce coefficient témoigne de l'atteinte de l'équilibre dans l'expérience. Contrairement à l'enstatite produite à la suite de la déshydratation d'antigorite à 3 GPa, la teneur en aluminium de l'enstatite formée dans les présentes conditions est très faible max. 0.95±0.37 wt.% Al_2O_3). La balangeroite observée présente une composition suivant la formule $(Mg_{34.4}Fe_{6.1}Mn_{0.1}Al_{0.3}Cr_{0.1})_{\sum 41.0}Si_{16.4}O_{54}(OH)_{40}$ et contient environ 11.1 % d'eau Sa présence à haute pression es surprenante. Elle a seulement été reportée dans des affleurements contenant de la chrysotile (forme de basse pression et basse température de la serpentine) dans

la zone Piémontaise des Alpes de l'Ouest en Italie. Des analyses au Raman ont permis de confirmer la nature de ce minéral. L'EBSD a également permis de l'identifier comme ayant une structure particulièrement proche de la gageite, qui correspond au pôle riche en manganèse, également décrit dans des échantillons naturels. Une étude de la structure cristallographique de la balangeroite présente dans ces expériences a également été menée, par diffraction de rayons X, et fait l'objet d'un manuscrit soumis à publication ne figurant pas dans cette thèse. La phase A $Mg_{6.3}Fe_{0.5}Si_{2.1}O_8(OH)_6$ contient environ 11.3 wt% d'eau, et la phase E $Mg_{1.67}Fe_{0.31}Al_{0.27}Si_{1.21}O_{3.55}(OH)_{2.60,}$ environ 11.9 wt%. La composition de la phase E est homogène dans chaque expérience, mais décrit des compositions variables en ce qui concerne sa teneur en aluminium d'une expérience à l'autre (5.5-8.9 wt. % Al_2O_3). Nous avons observé une diminution de cette teneur en aluminium avec l'augmentation de la pression, de la même façon que l'ont observé d'autres auteurs dans des systèmes riches en aluminium, pour des pressions variables : 12-13.8 GPa (Stalder and Ulmer, 2001), 10.3-15.5 GPa (Kawamoto et al., 1995) and 14-17 GPa (Kawamoto, 2004). Le grenat observé au sein des assemblages minéralogiques, principalement à haute température est caractérisé par la chimie suivante : $(Mn_{0.03}Mg_{2.47}Fe_{0.55})^{2+}(Fe_{0.17}Al_{1.64}Cr_{0.09})^{3+}Si_{3.04}O_{12.}$ Le rapport $Fe^{3+}/\sum Fe$ a été estimé entre 0.17 and 0.29 grâce aux données de microsonde électronique combinées à l'équation générale proposée par Droop (1987) (Fe^{3+}= 24*(1-8/∑cations). La méthode de "flank", également accessible à la microsonde électronique (Höfer and Brey, 2007), permet de corréler le ratio $Fe^{3+}/\sum Fe$ avec les raies d'émission FeLα/FeLβ et la teneur FeO totale. Ces résultats nous ont permis d'établir des valeurs du rapport$Fe^{3+}/\sum Fe$ légèrement inférieures variant entre 0.12 et 0.20. Ces gammes de variations restent néanmoins en accord avec les données présentées pour des grenats associées à des compositions de péridotite, avec une valeur maximale de of 0.3 à 4.8 GPa, et 680°C (Fumagalli and Poli, 2005). La Mg-sursassite forme des cristaux sub-

idiomorphiques d'environ 15 µm. Sa composition suit la formule $Mg_{4.6}Fe_{0.3}Al_{3.7}Si_{5.2}O_{21}(OH)_7$, elle contient environ 8 wt.% H_2O.

Une des spécificités de cette étude expérimentale est qu'elle met en avant le rôle de la magnétite dans les équilibres de phases pour le système serpentineux. En effet, l'antigorite seule (X_{Mg}=0.97) ne permet pas d'expliquer la production d'assemblages contenant des minéraux riches en fer tels que la balangeroite, la phase E ainsi que le grenat (X_{Mg}=0.82-0.85). Malgré l'impossibilité de contraindre les teneurs en fer ferrique dans la phase E et la balangeroite, il est fortement probable que ces deux phases en incorporent des quantités non négligeables, à hauteur de grenat par exemple. En effet, la balangeroite naturelle possède un rapport $Fe^{3+}/\sum Fe$ d'environ 0.2 (Deriu et al., 1994).

Une autre particularité de cette étude est la présence de la phase E à des pressions relativement faibles par rapport à son domaine de stabilité présenté dans la littérature au-dessus de 10 GPa. De plus, elle est ici observée avant l'apparition de la phase A (en termes de pression), ce qui est surprenant. Plusieurs hypothèses sont avancées pour expliquer ce phénomène. Dans un premier temps, le rôle de l'aluminium est considéré. En effet, l'aluminium contenu dans l'antigorite de départ est redistribué entre la Mg-sursassite, le grenat et la phase E alumineuse, tandis que la phase A n'en incorpore pas. Cela explique la formation de phase E riche en aluminium aux conditions pour lesquelles ni la Mg-sursassite ou le grenat ne sont stables. Dans un deuxième temps, l'effet de pression chimique exercé par l'incorporation de fer dans la structure des minéraux peut permettre d'expliquer une stabilisation vers de plus basses pressions de la phase E, aux dépends de la phase A. Finalement, la phase E étant un minéral décrit avec un désordre structural, ne présentant pas de stœchiométrie définie et étant qualifiée de phase métastable dans de précédents travaux expérimentaux, nous pouvons nous interroger sur l'éventualité que ce minéral ait bien été présent dans d'autres expériences mais n'ait pas été

identifié. Une texture de matrice à grains très fins comme nous l'avons ici observé pourrait également avoir contribué à l'impossibilité de l'identifier.

Il a été possible d'établir un diagramme de phase général pour le système étudié au cours de cette étude, en combinant nos résultats expérimentaux et la modélisation théorique d'équilibre de phases proposée par Perplex. Tandis que la limite entre les champs de stabilité de minéraux hydratés et les champs de stabilité de minéraux nominalement anhydre en coexistence avec une phase fluide était décrite comme la réaction de déstabilisation de la phase A, nos résultats suggèrent l'implication de la phase E alumineuse avec la réaction terminale Al-PhE = Ol + Grt + H_2O. Pour des températures supérieures à 750-800°C et entre 8 et 11 GPa, la phase E n'est plus stable, et l'assemblage minéralogique est totalement déshydraté. Grâce aux modèles thermique proposés pour un ensemble (à l'échelle du globe) de slabs paramétrisés (Syracuse et al., 2010 ; Van Keken et al., 2011), il est possible de confronter les domaines de stabilité des minéraux hydratés avec les chemins dans l'espace pression-température vraisemblablement empruntés par les slabs et d'en déduire si le transfert d'eau dans le manteau profond est viable ou non. Il apparait peu probable que des slabs de températures intermédiaires à chaudes puissent être vecteurs de transfert d'eau. Plus particulièrement, la réaction terminale de déshydratation de la phase E n'est probablement pas rencontrée par les assemblages minéralogiques d'une lithosphère plongeante. En effet, un slab suivant de telles conditions se serait préalablement déshydraté, et ce dès 600°C à approximativement 6-7 GPa. À l'opposé, un slab relativement froid pourrait permettre le transfert d'eau en profondeur grâce à la continuité des domaines de stabilité de l'antigorite, les phases E et A.

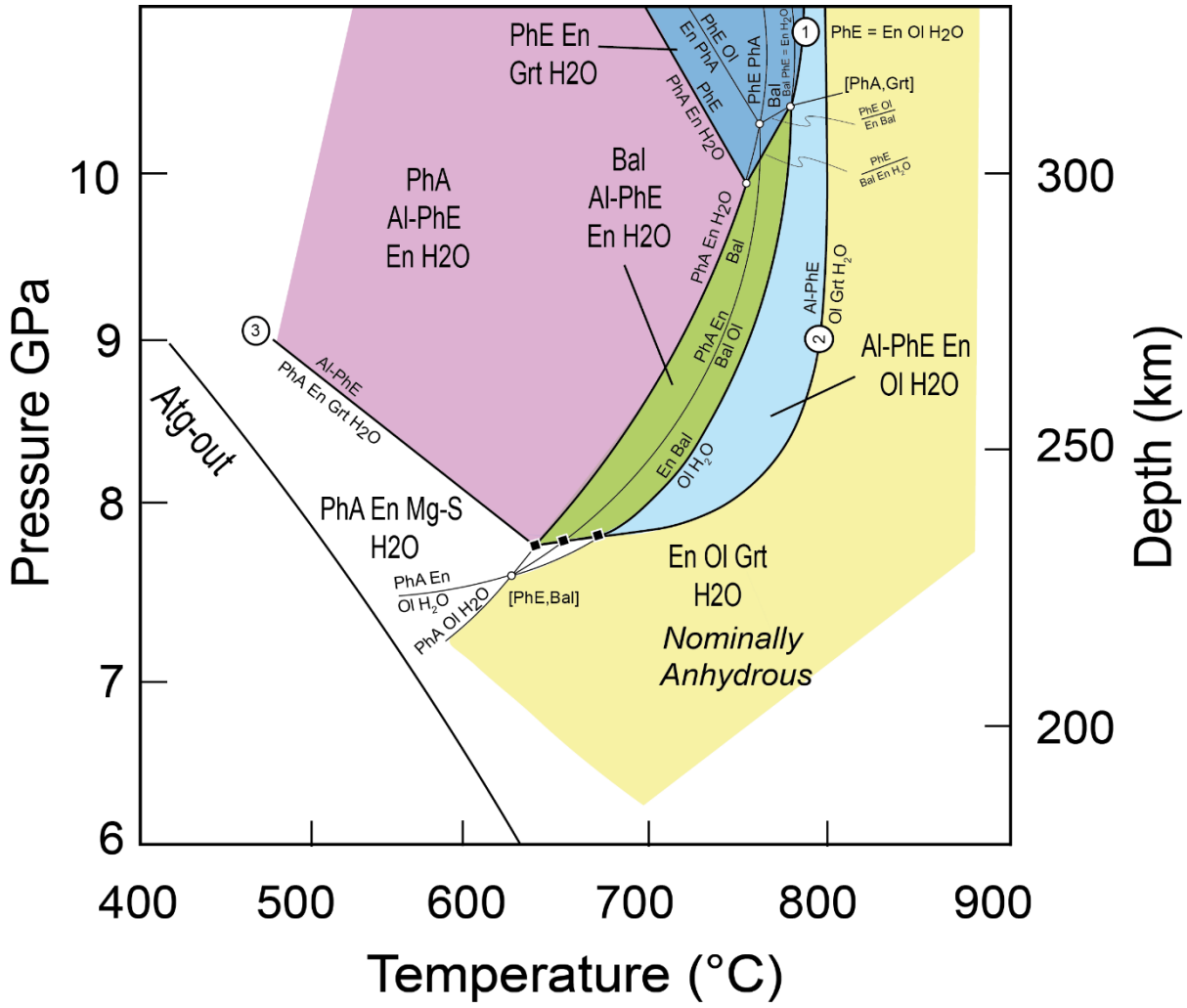

Figure 0-2. Diagramme de phases établi à l'issu de l'étude de déstabilisation d'antigorite naturelle à haute pression. Cette représentation est basée sur les résultats expérimentaux combinées avec une des solutions potentielles pour la projection de Schreinemakers dans le système FeO-MgO-Al2O3-SiO2-H2O (F)MASH impliquant les produits de déshydratation de l'antigorite : olivine (Ol), enstatite (En), Phase A (PhA), Phase E(E), Balangeroite (Bal), Phase E alumineuse (Al-PhE), grenat (Grt) et la phase fluide (H_20).

Des calculs de bilans de masse nous ont permis d'estimer la teneur en eau renfermée par les assemblages de phases expérimentaux. Pour une augmentation graduelle des conditions de pression et de température, les teneurs en eau (reportées en wt%) associées aux produits observés sont estimées à : 3.67 (PhA + En + Grt/Mg-S) ->4.89 (PhA + Al-PhE + En) -> 5.69 (Bal+ Al-PhE + En) -> 2.05 (Al-PhE + En + Ol). En conclusion, un slab relativement froid pourrait permettre le transfert de 2.0 à 3.7 wt% d'eau au maximum à des profondeurs

supérieures à 300 km dans le manteau. La récente découverte de ringwoodite hydratée provenant de la zone de transition (520 km de profondeur) atteste que le transfert d'eau est effectivement possible, au moins localement.

Discussion et conclusion

La pétrologie expérimentale permet de mieux comprendre les relations de phases à des conditions qui ne sont pas accessible via les observations de terrain. Cependant, contraindre des limites de champs de stabilité précisément en utilisant pour seule source d'information les résultats expérimentaux peut s'avérer une tache fastidieuse. Par exemple, la cinétique des réactions minérales à basse température est relativement lente, et nécessite des temps d'équilibrages dans la presse multi enclumes qui ne sont pas envisageables dans le cadre d'expériences de déshydratation (éventuelle perte de l'eau pour les expériences longues). Des méthodes complémentaires basées sur le calcul thermodynamique sont alors d'une aide cruciale. Il est en effet possible de simuler des équilibres de phases en fonction de la composition du système étudié, et basés sur les paramètres thermodynamiques connus des minéraux attendus. Ces paramètres sont principalement dérivés de données calorimétriques, mesurées sur des échantillons expérimentaux, et mis en relation avec les données de fractionnement des éléments dérivées de roches naturelles. Ces modélisations sont le plus souvent très bien contraintes dans le système MgO-SiO_2-H_2O, tandis que les bases de données concernant les propriétés des minéraux tels que la phase A, la phase E, ne sont pas connues pour des compositions impliquant l'aluminium ou le fer ferrique. Quelques exemples de calculs de pseudo sections à l'aide du logiciel Perplex sont utilisés dans cette thèse, dans le but de mettre en évidence les changements importants associés à la variabilité de la teneur en fer par exemple sur les domaines de stabilités. Il apparait très intéressant de contraindre les propriétés thermodynamiques des minéraux hydratés abordés au cours de cette thèse pour des

compositions mettant en jeu l'aluminium et aussi le fer ferrique. En effet, les serpentinites jouent un rôle clé dans le recyclage de l'eau dans la Terre profonde et sont des roches oxydées. Tout autant que dans le cas de l'aluminium, prendre en compte le fractionnement du fer ferrique entre le matériel de départ (antigorite + magnétite) et les produits de déstabilisation est nécessaire pour pouvoir approcher de façon plus réaliste les relations de phases impliquées dans la subduction.

Pour conclure, au cours de cette thèse, l'étude expérimentale de la déshydratation de l'antigorite à basse pression a permis de mettre en avant la nature oxydante de la libération des fluides, de par la présence d'hématite au sein de la magnétite préexistante dans l'échantillon. L'hématite témoigne en effet de la consommation d'oxygène excessif libéré lors des réactions réductrices de déstabilisation de la serpentine. Cette observation est en faveur d'une oxydation du coin mantellique par ces fluides (via des oxydes soufrés solubles en phase aqueuse), et permet d'expliquer l'oxydation des magmas d'arcs. L'étude de la déstabilisation à haute pression de l'antigorite a quant à elle permit de souligner l'importance des éléments tels que l'aluminium et le fer dans la stabilité des minéraux hydratés (antigorite, Mg-sursassite, balangeroite, phase A, Al-phase E). En particulier, dans le système naturel étudié, la phase de haute pression (phase E) est stabilisée vers des pressions inférieures à celles proposées dans la littérature. Elle a également mis en avant la restriction d'un potentiel de transfert d'eau lors de la subduction à des slabs relativement froids voire très froids.

Introduction

Background

Subduction processes allow water recycling at the global Earth scale. Spreading of the oceanic lithosphere created at Mid-Oceanic-Ridges (MOR) is associated with water incorporation into sediment, crustal and ultra-mafic lithologies. Eventually, the lithosphere sinks into the mantle and undergoes transformations due to pressure and temperature, affecting hydrous mineral stability. Partial melting of the mantle wedge is a consequence of slab-derived fluids and is triggering arc magmatism. Arc magmas display higher $Fe^{3+}/\Sigma Fe$ ratio (0.18 – 0.32, Kelley and Cottrell, 2009) compared to Mid-Oceanic-Ridge-Basalts (MORBs, 0.13 – 0.17, Bézos and Humler, 2005; Cottrell and Kelley, 2011). On the one hand, late stage processes such as assimilation, fractional crystallization or degassing are proposed to be responsible for such an oxidized character of arc magmas. Hence, this suggests that the source would not be oxidized but would be as reduced as the one of MORBs (Lee et al., 2005; Mallmann and O'Neill, 2009). On the other hand, supra-subduction xenoliths show fO_2 values for arc magmas source up to FMQ+2 (Brandon and Draper, 1996; Carmichael, 1991; Parkinson and Arculus, 1999). Such an oxidation of arc magmas source could be imposed by slab derived fluids (Evans, 2012; Kelley and Cottrell, 2012; Frezzotti et al., 2011; Tumiati et al., 2015).

Most of the water carried in the hydrated slab sinking in the mantle is outgassed at arc volcanoes. Some water is held in hydrous minerals and recycled to the deep mantle. Mantle convection allows mixing of this water, which is finally outgassed at ridges and oceanic islands. Flux estimation nevertheless suggests that the totality of this water is not returned to the surface

and that some water could be retained at depth in the mantle. Serpentinites are rocks of particular interest for the understanding of water fluxes in subduction zones. They are formed by peridotite hydration on the oceanic floor and fractures. Antigorite, the high pressure and high temperature polymorph, contains up to13 wt% H_2O. In the slab, this mineral is considered as a main carrier of water, and therefore plays a major role in fluids release as it breaks down when the slab deepens and heats up (Ulmer and Trommsdorff, 1995). As a consequence, the pressure-temperature location of antigorite dehydration reaction is critical for the fate of water in the mantle. Moreover, stability domains of intermediate pressure hydrous phases (clinohumite, 10Å phase, chondrodite, Mg-Sursassite...) and high-pressure hydrous phases (also known as the Dense Hydrous Magnesium Silicates – DHMS) define whether or not water transmitted by antigorite can be transported to greater depths in the mantle. The low pressure DHMS phase A is produced right after the high pressure – low temperature breakdown of antigorite phase A, while phase E overlaps phase A high pressure stability domain. Experimental investigations provided pressure and temperature constrains on phases boundaries related to high pressure antigorite breakdown in synthetic and simplified chemical systems. They allowed to estimate the maximum water amount that can be transferred at depth in the mantle by comparing phase stability pressure and temperature conditions with the thermal state of the subducting lithosphere. However, aluminum was found to have a thermal stabilizing effect on antigorite (Bromiley and Pawley, 2003), as well as on chlorite or the high pressure DHMS phase D, therefore changing phase relations. Iron is also believed to play a role on mineral stabilities. In addition, recent studies in more complex systems brought attention on the potential of new intermediate pressure hydrous minerals such as the hydrous Al-bearing pyroxene (HAPY phase), the 11.5Å and 23.5Å phases, on water transport in the slab.

Aims of this study

In this thesis, we focused on antigorite destabilization reactions to better understand subduction related water fluxes and associated phenomena. In particular, this works aims to provide a better knowledge on redox conditions of slab dehydration at low pressure (3 GPa) and the modalities of water transfer beyond antigorite stability, at high pressure (>6.5 GPa).

In order to understand whether or not the oxidation of the mantle wedge by slab related fluids is a viable assumption, we focused on redox conditions of antigorite dehydration reactions in the slab. In particular, the aim of this first study is to investigate the fO_2 associated with antigorite destabilization reactions in conditions relevant to slab dehydration and partial mantle wedge melting. For this purpose, we conducted experiments on a natural serpentinite sample at 3 GPa (i.e. 100 km depth, the location of partial mantle wedge melting that provides magma to arc volcanoes).

The second study conducted during this thesis aims at understanding the ability of structurally bound water to survive at greater depth, beyond antigorite stability, via the DHMS hydrous minerals phase A and phase E. In particular we investigated the role of aluminum and iron on the phase diagram of hydrated peridotite. We conducted high pressure experiment on the same natural serpentinite sample and provided phase relations between 6.5 and 10 GPa and from <500 to 850 °C.

Organization of the thesis

Chapter I is a review of the literature relevant to water recycling in the Earth through subduction processes. It first describes the Earth deep water cycle, and processes of hydration of the oceanic floor. The subduction zone is then presented focusing on the dynamism of the slab and mantle wedge interface, and modelling of the slab thermal structure. Seismic events and the production of magma associated with subduction zones are briefly described.

An overview of hydrous minerals involved in subduction zones is detailed in **Chapter II**. Hydrous phases in the crust are first mentioned while minerals containing structurally bound H_2O in the lithospheric mantle are presented in more details. Through this thesis, these minerals are divided in four categories according to the pressure dependence character of their stability. A detailed description of serpentine minerals formation, structure and stability and in particular of the antigorite polymorph is presented. Finally, an overview of the DHMS phase A and phase E is provided.

Chapter III deals on one hand with experimental methods and presents the starting sample, multi anvil experiments technique and the adopted procedure. On the other hand, it describes the analytical techniques that were used to characterize our samples.

Chapter IV corresponds to the experimental study on natural antigorite dehydration at 3 GPa, dealing with the first main goal treated during this thesis. This chapter is presented as an article manuscript to be submitted. This study aims to constrain the redox conditions of dehydration reactions occurring in the slab, at the depth of magma generation. This work is presented as an article manuscript. Phase assemblages produced after antigorite destabilization between 600 and 900°C are first described as well as their chemical compositions. Comparison with both natural and previous experimental data is provided. The redox state of reactions and its implications for the oxidation state of the mantle wedge and arc magmas are finally discussed.

Chapter V introduces the second main part of this thesis concerning post antigorite phase relations at high pressure. In the chapter, we present the details about the geometric approach that has been used to better constrain phases equilibria at high pressure in our experiments. Theory about the Schreinemakers' analysis is first described. This method allows to establish empirical phases boundaries and relations. Based on these assumptions and results, we present the method used to constrain water budgets that could be transferred to the deep mantle via DHMS.

Chapter VI is an article manuscript submitted to Contribution to Mineralogy and Petrology, closely related to hydrous phases stability beyond antigorite as presented in the chapter 5. The emphasis is put on mineral chemistry. A refinement of water budgets available in the slab for pressure, temperature and chemical conditions relevant for realistic subduction scenarios is established.

Finally, **chapter VII** is a general discussion based on a comparison of our experimental results on antigorite and DHMS stability at high pressure with empirical models produced with Perplex software. The importance of acquiring new accurate thermodynamic properties for hydrous minerals at high pressure and high temperature is then discussed.

Chapter I - Subduction zone and water

This chapter is a general introduction to the subduction zone and especially to water fluxes and related phenomena. It first proposes an overview of the Earth deep water cycle, consisting in water transfer from the oceans to the mantle through subduction processes and outgassing at the surface, at magma production locations. Secondly, evolution of the oceanic lithosphere is briefly described, from its formation at the ridge, its hydration while spreading, to its destruction at the subduction trench. Subduction zones processes are then reviewed with a description of the sinking lithosphere thermal structure and the mantle wedge-slab interface. These features play an important role in the location of dehydration reactions. Finally, subduction related events are described, such as earthquakes along the subducting plate and arc magmatism and its oxidized character.

I The Earth deep water cycle

II Hydration of the oceanic floor

III Oceanic subduction processes

III.1 Thermal structure and dynamism of the subduction zone

III.2 Models of the thermal structure of the slab

III.3 Seismicity

III.4 Arc magmatism

I The Earth deep water cycle

Processes transporting rock masses and allowing water transfer take place in different settings. Water outgassing at mid-ocean ridges and hotspots is recycled to the mantle through the sinking of the dense hydrated lithosphere (Rüpke et al. (2006), Figure I-1). Oceanic lithosphere is created at divergent plate boundaries, at mid-oceanic ridges. Because water is an incompatible and volatile component, its transfer from mantle material to the hydrosphere and atmosphere accompanies this process. As this newly formed lithosphere spreads away from the ridge, alteration caused by sea water hydrothermal circulation allows the re-incorporation of water, via the formation of hydrous minerals. A manifestation of this phenomenon can be seen in the vicinity of spreading centers or subduction zones with the “black smokers”. Seawater percolating through fissures down to the oceanic crust dissolves metals and sulfides at high temperatures (Charlou et al., 2002). When the particles-loaded fluid reemerges from hydrothermal vents, it mixes with near-freezing seawater and minerals solidify as they cool down, forming these typical dark chimney-like structures.

Mass transfer, and in particular water transfer induced by subduction is accompanied by the formation of arc volcanoes as a consequence of partial mantle melting, important seismic activity, deep hydrogen recycling. In this thesis, we focus on the modalities of water transfer via the slab. Moreover, it is not clear whether water rather escapes from the slab to the overlying mantle wedge or if it can be recycled at greater depths inside the mantle. In order to better comprehend these phenomena, the next section attempts to give a more precise description of subduction zones and their related features.

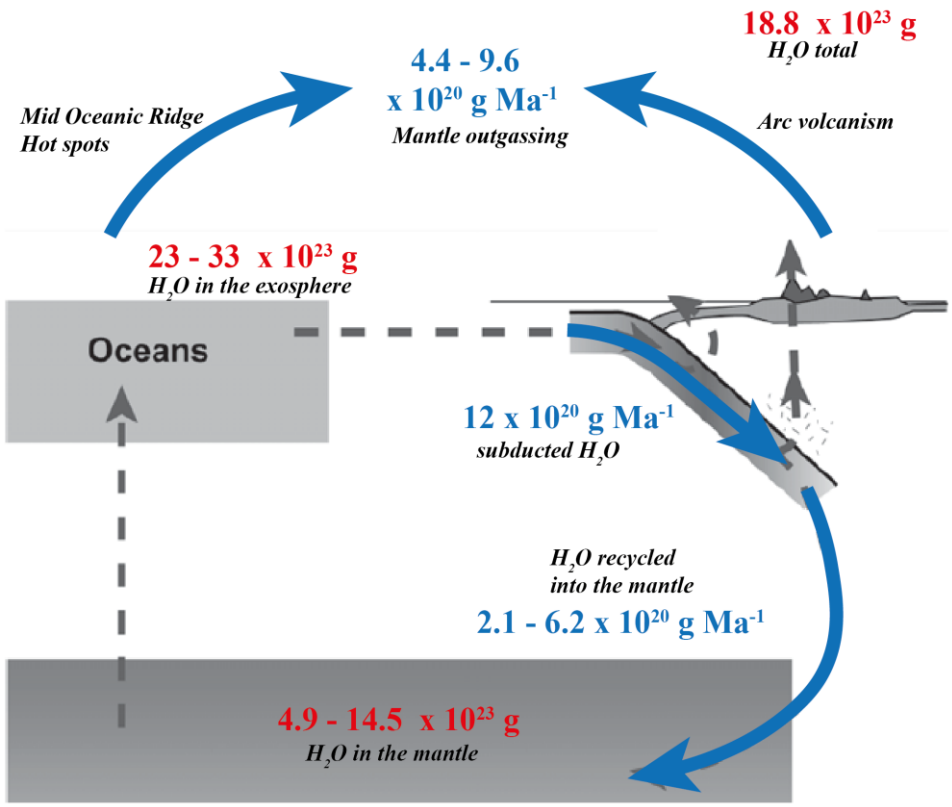

Figure I-1. Water cycle in the mantle is balanced between the incoming fluids from the subduction processes and fluids released at the location of mid-ocean ridges and hotspots (Rüpke et al., 2006)

The oceanic lithosphere created at the ridge is recycled inside the Earth at convergent margin. As the oceanic lithosphere sinks into the Earth's interior, the slab thermally equilibrates with the ambient mantle and heats up. Hydrous minerals eventually break down and released fluids penetrate the overlying mantle, inducing its partial melting beneath arc volcanoes. Nevertheless, it is not known if the totality of the fluids carried by the subducted lithosphere is released in the mantle below arcs and how much water from the sinking plate is recycled back to the deep Earth. (Ito et al., 1983) drew attention to the discrepancy between the budget of subducted volatiles into the mantle and that returning to the surface via arc volcanoes. Bebout (1996) actually suggested that only 5 to 15% of the amount of water subducted is returned to

the surface. Indeed, it is likely that a portion of the water budget from the sinking plate is recycled back to the deep Earth. Rüpke et al. (2006) constrained H_2O budgets involved in the earth global water cycle using prior estimations about the following parameters:

- The water recycling process is assumed to be initiated 2 Ga ago. At this date, the peak sea level was reached and marked the onset of subduction of plates that were cold enough to allow water transfer to the mantle.
- An estimation of the present-day H_2O budget in the exosphere (atmosphere, oceans, surficial water and crust) of 18.8×10^{23} g
- An estimation of the amount of subducted H_2O corresponding to the rate of 12.0×10^{20} g Ma^{-1}. This value is based on a lithosphere model composed of 500 m thick sediment layer containing 7 wt% H_2O (Plank and Langmuir, 1998), on top of a 8 km thick crust of different hydration degrees layers (1 km containing 2.7 wt% H_2O, 2 km containing 1 wt% H_2O and 5 dry km). The mantle is assumed to be serpentinized to about 10% for a thickness of 5km. As a result, the sediment + crust input corresponds to 2.5×10^5 $kg.m^{-2}$ and the serpentinized mantle input corresponds to 2.1×10^5 $kg.m^{-2}$.
- The mantle outgassing efficiency that depends on the incompatible character of water during melting and on its solubility in melts at magma production settings (Mid Oceanic Ridge, hot spots and arc volcanism) is evaluated to be between 50 and 90%
- The mantle overturn rate is assumed to be 9.8 Giga years (inferred from radiogenic heat production variations)

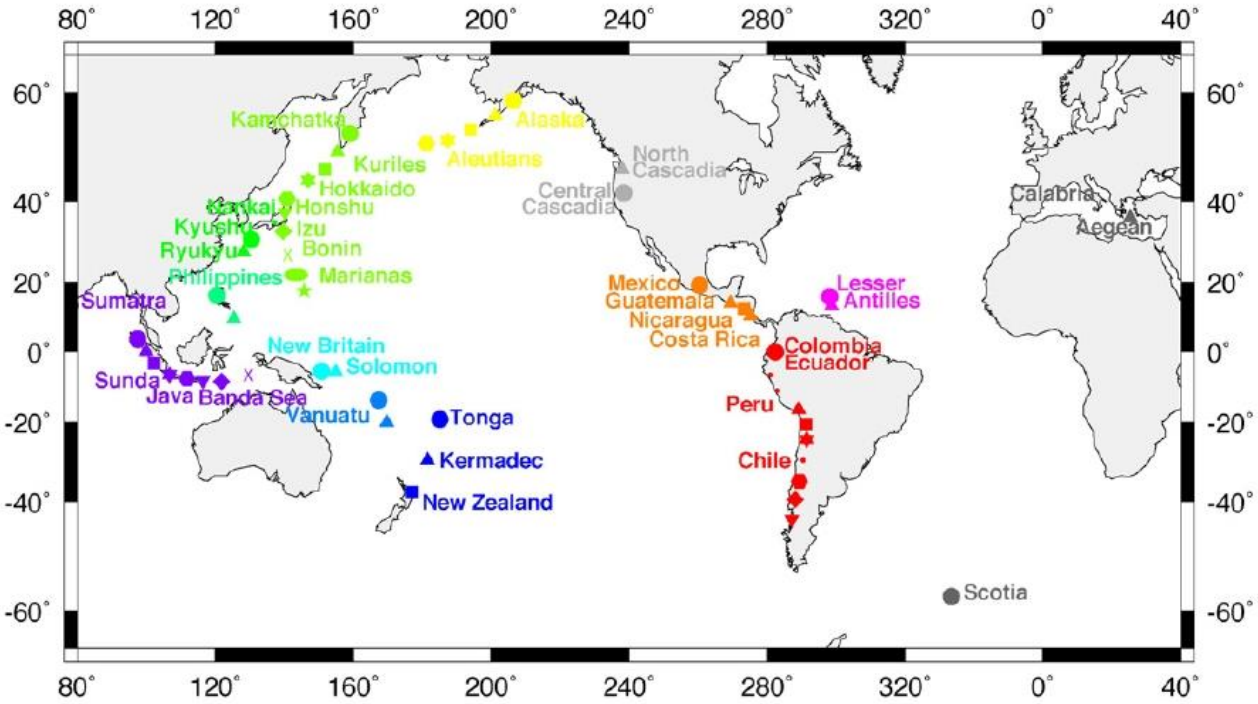

Figure I-2. Location of arc segments associated with subduction zones (Syracuse et al., 2010; Syracuse and Abers, 2006)

For example, water recycling is assumed to be particularly effective in the case of an old and cold slab, sinking relatively fast in the asthenosphere, like Tonga subduction zone (Hacker, 2008). The total of subduction zones on the Earth surface extends to about 67000 km. Most of the subduction segments are concentrated around the Pacific and defines the so-called Ring of fire (Figure I-2).

II Hydratation of the volcanic floor

The oceanic lithosphere is produced at divergent plate boundaries, along the mid oceanic ridge line. As a result, asthenospheric upwelling induces adiabatic melting of the decompressed mantle by crossing the peridotite solidus. The melting product (i.e. basalt) corresponds to the oceanic crust while the residual depleted material (i.e. harzburgite peridotite) corresponds to the lithospheric mantle underneath. Production of lithosphere across Earth surface occurs at

different rates. For instance, a relatively slow spreading ridge is characterized by a spreading rate of about 1-2 cm/yr (Atlantic Ridge), while a fast spreading ridge displays rates of about 6-8 cm/yr (Pacific Ridge). The oceanic lithosphere is commonly described as the piling of different layers, from which few outcropping occurrences are known as Ophiolites. For instance, a typical “Penrose-type” or “Layered” ophiolite sequence can be observed in Oman and is associated to a fast spreading ridge (Figure I-3). From the base to the top, such sequences are composed of ultramafic mantle rocks, layered gabbros, intrusive isotropic gabbros, and vertical basaltic sheeted dikes complex that is feeding the layer above. It consists in an extrusive sequence of basaltic pillow lavas. The top layer is made of pelagic sediments. On the other hand, ophiolites observed in slow spreading ridges environments, such as the example occurring at the Massif du Chenaillet in the Alps do not provide such a well-defined and complete sequence. Basaltic material is piled up directly on top of serpentinized peridotite, which can be observed outcropping. In these slow spreading settings, advection of the asthenosphere has been suggested and allows a more effective serpentinization of peridotite than in the case of fast spreading ridges (Mevel, 2003).

As the lithosphere goes away from the ridge, sea water circulation leads to rock hydrothermal alteration. New hydrous minerals are therefore appearing within the lithologies and allow significant water storage by the slab. For instance, the global subducted sediment (GLOSS, Plank and Langmuir, 1998) can hold up to 7 wt% H_2O , the basaltic layer up to 2-6 wt% H_2O (Poli and Schmidt, 1993). The most important water reservoir in the slab corresponds to the altered peridotite layer, with serpentinites water storage capacity of about 13 wt%. With increasing distance from the ridge, the slab cools down and hydrothermal alteration becomes less effective. The deep faults produced at the bending of the slab at the junction with the overlying plate are nevertheless providing another path for water circulation and deeper hydration of peridotite rocks from the subducted lithosphere. Serpentinization mechanisms are

discussed in more details in II.2.1. As the slab goes down, changes in pressure and temperature are ultimately leading to petrological transformation. The metamorphic series that is usually associated with lithologies within the slab is the high pressure – low temperature (HP-BT) series, also called Franciscan series and characterized by the succession of green schist, blue schist and eclogitic facies. Metamorphic reactions then experienced by mineral assemblages within the slab are determinant for elements mobility through the hydrous phases, from the subducted lithosphere to the mantle wedge, and ultimately arc magmas.

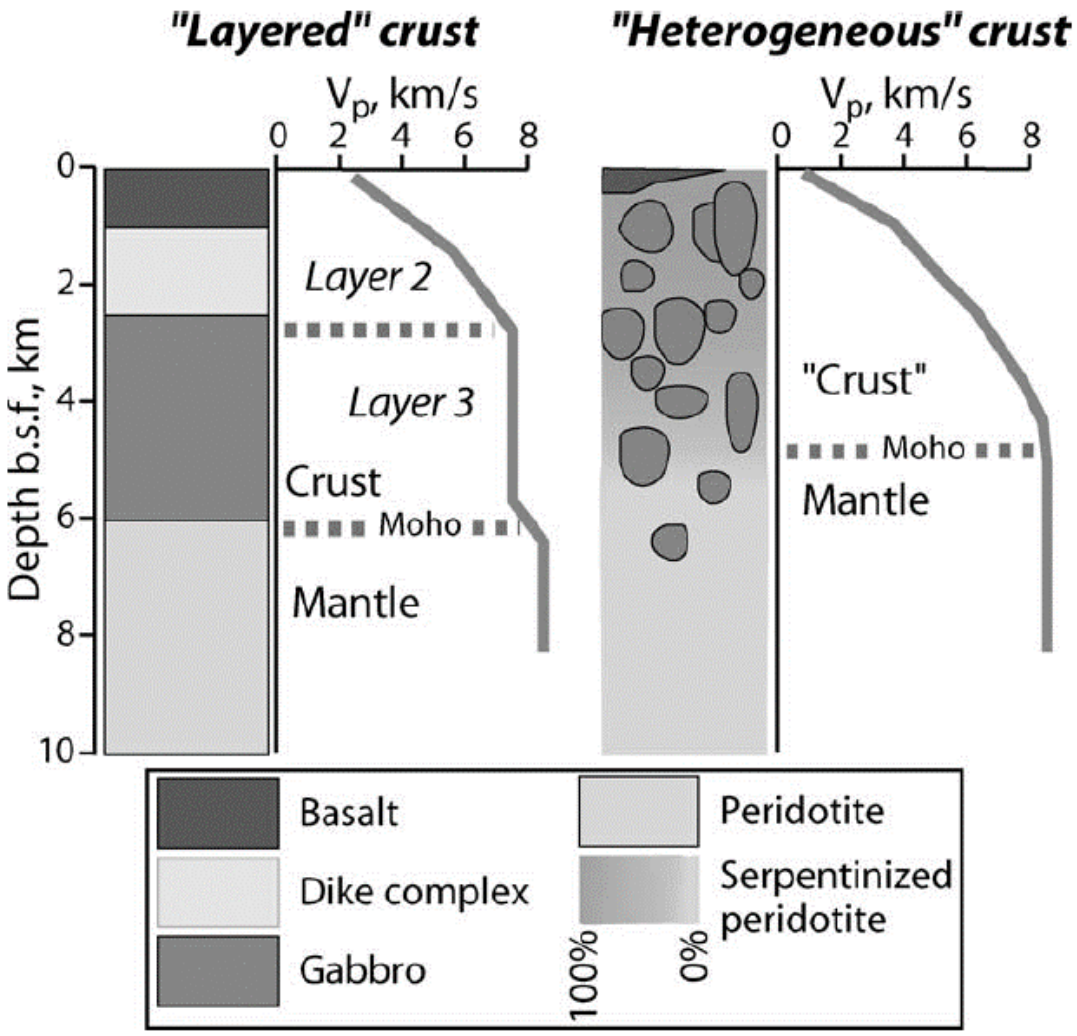

Figure I-3. Seismic velocity profiles for a layered crust and a heterogeneous crust (Mevel, 2003)

III Oceanic subduction processes

As briefly described above, a subduction zone corresponds to the location of convergent plates. More precisely, one of the two plates dips down below the other and further sinks into its asthenospheric mantle. This process is mostly driven by negative buoyancy: a dense and cold material, such as the subducting oceanic lithosphere, sinks into the other under its own weight. The other driving forces are due to tectonic constraints. Such a geological setting is characterized by a great relief contrast and dissymmetry between the subducted plate and the overlying plate. As the oceanic lithosphere deep dips inside the mantle below the other plate, a trench is "opened". As an example, the bathymetry at the convergence between the Pacific and Philippine plates, goes down to -8000 m at the Mariana Trench. On the opposite, the relief on the overlying plate can reach thousands of meters of altitude, such as in the Andes Cordillera that rises to 6000 m. The considerable dip hence formed between the two convergent lithospheres can in some cases be filled with an accretionary wedge, or prism. Sediments from the top of the subducted plate are actually accreted on top of the overlying plate as they are scraped off from the slab.

In addition to this important elevation contrast, a great thermal gradient between the relatively cold slab and the hot overlying plate is associated with subduction zones. For instance, Stein and Stein (1996) reported a thermal gradient of about 700°C from the colder core of the slab to the mantle wedge.

Arc volcanism on one side, and water transfer to the deep mantle on the other, are related to mineral dehydration reactions in the down going lithosphere. Moreover, the location of these reactions is strongly dependent on the temperature and pressure conditions in the slab. The age and speed of the subducting slab are parameters that are controlling its thermal structure. Peacock (1999) proposed a model suggesting that the temperature at the slab-wedge interface could differ by few hundreds of degrees comparing hot and young slabs with cold and old ones.

Therefore, two scenarios are particularly considered when investigating hydrous phase stability in the context of a down going slab. It is indeed frequent to oppose the case of a relatively hot slab (young < 25 Ma) to that of a cold slab at a given pressure. According to these two extreme cases, a review of which of the hydrous phases would remain stable or dehydrate can be drawn. Few studies have addressed a special attention to the thermal state of the slab in order to provide models (Peacock et al., 1996; Kincaid and Sacks, 1997; Hackers et al., 2006; Syracuse et al., 2010; Magni et al., 2014).

III.1 Thermal structure and dynamism of the subduction zone

Understanding the dynamics and thermal structure of subduction zones can only be established based on a well-defined set of parameters. The subduction zone parameterization distinguishes three different features: the slab, the overriding plate and the interface in-between. Each of these three entities display their own parameters. The slab surface is characterized by its geometry (dip angle), convergence velocity, thickness of sediment layer and age. While the interface with the overlying mantle wedge is characterized by the depths at which changes in coupling behavior between the slab and the mantle wedge occurs. The overlying plate is characterized by thickness and age.

The thermal state of the mantle wedge is modified by interaction with the sinking oceanic lithosphere, which has different density and temperature. Hence, the dipping of the slab inside the mantle wedge induces dynamic motions. More precisely, viscous coupling occurs between the slab and the mantle wedge and creates motions. The sinking motion of the slab is accompanied by dragging mantle wedge material to greater depth and creates a forced return flow from below the overriding plate and towards the mantle wedge corner (Figure I-4). The thermal state of the mantle wedge is hence modified, and warmer isopleths are dragged towards the wedge corner. This phenomenon is described as the corner flow model (Kincaid and Sacks,

1997). The low seismic velocities and seismic attenuation observed below volcanic fronts actually suggest that the mantle wedge material is abnormally hot and weakly viscous (van Keken, 2003), in agreement with the corner flow model. On the other hand, the wedge corner is characterized at its tip by a colder zone, the so-called “cold nose”. This region is isolated from the global corner flow in the mantle wedge and corresponds to the decoupled zone, while partial decoupling of viscosities between the slab and the overlying mantle wedge is initiated by the mobilization of hot mantle material to the wedge corner. This warm flux is balanced by the cooling effect of the slab which is in return dragging cooler isopleth from below the overriding plate at greater depths, away from the corner, also described by Kincaid and Sacks (1997) as the cold blanket.

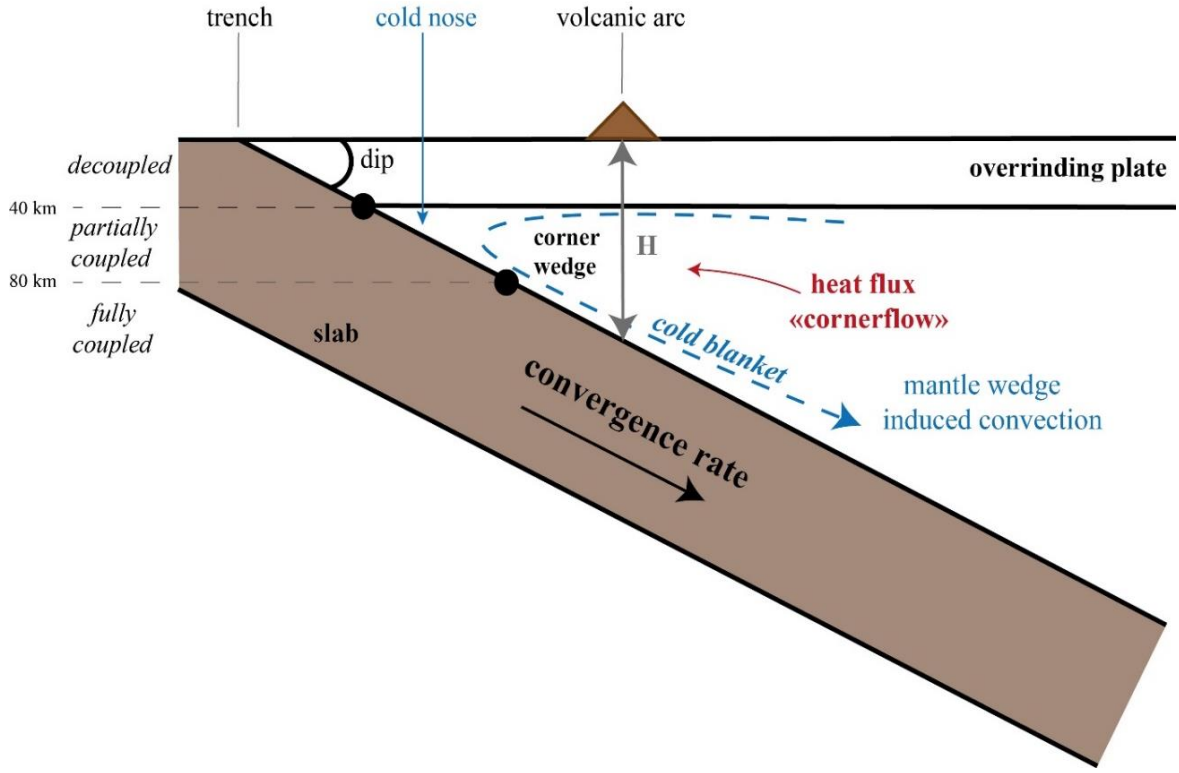

Figure I-4. Cross section of a subduction zone modified from Peacock et al. (1996) and Kincaid and Sacks (1997). Parameters implied in thermomechanical models are reported such as the partial and full decoupling depth (Syracuse et al., 2010).

III.2 Models of the thermal structure of the slab

Subduction processes have been numerically modelled in several studies, proposing thermal predictions for the slab and/or the mantle wedge. Depending on the modelling strategy, for instance the choice of varying parameters in the computation, different slab thermal structure has been established.

The effect of the slab thermal parameter, defined as the slab age multiplied by the convergence rate has been proposed as the main factor controlling the stab thermal structure (Davies and Stevenson, 1992; Peacock, 1996; Peacock et al., 1993). A similar approach has been used in a series of studies producing models of the slab thermal structure according to a partially kinematic model. Indeed, slab parameters such as the velocity were prescribed to understand their effect on the mantle wedge corner flow. These models are also based on the assumption of a depth of 80 km for the viscous coupling between the slab and the wedge (Syracuse et al., 2010; Syracuse and Abers, 2006; van Keken et al., 2011, 2002).

More recent studies used combined thermal and petrological models to investigate the potential depth of fluid release from hydrous minerals in the slab. For instance, Magni et al. (2014) proposed a limited control of the slab age and mantle temperature on the depth of dehydration reaction, compared to the important effect played by the slab velocity. For instance, the amount of water that would stay structurally bound in minerals would follow the same variation whether the slab would be 15 million years younger, the mantle 100°C hotter, or the subduction velocity decreased of 2 cm/yr.

On the other hand, the mantle wedge dynamics effect on the decoupling depth has been tested in order to perform thermomechanical simulations of subduction and wedge flow (Arcay et al., 2007). Slab dehydration induces weakening of the mantle wedge material which results in a decrease of the decoupling depth as well as a thinning of the upper plate. Such a

phenomenon could lead to a thermal structure of the slab about 130°C colder than what is predicted from models referring to the thermal parameter for example.

III.3 Seismicity

The slab-wedge interface is characterized by a planar distribution of earthquakes hypocenters either produced by slip along the thrust fault or slip within the subducting plate, under the effect of bending and extension while sinking in the mantle wedge. This plane is named the Wadati-Benioff zone and marks the position of the down going oceanic plate. Distribution of earthquakes is not continuous, in fact, Frohlich (1989) highlighted their bimodal depth-distribution. A first shallow concentration of earthquakes is located at about 50 km depth, and earthquakes frequency decreases downwards 300 km depth. Then, seismicity frequency increases below 300 km depth and reaches a peak at about 500 km at the transition zone, corresponding to "deep-earthquakes". These earthquakes reach a maximum depth of about 700 km.

This bi-modal repartition of earthquakes with depth is nevertheless not systematic and occurrence of intermediate-depth earthquakes has also been inferred between 50 and 250 km for a number of subduction zones. Intermediate-depth earthquakes are distributed on dipping planes, separated by 20-40 km and merging down dip: they correspond to the "double seismic zone" (Peacock, 2001; Brudzinski et al., 2007). Upper plane earthquakes are located within the oceanic crust while lower plane earthquakes occur within the subducting mantle. Existence of earthquakes at intermediate and deep levels in the mantle is surprising, in particular for the lower plan. Indeed, the plastic flow deformation of rocks at such warm condition is expected rather than sudden brittle failure. The spatial location of earthquakes has been correlated with the location of dehydration reactions in the down going plate. In particular, the hypothesis of hydraulic embrittlement of the slab region at the location of dehydration reaction of antigorite

was inferred in experimental studies (Peacock, 2001; Dobson et al., 2002; Omori et al., 2000, 2002). Furthermore, the contribution of any dehydration reaction, not only antigorite dehydration, in the slab has been suggested as an explanation for the double seismicity zone (Omori et al., 2004). This hypothesis is named the extended dehydration-induced earthquakes hypothesis (EDIE). Still, this explanation is challenged by other studies supporting the idea that serpentine dehydration cannot occur at such important depth and can therefore not be related to the cause of double seismic zones. Instead, instabilities related to anhydrous peridotite deformation are proposed as responsible for the double seismic zone (Kelemen and Hirth, 2007; Reynard et al., 2010). In particular, Seismic anisotropy related to anhydrous and deformed peridotite was proposed as a better explanation than serpentinization to the low seismic velocities in the lower seismic plan observed by seismic tomography (Reynard et al., 2010). This explanation is supported by the existence of localized plastic deformation of peridotite in the 680-800°C range, consistent with seismic lower plane temperatures (Kelemen and Hirth, 2007). Anisotropic shear planes in the anhydrous peridotite at the location of earthquakes could be a response to the stress produced down to 20-30 km below the oceanic crust by the unbending of the slab.

III.4 Arc magmatism

Arc magmas result from the mantle wedge partial melting, as a consequence of the lowering of peridotite solidus under the effect of slab derived fluids. These magmas provide indications of the presence of volatiles. Arc volcanic activity is particularly explosive, suggesting, as a matter of fact a high volatile content of the melts. They actually display different chemical composition compared to Mid-Oceanic-Ridge basalts (MORBs) or Oceanic Island basalts (OIBs). One of the most interesting feature of arc magmas in the framework of this thesis is their high water content. Melt inclusions indicate between 0.5 and 8 wt % H_2O in

arc magmas (Wallace, 2005). Numerous experimental studies addressed the effect of water content on peridotite solidus and on partial melts compositions (Hirose and Kawamoto, 1995; Tenner et al., 2012; Ulmer, 2001) and converge to the hypothesis of high water content of arc lavas. On the other hand, MORBs contain much less water: between 0.05 to 1.40 wt% H_2O (Danyushevsky et al., 2000; Mickael, 1995; Johnson et al., 1994) and plume-related magmas contain only 0.6 wt% H_2O at maximum (Nichols et al., 2002).

Moreover, arc lavas are more oxidized than Mid-Oceanic-Ridge basalts: they have Fe3+/ΣFe ratios of 0.18 - 0.38 (Kelley and Cottrell, 2009) while MORBs display Fe^{3+}/ΣFe ratios of 0.12 – 0.16 (Bézos and Humler, 2005; Cottrell and Kelley, 2011).

Oceanic water is recycled through subduction zones. On one hand, outgassing at arc volcanoes and arc magmas water content are evidence of water return to the surface. On the other hand, some amounts of the incoming water is transferred at depth in the mantle. Hydrous minerals stability domains are determinant for the fate of water in the slab.

Chapter II - Hydrous Minerals and water budget in the subduction zone

The hydration degree of the oceanic lithosphere represents a limiting parameter on the later transfer or release of water in the mantle. Hydrous minerals can crystallize in different environments and the stability conditions of these minerals depend on the bulk chemical system as well as their own chemical composition. This chapter is a review of their stability domains.

I The crust

II The Mantle

- II.1 Low pressure minerals
  - II.1.1 Talc
  - II.1.2 Amphibole
- II.2 Serpentine and chlorite minerals
  - II.2.1 Serpentinization processes
  - II.2.2 Structure
  - II.2.3 Stability
  - II.2.4 Chlorite
- II.3 Minerals stable beyond antigorite and chlorite stability at intermediate pressure
  - II.3.1 10Å-phase
  - II.3.2 Mg-susassite
  - II.3.3 Hydrous Al-bearing pyroxene (phase-HAPY)
  - II.3.4 Clinohumite
  - II.3.5 Chondrodite
  - II.3.6 Brucite
  - II.3.7 Other recently discovered intermediate pressure hydrous phases
- II.4 High pressure and DHMS
  - II.4.1 Phase A
  - II.4.2 Phase E

The attention was first drawn to hydrated basalts (amphibole) and ocean floor sediments (phengitic white micas) as potential water carriers in subduction zones (amphibole: Tatsumi 1986; Davies and Stevenson 1992/ micas: Massone and Schreyer 1989; Schmidt 1996, Domanik and Holloway 1996). No particular interest was then given to the peridotitic mantle underlying the oceanic crust. However, the existence of intensively serpentinized peridotitic rocks has been reported through the study of ophiolites (see the review from O'Hanley, 1996). Observation of serpentinized material has been confirmed by oceanic drilling projects in spreading ridge centers (Früh-Green et al., 1996; Muller et al., 1997) and reported at passive continental margins settings (Galicia margin, Boillot and Winterer, 1988). Finally, experimental studies suggested stability of hydrous silicates at higher P and T than amphibole (i.e. lawsonite, zoisite, chlorite and Mg-chloritoid Pawley, 1994; Poli. and Schmidt, 1995; Schmidt and Poli, 1994). The existence of phases called "dense hydrous magnesium silicates" (DHMS) stable up to 1000°C brought the idea of possible water transfer to deeper mantle levels.

The following sections aim to review hydrous minerals in the subduction setting. In particular, their stability conditions are very important because it influences the fate of water in the mantle.

I The crust

The crust of the subducted oceanic lithosphere corresponds to hydrated Mid-Ocean-Ridge basalts. Tatsumi (1986 a, b) and Tatsumi et al. (1986) suggested the importance of coupled oceanic crust dehydration and induced mantle wedge convection in magma generation at subduction zones. They proposed that dehydration of hydrous minerals within the oceanic crust of the down going slab would happen at depths shallower than 100 km, meaning only in the fore-arc region.

Fluids hence released would migrate upwards in the mantle wedge and produce amphibole peridotite, which would in turn be dragged by slab induced convection and enable water release at greater depths, ultimately causing partial melting of the overlying mantle wedge material at about 110 km depth, below the volcanic front. This theory is also supported by geophysical arguments (McKenzie 1969, Toksoz and Bird 1977) and combined experimental and classical petrology argument on amphibole stability in a peridotite system (Tatsumi 1986a; Millhollen et al., 1974). As the crust is dragged down with slab motion, rocks from the basaltic crust is equilibrated in the blue schist to eclogite metamorphic facies (Figure II-1). In the blue schist facies, at depths between 10 to 50 km (below 2 GPa) and below 550 °C, the hydrous mineral phases existing in the basaltic assemblages are lawsonite, glaucophane, chlorite and phengite (Hacker et al., 2003; Peacock, 1990; Schmidt and Poli, 1998).Above 600°C, at low pressure, the crust evolves in the amphibole eclogite facies, with continuous dehydration reactions following the series lawsonite > epidote/zoisite; chlorite > garnet and leading to complete disappearance of epidote at the solidus. At higher pressure, amphibole breaks down to form chloritoid at about 2.2 GPa, and the crust is equilibrated in the lawsonite eclogite facies. The high-pressure stability of lawsonite (8.4 GPa) allows water transfer to depths of about 250 km assuming temperatures below 830 °C. At higher temperatures, the mineral assemblage of the metamorphosed hydrous basalt is that of a dry eclogite. In the KCMASH system and for conditions above 3 GPa and 800°C, continental crust lithologies are thought to be able to carry more than 1 wt% H_2O (Hermann, 2002).

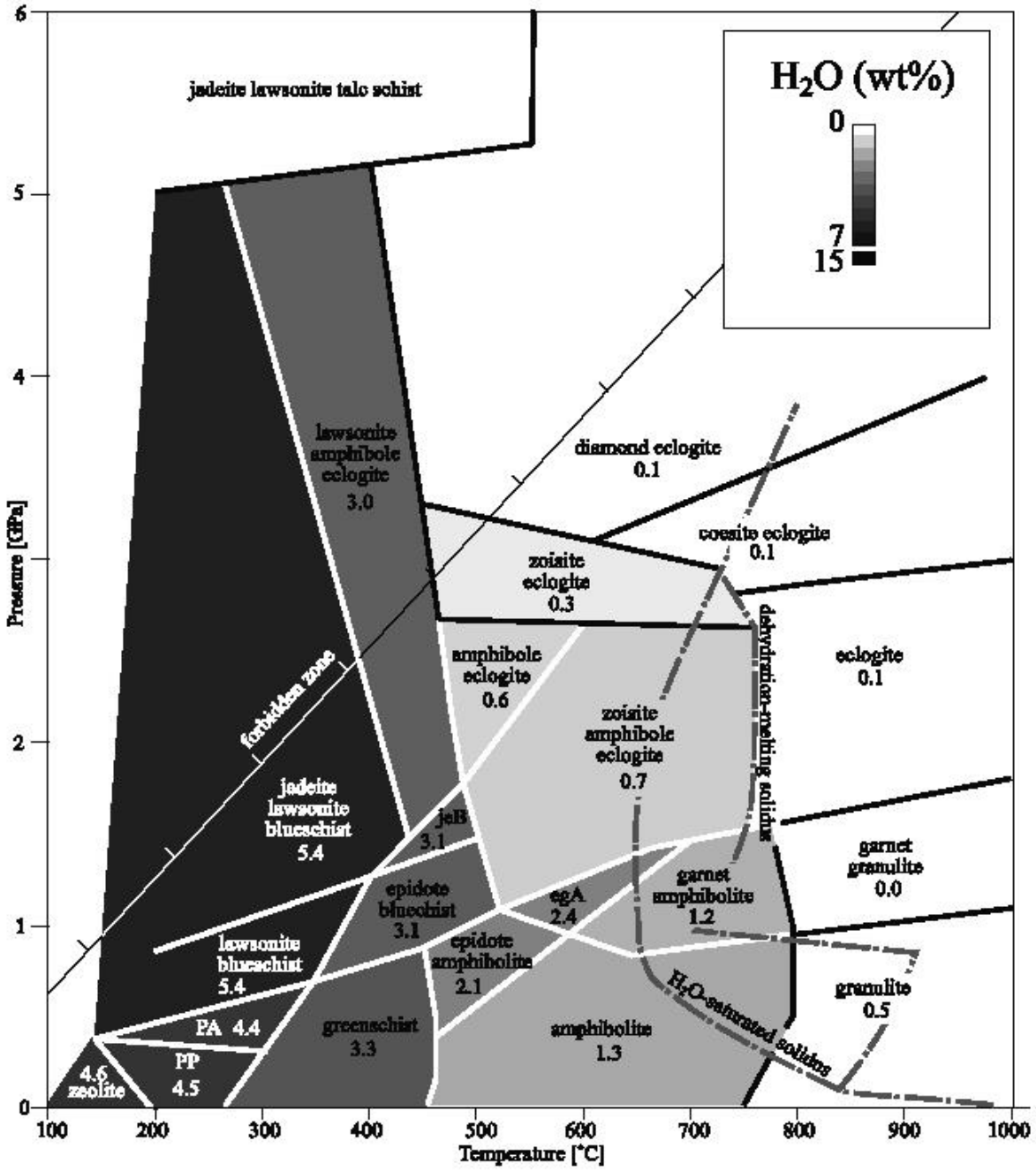

Figure II-1. Phase diagram showing the metamorphic facies equilibration for H_2O-basalt composition (Hacker et al., 2003).

In potassium rich systems, phengite can carry water up to 10 GPa (about 300 km depth). In K-rich environment, the role of hydrous minerals phlogopite, K-amphibole and phase X have been established. It is nevertheless not the purpose of this study to address the stability of these

K-rich hydrous phases, of limited abundances in the mantle and hence limited contribution to the global water budget in subduction zones.

II The Mantle

Serpentine is considered as the dominant hydrous mineral phase in the oceanic spreading lithosphere. It also represents the main water carrier in the slab, because of, its abundance and its high-water content (about 13 wt %). Even if serpentine dominates phase assemblages in the hydrated peridotite system at subduction zones, other hydrous mineral also plays a role in the release of water in the mantle wedge, or in the transfer of their bound H_2O beyond serpentine stability. This section aims to summarize the existing knowledge about the most relevant hydrous phases for hydrated peridotites.

Low pressure conditions are associated to talc and amphibole (Fumagalli and Poli 2005, Figure II-2). Antigorite and chlorite coexist in hydrous peridotite assemblages at low pressure and low temperature. Antigorite subsists to higher pressures (to 6 GPa, Bromiley and Pawley, 2003; Ulmer and Trommsdorff, 1995; Wunder and Schreyer, 1997), while chlorite thermal stability oversteps that of antigorite for at least 100°C. Water can be carried to higher pressures through intermediate-pressures hydrous phases such as the 10Å phase (or Mg-sursassite, hydrous Al-bearing pyroxene) at slightly higher temperature than that of the antigorite breakdown. Dense hydrous magnesium silicates are stable beyond antigorite dehydration to greater pressures, such as phase A and phase E, which characteristics and stabilities are discussed at the end of this chapter.

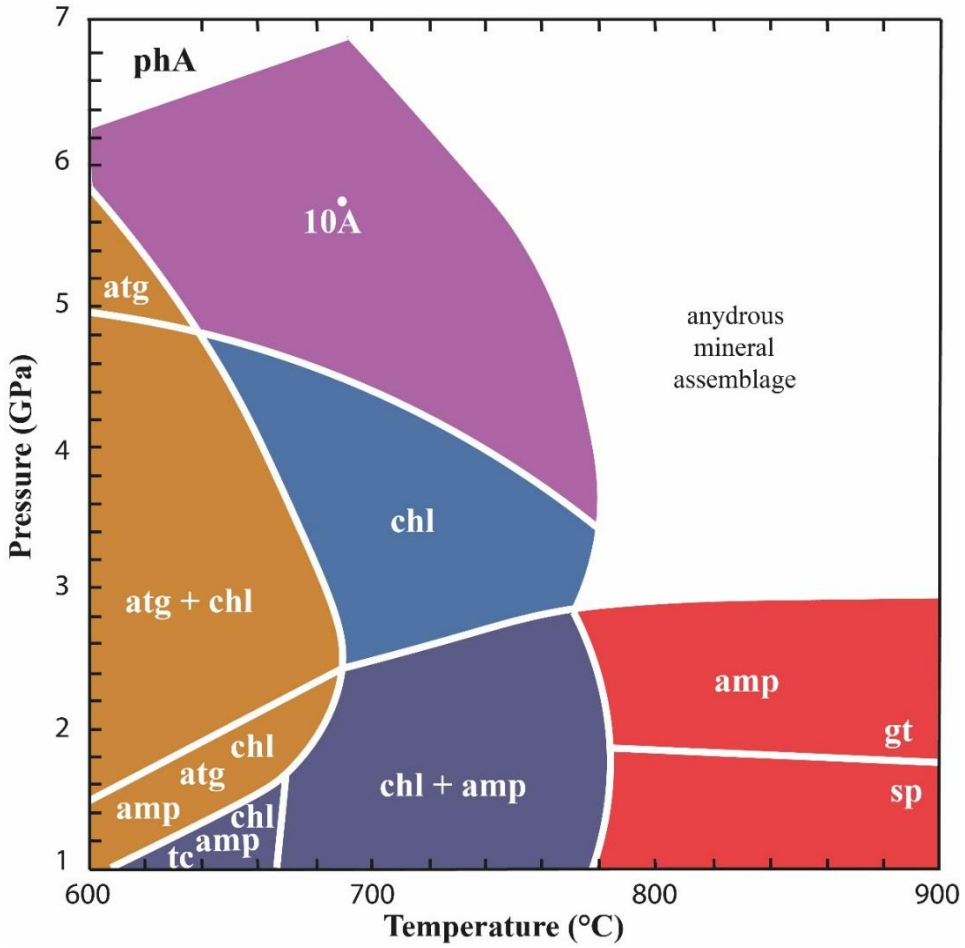

Figure II-2. Hydrous phase relations for the water saturated lherzolite, modified after Fumagalli and Poli (2005).

II.1 Low pressure minerals

II.1.1 Talc

In ultramafic compositions, talc ($Mg_3Si_4O_{10}(OH)_2$, 4.7 wt% H_2O) forms at low pressure (below 2.1 GPa) as a product of serpentine destabilization with increasing temperature:

Serpentine = talc + olivine + H_2O (reaction II.1)

Its stability field is limited with less than 100°C width. It reacts with olivine between 1 GPa, 690°C and 2 GPa, 720 °C according to the reaction:

$$\text{Talc + olivine = enstatite + } H_2O \qquad \text{(reaction II.2)}$$

Talc stability is strongly dependent on Si enrichment, and might persist to slightly higher pressure and temperatures, in particular when crystallized in silica-rich veins (Bose and Ganguly, 1995a; Jenkins and Chernosky Jr, 1986). Fe-bearing talc is stable at lower temperatures than the Mg-rich endmember: it starts to dehydrate at ~ 600°C, while partitioning Fe into ferrosilite (Howe et al, EMPG abstract 2016). The location of talc dehydration reaction might be influenced by the low pressure-clinoenstatite to orthoenstatite transition. Its contribution to the water budget from the slab is limited by its modal abundance of less than 15%. Talc is expected to be more abundant in the mantle wedge (up to 41%), after antigorite dehydration (Hacker et al., 2003).

II.1.2 Amphibole

Amphibole designates a super group of inosilicate minerals of the general formula $A\ X_2\ Z_5\ (Si,Ti,Al)_8\ O_{22}\ (OH)_2$. In hydrated peridotite amphibole is stable up to 2.2-3 GPa for a wide range of temperatures. Its higher stability is delimited by the intersection with the hydrous solidus, at about 3 GPa and 950-1000°C. At low temperatures, amphibole breaks down to serpentine and chlorite assemblages while at higher temperatures its breakdown produces anhydrous garnet assemblages. Therefore, the temperature at which it reaches its maximum pressure stability determines whether its breakdown follows a water conserving or liberating reaction (Figure II-3). Amphibole in hydrated peridotite conditions corresponds to a solid solution between the endmembers pargasite $NaCa_2Mg_3Fe^{2+}Si_6Al_3O_{22}(OH)_2$, hornblende $(K,Na)_{0-1}\ (Ca,Na,Fe,Mg)_2(Mg,Fe,Al)_5(Al,Si)_8O_{22}(OH)_2$ and tremolite $Ca_2Mg_5Si_8O_{22}(OH)_2$. Its

composition and therefore stability boundaries are strongly dependent on the bulk composition and solid solution. For instance, substitution of Fe for Mg triggers an extended amphibole stability of several tens of kilo bars (Evans and Guggenheim, 1988).

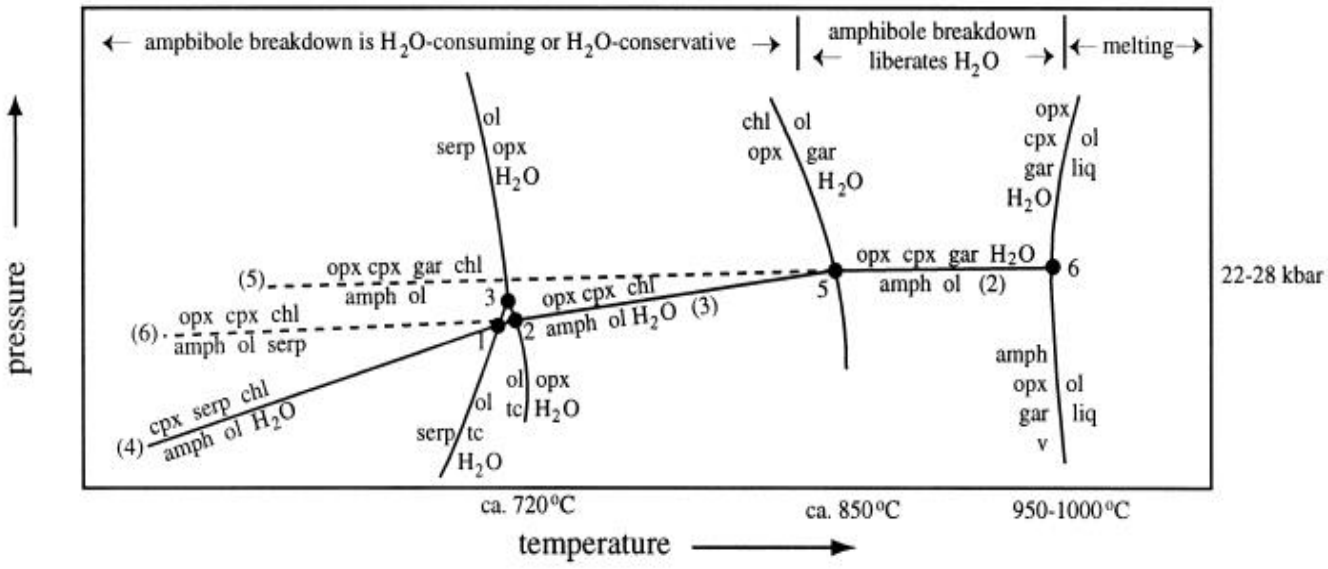

Figure II-3. Reactions for amphibole breakdown in hydrous peridotite, Schmidt and Poli 1998.

Wallace and Green (1991) noted that amphibole is stabilized to 100°C higher in a lherzolite bulk composition compared to harzburgite. Fumagalli (2005) nevertheless did not notice any shift in amphibole stability at 700°C in either a pyroxenite or lherzolite bulk composition. On the other hand, a comparison made by the same authors and with data from Mysen and Boettcher (1975) and Niida and Green (1999) on amphibole compositional variations suggests a strong temperature dependence of Na content. However, they observed a very modest, or even non-existent pressure dependence. They highlighted the importance of Na-bearing clinopyroxene as a buffering phase for amphibole stability, as it would influence Na-exchange vectors. Water content of amphibole is a function of pressure. The maximum amount of 2.3 wt% H_2O is found in the pargasite solid solution near the solidus and decreases to 2wt% H_2O at lower pressures.

II.2 Serpentine and chlorite minerals

Serpentinites are rocks composed by serpentine-group minerals: chrysotile, lizardite and antigorite. The general serpentine formula is $Mg_3Si_2O_5(OH)_4$. It forms by hydrothermal alteration of Mg-rich minerals in peridotite. As mentioned before, it constitutes the most important source of water in the oceanic spreading lithosphere, with about 13 wt% H_2O. Serpentine has therefore been intensively investigated through experiments, because of its importance in subduction related water fluxes but not only. Indeed, because of its low density and mechanical strength, it also plays an important role on subduction zones dynamics and rheology (Hattori and Guillot, 2003).

II.2.1 Serpentinization processes

Most of the serpentinization reactions occur in two principal geodynamic contexts, at mid-oceanic ridges and at subduction zones. Hydration of "abyssal peridotite" minerals is favored at mid oceanic ridges by the extensive fracturing of the crust associated with high thermal gradient related to magmatic activity (Cannat et al., 1990). These abyssal peridotites are thought to be highly serpentinized (70 to 80%; Dick et al., 1984). Permeability through normal faulting is indeed generated and allows a low temperature (<500°C) hydrothermal alteration of peridotite through fluids circulation (Mevel, 2003). Abyssal peridotite actually corresponds to depleted harzburgite whose mineral assemblages is mostly composed of olivine and orthopyroxene (minor clinopyroxene) and the low-pressure aluminous phase spinel as an accessory phase. Serpentine formation can occur through different reactions. For instance, olivine hydration results in serpentine crystallization and is accompanied by hydrogen and magnetite formation according to the reaction:

$$6\ \text{olivine} + 7\ H_2O = 3\ \text{serpentine} + \text{magnetite} + H_2 \qquad \text{(reaction II.3)}$$

Serpentine mineral formation via orthopyroxene hydration produces talc:

6 orthopyroxene + 3 H_2O = serpentine + talc (reaction II.4)

Serpentine displays Mg/Si ratio intermediate between olivine and orthopyroxene, therefore the following reaction can also be considered

olivine + orthopyroxene + 2 H_2O = serpentine (reaction II.5)

During the peridotite serpentinization, spinel recrystallizes into chromite and then into magnetite. This phenomenon has been interpreted as progressive spinel oxidation into chromite and further magnetite (Bliss and MacLean, 1975).

The occurrence of serpentinites within the subducted lithosphere has been established from geophysical observations. As detailed in the first chapter (section III.3.3), the earthquakes along the lower plan of the double seismicity zone, 20 to 40 km below the oceanic crust, have been correlated with serpentine dehydration events (Peacock, 2001). This hypothesis was controversial, based on the assumption that only slow spreading ridges would allow intensive serpentinization of the upper part of the lithosphere (Mevel, 2003). Nevertheless, serpentinization of the peridotite component from the down going lithosphere is promoted by slab-bending faults in the trench region (Figure II-4; Ranero et al., 2003).

Serpentinite production in the mantle wedge has also been suggested, as a result of slab derived fluids release. It is supported by the occurrence of low seismic velocities and low frictional stress along the subducting surface (Furukawa, 1993) and in agreement with the thermal model proposed by Kincaid and Sacks (1997); as well as the observation of high electrical conductivity (Wang et al, 1999). Natural occurrence of serpentinized mantle wedge

were observed in eastern Ladakh, northwest Himalaya (Deschamps et al., 2010; Guillot et al., 2000). Mantle wedge serpentinization degree depends on the slab thermal state and is particularly effective in the case of a slab with a relatively hot geotherm (Figure II-5).

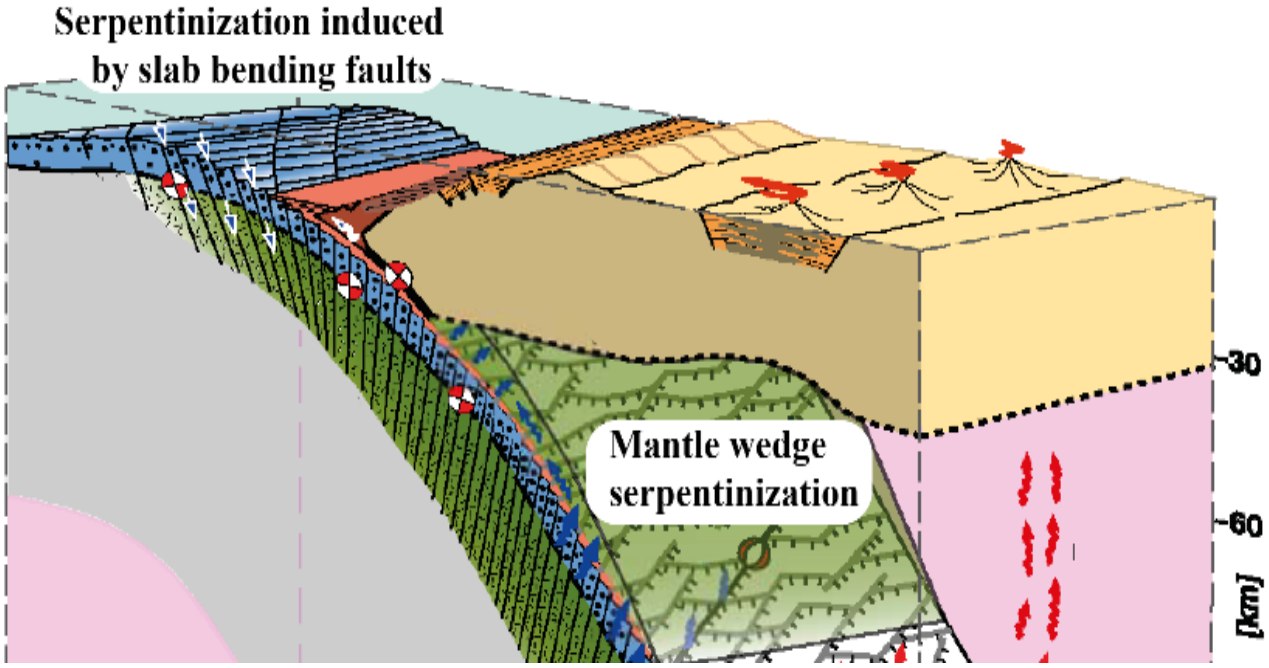

Figure II-4. Structure of the trench region of a subduction zone. As proposed in Ranero et al. (2003), extension due to the plate sinking results in deep faulting opening paths for water circulation down to 20 km depth in the dipping lithosphere.

The different varieties of serpentine are related to different stability domains. Lizardite and chrysotile are stable at low pressure while antigorite is the high-pressure form. While at mid-oceanic ridges the pressure and temperature conditions favor stability of lizardite minerals, it is completely transformed into antigorite in the downgoing slab (Schwartz et al., 2013).

For the purpose of this thesis, the serpentine form in which we are interested in is antigorite, because of its ability to survive higher pressures and temperatures. As a consequence, it controls the water budget associated with the serpentine component of the subduction zone, which is either transferred to depth or released in the mantle wedge.

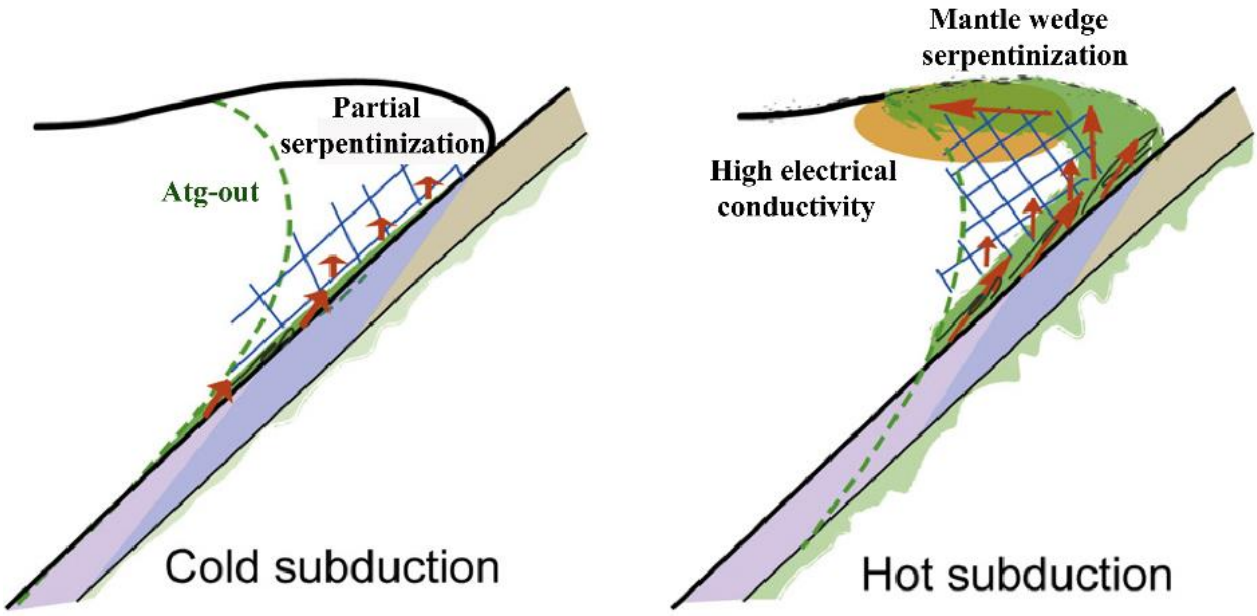

Figure II-5. Mantle wedge serpentinization processes, modified after Reynard (2012). Release of fluids from serpentine from the slab in hot subduction zones occurs at shallower levels, promoting the rehydration of the overlying mantle wedge and its serpentinization. On the other hand, only partial serpentinization takes place in the case of a cold subduction.

II.2.2 Structure

Serpentine minerals belong to the phyllosilicates group: it presents a corrugated microstructure, made of piling bi-dimensional silicon tetrahedra (T) and magnesium octahedra (O) sheets (Figure II-6). Oxygen atoms are shared between neighboring tetrahedra in a hexagonal fashion, forming the T layer. The fourth apical oxygen from the tetrahedron is shared with the superposed O layer, insuring the chemical bound between T and O layers. The O layer is characterized by an Mg^{2+} cation connected to 6 oxygen atoms and hydroxyl groups (OH). The elementary sheet of serpentine structure is then composed of a T and O layer, of about 0.72 nm thickness, piled on top of one another and connected by H bounds that make up the inter foliar spaces between elementary sheets.

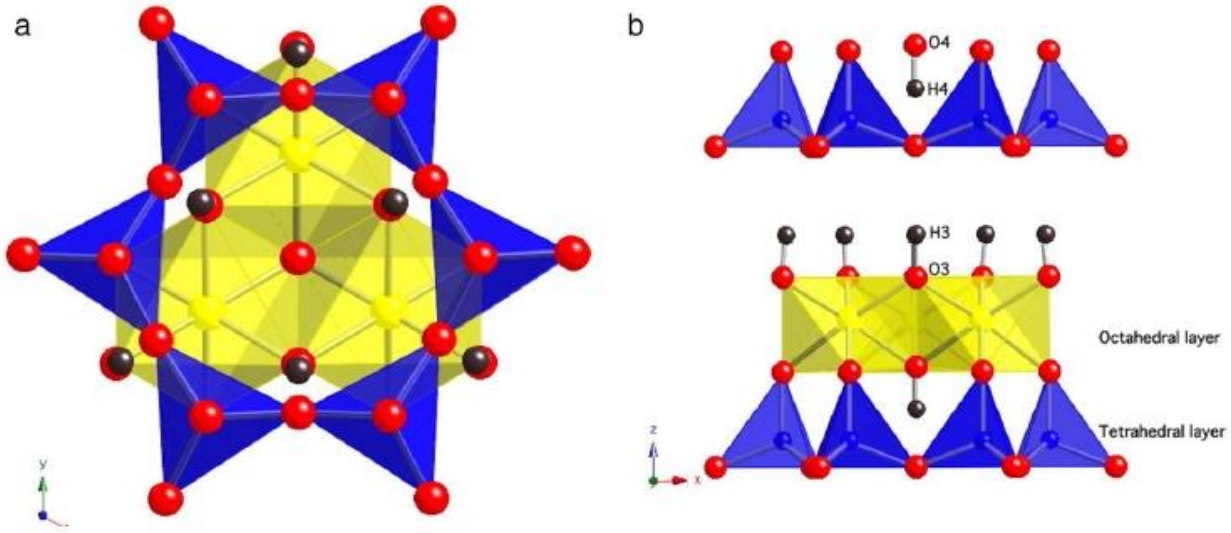

Figure II-6. Serpentine mineral structure (Mookherjee and Stixrude, 2009). Silicon tetrahedra are represented in blue and magnesium octahedra in yellow.

Larger lateral lattice dimensions of the octahedral sheet compared to the tetrahedral one is responsible for a lateral shift between them. As a consequence, different compensation of this misfit can be possible in order to insure structure stability (Wicks and Whittaker, 1975), ultimately producing different microstructure types (i.e. different serpentine mineral varieties).

The serpentine mineral relevant for this thesis, is antigorite, the high pressure and high temperature structural variety. For this serpentine form, compensation of the misfit is insured by curved and wavy layers. The tetrahedral sheet is periodically reversed along the a-axis, allowing connection with the octahedral continuous and wavy sheet, on concave half-waves. Antigorite structure is then described by the number *m* of tetrahedra within a period Figure II-7, defining the structural formula $M_{3m-3}T_{2m}O_{5m}(OH)_{4m-6}$ where M corresponds to cations in the octahedral position (Mg , Fe^{2+}, Ni, Al) and T corresponds to cations in the tetrahedral position (Si, Al, Fe^{3+}). This *m* parameter can range between 13 to 40, and an average value of $m = 17$ has been suggested (Wunder et al., 2001), giving the chemical formula $Mg_{48}Si_{34}O_{85}(OH)_{62}$. Because of these variations in antigorite structure, different polysomes can be found with

slightly different chemical compositions. Substitutions in the octahedral or tetrahedral site are one of the possible compensation mechanisms. Al^{3+} or Fe^{3+} substitution for Si^{4+} on the T position and Al^{3+}, Fe^{2+} or Fe^{3+} substitutions for Mg^{2+} in the O position. For example, the Tschermak ($Al_2Mg_{-1}Si_{-1}$) solid solution has been observed in antigorite. Concomitant l substitution in both sites can therefore take place in antigorite structure according to the mechanism $^{[6]}M^{2+} + {}^{[4]}Si^{4+} = {}^{[6]}Al^{3+} + {}^{[4]}Al^{3+}$ (Padrón-Navarta et al., 2013).

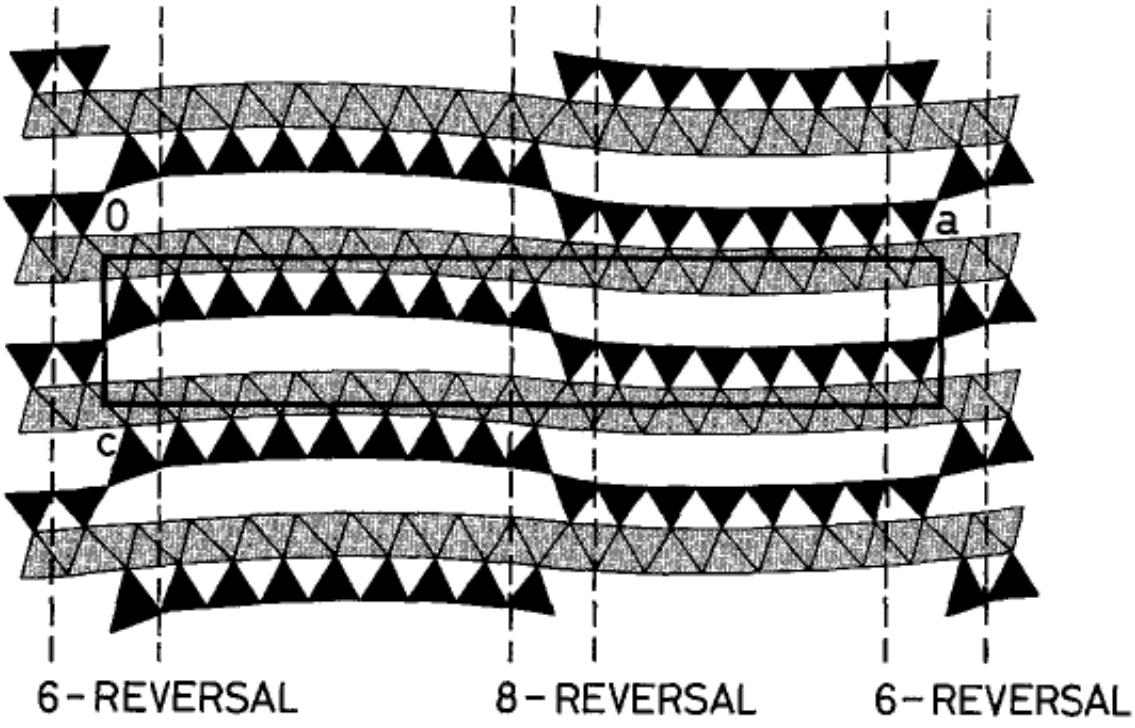

Figure II-7. Structure of antigorite model (Mellini et al., 1987). Tetrahedra are represented in black (m=17) and octahedra in grey.

II.2.3 Serpentine Stability

Antigorite survival to 2 GPa and 550°C (in the eclogite facies) as first been observed through field evidences from the western Alps (Scambelluri et al., 1995). Owing to these observations, the crucial role of antigorite as the most effective mechanism of water transfer at great depth within the mantle could be confirmed. Further experimental studies thus gave a

particular attention in constraining the pressure and temperature dependences for antigorite stability. The conditions of antigorite destabilization proposed over these works are dependent on its composition. Many investigations were conducted and refined in the simplified MgO-SiO_2-H_2O system (Figure II-8). Antigorite stability was also addressed in the MgO-Al_2O_3-SiO_2-H_2O system and in the natural bulk composition close to MgO-FeO-Al_2O_3-SiO_2-H_2O. Thermodynamic modelling based on experimental results also contributed to better constrain antigorite stability limits. Numerous attempts to bracket antigorite thermal stability limit are therefore available for comparison. This section is, however, a non-exhaustive presentation of different data proposed in the literature that are relevant for comparison with our study.

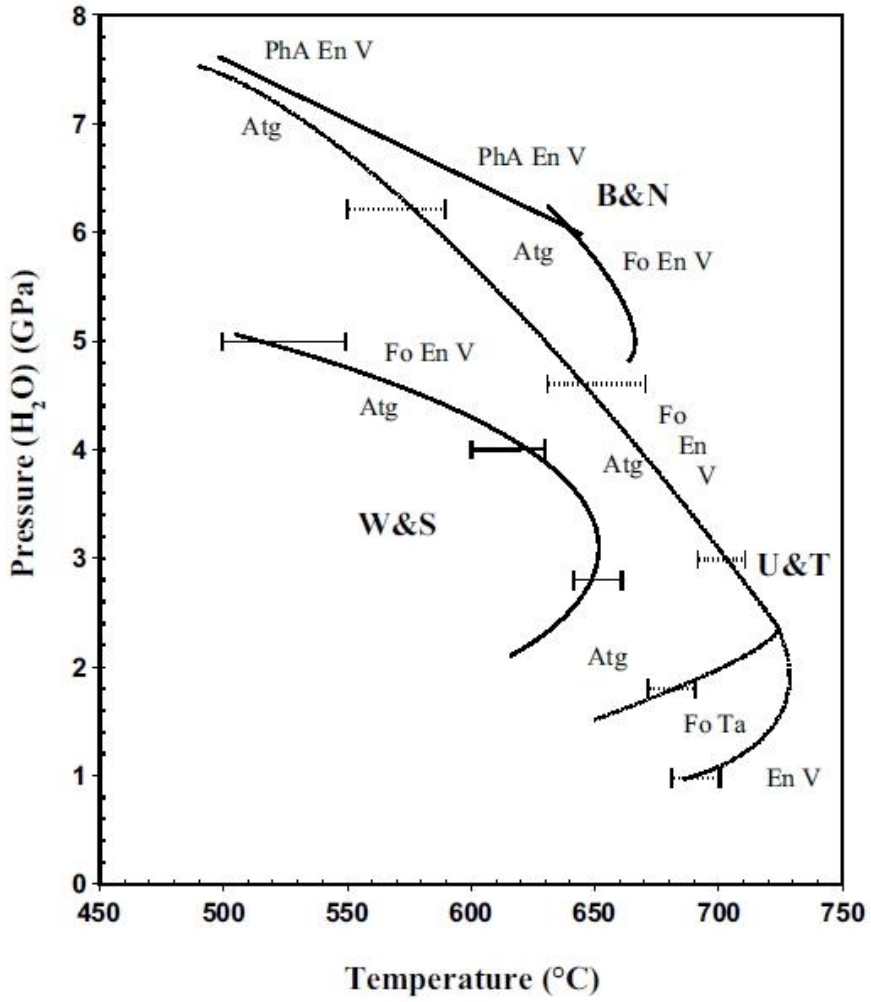

Figure II-8. Antigorite stability experimentally determined in the MSH system (from Bromiley and Pawley, 2003). W&S: Wunder and Schreyer (1997), U&T: Ulmer and Trommsdorff (1995); B&N: Bose and Navrotsky (1998).

Thermal destabilization of antigorite follows the reactions (II.6), (II.7) and (II.8), respectively at low, intermediate and high pressure

$$\text{Antigorite} = \text{talc} + \text{forsterite} + H_2O \qquad \text{(reaction II.6)}$$

$$\text{Antigorite} = \text{forsterite} + \text{clinoenstatite} + H_2O \qquad \text{(reaction II.7)}$$

Antigorite = phase A + clinoenstatite + H_2O (reaction II.8)

These destabilization reactions have been addressed in the experimental study conducted by Ulmer and Trommsdorff (1995) on a hybrid sample. They used 90% volume of a natural serpentinite containing 1.30 wt% Al_2O_3, 3.10 wt% FeO and 0.23 wt% Cr_2O_3 mixed with 10 % volume of the dehydration product olivine + orthopyroxene (obtained in preliminary dehydration of their material). Their starting mixture can therefore reasonably be considered to belong to the natural serpentine system, close to the Cr_2O_3-MgO-FeO-Al_2O_3-SiO_2-H_2O system.

Wunder and Schreyer (1997) investigated antigorite stability in a similar MgO-FeO-Al_2O_3-SiO_2-H_2O system (gels or oxide mixtures partly seeded with natural antigorite sample with 0.68 wt% Al_2O_3 and 2.06 wt% FeO) and bracketed the reactions (II.6) and (II.7) at about 50 to 100°C lower temperatures than Ulmer and Trommsdorff (1995).

Another experimental investigation on high pressure phase relations in the MgO-FeO-Al_2O_3-SiO_2-H_2O system confirmed reactions (II.7) and (II.8) (Bose and Navrotsky, 1998). Despite the reduced range of pressure (5 - 7.8 GPa) investigated in this study, the extrapolation of the results into a self-consistent thermodynamic data set allowed the determination of phase equilibria over a pressure panel of about 10 GPa, and reaction (II.6) was confirmed.

These works display considerable discrepancies on the definition of antigorite stability domain, which are actually attributed to compositional differences between starting materials. Trivalent cations (Al^{3+}, Fe^{3+}, Cr^{3+}) substitution for the divalent Mg^{2+} would therefore stabilize antigorite to higher temperatures.

In fact, Bromiley and Pawley (2003) tested the influence of aluminum incorporation in antigorite structure on its thermal stability. They suggested its stabilization at considerable higher temperature for an Al-rich material (3.06 wt% Al_2O_3) compared to an Al-poor material

(0.01 wt% Al_2O_3), (Figure II-9). The larger lateral lattice dimension associated with the occupancy of the octahedral sites by $^{[6]}Mg^{2+}$ in the O-layer compared to the tetrahedral sites $^{[4]}Si^{4+}$ in the T-layer is responsible for the lateral shift and hence the corrugated structure of antigorite. Therefore, aluminum substitution in antigorite following a Tschermak's type substitution ($^{[6]}Mg^{2+} + {}^{[4]}Si^{4+} = {}^{[6]}Al^{3+} + {}^{[4]}Al^{3+}$), as it has been observed by Padrón-Navarta et al. (2013) can decrease this lateral shift and the associated structural misfit, and in turn be a stabilizing mechanism. However, it can be noted that despite the lower Al content of antigorite used in Ulmer and Trommsdorff (1995), it is stabilized at higher temperature than the Al-richer antigorite used in Bromiley and Pawley (2003). Different experimental protocols might be responsible for the variation in stability conditions observed, as well as additional phases appearance such as brucite in Wunder and Schreyer (1997) or chlorite in Trommdsorff et al (1995), hence producing more complex mineral assemblages, and making the precise identification of P-T antigorite stability more difficult.

Komabayashi et al. (2005) investigated antigorite stability at high pressure on a synthetic Mg-end-member composition (MSH system) and were able to locate the invariant point between reaction (II.7) and (II.8) at about 5.1 GPa and 550°C. In order to accurately compare their results on the thermal stability of antigorite with those of other studies, they calculated a correction of the e.m.f. of the thermocouple at high pressures. Indeed, Takahashi et al. (1993) reported notable differences in the nominal temperature values between the types of thermocouple used during the experiment. The results are displayed in Figure II-10.

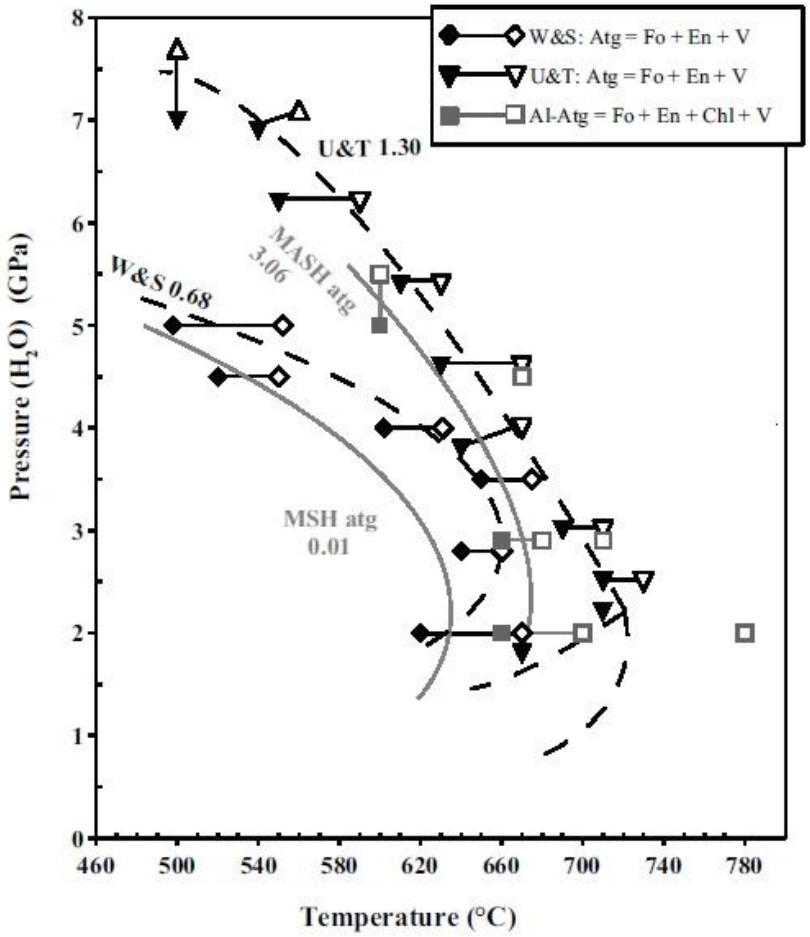

Figure II-9. Antigorite thermal stability is increased as suggested by experiments conducted on Al-rich materials. Bromiley and Pawley (2003).

It appears clearly that the composition of the starting antigorite sample and the experimental techniques, provide different stability domains for antigorite, offering different scenarios for water conservation of release by the slab. Comparing the slab thermal models such as those proposed in Syracuse et al. (2010) for instance with different antigorite stability boundaries permits to estimate a range of slab P-T path that would open the hypothesis of water conservation to great depth. This is discussed in more details in chapters V and VI.

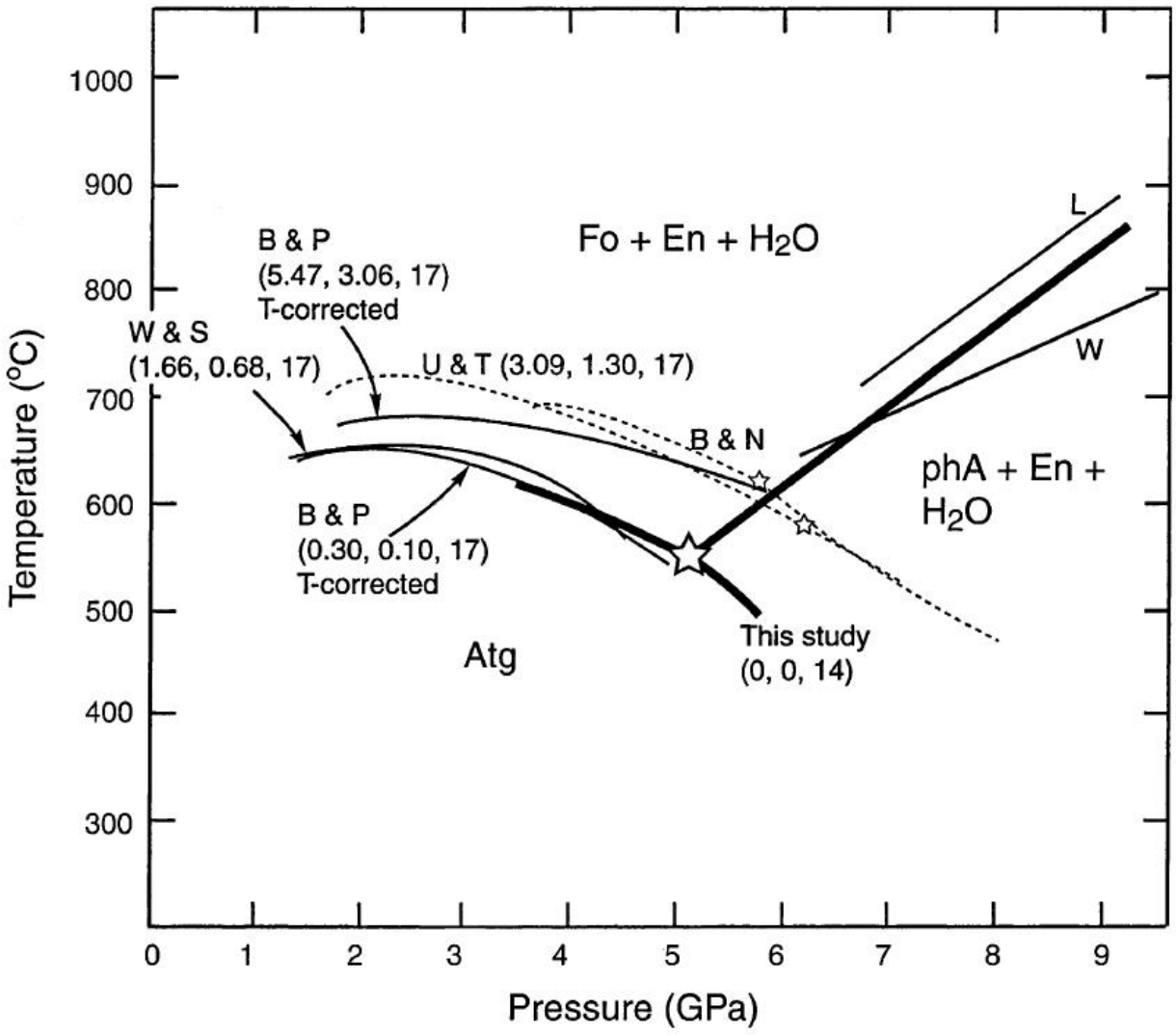

Figure II-10. Location of the invariant point involving antigorite and phase A, Komabayashi et al. (2005). Reactions bracketed in their study correspond to the thick black lines. Thermal destabilization of antigorite through reaction antigorite = forsterite + enstatite + H_2O is reported also for different starting material nature (FeO, Al_2O_3, m-value) and highlights the thermal stabilizing effect of aluminum incorporation in antigorite. U&T: Ulmer and Trommsdorff, 1995; B&P: Bromiley and Pawley, 2003; W&S: Wunder and Schreyer, 1997; B&N: Bose and Navrotsky, 1998. The high-pressure breakdown of antigorite into phase A + enstatite + H_2O is consistent with the results from Luth, 1995 (L) and Wunder, 1998 (W).

II.2.4 Chlorite

Chlorite in peridotite bulk composition usually displays the composition of clinochlore endmember $Mg_5Al(AlSi_3O_{10})(OH)_8$. It contains about 13 wt % H_2O and allows water transfer at a given pressure at higher temperature than antigorite. It breaks down with increasing pressure and temperature following the reaction: (Pawley (2003))

Clinochlore + enstatite = forsterite + pyrope + H_2O (reaction II.9)

This reaction has a sub vertical negative P-T slope at low pressure and flattens at higher pressure as it can be seen on (Figure II-11). In the MgO-Al_2O_3-SiO_2-H_2O system, chlorite remains stable at temperatures up to 880 °C at 2.5 GPa and at pressures up to 5 GPa for about 650 °C (Pawley, 2003; Ulmer and Trommsdorff, 1995).

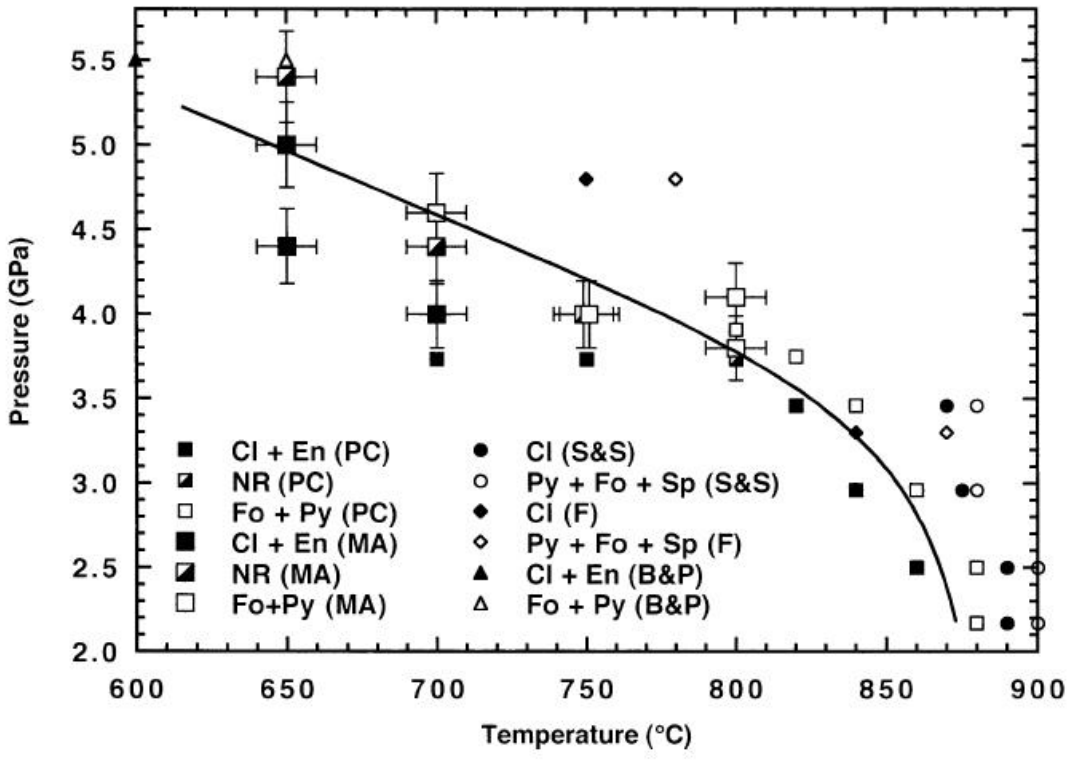

Figure II-11. Experimental data for chlorite destabilization according to reaction I.8, Pawley (2003).

Fumagalli and Poli (2005) noted a small extension of the thermal stability of pure chlorite compared to that observed in a peridotite bulk. In the latter, pyroxene is involved in chlorite destabilization, while pure chlorite breaks down to the assemblage garnet + olivine + spinel + water, without coexisting with pyroxene. Preferential partitioning of iron for garnet over pyroxene forces chlorite destabilization in the peridotite bulk composition. Moreover, chromium has been suggested as a thermal stabilizing component while incorporated into chlorite minerals. It remains stable up to 800°C at 3.6 GPa while containing about 1.47 Cr_2O_3. Recently, the effect of 2.2 wt% Cr_2O_3 in chlorite has been shown to increase its stability of about 50°C per 0.5 GPa compared to a chromium free mineral, extending its survival to 840°C (Fumagalli et al., 2014).

Water transfer at depth in the mantle thus relies on antigorite (and chlorite) stabilization depending on the actual slab geotherm. However, water transfer via antigorite to great depth is a viable hypothesis only if higher pressure hydrous phases allow antigorite water conservative reaction with overlapping stability domains. The next sections examine the stability of intermediate pressure hydrous minerals and of Dense Hydrous Magnesium Silicates (DHMS).

II.3 Minerals stable beyond antigorite (and chlorite) stability

Experimental works revealed the existence of hydrous phases as products of antigorite and chlorite dehydration reactions. The principal minerals involved are the 10Å-phase, Mg-sursassite, hydrous Al-bearing pyroxene (phase-HAPY) and phase A. Natural evidence of the 10Å -phase has been suggested in chlorite-rich peridotite xenoliths from the diatreme at Moses Rocks (Colorado Plateau, Utah, see Smith, 1995) and confirmed as inclusions in olivine crystals from ultrahigh pressure rocks (Khisina and Wirth, 2002). However, the rest of these high-pressure hydrous minerals has only been experimentally observed.

II.3.1 10Å-phase

The 10Å-phase is a phyllosilicate that was synthesized by Sclar et al. (1985) in the MgO-SiO_2-H_2O system. It contains interlayered bound water (8-13 wt% H_2O), its chemical composition follows the formula $Mg_3Si_4O_{10}(OH)_2.nH_2O$ with *n* values of 0.65; 1; 2. Even though experimental studies reveal pressures and temperatures discrepancies for the formation of the 10Å -phase, its stability field can be located on the high pressure, high temperature side of antigorite and chlorite respective destabilization lines and below phase A stability.

The metastability of this phase has been raised, and experimental data show some discrepancies. Therefore, it is complicated to estimate its contribution to the water budget from the hydrous peridotite layer or the slab. Nevertheless, based on mass balance calculations from their experiments, Fumagalli and Poli (1999) assumed that a 10Å-phase carrying 9 wt% H_2O would allow transfer of 0.8 wt% H_2O in hydrous peridotite beyond antigorite or chlorite stability. 10Å-phase is compositionally a hydrated form of talc, and therefore its crystallization is favored in Si enriched environments.

In the MSH system, 10 Å-phase breaks down at conditions between 4 and >6 GPa, and for temperatures ranging between 450 and 600°C (Yamamoto and Akimoto, 1977; Khodyrev and Agoshkov (1986)) and up to 700°C (Pawley et al., 1995). The reactions associated are

$$\text{Talc} + 2\ H_2O = \text{10Å-phase} \qquad \text{(reaction II.10)}$$

$$5\ \text{chrysotile} = 6\ \text{forsterite} + \text{10Å-phase} + 7\ H_2O \qquad \text{(reaction II.11)}$$

$$3\ \text{chrysotile} = 3\ \text{phase A} + 4\ \text{10Å-phase} + H_2O \qquad \text{(reaction II.12)}$$

$$\text{Phase A} + 3\ \text{10Å-phase} = 22\ \text{forsterite} + 24\ H_2O \qquad \text{(reaction II.13)}$$

Although conducted in a similar system, the experimental investigation carried by Wunder and Schreyer (1992) inferred a highly metastable nature of the 10Å-phase, destabilizing in the range 3 -7 GPa, 200-700°C to produce talc again. They actually used a MSH synthetic mixture, seeded with natural antigorite, which might give a bulk departing from a strict MSH nature. The reaction antigorite = forsterite + 10Å-phase + H_2O was inferred from antigorite dehydration on a natural sample close to the MSH, but still containing minor amounts of aluminum (1.30 wt%), iron (1.8 wt%) and chromium (0.23wt%). The stability domain of the 10 Å-phase associated with this chemical system lies on the high pressure side of antigorite destabilization curve, on a thin line for pressures of 6 to 7.1 GPa and on the narrow temperature range 500 to 560°C (Ulmer and Trommsdorff, 1995). Based on their previous results Wunder and Schreyer (1997) favored an absence of overlapping of the 10Å-phase stability field with that of antigorite, establishing that the reaction of antigorite destabilization into 10Å-phase would not occur in the MSH, and constrained it stability to temperatures below 580°C at 7 GPa.

The 10Å-phase can contain a significant amount of aluminum in its structure. For example, a Tschermak component can be observed: $Mg_2Al^{VI}Si_3Al^{VI}O_{10}(OH)_2$. Al-10Å -phase has actually been produced after chlorite destabilization at 5.2 GPa and 680 °C in the Na_2O-CaO-FMASH system (Fumagalli and Poli, 1999). Its destabilization has even been bracketed in different starting bulk compositions between 700 and 800°C for pressures ranging between 3 and 6 GPa. On the other hand, iron incorporation in 10Å-phase (up to 6 wt% FeO) displays a limiting effect on its thermal stability. Instead of destabilizing at about 690°C, the Fe-bearing 10Å-phase disappears at about 580°C at high pressure (6.5 GPa) (Howe et al., EMPG abstract 2016). Its destabilization leads to Fe partitioning into ferrosilite, at high pressure, and into talc at lower pressure (5 GPa).

II.3.2 Mg-sursassite

MgMgAl-pumpellyite (Shreyer et al., 1986; Artioli et al., 1999; Fockenberg, 1995) was renamed by Gottschalk et al. (2000) into Mg-sursassite. This mineral actually corresponds to the isostructural phase Mn-sursassite $Mn_4Al_2Al_4Si_6O_{22}(OH)_6$ in which Mn to Mg substitution takes place as well as Al replacement by Mg + H, leading to the formula $Mg_5Al_5Si_6O_{21}(OH)_7$. Its water content is about 7 wt%.

While its stability covers the domain 3.5 – 10 GPa for a wide range of temperature in the endmember composition (Fockenberg, 1995), it has been observed between 6 and 9 GPa for a maximum thermal stability of 730°C the MgO-Al_2O_3-SiO_2-H_2O system (Figure II-12, Bromiley and Pawley, 2002). This still provides to Mg-sursassite the ability of transferring water from hydrous phases such as antigorite and chlorite to the higher pressure dense hydrous magnesium silicate phase A. For instance, a chlorite-bearing peridotite containing 2.8 wt% water could provide transfer of 0.98 wt% water via the reaction chlorite + enstatite = Mg-sursassite + forsterite + fluid (Luth, 2003). Chromium substitution for Al have been noted in the form Cr^{3+} to the extent of 0.22 atoms per formula unit without any further observations on the effect on its stability (Fumagalli et al., 2014). Investigation along the Mg-Fe join pointed out the importance of Fe-Mg substitutions and that the Fe-bearing sursassite would be stable at lower pressures than the Mg-bearing one (Wunder and Gottschalk, 2002). The later observation suggests that low pressure Fe-bearing sursassite could actually play a role in water transport into the mantle from the metapelitic and metabasaltic component of the slab.

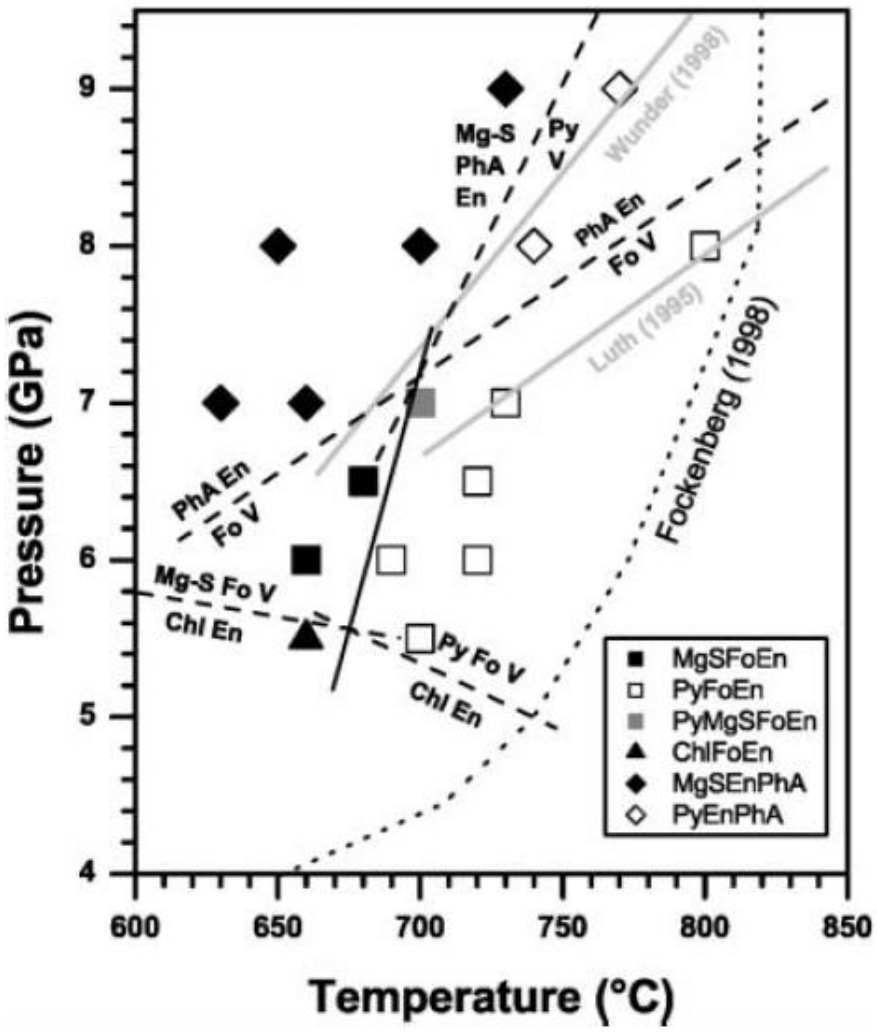

Figure II-12. Stability of Mg-sursassite in the MASH system determined by Bromiley and Pawley 2002.

II.3.3 Hydrous Al-bearing pyroxene (phase-HAPY)

The phase-HAPY is structurally very similar to pyroxene and contains 7 wt% H_2O. It has been discovered in the MgO-Al_2O_3-SiO_2-H_2O system with the composition $Mg_{2.1}Al_{0.9}(OH)_2Al_{0.9}Si_{1.1}O_6$ as a high-pressure product of chlorite destabilization at 5.4 GPa and 720°C (Gemmi et al., 2011). In a Cr-bearing bulk, phase-HAPY has been inferred to incorporate 0.11-0.09 Cr atoms per formula unit, equivalent to a maximum of 3.21 wt% Cr_2O_3. Phase-HAPY, because of its Mg/Si ratio > 1, cannot exist in garnet + pyroxene + fluid assemblages.

II.3.4 Clinohumite

Clinohumite occurs principally as titanium clinohumite, sometimes fluorine-bearing ($Ti_{0.5}Mg_{8.5}Si_4O_{17}(OH,F)$) in natural antigorite serpentinite in the low metamorphic grade of the green schist facies. It breaks down into an assemblage of olivine + ilmenite at low pressure (Trommdsorff and Evans, 1980), and can persists to the high pressure eclogite facies for low temperatures (Scambelluri et al., 1995; Zhang et al., 1995). Ulmer and Trommdorff (1999) estimated the maximum water amount hosted in clinohumite to 1000-1500 ppm.

On the other hand, OH-clinohumite contains 2.9 wt% water, it coexists after antigorite destabilization with enstatite and fluid but displays a reduced stability domain (Figure II-13) due to the limiting amounts of titanium and fluorine available in the mantle. In other words, clinohumite stability is strongly enhanced at higher temperatures by the incorporation of minor amount of Fluor ($Mg_9Si_4O_{16}(OH,F)_2$) compared to OH-clinohumite in the pure $MgO\text{-}SiO_2\text{-}H_2O$ system, up to 975 °C at 5 GPa and 1100°C at 12 GPa, and is therefore thought to play an important role in water transfer processes at depth beyond antigorite stability (Stalder and Ulmer, 2001a).

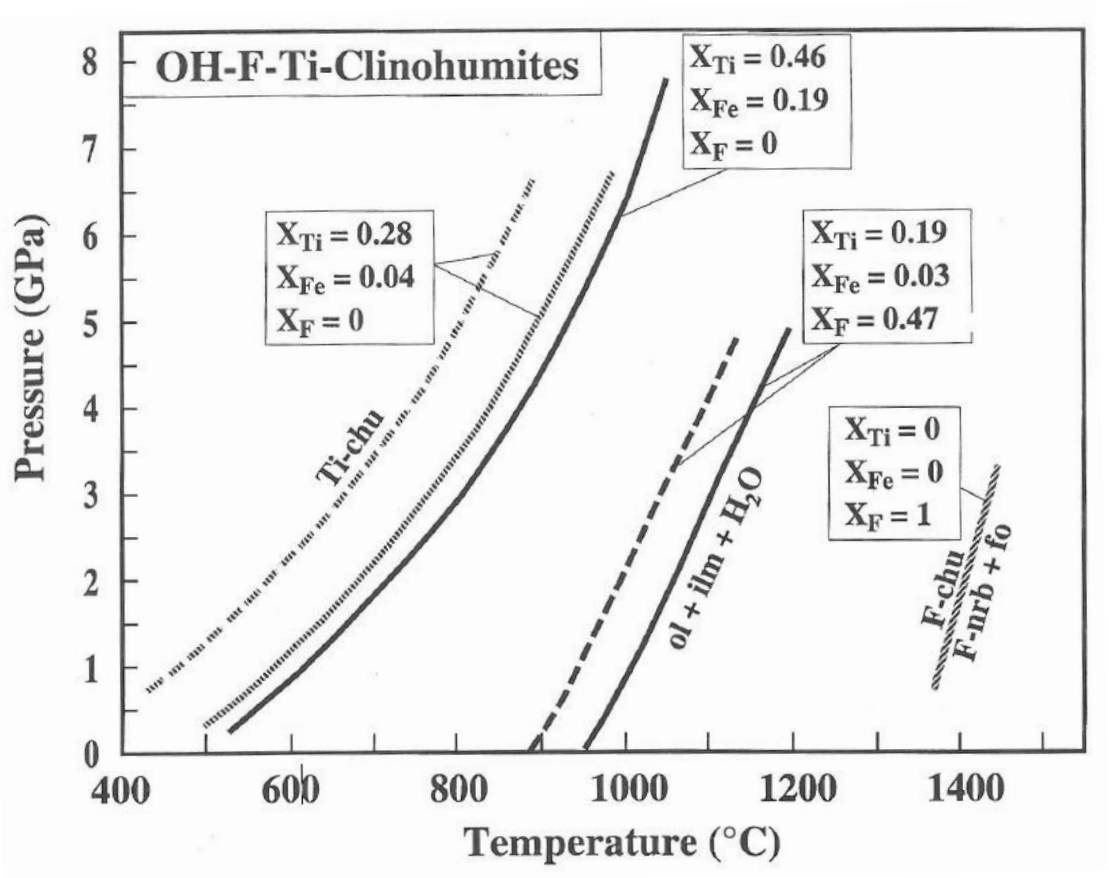

Figure II-13. Thermal stabilizing effect of titanium and fluorine on clinohumite, Ulmer and Trommsdorff (1999).

II.3.5 Chondrodite

Chondrodite $(Mg,Fe)_5^{2+}Si_2O_8(OH,Ti)_2$ is quite rare in both natural and experimental samples. Its stability and occurrence have been discussed in the MSH and Wunder (1998) proposed that chondrodite would be absent from olivine + orthopyroxene assemblage, while Stalder and Ulmer (2001) concluded that it would only be stable in a bulk with more than 2 wt% water.

II.3.6 Brucite

Brucite ($Mg(OH)_2$) is most likely forming at high pressure and high temperature associated in assemblages with high pressure dense hydrous magnesium silicates such as phase E, D or F. It has been observed in the MSH system at the conditions 5-8 GPa and 600-1200°C

in the assemblage phase D + water, after destabilization of phase A (Yamamoto and Akimoto, 1974). (Inoue, 1994) inferred brucite stability at 15.5 GPa and 1200°C, with phase E. Brucite stability has even been established up to 22.5 GPa for temperatures about 1000° C (Ohtani et al., 1995), in coexistence with phase F. Such an extended stability brings up the possibility of brucite as a candidate for hydrous phase at conditions of the uppermost part of the lower mantle, i.e. above 20 GPa, for temperatures below 1200°C.

II.3.7 Other recently discovered hydrous phases

More recently, a new phase has been introduced, with the characteristic diffraction peak at 11.5 Å. Fumagalli et al. (2014) characterized this 11.5Å-phase coexisting with Mg-sursassite, forsterite and spinel at 6 GPa and 650 °C, while it appears in the assemblage garnet + forsterite + diaspore + guyanaite (CrO(OH)) at 6.5 GPa, 700°C. Its water content is estimated to 14-15 wt% with the approximate composition of $Mg_{6.3}Si_{2.4}Al_{1.2.}$ It can therefore be considered as an hydrous mineral of interest for assemblages in the MASH or Cr-MASH hydrated peridotite bulk.

Another new hydrous Mg-rich phase, the 23Å-phase appears at 5.9 GPa and 720°C in the high-pressure products from chlorite dehydration (with garnet, olivine and spinel). It is characterized with a strong peak at 23 Å. It is stable over a very narrow temperature domain which extends to 750 °C at 6 GPa. Therefore, it could play an important pivotal role in transferring water beyond chlorite thermal stability. An Al-bearing version of this mineral ($Mg_{11}Al_2Si4O_{16}(OH)_{12}$) has been found at 10 GPa and 1000°C. It coexists with diaspore, pyrope in a MASH system, composed of phase A + Al_2O_3 + H_2O (Cai et al., 2015). Its water content is estimated to 12.1 wt%. This Al-rich 23Å-phase is very interesting in terms of both aluminum and water transfer to the deep upper mantle, and possibly mobilizes alumina for other DHMS in the transition zone and below. In addition to the aluminum stabilizing effect observed for

antigorite minerals (Bromiley and Pawley, 2003), extended stability of the aluminous 23 Å-phase confirms that Al incorporation in hydrous phases could be a key mechanism in water transfer in the mantle. In particular, its effect on DHMS stability is to be investigated and is developed in more details with our experimental study on natural antigorite phases relations at high pressure (Chapter IV).

II.4 High pressure and DHMS

II.4.1 Phase A

Phase A stability boundary is commonly associated to the *Choke Point*, i.e. the limit between structurally bound water in a mineral phase from the fluid phase released in the mantle. Therefore, constraining the location of the water line in the P-T space and reactions involving phase A is crucial in determining the fate of subduction related water in the deep mantle. Its stability has been delimited through experimental studies in different systems.

II.4.1.a Stability in the MSH

The first synthesis of DHMS was performed by (Ringwood and Major, 1967). They investigated this system between 10-18 GPa and 600-1100°C on a material characterized by a MgO/SiO_2 ratio varying between 1 and 5 (gel and oxide mixtures). They observed the existence of phase A through X-Ray diffraction photographs, mainly in the range of 10 to 15 GPa, with the MgO/SiO_2 ratio of 1.5 and 2, and suspected that this phase was hydrated, without any precise temperature indications.

Other experimental studies have contributed to better constrain the stability of phase A in the MSH system, such has (Yamamoto and Akimoto, 1977, 1974) who investigated a lower pressure range than Ringwood and Major (1967) (i.e. 3.5 to 9.5 GPa) and a wider temperature

range (500-1400°C). Their experiments were run using starting materials made from mixture of reagent oxides. They established the chemical formula of phase A as $Mg_7Si_2O_8(OH)_6$ and demonstrated that it is stable at 7.7 GPa and up to 1025°C. The reaction forming phase A (phA) (II.14) was first established by Liu (1987) in the MSH systems.

forserite + H_2O = phase A + enstatite (reaction II.14)

$$10\ Mg_2SiO_4 + 6\ H_2O = 2\ Mg_7Si_2O_8(OH)_6 + 3Mg_2Si_2O_6$$

Luth (1995) experimentally determined the reaction (reaction II.14) for the pressures 7, 8, and 9 GPa and the respective temperatures 720-740°C, 800-820°C, 860-880°C, in agreement with the results from Yamamoto and Akimoto (1977). At 10 GPa and between 920-940°C phase A was found to react with enstatite to produce clinohumite and finally forsterite + fluids between 940-960°C.

The location of reaction (reaction II.13) has also been addressed by Wunder (1998), still in the MSH system between 6 and 10.5 GPa and 650-800°C, with a steeper dP/dT slope compared to Yamamoto and Akimoto (1977) and Luth (1995), (Figure II-14).

Thermodynamic estimation of antigorite and phase A stability have been carried out by Bose and Ganguly (1995), considering the phases antigorite, talc, forsterite, enstatite and phase A, between 7-10 GPa and 700-1000°C. Their calculation was based on the retrieved Gibb's free energy of formation of phase A as a function of pressure and temperature, based on the experimental data presented by Luth (1995) on the equilibrium forsterite + H_2O = phase A+ enstatite. Therefore, they were able to place the invariant point at the intersection of this reaction and the dehydration curve of antigorite at 7 GPa and 700°C.

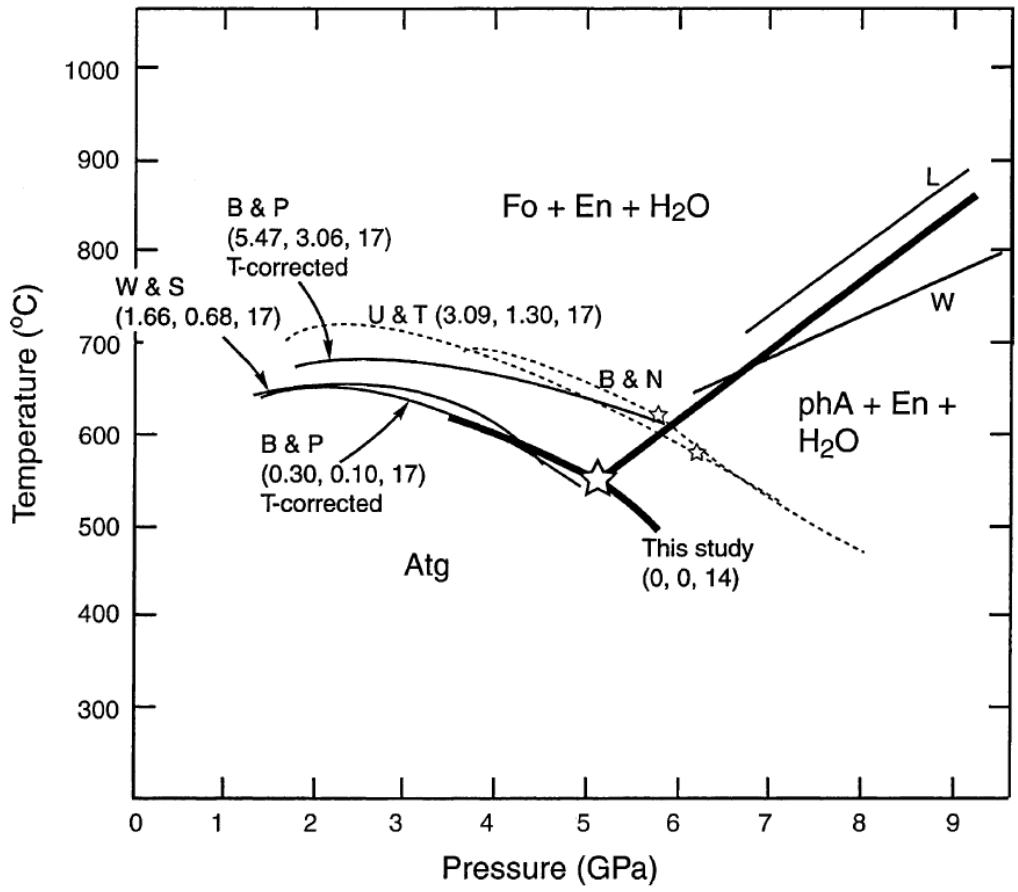

Figure II-14. Phase diagram for the join antigorite-phase A, (Komabayashi et al., 2005). B&P: Bromiley and Pawley (2002); W&S: Wunder and Schreyer (1997); U&T: Ulmer and Trommsdorff (1995); B&N: Bose and Navrotsky (1998); L: Luth (1995); W: Wunder (998)

Stability of phase A in the MSH system has later on been more precisely determined in the Mg-end member antigorite bulk composition (Komabayashi et al., 2005). In situ X-Ray diffraction experiments at high-pressure and temperature were conducted to bracket the transition forsterite + H_2O → phase A + enstatite. Combined with an investigation of the dehydration curve of antigorite, the invariant point at which antigorite, forsterite, enstatite, phase A and water coexist in the MSH system was found at 5.1 GPa and 550°C (

Figure II-14). The forsterite + H_2O = phase A + enstatite reaction was found to follow

P (GPa) = -2.38 + 0.0136 T(°C).

In a descending slab context, phase A (the lowest-pressure DHMS) can potentially carry H_2O according to two different paths. According to phase relation in the MSH system, the temperature profile of a relatively cold slab would intersect the reaction of antigorite dehydration antigorite = enstatite + phase A + H_2O, so that the water contained in antigorite would be transferred into phase A. The other possibility for water transfer through phase A occurs in the case of a slab following a higher temperature profile. It would cross on the high temperature limit of antigorite stability the reaction antigorite = enstatite + forsterite + H_2O. The water is then released as a fluid phase. It can be re-integrated in a mineral phase by crossing the equilibrium described by reaction II.14 as the slab is going deeper and pressure increases.

There is significant discrepancy in the location of the invariant point and the water line among the different experimental studies and the thermodynamic calculation from Bose and Ganguly (1995). The slope presented in Wunder (1998) is different from that of Yamamoto and Akimoto (1974, 1977), Luth (1995) and Komabayashi et al. (2005). The discrepancies have been correlated to HP calibration uncertainties and the use of different thermocouple material leading to differences in temperatures. The differences in the location of the invariant point and the antigorite-out curve can also be related to differences in the experimental procedures, including the choice of the starting sample (even if this last point should not have a strong effect on phase relations in the MSH system).

II.4.1.b Stability in other chemical systems

The stability of phase A in more complex systems has also been investigated. Luth (1995) evaluated phase relations in the systems MASH, MSH+CO_2, CaO-MSH and FMSH by respectively adding pyrope, magnesite, diopside and decreasing the bulk Mg/(Mg+Fe) from 1

to 0.9. The addition of new mineral phases results in different reactions of phase A destabilization and leads to slightly different P-T conditions for water structurally bound in minerals.

In the MASH and FMSH system, phase A breaks down at 8 GPa and respectively ~750°C and < 800°C into an assemblage containing clinohumite. Crystallization of clinohumite allows water transfer beyond phase A stability, up to 800-830°C in the MASH system and 850-900°C in the FMSH system. The addition of carbonate is believed to lower the temperature of dehydration reactions compared to the carbonate-free system (Ellis and Wyllie, 1980). The reaction of phase A destabilization encountered in the MSH+CO_2 system in the study conducted by Luth (1995) occurs between 800-850°C. However, within errors these conditions do not show significant displacement of the reaction. Destabilization of phase A occurs at lower temperature (700-730°C) in the CaO-MSH system.

II.4.2 Phase E

The hydrous silicate phase E was first synthesized by Kanzaki (1991) between 13 and 17 GPa and 800 to 1000°C in the MgO-SiO_2-H_2O system. Phase E is characterized by a nonstoichiometric nature, and a disordered crystal structure. Its composition has nevertheless been approached in the MgO-SiO_2-H_2O and falls along the forsterite-H_2O tie line with the formula $Mg_{2.3}Si_{1.3}H_{2.4}O_6$. Its structure comprises brucite-like layers of MgO_6 octahedra, cross linked by layers made of SiO_4 tetrahedra and MgO_6 octahedra and hydrogen bonds. Layers are arranged in a rhombohedral fashion and MgO_6 octahedra connect between layers by sharing edges. In front of the silicon tetrahedra, the brucite like layer has a missing cation, with no long range ordering (Kudoh et al., 1993). This cation disorder is assumed to be responsible for the particular broad Raman spectra of phase E (analogous to an amorphous material), reported by Frost and Fei (1998).

Numerous investigations of phase equilibria in the MgO-SiO_2-H_2O have led to inconsistent stability field for phase E over a very wide range of pressure and temperature spread between 11 and 20 GPa for 800 to 1300°C. Phase E at relatively low temperatures (900-1000°C) has been identified between 15 and 17 GPa (Ohtani et al., 1995) in agreement with Kanzaki (1991). On the other hand, survival of phase E to 1300°C has been suggested at lower pressures (11-12 GPa, Luth, 1995), intermediate pressure (15.5 GPa, Inoue, 1994) and higher pressure (to 20 GPa, Frost and Fei, 1998). A weak trend of Mg/Si increase associated with pressure increase has been suggested (Frost, 1999).

II.4.2.a Effect of Al and Fe on the stability of phase E

Experimental investigations on a serpentine bulk composition (still close to the MgO-SiO_2-H_2O) display stability conditions of phase E in agreement with some of the previous studies, between 800 and 1100°C at 12-17 GPa.

Aluminum appears to provide thermal stabilization for phase E, as well as it was observed for other hydrous minerals (antigorite, chlorite, even the higher pressure dense hydrous magnesium silicate phase D). Aluminum incorporation up to 3 wt% in phase E has been reported in the experimental work of Stalder and Ulmer (2001) with no particular effect on the stability domain of this mineral (12-14 GPa; 850-1110°C), while Kawamoto et al. (1995) noted the stabilization of aluminous phase E (9 wt% Al_2O_3) towards lower pressure (9 GPa) and to 1400 °C. Phase E has also been found in water saturated peridotite assemblages as a sub-solidus phase between 950 and 1000°C at 11 GPa (Kawamoto et al., 1996; Kawamoto and and Holloway, 1997), in agreement with some of the previous studies. Stabilization of phase E to lower pressures within an aluminum rich bulk composition has been suggested, due to selective incorporation of Al in phase E (Stalder and Ulmer, 2001a).

In addition to the aluminum effect on phase E stability, reasons for these important discrepancies (see Figure II-15) could also be related to the nonstoichiometric nature of this phase, its disordered crystal structure, the difficult characterization due to poor data quality (i.e. small crystal size). Frost (1999) even suggested that identification of phase E at the highest thermal conditions could be biased by the possibility that it would have been a quenched product instead of a stable phase.

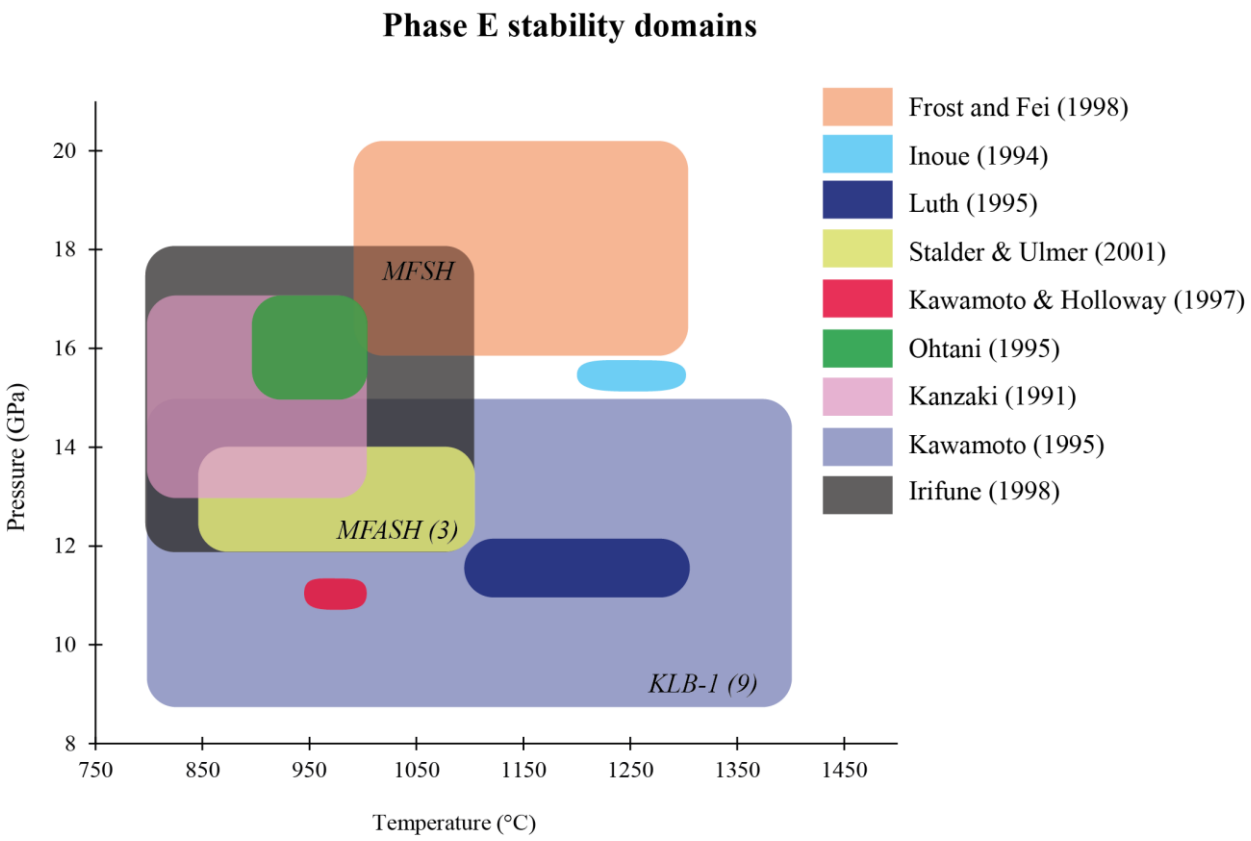

Figure II-15. Comparison of stability domains experimentally determined for phase E. Most of the studies were conducted in the MSH, or very close chemical system. Irifune et al. (1998) provided data in the FMSH system, Kawamoto et al. (1995) and Stalder and Ulmer (2001) in the MFASH system (Al_2O_3 maximum contents found in phase E minerals are reported into brackets).

Even though most of the experimental works agree on the stability domain of antigorite, those of the DHMS phase A and phase E are presented in the literature with considerable discrepancies. This might be related to different experimental procedures, as well as different

composition of starting materials. In particular, addition of aluminum to the simplified MSH system seems to play an important role on shifting hydrous phase boundaries to higher temperatures. In Chapter V and VI, we propose an investigation of hydrous phase (antigorite, clinohumite, phase A and phase E) stability in the natural Al and Fe rich serpentinite composition.

Chapter III - Experimental and analytical methods

Antigorite dehydration at low pressure (3 GPa) and phase equilibria in the serpentine bulk at higher pressure (6.5-10 GPa) were conducted. In this part, experimental methods related to this thesis are presented. First, we introduce the starting material used for antigorite and dense hydrous magnesium silicates (DHMS) stability investigations. The reasons why we chose this sample are there detailed, as well as its composition and homogeneity. Multi-anvil techniques used to bring our sample to conditions typical of a descending slab are described. The second section deals with preparation of recovered samples for analyses, and the different analytical techniques that allowed characterization of the experiments.

I Experimental methods

I.1 Starting material

I.1.1 Choice of the sample

In order to stay as close as possible to natural conditions, we chose a natural antigorite sample to run the high-pressure experiments. In the literature, most of experiments meant to deal with mantle composition are conducted using samples in a simplified chemical system. In the case of serpentine or dense hydrous magnesium silicates stability investigations, the $MgO\text{-}SiO_2\text{-}H_2O$ and $MgO\text{-}Al_20_3\text{-}SiO_2\text{-}H_2O$ systems are the most common. Synthetic mixes are therefore prepared from oxide reagent powders (or gels) in order to match the composition of the system chosen for the experiments. As described in the chapter II-II.2 (composition and structure of serpentine minerals) serpentinites are extremely complex chemically, and replicating their composition is very difficult. Moreover, the very specific structure of antigorite should affect its behavior at pressure and temperature and play a role on its stability. Synthesis that would reproduce such a complex structure is not possible, therefore a natural sample has been chosen for the purpose of this thesis.

Still, using synthetic simplified systems for experimental studies is very useful for identification of a mineral reaction as a function of temperature and pressure or for thermodynamic interpretation. The composition is entirely controlled and the kinetics or reactions are improved. On the other hand, experimental studies conducted on individual natural rock compositions are more difficult. The crystal sizes are smaller, some textures can display disequilibrium, and kinetics are not accelerated. They involve many components and phases, therefore allowing for a higher degree of freedom and cannot be reversed as easily as experiments in simple systems. Because reactions are continuous, attainment of equilibrium can be difficult to assess. Nevertheless, combination of this type of experiments with information derived from simple systems is useful and allow us to bring our understanding and

knowledge of phase relations to a level that is closer to the actual evolution of mineral systems within the Earth's mantle.

The choice of using a natural sample is risk, regarding the relatively large grains forming the serpentinite used as a starting material. As a result, equilibration time is higher than what would be sufficient in the case of experiments conducted using synthetics gels or powders. However, and despite our relatively short run duration times (discussed later in this section) we were able to confirm the attainment of equilibrium (at least at the local scale) in our experiments. The attainment of equilibrium in complex systems is difficult to demonstrate using reversal experiments, especially due to the continuous character of the reactions. However, several lines of evidence (seen in more details in the result chapters) point out to chemical equilibrium: (1) the growth of chemically homogenous new minerals, (2) systematics in element partitioning, (3) mass balance conservation (see also Fumagalli et al., 2014).

Besides chemical homogeneity of newly formed phases developed in the following chapters and as demonstrated by low standard deviations on the chemical compositions, Fe and Mg exchange between olivine and orthopyroxene is an indicator of equilibrium. Such partitioning can be represented by the reaction:

$$½\ Mg_2SiO_4 + ½\ Fe_2Si_2O_6 = ½\ Fe_2SiO_4 + ½\ Mg_2Si_2O_6$$

With the distribution coefficient defined as

$$Kd_{Fe\text{-}Mg}^{Ol/Opx} = (X_{Fe}^{ol} .X_{Mg}^{opx}.)/ (X_{Mg}^{ol}. X_{Fe}^{opx})$$

In the case of olivine and orthopyroxene coexisting after antigorite dehydration at 3 GPa microprobe analysis of the run products indicate a $Kd_{Fe\text{-}Mg}^{Ol/Opx}$ close to 1, then confirming that local equilibrium was reached (see chapter V).

For those experiments conducted at the same temperature but different run durations of 3 or 12 hours the similar $Kd_{Fe\text{-}Mg}$ indicates that local equilibrium was probably reached before 3 hours. Such a fast equilibration makes sense even at such low temperatures (below 900°C), because grain size is small and the reaction at stake is a breakdown involving fluid, which should help equilibration. At such low temperatures the Fe-Mg inter-diffusivity is very sluggish (of the order of 10^{-15} cm^2/s at 800°C, Meissner and Seifert, 1995), but diffusion distance is still of the same order of magnitude as the grain size. Also, the similarity of the $Kd_{Fe\text{-}Mg}^{Ol/Opx}$ to the Fe-Mg partitioning data reported in the work of Von Seckendorff and O'Neill (1993) shows good equilibrium behavior.

Attainment of equilibrium is also supported by systematics in iron partitioning. Moreover, the newly formed minerals display chemical homogeneity. In addition, mass balance calculations are satisfying and indicate no mass loss. Finally, we did observe phases boundaries at similar conditions than those reported in previous studies, which indicates that local equilibrium was reached.

Using a natural sample also provides some advantages that are not negligible regarding the redox modalities of antigorite dehydration. First, it is well established that antigorite minerals are characterized by high Fe^{3+}/Fe_{total} ratios ranging between 0.5 and 0.7 (Andreani et al., 2013; Debret et al., 2015; Marcaillou et al., 2011). Such an oxidized character is not easy to reproduce using synthetic material. Hence, the use of a natural sample with its intrinsic redox state seems to be the most straightforward method to perform experiments that would reproduce as close as possible the redox environment of serpentine dehydration reactions occurring in nature. The redox state of antigorite dehydration during subduction is intimately related to the presence of magnetite. For example, Debret et al. (2014, 2015) noted the diminution of magnetite modal amount from 7 to less than 2 % in natural subducting serpentinite rocks, associated with a redistribution of iron into secondary minerals. These works

emphasized a Fe^{3+}enrichment in the secondary antigorite and a decrease of the Fe^{3+}/Fe_{total} ratios in the bulk composition. The natural serpentinite sample that we used contains about 5 percent of iron-bearing oxides mostly composed of magnetite, which is representative of natural serpentinite rocks (Debret et al., 2015, 2014, Padrón-Navarta et al., 2013, 2011; Schwartz et al., 2013). The presence of such oxides is a very interesting particularity of our starting sample because it contributes to setting the intrinsic redox conditions of the investigated reactions at natural-like conditions. The magnetite contribution to antigorite phases relations was actually approached in another study, by adding 5 wt% of magnetite to the synthetic antigorite starting material (Merkulova et al., 2016). Also, with respect to the stability of hematite, our study is the first one to report it because we used cored samples with sufficiently large initial magnetite grains so that hematite overgrowth could be identified. Moreover, we still have magnetite present in coexistence with chlorite in the transitional lithology in agreement with Almirez field observations. Even if magnetite content decreases with increasing degree of metamorphism in natural samples (see Debret et al., 2014, Fig. 6), magnetite does not disappear completely and 1% of it remains.

Secondly, using a natural sample, in particular an uncrushed material eliminates carbon contamination issues. Synthetic powders easily absorb carbon when ground under ethanol for instance, resulting in the presence of uncontrolled amounts of CO_2 to the system. This carbon phase in turns modifies phases relations and the water fugacity. For instance, Luth (1995) noticed the change of phase A destabilization reaction from phase A + clinoenstatite = forsterite + H_2O in the pure MSH system to phase A + clinoenstatite + magnesite = forsterite + H_2O-CO_2-bearing fluid while adding carbonate to the starting materials. Other previous investigations used mixtures of natural antigorite with synthetic forsterite and enstatite (Ulmer and Trommsdorf, 1995; Bromiley and Pawley, 2003; Perillat et al., 2005) or with magnetite (Merkulova et al., 2016; see review of previous experiments in chapter II), or oxide gels +/-

seeds (Fumagalli et al., 2005; 2014). These reports constrain the determination of the stability field of antigorite and chlorite. However, while investigating the redox conditions for antigorite breakdown we are interested in the minute amounts of oxides that may crystallize after antigorite dehydration and that may be difficult to detect in fine grained material.

Antigorite structure and chemistry is particularly complex. It is characterized by a wavelike structure, made of silicon tetrahedra and magnesium octahedra sheets. The *m-value* is traditionally used to describe antigorite structure and chemistry according to the formula $M_{3m-3}T_{2m}O_{5m}(OH)_{4m-6}$ where O is for the octahedral cations (Mg, Fe^{2+}, Ni, Al) and T is for the tetrahedral cations (Si, Al, Cr, Fe^{3+}). It ranges between 13 and 24 for typical natural antigorite structures (Mellini et al., 1987). As discussed in Wunder et al. (2001), the m parameter (of the average value of 17) is supposed to be temperature dependent and therefore would play a role on antigorite stability or vice versa. A possible correlation between the m value and the high aluminum content found in antigorite from the most advanced metamorphic grade was actually suggested (Uehara and Shirozu, 1985), and confirmed by Al-rich antigorite (3.45 wt% Al_2O_3) studied by Hilairet et al. (2006), displaying a m-value of 14. Mellini et al. (1987) denoted the heterogeneous distribution of the m-parameter in natural antigorite samples, down to the scale of a grain.

All the above makes it difficult to choose the right *m*-value for one's experiment, especially if TEM is requested. Anyway, the agreement between the thermal stability of antigorite in our experiments and previous ones (see Chapter V) indicates that the modulation of the antigorite structure is not affecting our results significantly.

I.1.2 Initial sample characterization

I.1.2.a Mineral assemblages and their chemical composition

The starting sample used for experiments conducted in this thesis is cored from a natural serpentine from the Iron Mountain, North Cascades, Washington (USA), kindly donated by David Mainprice (Geosciences Montpellier). It is composed of a matrix of antigorite minerals with antigorite composition $Mg_{2.7}Fe_{0.1}Al_{0.09}Si_{2.02}O_5(OH)_4$. Optical microscope photographs and backscattered electron image on a thin section from the sample reveal the presence of iron-bearing oxides as aggregates and veins, crossing the homogeneous antigorite matrix (Figure III-1).

Electron probe micro-analysis on the metallic oxides allowed us to identify three different types of minerals: spinel $(Mg,Fe)Al_2O_4$, chromite $(Mg,Fe)Cr_2O_4$ and magnetite $(Mg,Fe)_3O_4$. These structures correspond to inherited material form the mantellic peridotite protolith (Bliss and MacLean, 1975). Aggregates of spinel up to 900 µm width display a double corona composed of Fe-chromite and magnetite. Composition of metallic oxides is given in Table IV-4 in the following chapter. The mantle spinel cores are Al_2O_3 and Cr_2O_3 rich (25.27 wt% and 37.10 wt%, respectively) with an X_{Mg} of 0.53. The chromite rims (26.69 wt% Cr_2O_3) are Fe_3O_4 rich (67.35 wt %) and contain Al_2O_3 (1.05 wt %). Magnetite also occurs as mall grains of about 100 µm width forming veins up to 3 mm long. It is mainly composed of iron and contains small amounts of Cr_2O_3 (1.48 wt %).

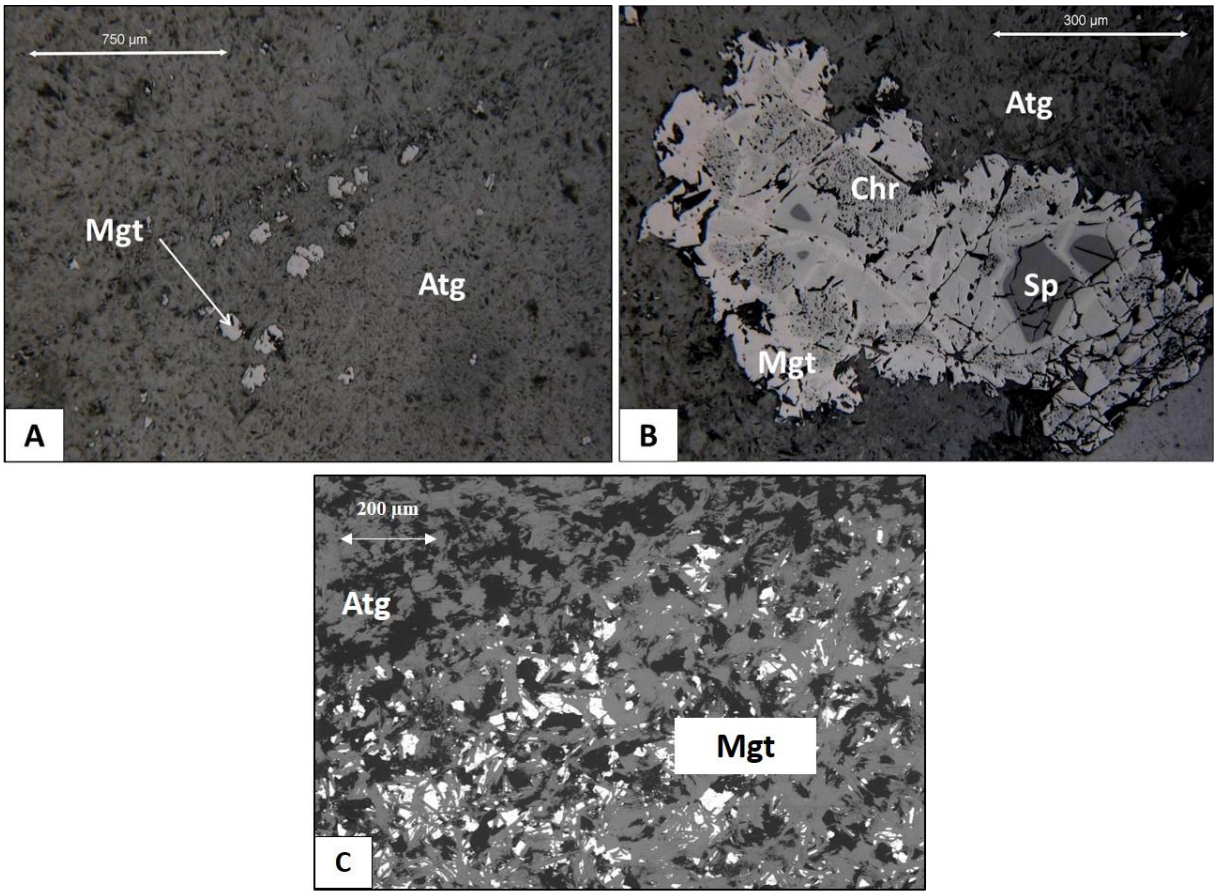

Figure III-1. Reflected light optical microscopy image of the starting serpentinite core sample showing A. magnetite veins within the porous antigorite matrix, B. inherited spinel core with chromite and magnetite corona. C. Backscattered electron image of the sample obtained using scanning electron microscopy. Magnetite concentration in a larger vein can be observed. Porosity in the sample can be observed, it is due to polishing for thin section preparation

Modal amounts of the phases in the starting sample were calculated by mass balance based on the serpentinite bulk composition and minerals average composition (antigorite, magnetite, chromite and spinel): 95 % of the sample corresponds to antigorite, 5 % is magnetite, while chromite represents less than 0.005. Spinel is present in the sample in very small amounts, so that the calculation produces a negative number (-0.01) for its modal amount. Another simple way to check these proportions for antigorite and magnetite is to neglect spinel and chromite in

the mass balance, since they are of low abundance in the starting sample. Given the very high iron content of magnetite (97.95 wt% compared to 23.36 wt% and 67.35 wt% for spinel and chromite respectively), it is reasonable to assume that most of the iron brought to the bulk by metallic oxides corresponds to iron from magnetite. Therefore, it can easily be established that 5 % of magnetite and 95 % of antigorite (2.62 wt% FeO) leads to 7.79 wt% FeO in the bulk. This estimation is also in agreement with that based on water content of antigorite mineral. The sum of oxides analyses obtained using EPMA on the starting antigorite crystals is 87 ± 0.6 %. If we assume that the amount of missing analyzed elements to 100% accounts for water, it leads to about 12.4 wt% H_2O. Therefore, 95.4 % of antigorite characterized by this water content can provide the 11.4 wt% H_2O measured in the bulk by loss on ignition.

I.1.2.b Homogeneity of the starting natural sample

To check for the metallic oxide homogeneous distribution and insure a controlled chemical composition of the starting material in all experiments, we conducted Inductively Coupled Plasma Atomic Emission Spectroscopy (ICP-AES) bulk rock analysis on 5 distinct batches of about 100 mg each. These batches were separated from the sample by a coarse crushing at first, and then finely ground separately, prior to analysis. The results suggest compositional homogeneity from one batch to the other with 40.04 ± 0.3 wt% SiO_2, 1.63 ± 0.11 wt% Al_2O_3, 7.79 ± 0.48 wt% FeO, and 38.94 ± 0.40 wt% MgO (Table III-1).

A departure of 0.5% from modal amounts for antigorite and magnetite previously calculated can explain the deviation of 0.48 wt% that we observe on the iron average bulk value, while comparing the five distinct batches analyzed. We conclude that our starting sample is homogeneous in composition and in mineral modal abundances, making it suitable for reproducible experiments.

The sample was drilled in small cylinders of two different diameters that were used on one hand at low pressure (3 mm – 25/17 assembly, see Table III-2**Erreur ! Source du**

renvoi introuvable.) for antigorite dehydration experiments (see chapter IV) and on the other hand for antigorite, phase A and phase E stability investigation (chapter V and VI, at higher pressure (2 mm – assembly 18/11). This approach is different from all previous studies where either synthetic mixtures or ground natural material were used.

Table III-1. Bulk rock composition of the starting serpentinite sample. Induced coupled plasma atomic emission spectroscopy was conducted on 5 different batches, ground separately for statistic on the magnetite repartition inside the sample. Average data are presented and considered as the representative composition of the sample while the standard deviation shows compositional homogeneity. Chemical composition of the antigorite, spinel, chromite and magnetite obtained by electron microprobe analysis are also presented

	Starting mat. Bulk Rock						Antigorite	Spinel	Chromite	Magnetite
Batch #	1	2	3	4	5	Average				
SiO_2	39.68	40.03	40.14	39.87	40.47	40.04 (0.30)	43.42 (0.52)	-	-	-
TiO_2	0.03	0.03	0.05	0.03	0.03	0.03 (0.01)	0.03 (0.03)	0.08	1.11	0.22
Al_2O_3	1.82	1.56	1.59	1.57	1.60	1.63 (0.11)	1.66 (0.36)	25.27	1.05	0.01
Cr_2O_3	0.27	-	-	-	-	0.27 -	0.22 (0.08)	37.10	26.69	1.48
FeO	7.98	7.20	7.92	8.42	7.43	7.79 (0.48)	2.62 (0.18)	23.36	67.35	97.95
NiO	0.25	-	-	-	-	0.25 -	0.15 (0.03)	-	-	-
MnO	0.09	0.09	0.09	0.09	0.09	0.09 (0.00)	0.07 (0.04)	0.53	2.42	0.12
MgO	38.36	39.12	39.15	38.71	39.36	38.94 (0.40)	38.79 (0.42)	13.65	1.39	0.22
CaO	0.02	0.01	0.01	0.06	0.01	0.02 (0.02)	0.02 (0.02)	-	-	-
Total	88.49	88.04	88.95	88.76	88.97	88.64 (0.39)	86.99 (0.60)	-	-	-
Structural formulae based on the indicated oxygens										
Si							2.02 (0.01)	-	-	-
Ti							0.00 (0.00)	0.00	0.03	0.01
Al							0.09 (0.02)	1.08	0.06	0.00
Cr							0.01 (0.00)	0.74	0.76	0.04
Fe							0.10 (0.01)	0.47	1.92	2.90
Ni							0.01 (0.00)	-	-	-
Mn							0.00 (0.00)	0.01	0.08	0.00
Mg							2.69 (0.02)	0.52	0.08	0.01
Ca							0.00 (0.00)	-	-	-
O							7.00	4.00	4.00	4.00
XMg							96.35 (0.27)	0.53	0.04	0.00

I.2 Multi-anvil experiments

Experiments for this thesis have been conducted at high pressure (HP) and high temperature (HT) using the two Kawai-type multi-anvil presses (Figure III-2) at the Laboratoire Magmas et Volcans (National facility, Clermont-Ferrand, France).

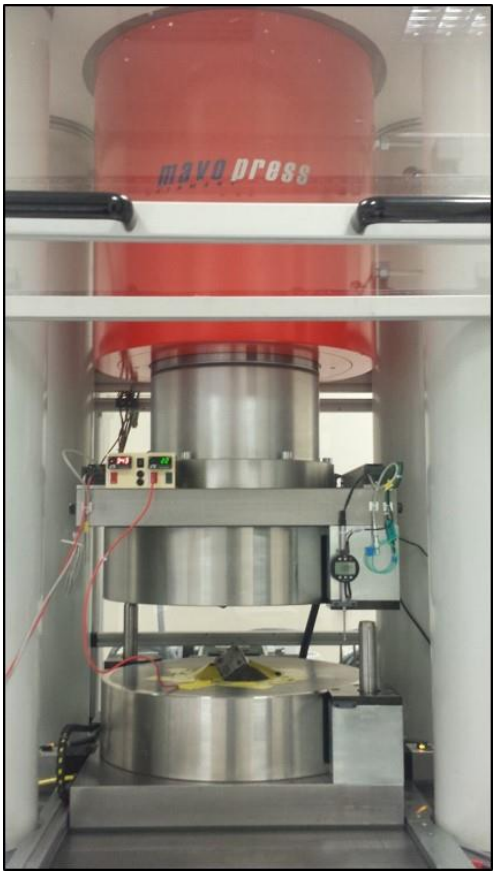

Figure III-2. The 1500 tons multi-anvil apparatus, Laboratoire Magmas et Volcans. The two parts of the split cylinder can be seen, with the primary anvils on the bottom part, containing the 8 WC cubes assembled, before starting compression.

A multi-anvil apparatus is capable of generating pressures through a hydraulic system. This technique is suitable to conduct experiments reproducing phase equilibria at pressure-temperature conditions representative of mantle conditions. The pressure is produced by a hydraulic ram and transmitted to the sample via two stages of anvils. It can reach ~ 25 GPa (750

km depth). The first stage is composed of 6 primary hardened steel anvils cut as segments from a cylinder, to allow compression of a cubic set of secondary tungsten carbide (WC) cubic anvils. The corner truncations of the WC anvils form an octahedral cavity when assembled.

An octahedral shaped pressure transmitting medium containing the sample is placed in that chamber so that the uniaxial force first generated by the hydraulic press and then received by the sample is isostatic. This medium is made out of MgO (doped with 5% Cr_2O_3), which behavior at high temperature and high pressure allows a quasi-hydrostatic pressure (i.e. no oriented frictional and inertial stress). Since the pressure received by a body results from application of a force applied over a given surface, at a constant force, a body exposing a smaller surface would receive a higher pressure than a body exposing a higher surface. As a consequence, decreasing the octahedral edge length (OEL) and the truncation edge length (TEL) of the tungsten carbide cubes permits to reach higher pressure conditions at a given force generated by the hydraulic press. Different sizes of OEL/TEL define different types of assemblies. For example, a 25/17 assembly corresponds to a 25 mm edge length octahedra used with a 17 mm anvil truncation. For this thesis, experiments at 3 GPa have been conducted using 25/17 assembly and experiments at 6.5-10 GPa, using 18/11 assembly. Ultimately, the size of the octahedral pressure medium controls the size of the inner assembly and the volume of the sample. The octahedron is drilled through two opposite faces and a low thermal conductivity material (ZrO_2) sleeve is inserted as a thermal insulator, to prevent heat transfer to the WC cubes (during experiment heating they can still reach 100°C), that would increase their plastic deformation and eventually increase the probability of breaking (Figure III-3).

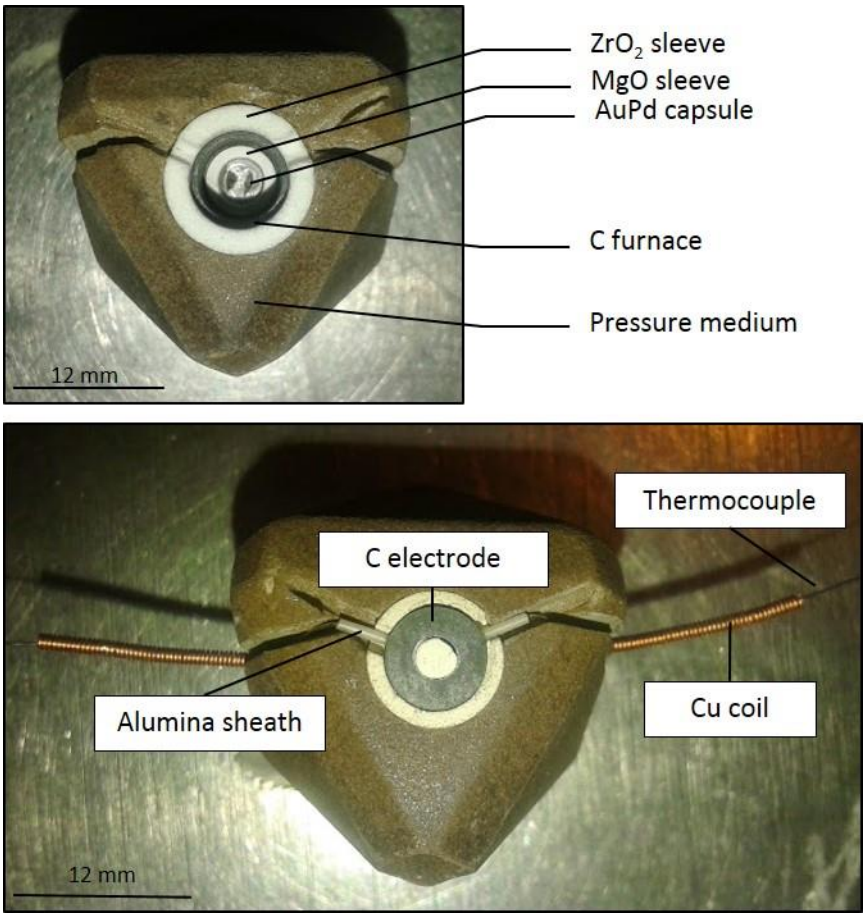

Figure III-3. Octahedral pressure medium used for the multi-anvil experiments with the 25/17 assembly. On top the octahedra contains the internal pieces of the assembly and the sample inside the metallic capsule. On the bottom picture, before adding cement, the thermocouple has been set, as well as the electrode to allow current transfer from the WC anvils to the heater.

The capsule containing the sample is located in the center of a 3 pieces tubular resistance heater (stepped furnace). It is a cylinder made of noble metal such as platinum (Pt) or gold-palladium alloy ($Au_{80}Pd_{20}$) sealed on each side of the sample. AuPd capsule is interesting for experiments with samples containing iron since the Fe-alloying is limited with this material compared to Pt. It also limits the water loss. Nevertheless, its melting point is at about 1400°C, which can be too low in the case of partial melting experiments that require higher temperatures. On the other hand, Pt can subsist to higher temperatures but incorporates considerable amounts of iron. An additional inner capsule can be placed between the AuPd or Pt outer capsule and

the sample to prevent hydrogen diffusion through the capsule, for example if the experiment is conducted under hydrous conditions.

Table III-2. Assemblies used for the experiments in this thesis and their associated parameters.

OEL/TEL (mm)	Max. Pressure (GPa) (GPa)	Capsule Ø (mm)	Capsule length (mm)
25/17	6	3	4
18/11	12	2	3.5

The heater wall thickness is increased in the central part (lower resistance; i.e. lower heat for a given power) while the heater walls above and below the capsule are thinner (higher resistance; i.e. higher heat for a given power, Figure III-4) in order to reduce the thermal gradient, and avoid heat loss from the extremities. The thermal gradient can also be minimized by favoring the use of material with a negative dependence of temperature with resistance. The thermal gradient effect can still be noticed within the sample. For example, on Figure III-5, we can see a zoning that is caused by small temperature variations within the sample. Indeed, the expected hotter area corresponds to a relatively high-temperature mineral assemblage while the one on the central part corresponds to a low-temperature mineral assemblage. We used the finite element model developed by Hernlund et al. (2006) to estimate the thermal gradient in our assembly. For the 25/17 assembly using LaCrO3 furnace and at 100°C, the thermal gradient is negligible. At 700°C it corresponds to less than 30°C/mm and at 800°C it represents less than 35°C. It is reduced to less than 11 °C at 700°C for an assembly with graphite furnace. Graphite's resistance is almost independent of temperature, this is why this material is commonly used as a heater in multi-anvil experiments. It can be used up to 10 GPa, above that pressure graphite turns into diamond and the heater would fail. At higher pressures, lanthanum chromide ($LaCrO_3$) is chosen as heating material for its decreasing resistance with increasing temperature (semi-conductor).

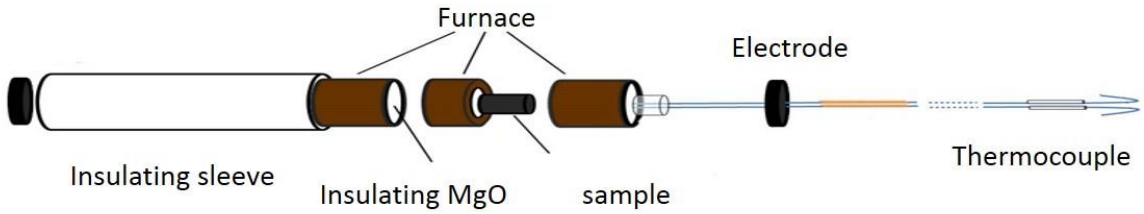

Figure III-4. Geometry of the assembly inside the octahedral pressure medium.

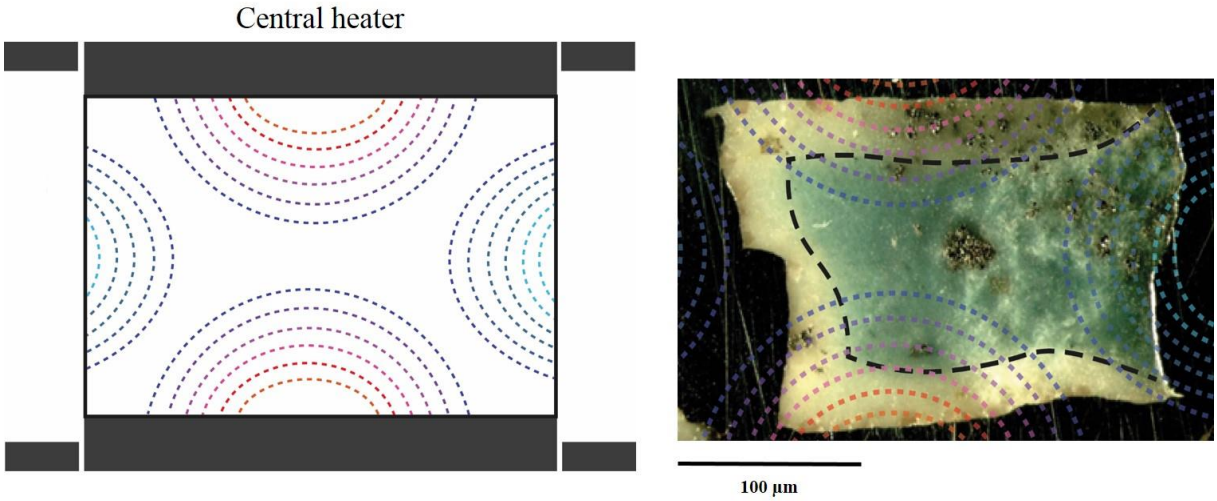

Figure III-5. Thermal gradient in the sample shown schematically. The hotter spots are located on the lateral walls, inside the capsule. Thermal variations can favor different mineral assemblages inside one sample. This example (experiment M450, more details in Chapter VI-III.1) shows an assemblage of olivine + enstatite + phase E in blue and the high temperature assemblage garnet + olivine + enstatite in white, at the location of hotter spots.

In this thesis all experiments were conducted below or at 10 GPa, the two types of heaters have nevertheless been used, depending on the imposed redox environment required for the experimental purpose (i.e. graphite for reduced conditions, $LaCrO_3$ for oxidized conditions).

An MgO sleeve is inserted between the furnace and the capsule, as well as MgO spacers above and below the capsule, inside the top and bottom heater tubes. The spacer above the capsule is drilled for the insertion of a thermocouple, connected inside a 4-hole alumina tube.

The thermocouple junction is placed at the top of the sample. It consists in two wires made of different composition, hence providing an electromotive force (e.m.f) measured by a voltmeter from which is deduced the temperature. Pt-PtRh10% (S-type) or W5%Re-W26%Re (W-type) thermocouple have been used for the experiments of this thesis. S-type thermocouple is efficient for the temperature range 600-1600°C with ±0.25% incertitude while the W–type is efficient between 425 and 2320°C with ±1% incertitude.

Figure III-6. Assembly for multi-anvil experiments.

Thermocouple wires can break easily because of the tension during the experiment, to reduce this risk they are inserted in troughs on both sides of the central drill of the octahedra. They are hold by alumina cement and exit the octahedra on the side, perpendicularly to the edges, guided and protected from rupture by a copper wire coil. This coil can accommodate deformation during compression and help the thermocouple wires to stay intact on the way out of the octahedral cavity between the cubes through the gaskets fixed along

the cubes truncation. Pyrophyllite gaskets are placed in a way to prevent contact between cubes, and to accommodate the pressure gradient between the octahedral cavity and the exterior of the assembly. The gaskets are held using paper glued on the WC anvil to prevent them from moving before the compression (Figure III-6).

The 8 cubes once assembled are fixed together with epoxy sheets directly glued to the WC and current is carried from the electrical heating device connected to the press system through two electrodes placed at the extremities top and bottom of the assembly, in contact with the furnace. Molybdenum electrodes are used together with $LaCrO_3$ furnace while graphite is used for the graphite furnace. Electrical insulating tape is preliminary placed on the WC cubes inner faces that could possibly be in contact with each other inside the assembly inner part. Two small pieces of copper foil are inserted on the epoxy sheets on top of the two anvils in contact with the electrodes in order to allow current flow to the furnace tube and create the resistive heating. The so formed assembly is then placed inside the cubic cavity left by the primary anvils and thermocouples wires are connected to the voltmeter of the press heating system (Eurotherm regulator/programmer system).

I.3 Experiment procedure

I.3.1 Compression and decompression

The press is controlled by the RT (real time) computer via a user interface (HOST) connected to the system. This interface allows the input of commands on the pressure and temperature instructions and the direct reading the experimental parameters. During this thesis, the two multi-anvil presses at the Laboratoire Magmas et Volcans have been used. Their operation presents some little variations as the 1000 tons requires the user's intervention to open or close valves of the hydraulic compression system.

Once the primary anvils are closed around the secondary cubes, the pre-compression stage can begin. It is crucial that this first compression stage follows a slow ramp to enable all elements of the assembly to fit properly and avoid any rupture. Therefore, it is chosen to slowly reach 10 bars before starting the actual compression ramp. The speed usually used is of about 0.5 bar.min^{-1}. The target pressure is then reached on a ramp of about 1 to 1.5 bar.min^{-1}. Heating is initiated while the target pressure is reached, and decompression starts once the heating is turned off (quench). Decompression can cause cracks in the sample and/or breaking of the WC cubes if it is set too fast, hence a long decompression duration favors the chances of avoiding these problems. An adequate decompression speed is for example 0.2 bar.min^{-1}

For the present experiments, no direct pressure measurement is possible. As a consequence of frictional loss of force through the gaskets thermal relaxation, and/or thermal pressure through the assembly, pressure calculation is unreliable to assess the real pressure in the sample. A pressure calibration as a function of the applied load and temperature is therefore required (Figure III-7). Such a calibration can be obtained for each assembly using known mineral transitions at given pressure-temperature conditions. The calibration at room temperature usually relies on the location of phase transformation of Bi(I)-Bi(II) transition at 2.55 GPa and Bi(III)-Bi(V) transition at 7.7 GPa.

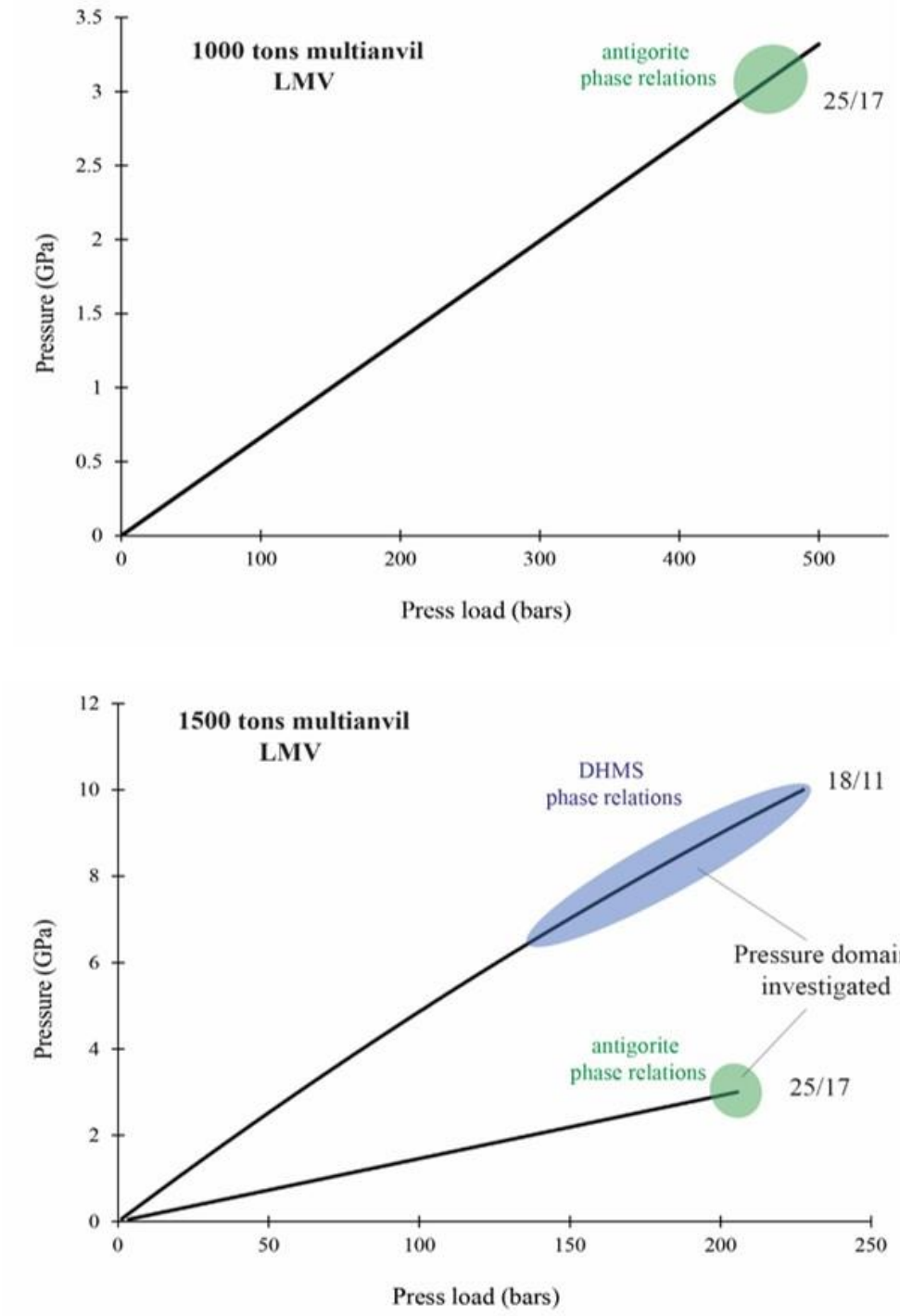

Figure III-7. Pressure calibrations for the 18/11 and 25/17 assemblies used during this thesis.

I.3.2 Heating

Heating of the sample is started once the target pressure is reached. Electrical current travelling through the anvils produces heating by Joule effect in the furnace. The thermocouple allows the user to follow the temperature evolution at the top of the capsule and adapt the intensity of the current applied. Once the sample is assumed to be equilibrated at the P-T conditions applied, the experiment is quenched by turning off the heating system power and cools down to 80°C within less than 10 seconds. The thermocouple can nevertheless break during compression, leaving the user with a possible estimation of run temperature using the electrical power applied. The correlation between the power and the temperature can indeed be obtained during previous experiments in the same conditions (pressure range, assembly materials) and compared with a later experiment (see Figures III - 8, 9, 10, 11, and 12). A gap between the thermocouple and the capsule can also be the cause of bias in temperature assessment during the experiment. As a consequence of the thermal gradient, the temperature reading on the interface would then be lower than the actual temperature in the sample. Heater failure (breaking of one piece of the tubular heater, lack of continuous connection between the conductive parts of the assembly) can also be encountered and leads to a failed experiment.

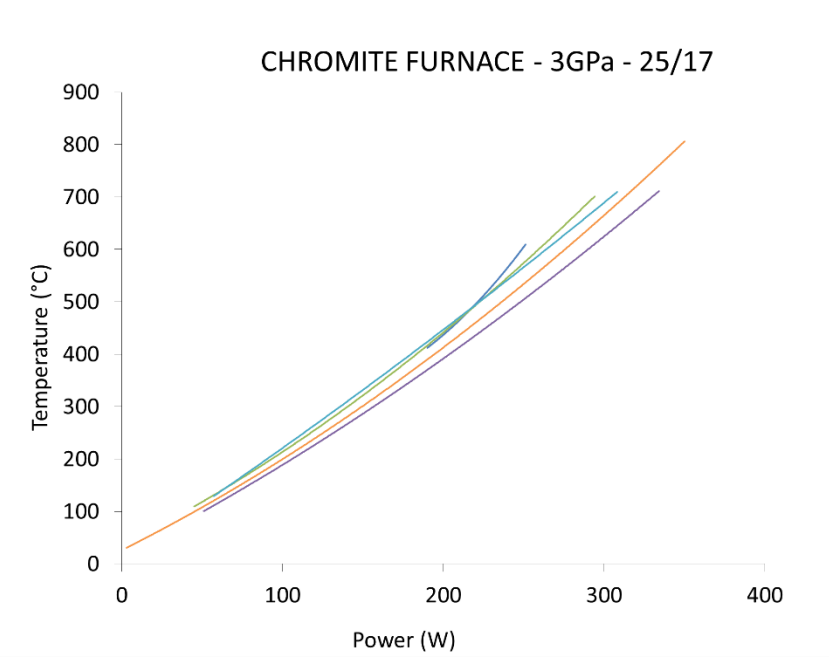

Figure III-8 : Heating calibration based on the measured temperature with the thermocouple versus the power. The curves represent data obtained during the monitoring of the heating stage of experiments conducted at 3 GPa, with the 25/17 assembly, using $LaCrO_3$ furnace.

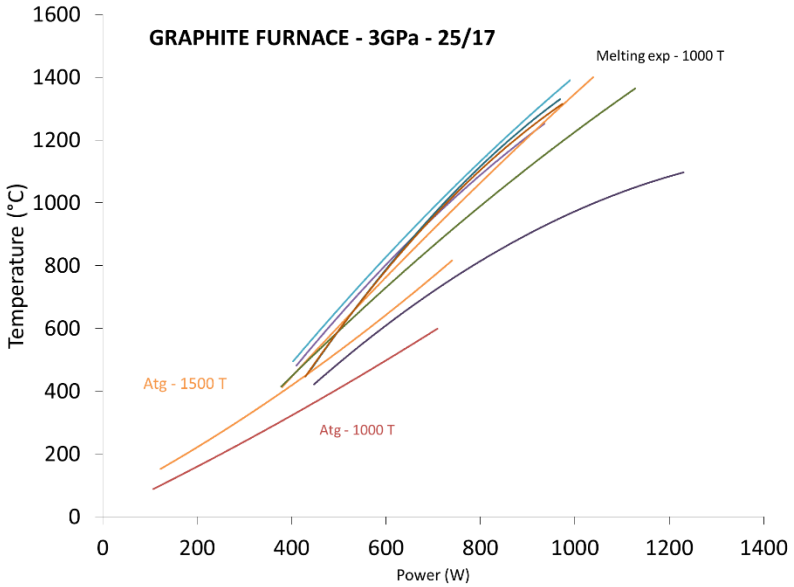

Figure III-9. Heating calibration based on the measured temperature with the thermocouple versus the power. The curves represent data obtained during the monitoring of the heating stage of experiments conducted at 3 GPa, with the 25/17 assembly, using graphite furnace. It is worth noting the relatively good agreement of the calibration curve while using the 1000 tons or 1500 tons press. Additional curves related

to hydrous partial melting experiments are reported for comparison, even though this work is not part of the present thesis.

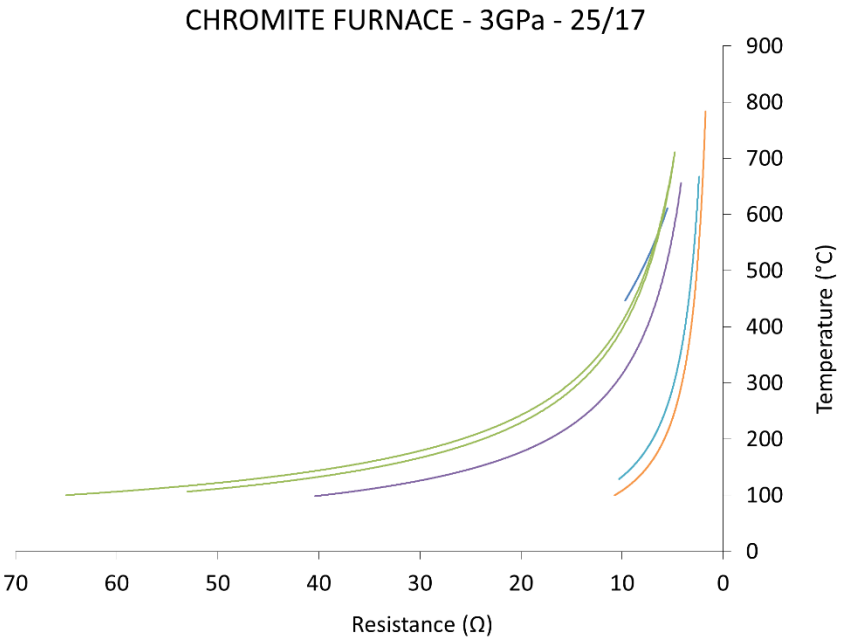

Figure III-10. Heating calibration based on the measured temperature with the thermocouple versus the furnace resistance. The curves represent data obtained during the monitoring of the heating stage of experiments conducted at 3 GPa, with the 25/17 assembly, using $LaCrO_3$

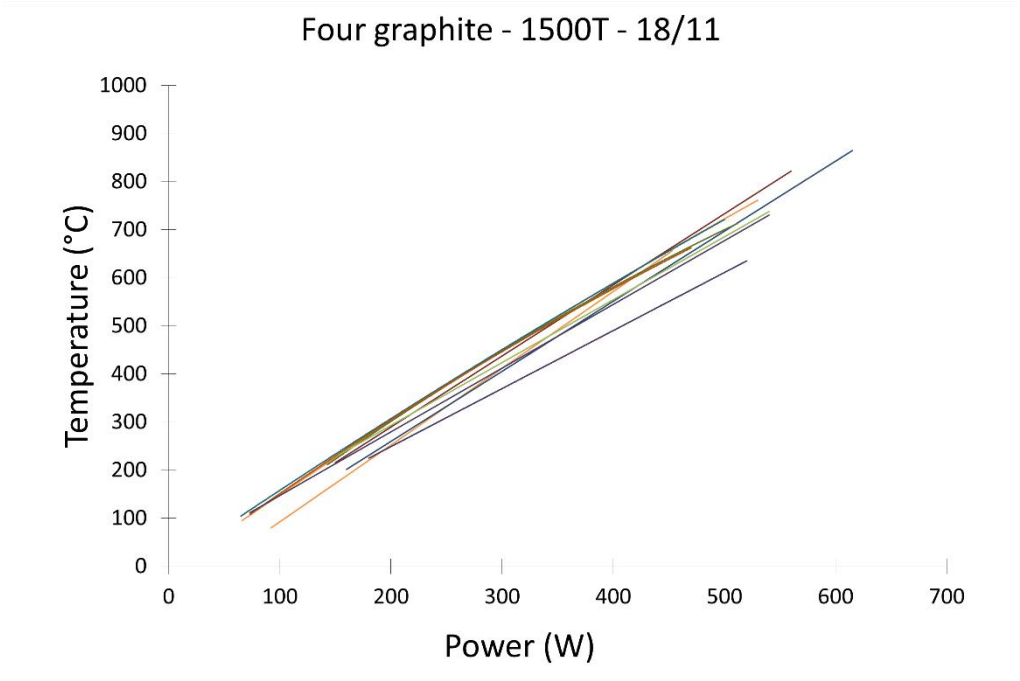

Figure III-11. Heating calibration based on the measured temperature with the thermocouple versus the power. The curves represent data obtained during the monitoring of the heating stage of experiments conducted between 6 and 11 GPa, using the 18/11 assembly and graphite furnace.

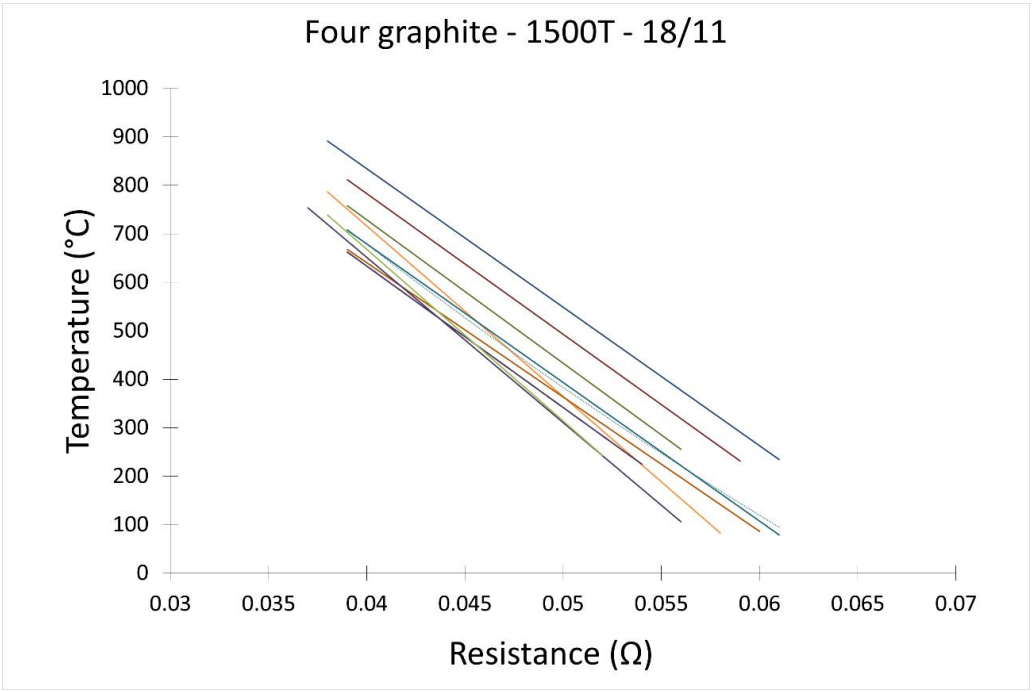

Figure III-12 : Heating calibration based on the measured temperature with the thermocouple versus the furnace resistance. The curves represent data obtained during the monitoring of the heating stage of experiments conducted between 6 and 11 GPa, using the 18/11 assembly and graphite furnace.

I.4 About the choice of using multi-anvil at 3 GPa instead of piston-cylinder

Antigorite dehydration experiments were performed at 3 GPa. Such pressure conditions are traditionally attained using piston cylinder experiments. One could argue that multi anvil technique for 3 GPa experiments would display significant bias in pressure estimation at such low-pressure conditions. The consistency of our results with those of previous studies concerning the thermal stability of antigorite proves the contrary (see discussion in Chapter IV).

We actually chose to perform multi anvil experiments rather than piston-cylinder experiments because it allows to modify the redox environment of phase transformations occurring in the sample by changing the nature of the furnace material. As we aim to reproduce natural redox condition for antigorite dehydration, it is very important to not modify it by imposing a different fO_2. Indeed, hydrogen diffusion thought the metallic capsule takes place, to equilibrate the sample's oxygen fugacity with the oxygen fugacity of the assembly. According to the study of Hempelmann (1984), hydrogen diffusion rates at 700°C in metals are estimated to be in the magnitude order of 10^{-4} $cm^2.s^{-1}$. That means that an atom of hydrogen diffusing at 700°C would cross the 0.5 mm thick capsule walls in less than 10 minutes.

Still, there are some experimental procedures to avoid hydrogen exchanges between the sample and the surrounding materials. First, using an insulating sleeve between the capsule and the furnace can prevent the diffusion of hydrogen and therefore preserve the intrinsic redox character of the sample. Such material is available for multi anvil experiments, for instance boron nitride can be used. Using a furnace of a similar fO_2 than the sample's one also reduces H_2 exchanges during the experiment. Chromite lanthanum and graphite furnace are the two most common options to provide heating in multi-anvil experiments **(**Figure III-13). The "reducing" character of graphite furnace (1 to 2 log units below the hematite-magnetite buffer at 700°C; Ulmer and Luth, 1991) leads to hydrogen exchanges with the sample. On the other hand, the more oxidizing character of the chromite lanthanum furnace provides only little H_2

exchanges from the furnace to the sample. This exchange might actually follow the reverse path, and little hydrogen amount could diffuse from the sample to the furnace. The oxygen fugacity of $LaCrO_3$ furnace is not yet determined by previous studies but is well known to be oxidizing.

Actually, in this study we cumulate difficulties for controlling the oxygen fugacity: low temperature, where few sensors have been calibrated (for example the "Fe in AuPd" sliding sensor is calibrated for the reaction between metal and melt), and high oxygen fugacity where (the "Fe in Iridium" sliding sensor would not be accurate). Fixing the oxygen fugacity by adding redox buffers is the last thing to do since we seek for an intrinsic control of f_{O2} by the sample.

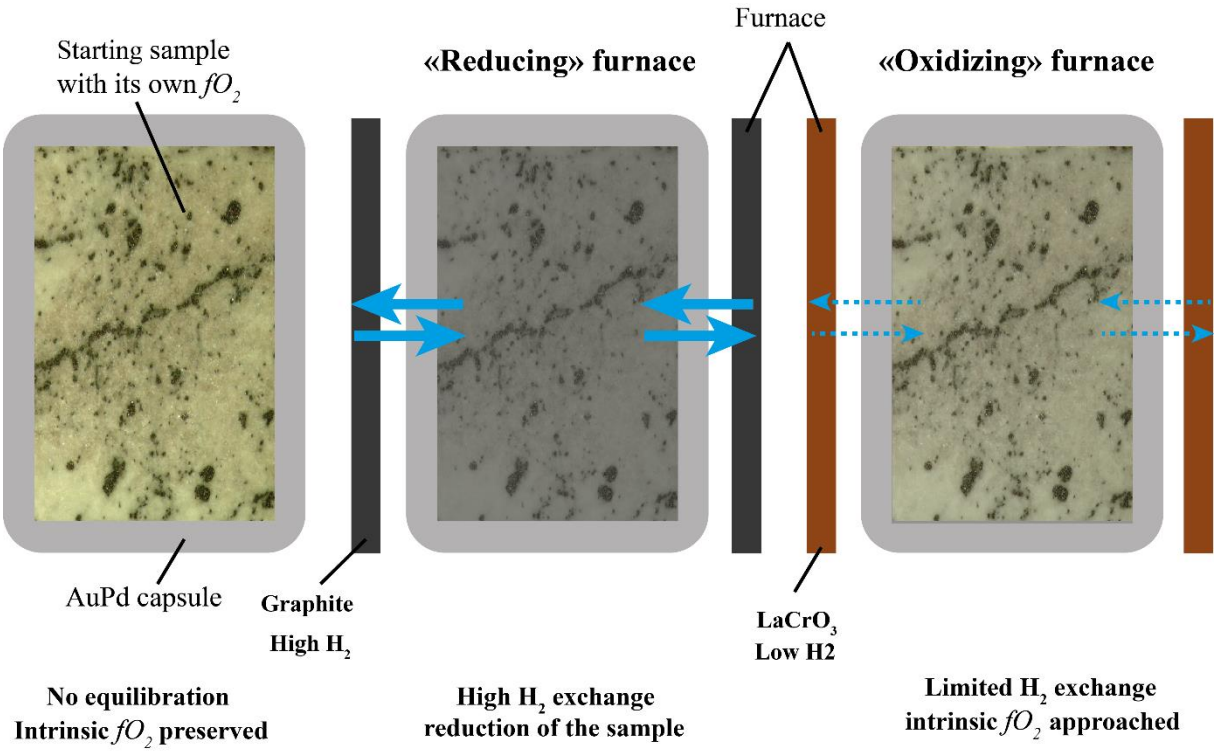

Figure III-13 : Schematic representation of the sample and the oxygen fugacity modifications induced by H_2 exchanges with the furnace material.

I.5 Kinetics of antigorite dehydration and run duration at 3 GPa

According to the antigorite dehydration study conducted by Perillat et al (2005) on a natural ground sample, 3 hours are sufficient to reach reaction equilibrium at 4.1 GPa and 530°C. It is worth noting that because of these experiments were performed in-situ, the sample was not sealed and as a result H_2O loss is to be considered. Water presence could enhance antigorite dehydration reaction kinetics. On the other hand, Merkulova et al. (2016) performed antigorite dehydration experiments at 2 GPa and 700°C for varying run durations and noted that 2.5 days long experiments did not provide equilibrium for antigorite dehydration reaction. But we think that there is no reason for magnetite to disappear, at least not before all the antigorite is consumed (in agreement with field observations, Debret et al., 2014, 2015). The experiments performed in Merkulova et al. (2016) experiments lasted for up to 10 days. Considering that they used piston cylinder with graphite furnace, it is very likely that the intrinsic redox state of their sample was modified and buffered by the furnace.

II Analytical methods

This section presents the different techniques used to obtain qualitative information from the recovered samples such as the general texture of mineral assemblages, and the nature of the phases (scanning electron microscopy, Raman spectroscopy) and quantitative information such as mineral chemical composition (electron probe micro-analysis).

II.1 Sample preparation for characterization

The assembly is taken out of the press, the octahedral pressure medium is opened by gently breaking and the capsule is removed from the rest of the assembly using tweezers and cutting pliers. Samples synthesized during this thesis contain hydrous mineral assemblages or dehydration products revealing high porosity textures. Mineral phases produced after dehydration reaction of antigorite are often very small (1 to 10 µm for the smallest) and included

in a fibrous matrix. Hardness differences between the mineral material and the capsule is contributing to the challenging task of sample polishing. These particularities observed in our hydrous experiments are responsible for the very fragile nature of the samples here studied, hence requiring extremely careful steps for polishing.

First, the recovered sample is either embedded in epoxy or a dental resin, and opened by gently hand polishing with 1200 µm silicon carbide polishing paper. The first opening of the capsule through a small hole is established by a regular visual control using binocular microscope. The sample is then soaked into ethanol to check for water bubble escape, that insures that the system was closed. Because of the fragility of our samples, polishing time with 1200 µm paper is reduced to the shortest possible, still providing a sufficient surface to be further polished and widened by finer polishing paper. Before continuing polishing with 2400 µm carbide paper, samples exposing a significant porosity to the surface, are impregnated under vacuum by leaving a drop of cyanolite (superglue) on the surface of the sample. The superglue provides a better cohesion between grains and avoids material loss while polishing. It also helps to improve the quality of the surfacing of mineral assemblages, by filling the porosity and remove surface irregularity interfering with probe analysis. As glue is more fluid than epoxy and dries faster, it also allows relatively fast preparation of the sample for analysis, even if successive times are required in between polishing steps. This is nevertheless not appropriate for experiments containing important volume of voids, due to dehydration reactions at higher pressures (6.5-10 GPa) and epoxy is favored instead, following the same procedure. Once the sample is well exposed to the surface it is hand polished with 6, 3 and ¼ µm diamond suspension. A very fine layer of carbon is diffused on top or the sample surface (carbon coating) to improve the conductivity during electron probe analyses.

II.2 Sample characterization

Bulk rock analysis of the starting material was performed using ICP-AES technique (Inductively Coupled Plasma Atomic Emission Spectroscopy), the results are displayed in the section about the choice of starting sample (I.1.1).

II.2.1 Optical microscopy

A first look at the sample under optical microscope can help to identify mineral transformations. For instance, it is possible to see from the color and the texture of the recovered material whether or not a dehydration reaction occurred during the experiment. Figure III-14 shows the products of antigorite dehydration at high pressure (8 GPa) for two different temperatures: 750 (run M450) and 850 °C (run M451). The blueish center of M450 corresponds to phase assemblages not completely dehydrated (containing the hydrous phase E), while the white borders of the capsule correspond to a anhydrous assemblage, in which we can see pink garnet phenocrysts. The experiment M451 experienced a temperature higher by 100°C compared to M450 and a relatively more homogeneous texture can be observed, with a fully dehydrated assemblage.

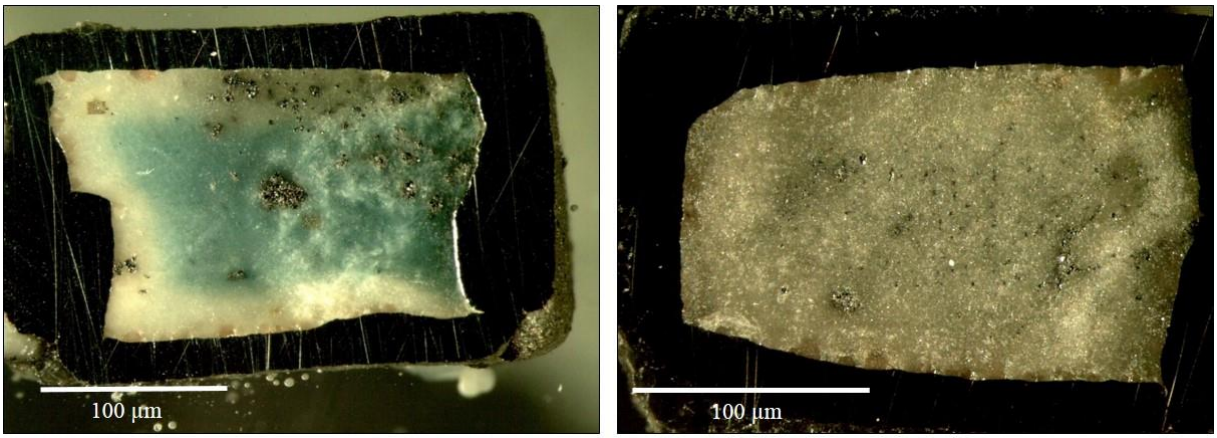

Figure III-14 : Optical microscope pictures of experiments of antigorite dehydration at 8 GPa and 750°C (left; run M450); and 850°C (right; run M451). Color of the matrix helps to identify if dehydration reaction is completed. The blueish zone in the center of the run M450 indicates a hydrous assemblage while the white border is anhydrous. The reaction was complete in the run M451, with a full dehydrated assemblage.

Identification of two different valence states of iron in our samples as also been established using optical microscope imaging. Hematite (Fe_2O_3) lamellae stand out as bright white stripes as they crystallize on the grey magnetite minerals (Fe_3O_4) as it can be observed in Figure III-15.

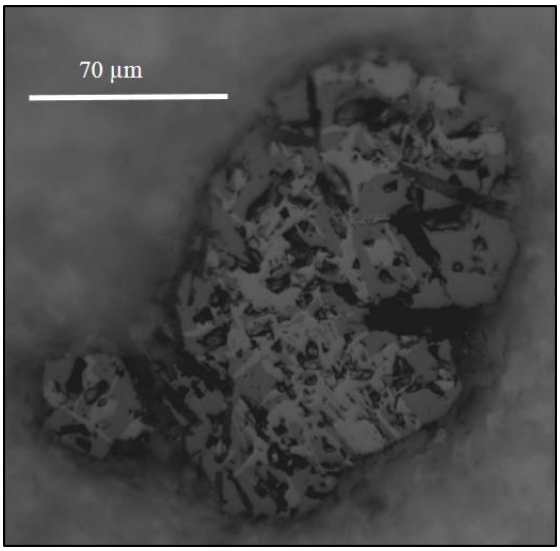

Figure III-15. Optical microscope image (reflected light) from sample #1224, after antigorite dehydration at 3 GPa and 700°C. White stripes correspond to hematite crystalizing on the grey pre-existing magnetite.

II.2.2 Scanning electron microscopy (SEM)

Pictures of the samples presented in this thesis have been acquired using the scanning electron microscopy imaging technique. Mineral phases identification based on semi-quantitative information on the mineral composition was performed at the Laboratoire Magmas et Volcans using Jeol JSM-5910 LV SEM. This technique consists in the collection of signals generated at the surface of the sample in response to a focused beam of high energy electrons. These signals provide information on the structural, chemical and crystallographic properties of the sample. The beam is thermionically emitted from an electron gun with a tungsten filament cathode located in the electronic column (**Erreur ! Source du renvoi introuvable.**Figure III-16), collimated and focused by electromagnetic condenser lenses and apertures, and deflected in the x and y axes to raster scan the surface of the sample.

Experimental samples are placed in a vacuum chamber, the settings of the analysis are controlled via a computerized user interface. Images and data are displayed and processed using the software interface.

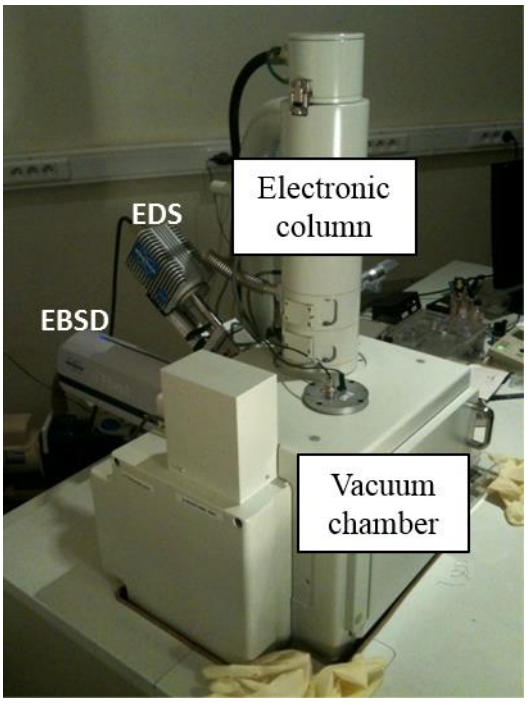

Figure III-16 : Picture of the scanning electron microscope at the Laboratoire Magmas et Volcans displaying the geometry of the EDS spectrometer and the EBSD detector at the back of the vacuum chamber containing the sample. Electrons are generated and focused in the electronic column.

II.2.2.a Secondary and backscattered electrons imaging (SEI-BSEI)

Primary beam electrons interact with atoms from the sample, by losing some energy to weakly bounded electrons in the sample and consequently producing different type of secondary emissions. Topographic information is obtained collecting weakly bounded secondary electron (SE) at the sample surface, from which intensity is directly correlated with surface structure of the analyzed object. A sensor synchronized with the scanning beam allows collection of the signal and the construction of secondary electron image (SEI). Backscattered electrons (BSE) are produced by elastic diffusion from emitted electrons, they have a higher energy than SE. The number of backscattered electrons depends on the atomic mass of the analyzed object, which is why collected backscattered electrons signals informs on the chemical nature of the sample.

Backscattered electrons pictures are then produced and heterogeneities in the sample can be correlated to different mineral phases, through brightness variations: heavy elements are assigned to light shades while light elements are noticeable with darker shades. Since backscattered electrons possess higher energies than secondary electrons, they originate from deeper layers in the sample, hence providing a reduced spatial resolution compared to secondary electron imaging. The beam penetrating in the sample creates a teardrop-shaped volume, also called interaction volume that defines the spatial resolution of analyses. The interaction volume extent is on one hand a function of the beam size, electrons acceleration tension and on the other hand dependent on the composition and density of the sample. BSE pictures in this thesis were acquired under high vacuum, with a 15 KeV beam.

II.2.2.b X-Ray energy dispersive spectrometry (EDS) for chemical maps

The combined use of chemical maps with BSE images allowed us to better constrain the chemical heterogeneities in our samples. Together with a prior assumption on the mineral assemblages that could occur at experimental conditions investigated, this technique provided a more precise idea of mineral phases existing in our samples. When the electronic beam hits the sample, inner electrons from the sample atoms are removed and propagate to the outer layers by gradually filling the vacancies. Electrons of different energies originate from different elements and provide qualitative information on the sample composition collected by an energy dispersive spectrometer (EDS). Our experiments conducted in the natural antigorite bulk are composed by mafic silicate, aluminous and hydrous minerals. Therefore, we chose to systematically perform analyses in the ternary system Mg-Si-Al. The relative amounts of Mg, Si or Al elements inferred after EDS analysis was respectively assigned to the colors red, green and blue (RGB system) in order to visually separate the main phases. As an example, in Figure III-17, the Mg-rich phase (olivine) stands out in red-orange, the Si-rich phase (orthopyroxene)

in green and the Al-rich (garnet) in blue. Chemical maps were produced with the same setting than the BSE pictures, with 0.24 µm per pixel resolution, 512 µs counting signal per pixel. Data are acquired line by line over the area set by the user on the sample surface. It is possible to average the signal by repeating the number of acquisitions per line and also by setting more than one cycle of acquisition over the entire area. Depending on the texture, the map was built on 5 to 8 lines accumulations and for 1 to 3 cycles of acquisition. Indeed, increasing the number of line accumulations and acquisition cycles improves the quality of the image in the case of very fine textures. Careful polishing is also determinant for the quality of analysis. Despite the very fine grain size and porosity of the sample, such quality of backscattered electron image and chemical map (example displayed in Figure III-17) can be obtained by hand polishing over an hour and repeatedly vacuum impregnating the sample.

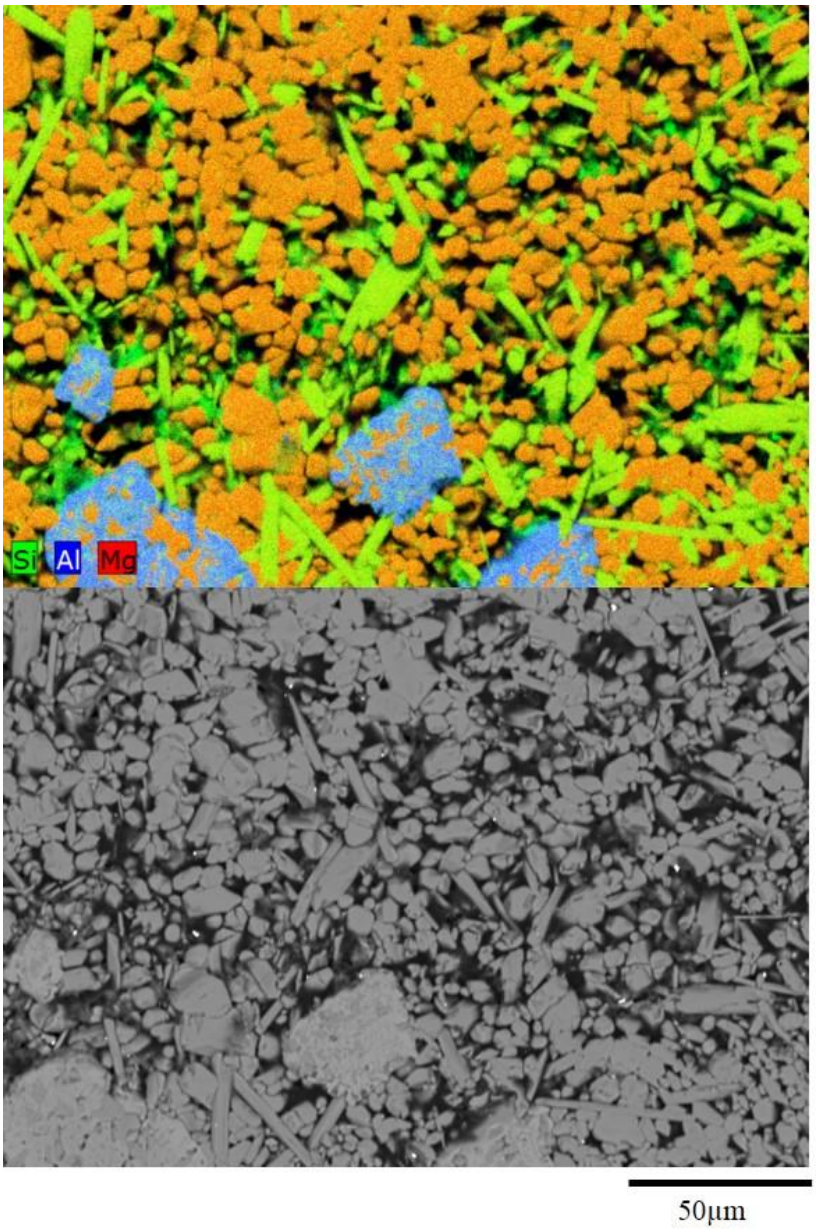

Figure III-17 : Backscattered electron image is shown on the bottom. On the top is displayed the associated X-Ray energy dispersive spectrometry map allowing further semi quantitative characterization of phase assemblages in our samples: Al-rich garnet (blue), Si-rich orthopyroxene (green) and Mg-rich olivine (red) produced in the experiment M451 are visible. Assigning colors code to the relative abundance of chemical component allows to discriminate the mineral phases of the assemblage. This is helpful to locate minerals of interest for structural analysis using electron backscattered diffraction technique, precise chemical analyses using electron microprobe, or Raman spectra acquisition for mineral confirmation.

II.2.2.c Electron backscattered diffraction (EBSD)

Electron backscattered diffraction analyses were performed using the scanning electron microscope with different configuration and settings than those used to obtain secondary electron, backscattered electron or energy dispersive spectrometry pictures. It is used to explore the crystallographic structure of minerals. This technique requires an EBSD detector composed of a phosphor screen, compact lenses and a low light charge coupled device (CCD) camera. To explore the structure of our materials, an additional step of preparation was necessary to improve the quality of the surface. Sample were hand polished very carefully with colloidal silica suspension until grain boundaries could clearly be seen with optical microscope (1 to 2 hours of preparation are necessary). The sample is placed in the chamber at a tilted angle (70°) towards the diffraction camera. Compact lenses are used to focus the image from the phosphor screen to the CCD camera. Electrons from the beam are projected on the surface of the sample and backscattered electrons are emitted at the Bragg conditions in agreement with the periodic atomic lattice planes of the crystalline structure, hence leading to their diffraction. When these electrons reach the phosphor screen, they produce its fluorescence. The production of diffraction patterns formed by an ensemble of Kikuchi lines indicates the lattice diffraction crystal planes related to the mineral structure observed (see the related figures in the supplementary materials at the end of the thesis). Indexation of these lines according to the Miller indices of the corresponding diffracting plane from which it originated allows to relate the diffraction pattern to a known phase and asses its orientation within the sample. Some limitations can nevertheless be encountered, mostly because of the sample's surface state. For example, a very porous sample composed of fine grained minerals does not offer the possibility to obtain a completely flat surface, and well-defined grain boundaries. The nature itself of the analyzed phase can constitute a limitation for this kind of analysis as well. Since the diffraction patterns indexation is based on pre-existing data, exploring crystallographic structure of

recently discovered or unknown from the database mineral (even as a solid solution of an indexed mineral) is ambitious. For these reasons, conducting electron backscattered diffraction analysis on our samples was challenging.

II.2.3 Electron probe micro-analyses (EPMA)

Accurate chemical composition of the mineral phases in our experiments were obtained using electron microprobe analysis. The principle of this technique is similar to the scanning electron microscopy principle. For the scanning electron microscope, the microprobe includes an electron gun, a column containing sensors and an X-Ray energy dispersive spectrometer. In addition, it has wavelength dispersive spectrometers (WDS) that allow for quantitative estimation of X-ray emission from the sample.

The beam of focused electrons is also produced by a tungsten filament and accelerated in the direction of the sample, deflected in a raster fashion to the surface. Under the incident electron beam, electrons from the sample atoms can be ejected. This provokes electron replacement from more outer shells to fill the vacancies, associated with high energy (X-ray) emission. The wavelength associated to this photon is characteristic of the excited atom. Wavelength dispersive spectrometers (WDS) have monochromator crystals with known interplanar spacing. According to the relation between the emitted electron incident angle (Θ), the crystal interplanar space (d) and the photon wavelength (λ), (Bragg law: $2d \sin \Theta = n \lambda$). Incident angle is adjusted by rotation of the monochromator and the detector, so that photon counting is possible.

Due to geometrical restrictions, a limited range of wavelengths can be measured by a spectrometer equipped with one crystal. This issue is circumvented by using several spectrometers covering each a given angular range for photon detection. These spectrometers

use synthetic monochromator crystals. The detection of a particular range of wavelength, corresponding to particular chemical elements is then assigned to one of these crystals (PET, PC1, LLIF, TAP) for the analysis. The precision of EPMA analysis lies in the systematic comparison of the sample derived signal with that of a standard of well-known composition in the exact same analysis conditions.

Figure III-18 : Electron probe micro-analysis at the Laboratoire Magmas et Volcans. Picture of the Cameca SX100 used to obtain chemical composition of all the mineral phases from samples produced during this thesis.

The electron microprobe used to obtain the chemical composition of our samples is a Cameca SX 100 (Figure III-18). Accelerating voltage was 15 kV. The beam current was set to 15 nA for anhydrous mineral phases and 8 nA for hydrous phases. The beam was focused to 1 µm. For all of our experiments, detection of Ti and Cr was performed with PET diffraction crystals, oxygen with the PC1 crystal, Fe and Mn with the LLIF crystal, and Al and Mg with the TAP crystal. Settings of the microprobe diffraction crystals were modified for oxygen

quantification, in order to provide an oxygen/Σcations ratio and allow discrimination between hematite and magnetite. The ratio associated with magnetite (Fe_3O_4) is 1.33 while hematite (Fe_2O_3) corresponds to a ratio of 1.50. Prior verification of the correspondence between the mineral and the oxygen/Σcations ratio was obtained by using the same procedure on the standards of magnetite and hematite that were also used for calibration. This technique allowed the identification of these two phases in our samples, which we could not infer by a classical examination of atoms per formula unit data. Chemical composition of spinel and chromite have been obtained with the same diffraction crystal configuration.

As for the SEM analyses, an interaction volume is produced by the probe beam, leading to spatial analytical limits. Indeed, due to the high porosity and the small grain size of our samples an interaction of the beam projected on a single crystal with the surrounding material is frequently observed. This represents a challenge acquiring high quality data. A satisfying analysis provides a total of quantified elements of 100 weight percent (wt %). For instance, totals obtained while analyzing very small crystals present in our experiments (such as dendritic enstatite < 2 µm width, or chlorite crystallizing in the porosity gaps) totals express a variation of ± 3 wt% compared to the expected value. Two methods of data processing were settled in order to reduce the dispersion of data caused by this resolution limit.

One solution was to normalize the data to the theoretical total value (i.e. 88 wt% for chlorite, 100 wt% for enstatite) in order to allow comparison between our data and literature data. The other method, applied to prevent any inaccurate analysis of dendritic enstatite due to interaction of the beam with other surrounding phase, was to keep only analyzed displaying formula unit accurate i.e. closely corresponding to $(Mg,Fe)_2Si_2O_6$ +/- Al. This was executed even though the total was not systematically close to 100 wt%.

II.2.4 Raman spectroscopy

Raman spectroscopy can be used for a relatively quick identification of mineral phases present on geological samples. A focused monochromatic light beam (laser) is projected on the sample surface over 1 µm area, under an optical microscope. Photons from the incident beam hit the sample material, which in turn re-emits a photon collected by a sensor.

Information on the molecule vibrating energy level is inferred from the variation of energy between the emitted photon and the collected one. Molecules vibration frequency (cm^1) is then plotted on the x axis versus intensity of the signal, generating peaks (Figure III-19). The size, valence and mass of a molecule are parameters controlling its vibration frequency while the associated peak intensity is determined by the laser initial energy together with the molecule concentration in the analyzed area and the crystal orientation. For instance, Si-O bounds possess a lower vibration frequency than hydroxyl (O-H) bounds.

In this study Raman spectra acquisition was performed on metallic oxides in antigorite matrix. Raman spectra were acquired using an Invia spectrometer from Renishaw equipped with a 532-nm diode laser (emission power of ~136 mW), a CCD detector, a Leica DM 2500 M confocal microscope, and a motorized XY stage. Scattered light was collected by a back-scattered geometry, using objective lens and a grating with 2400 grooves/mm. In order to avoid thermal oxidation of magnetite into hematite (de Faria et al., 1997), irradiation power was 800µW at the sample surface. Acquisition time was typically 120 seconds for each spectrum. The spectra were recorded using Wire 4.2 Software from 0 to 1300 cm^{-1}. Daily calibration of the spectrometer was performed based on a Si 520.7 ± 0.5 cm^{-1} peak.

Hydrous phases such as phase A and phase E have also been identified using Raman spectroscopy. Identification of these minerals was challenging because of their fine intergrowth with other minerals. Hence a grid of punctual analyses was set on the sample. The beam was

set to 800µW and the signal collected over a short time of 20 seconds, increasing statistics to locate the sought phase and perform a more precise analysis. The second analysis was performed using same settings than previously described, over 30 seconds in two accumulating cycles.

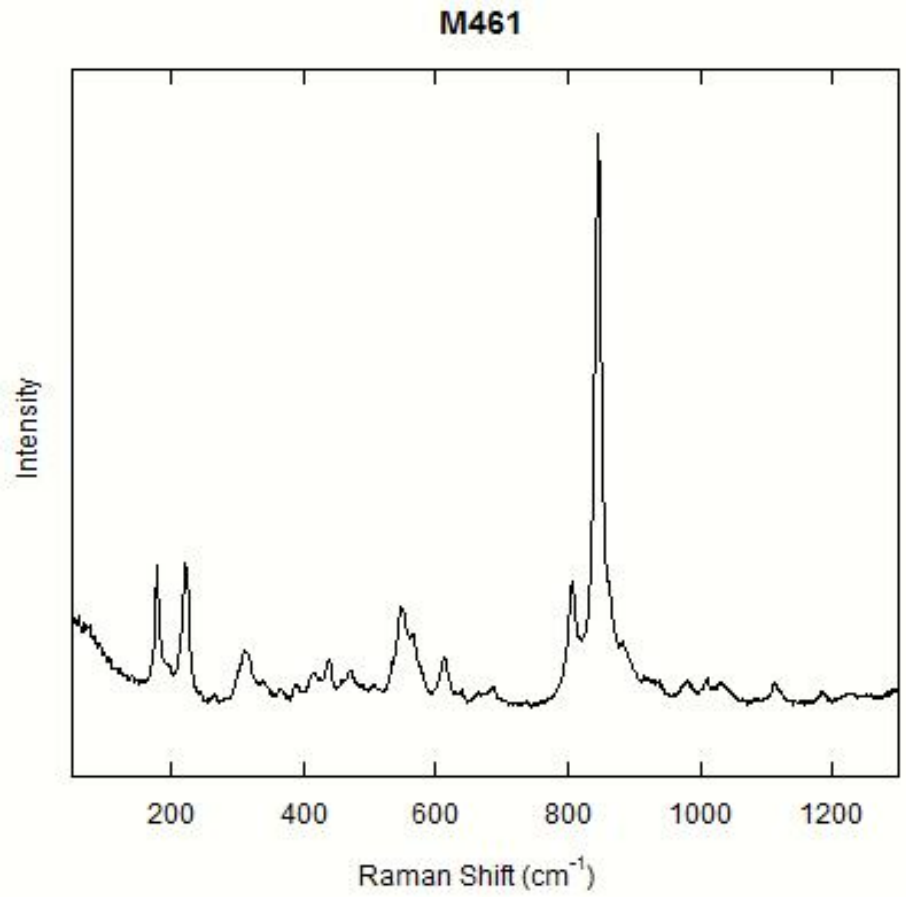

Figure III-19 : Example of a Raman spectra of phase A obtained during this thesis. Intensity of the signal describes peaks, the associated molecule vibration frequency (cm^{-1}) is a function of the molecule parameters, such as its mass, valence and size while the intensity is function of the molecule concentration and crystal orientation.

Chapter IV - The intrinsic nature of natural serpentinite dehydration at 3 GPa: Implications for the oxygen fugacity conditions of slab dehydration

Juliette MAURICE[1*], Nathalie BOLFAN-CASANOVA[1], Sylvie DEMOUCHY[2], Baptiste DEBRET[3]

[1] Laboratoire Magmas et Volcans, 5 rue Kessler, 63038 Clermont-Ferrand, France (*correspondence: J.Maurice@opgc.univ-bpclermont.fr)
[2]Géosciences Montpellier, Université Montpellier 2, Place Eugène Bataillon , 34095 Montpellier France.
[3] Department of Earth Sciences, Durham University, Durham, DH1 3LE, UK.

This chapter is presented as an article that will be submitted for publication. The section concerning the methods repeats information from Chapter III of this thesis. Sections, figures and tables numbering has been updated with the general numbering of the thesis.

I Abstract

Antigorite is considered as the most important source of water in the subducting hydrated oceanic lithosphere and plays a key role in water release in the mantle wedge. Fluids released by the dehydration of subducted oceanic lithosphere are known to trigger partial melting of the mantle wedge, thus producing arc magmas. Although, these magmas are more oxidized than Mid-Oceanic-Ridge basalts (MORBs), the possible inherent link between the redox state of arc magmas and slab-derived hydrous fluids is not well established. We performed dehydration experiments of natural antigorite-rich serpentinite containing 5wt% magnetite at 3 GPa and 600 to 900°C using a multi-anvil apparatus. These experiments reproduce the H_2O liberating serpentinite dehydration stages, forming secondary antigorite, chlorite, olivine and orthopyroxene that are observed in nature. In addition, the use of a "neutral" experimental setup to the intrinsic high oxygen fugacity of serpentinites, highlighted the presence of hematite formation within the pre-existing magnetite minerals. This indicates that the fluids released during the dehydration of antigorite-bearing serpentinite are in equilibrium with magnetite and hematite, hence constraining the oxygen fugacity (fO_2) to $\log(fO_2)$ of -10 to -12, which is equivalent to FMQ+5 (Fayalite-Magnetite-Quartz buffer). The formation of hematite is in agreement with observations of the outcrop massif of Almirez (Spain) demonstrating that this process can indeed occur in nature (i.e. hematite is not a retrograde product). Such oxidizing conditions for serpentinite dehydration can also explain the oxidized character of arc magmas and mantle wedge xenoliths.

II Introduction

Subduction of oceanic lithosphere is associated with material recycling in the mantle. In particular, H_2O fluxes generate mantle wedge partial melting at the origin of arc magmas (Gaetani and Grove, 1998; Grove et al., 2006; Plank and Langmuir, 1998). While hydrous lithologies among pelitic sediments and basalts mostly dehydrate at relatively shallow depth in the fore-arc region (to approximately 100 km, Tatsumi, 1986), ultramafic hydrated lithologies, such as serpentinites, can release large amounts of water to greater depth (150-200 km, Ulmer and Trommsdorff, 1995). Serpentinites are rocks formed by the hydrothermal alteration of Mg-rich minerals in peridotite. Such serpentinization of ultramafic rocks occurs in different geological settings: for example: on the oceanic seafloor of slow and ultra-slow spreading ridges (Cannat et al., 1990; Mevel, 2003), at slab bending related faults (Ranero et al., 2003) and at the mantle wedge – slab interface as a consequence of the release of slab related fluids (Deschamps et al., 2010; Guillot et al., 2000), rendering serpentine rocks ubiquitous in subduction zones. Antigorite, the high pressure polymorph (Schwartz et al., 2013), is considered as the most important water carrier within the ultramafic down-going lithosphere, as it contains up to 13 wt% H_2O. Therefore, antigorite is a key mineral in fluid release as it breaks down when the slab deepens and is heated up by the surrounded mantle (Ulmer and Trommsdorff, 1995).

Samples of exhumed high-pressure serpentinites from ophiolites have allowed petrological study of antigorite dehydration in natural settings. For instance, natural serpentinites from Cerro Del Almirez (Debret et al., 2014, 2015; Garrido et al., 2005; López Sánchez-Vizcaíno et al., 2005; Padrón-Navarta et al., 2010a, 2010b, 2011; Trommsdorff et al., 1998) and Cima Di Gagnone (Evans and Trommsdorff, 1978) have brought constrains on the reaction of antigorite destabilization (below ~ 5 GPa). Observations point out the following reactions involving olivine (ol), enstatite (en), and chlorite (chl) in Al-rich systems:

$$Mg_{46.5}Al_3Si_{32.5}O_{85}(OH)_{62} = 11\ Mg_2SiO_4 + 8.5\ Mg_2Si_2O_6 + 1.5\ Mg_5Al_2Si_3O_{10}(OH)_8 + 25\ H_2O \quad \text{Reaction 1}$$

Al-bearing atg — *ol* — *en* — *chl*

$$Mg_{48}Si_{34}O_{85}(OH)_{62} = 14\ Mg_2SiO_4 + 10\ Mg_2Si_2O_6 + 31\ H_2O \quad \text{Reaction 2}$$

Atg — *ol* — *en*

Experimental observations of antigorite dehydration confirmed the destabilization reactions observed on natural specimens and demonstrated that it can be stable up to 620-710°C for pressures of 2.2-5.2 GPa (Bose and Navrotsky, 1998; Bromiley and Pawley, 2003; Padrón-Navarta et al., 2010a; Ulmer and Trommsdorff, 1995; Wunder and Schreyer, 1997).

In addition to water transfer from the slab to the mantle wedge, a redox transfer should be associated with the subduction of serpentinites. These rocks are highly oxidized, as indicated for example by $Fe^{3+}/\Sigma Fe$ ratios up to 0.7 in oceanic serpentinites (Andreani et al., 2013; Marcaillou et al., 2011), ~ 0.6 in atg-serpentinites associated with meta-ophiolites from the Cerro Del Almirez massif (Debret et al., 2015) or up to 0.81 in antigorite associated with meta-ophiolites from north western Alps (Merkulova et al., 2016; Muñoz et al., 2013). The oxidized character of mantle xenoliths in subduction settings is in agreement with redox fluxes in these tectonic regions (Brandon and Draper, 1996; Carmichael, 1991; Parkinson and Arculus, 1999). Finally, arc magmas display an $Fe^{3+}/\Sigma Fe$ ratio (0.18 – 0.32, Kelley and Cottrell, 2009) higher than in MORBs ($Fe^{3+}/\Sigma Fe$ ratio of 0.13 – 0.17, Bézos and Humler, 2005; Cottrell and Kelley, 2011). The origin of the oxidation of arc magmas is nevertheless debated. Some studies discuss, based on chemical ratios such as V/Sc (Lee et al., 2005), Zn/Fe (Lee et al., 2010), or V partitioning between minerals and melts (Mallmann and O'Neill, 2009) that the source of arc

magmas is as reduced as the one of MORBs, which is close to FMQ (Fayalite-Magnetite-Quartz buffer), and invoke late stage processes such as fractional crystallization, assimilation or degassing to explain the observed oxidation state of arc lavas. Alternatively, it has been suggested that the oxidation state of the source of arc magmas, could be imposed by slab derived fluids (Evans, 2012; Kelley and Cottrell, 2012; Frezzotti et al., 2011; Tumiati et al., 2015). In addition, two lines of evidences suggest the potential role of serpentinite derived fluids in the oxidation of the mantle wedge and subsequently of arc magmas: fluids released from serpentinite dehydration are considered to dominate the slab-derived fluid (Ulmer and Trommsdorff, 1995) and the composition of fluids released by serpentinites and arc magma compositions are correlated (Elliott et al., 1997; Gill, 1981; Hattori and Guillot, 2007; Savov et al., 2007; Scambelluri and Tonarini, 2012).

Recent studies have demonstrated that atg-serpentinite destabilization is associated with reactions of reduction between mineral phases and takes place at high oxygen fugacities (Debret and Sverjensky, 2017; Merkulova et al., 2017). In addition, Debret et al. (2015) have observed the presence of hematite growth on magnetite in partially dehydrated serpentinites from Almirez massif. This attests of the oxidizing nature of fluids released from serpentine dehydration. Nevertheless, a doubt may still persist regarding the possible retrograde nature of such hematite lamellae, especially regarding its rare occurrence in natural samples and since such mineral has never been evidenced in experimental assemblages.

This study aims to experimentally reproduce atg-serpentinite dehydration under realistic conditions, while preserving its intrinsic redox conditions during destabilization. We conducted atg-serpentinite dehydration experiments at 600-900°C and 3 GPa, on an un-crushed rod of natural antigorite containing 5 wt% magnetite. Such experiments intended to let the sample evolve in a closed system as much as possible, by using a “neutral” redox environment with respect to the redox of starting material. The effect of the furnace material on the resulting

phases after dehydration (i.e. lanthanum chromite furnace, considered as an oxidizing environment, was used as well as graphite furnace, considered as a reduced environment) is discussed.

III Methods

III.1 Natural antigorite sample

Experiments were conducted using a natural serpentinite from the Iron Mountain, North Cascades, Washington USA. It is composed of a matrix of pure antigorite and cubic oxides from the spinel group, which mainly occurs as magnetite (Figure IV-1) with occasionally unreacted cores of chromite and minor spinel. No olivine nor calcium phases (diopside or tremolite) have been observed in the investigated sample. In order to avoid H_2O and CO_2 absorption by using a grinded material, our starting sample was prepared by drilling a cylindrical core from the rock.

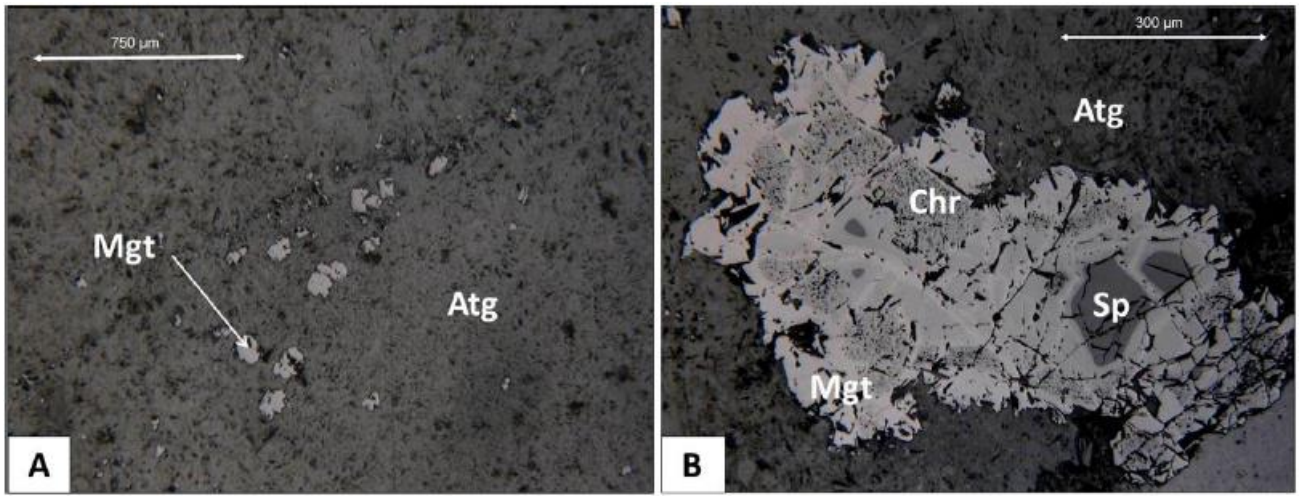

Figure IV-1 : Optical microscope photograph in reflective light of the starting material. (a) Magnetite grains within the fine and dense antigorite matrix, (b) Spinel core surrounded by chromite and magnetite rims.

Additionally, this has the advantage of preserving a heterogeneous distribution on the modal amount of magnetite (see below), and thus reproducing natural conditions. Samples from the same locality (IM3) were investigated by Evans et al. (2012) using Mössbauer spectroscopy. They estimated a $Fe^{3+}/\sum Fe$ ratio of 0.23 for this sample and the same is assumed in this work. The composition of antigorite $Mg_{2.62}Fe^{2+}_{0.08}Fe^{3+}_{0.02}Al_{0.09}Cr_{0.01}Si_{1.97}O_{6.82}(OH)_{3.65}$ was obtained by means of an electron probe micro-analyzer and its water content (12.05 wt. % H_2O) by calculation from its structural formula corresponding to an assumed polysome (m = 17). Bulk analyses were performed using Inductively Coupled Plasma Atomic Emission Spectroscopy on 5 distinct batches of about 100 mg, separately grinded, in order to test the homogeneous distribution of magnetite grains within the bulk rock. The average bulk rock composition (BR_1) is reported in Table IV-1, as well as the standard deviation calculated on the 5 analyses. The only marginally higher amount of chromium in BR_1 (0.27 wt% Cr_2O_3) compared to antigorite (0.22 wt% Cr_2O_3) indicates the very minor proportion of chromite and associated spinel. Therefore, the ferric and ferrous iron in the bulk rock is mostly controlled by the modal amount of magnetite. Mass balance calculation based on total iron content of the bulk and of magnetite and antigorite (with a $Fe^{3+}/\sum Fe$ ratios of 0.23 in the latter) already suggests that the sample contains up to 5.5 wt% magnetite in average, in agreement with analyses of backscattered images (Figure IV-1). This results in a ratio of FeO/Fe_2O_3 of 2.87 in the bulk rock (BR_2 in Table IV-1). The water content of the bulk (11.40 wt% H_2O) measured by loss on ignition is also in agreement with 5.5 wt. % magnetite (Table IV-1).

The matrix of antigorite is rather dense, despite some porosity appearance displayed on (Figure IV-1), due to thin section preparation and the softness of the starting material. Two different occurrences of spinel group oxides have been observed: small grains of pure magnetite (100 µm of width) and coronitic oxides displaying spinels cores surrounded by chromite layers and peripheral magnetite (Figure IV-1). These oxides occur as large aggregates, up to 900 µm

width. This type of oxides clusters is typical in natural serpentinites (see Debret et al., 2014, their Figure 3). The spinel cores, of the composition $Mg_{0.52}Fe_{0.47}Al_{1.08}Cr_{0.74}O_4$ are solid solutions of Al-spinel $MgAl_2O_4$ and ulvöspinel Fe_2TiO_4 with minor chromite component $FeCr_2O_4$ (Table IV-1). In average, the chromite minerals $Mg_{0.08}Fe_{1.92}Cr_{0.76}O_4$ are solid solutions of chromite ($FeCr_2O_4$) and magnesioferrite ($MgFe_2O_4$). Magnetite displays a composition close to the endmember with the formula $Fe^{2+}_{0.98}Fe^{3+}_{1.96}O_4$. Despite intensive search, no pre-existing hematite is observed in the starting antigorite.

Table IV-1. Average Bulk Rock chemical composition from ICP-AES (BR1) and standard deviation (from 5 distinct batches). Bulk Rock composition calculated for 94.5% antigorite and 5.5% magnetite is reported as BR2.Wavelength-dispersive (WDS) compositions of starting material minerals (Sp, spinel; Chr, chromite; Mt, magnetite). Chemical composition of natural samples from Cerro del Almirez are reported with total normalized to 87 wt% for to allow easier comparison with our data.

	Starting mat.		Antigorite	Sp	Chr	Mt	Almirez Atg (Al06-37)[a]	Almirez Atg (Al06-44)[b]
	BR_1	BR_2						
	(ICP-AES)	calc.		(WDS)				
SiO_2	40.04 (0.30)	40.79	43.17 (0.51)	-	-	-	41.27 (0.61)	42.43 (0.19)
TiO_2	0.03 (0.01)	0.04	0.03 (0.03)	0.08	1.11	0.22	0.02 (0.01)	- -
Al_2O_3	1.63 (0.11)	1.57	1.66 (0.36)	25.27	1.05	0.02	3.60 (0.34)	2.65 (0.16)
Cr_2O_3	0.27 (0.00)	0.28	0.22 (0.08)	37.10	26.69	1.26	0.57 (0.08)	0.25 (0.04)
FeO_{Total}	7.79 (0.48)	7.48	2.60 (0.17)	23.36	67.35	91.32	3.94 (0.16)	3.61 (3.61)
FeO	- -	3.57	2.00 (0.13)	-	-	30.44	- -	- -
Fe_2O_3	- -	4.35	0.66[c] (0.04)	-	-	67.65[d]	- -	- -
NiO	0.25 (0.00)	0.15	0.16 (0.03)	-	-	-	0.09 (0.03)	0.20 (0.10)
MnO	0.09 (0.00)	0.07	0.07 (0.04)	0.53	2.42	0.12	0.04 (0.01)	0.03 (0.03)
MgO	38.94 (0.40)	36.45	38.56 (0.41)	13.65	1.39	0.22	37.44 (0.39)	37.84 (0.43)
CaO	0.02 (0.02)	0.02	0.02 (0.02)	-	-	-	0.02 (0.01)	- -
Total	88.64 (0.39)	87.28	86.55 (0.59)	-	-	99.93	87.00 (0.00)	87.00 -
H_2O	11.4[e]	11.39 [f]	12.05 [g]	-	-	-	- -	- -
Ions calculated on the basis of 6.824 equivalent oxygens (polysom m=17) for antigorite, 4 oxygens for spinel, chromite and magnetite.								
Si	1.844	1.891	1.97	-	-	-	1.89	1.94
Ti	0.001	0.001	0.00	0.00	0.03	0.01	0.02	0.01
Al	0.088	0.086	0.09	1.08	0.06	-	0.19	0.14
Cr	0.010	0.010	0.01	0.74	0.76	0.02	0.02	0.01
Fe^{2+}	0.300	0.138	0.10	0.47	1.92	0.98	0.15	0.14
Fe^{3+}	-	0.152	-	-	-	1.96	-	-
Ni	0.010	0.010	0.01	-	-	-	0.00	0.01
Mn	0.004	0.003	0.00	0.01	0.08	-	0.00	0.00
Mg	2.673	2.519	2.62	0.52	0.08	0.01	2.56	2.58
Ca	0.001	0.001	0.00	-	-	-	0.00	0.00
O	6.824	6.824	6.82	4.00	4.00	4.00	6.82	6.82
OH	-	-	3.647	-	-	-	-	-
X_{MgO}	).833 [h]	0.911[i]	-	-	-	-	-	-
X_{Mg}	0.9 [h]	0.95 [i]	0.96	0.53	0.04	0.01	0.94	0.95

[a] Padrón-Navarta et al. (2009)

[b] Debret et al. (2015)

[c] Fe_2O_3 estimated from $\sum Fe^{3+}/Fe_{total}$ of 0.23 (similar to sample IM3, Evans et al., 2012)

[d] Fe_2O_3 estimated from $\sum Fe^{3+}/Fe_{total}$ of 2/3, from Magnetite stoichiometry

[e] H_2O content calculated from loss on ignition

[f] H_2O content estimated from modal amount of antigorite in BR

[g] H_2O content from structural formula

[f] $X_{MgO}=MgO/(MgO+FeO_{Total})$; $X_{Mg}=Mg/(Mg+Fe_{Total})$

[g] $X_{MgO}=MgO/(MgO+Fe^{2+}O)$; $X_{Mg}=Mg/(Mg+Fe^{2+})$

III.2 Experimental methods

Breakdown of antigorite was produced using a multi-anvil press apparatus at 3 GPa and 600 to 900°C with varying run durations. We chose multi-anvils over pistons-cylinder to reduce quench-induced fractures and decompression cracks. Experimental conditions are reported in Table 2. Experiments were conducted with 25 mm edge length octahedra made of MgO + 5% Cr_2O_3 and WC cubes of 32 mm edge with 17 mm truncation. To insure pressure accuracy of the multi-anvils runs compared to more standard piston-cylinder runs, the pressure was calibrated using the three systems: (i) Bi I-II phase transition occurring at 2.5 GPa and room temperature (Bean et al., 1986), (ii) the coesite/stishovite phase transition of SiO_2 at 8.01 GPa at 800°C (Zhang et al., 1996) and (iii) the garnet to perovskite phase transition of $CaGeO_3$ at 6.2 GPa and 1000°C (1985). The antigorite core (length: 4 mm, diameter: 2.3 mm) is placed inside an $Au_{80}Pd_{20}$ cylinder (length: 4.3 mm, diameter: 3 mm), which is arc welded at the top and bottom. The capsule was insulated from the furnace by an MgO sleeve. The furnace was a steeped heater to reduce thermal gradients and made either of $LaCrO_3$ or C (graphite) in order to generate an environment around the capsule imposing either high or low oxygen fugacity, respectively. Temperature was measured using a Pt/Rh thermocouple in contact with the capsule. The thermal gradient was simulated using the finite element method by Hernlund et al. (2006) and points out to less than 30°C/mm when using $LaCrO_3$ furnace and less than 11°C when using graphite furnace. The final pressure was raised following a steady increase ramp within 2 hours to reach 3 GPa and pressure was maintained for 3 to 12 hours (Table IV-2). The experiments were quenched by turning off the power and the pressure was slowly and automatically decreased (over 9 hours) to minimize decompression cracks.

III.3 Characterization of run products

After the experiments, the capsules were embedded in a dental resin and gently polished with 1200 µm silicon carbide polishing paper, then polished using 6, 3 and ¼ µm diamond paste and carbon coated for chemical analyses. A first chemical characterization was performed using a chemical SEM-EDS mapping (Energy-dispersive X-ray spectroscopy). Then, EPMA analyses were used to obtain the chemical composition of the products of antigorite dehydration. The beam current and intensity was set to 15 keV and 15 n, respectively, for olivine and enstatite µm and the intensity was lowered to 8 nA for hydrous phases. Point beam set up (1 µm in diameter) was used.

The quality of point beam analyses is however poor for very small grains such as dendritic enstatite (less than 2 µm of width) and chlorite, mainly due to the high porosity created by dehydration and the beam interaction with the surrounding material. This analytical problem was partially solved for some chlorite analyses by normalizing the data, to match totals of theoretical composition (88 wt%). This normalization was systematically applied on analyses with totals lower than 87 and over 89 wt%. To improve the analysis of dendritic enstatite, only analyses displaying formulae closely corresponding to $(Mg, Fe)_2Si_2O_6$ +/- Al were considered in the results, even though their sum is not systematically close to 100 wt%. Olivine and antigorite phases were abundant and/or large enough to obtain satisfying quality of analyses.

Regular settings of the EPMA analyses were modified for the iron oxides in order to allow quantification of oxygen. Detection of Ti and Cr was performed with pentaerythritol (PET) diffraction crystal, oxygen with the pseudocrysal 1 (PC1), Fe and Mn with the lithium fluoride (LIF) crystal, and Al and Mg with the thallium acid phthalate (TAP) crystal. For regular silicates analyses, oxygen is only calculated from stoichiometry, the rest of the elements are detected on the same diffraction crystals with addition of Ca, K (PET), Ni (LiF), Si, Na (TAP). Magnetite end member displays an oxygen/Σcations ratio of 1.33 while the ratio for hematite is

equal to 1.50, as confirmed by analyzing the standards of magnetite and hematite used for calibration. It allowed the identification of these two phases in the samples. Spinel and chromite composition were obtained subsequently. Iron was assumed to be in the Fe_3O_4 state for all opaque minerals, except for hematite for which it was calculated as Fe_2O_3. Data were normalized to 4 oxygens for spinel, chromite and magnetite, and to 3 oxygens for hematite. Given the zoned nature of the coronitic spinels and iron oxides, EPMA analyses values display some variations. Therefore, we chose to approximate an average composition (with no focus on the standard deviation, considered as irrelevant for the scope of this study) for each spinel mineral of this study refereed as Al-spinel, chromite, magnetite and hematite.

To confirm independently the identification of hematite and magnetite, Raman spectroscopy was performed on the oxides. Raman spectra were collected at LMV using an InVia confocal Raman micro-spectrometer manufactured by Renishaw and equipped with a 532nm diode laser (200mW output power), a Peltier-cooled CCD detector, a motorized XY stage and a Leica DM 2500M optical microscope. Scattered light was collected by a backscattered geometry. Laser power on the sample was reduced by filters in order to operate at 8 mW in order to avoid thermal oxidation of magnetite into hematite (de Faria et al., 1997). A 100× microscope objective and 20 μm slit aperture were used along with a 2400 grooves/mm grating, which resulted in a spectral resolution better than 1 cm^{-1}. Daily calibration of the spectrometer was performed based on a Si 520.5 cm^{-1} peak. The spectra were recorded from 100 to 1800 cm^{-1} using Wire 4.2 software. Acquisition times were set to 120 s. After each analysis, the surface of the sample has been checked using an optical microscope in reflective light to ensure that the minerals have not been damaged nor oxidized by the laser.

IV Results

IV.1 **Phase assemblages**

After each experiment the capsule was pierced and put into ethanol to check for H_2O excess. Fluid release was observed for all experiments. Four different mineral assemblages were found as results of different antigorite dehydration stages, from antigorite + H_2O (stage 1: #1275), to antigorite + chlorite + olivine + enstatite + H_2O (stage 2: #1110 and #1111), chlorite + olivine + enstatite + H_2O (stage 3: #1228, #1224, #1070, #262) and olivine + enstatite + H_2O (stage 4: #1273). Run conditions and product phases are reported in Table IV-2 and in the pressure-temperature space in (Figure IV-2).

The composition of major elements in all silicate phases is reported in Table IV-3. Spinels and iron oxides compositions are reported in Table IV-4. In this study antigorite is stable up to 690°C at 3 GPa, in agreement with the temperature range of antigorite breakdown presented in previous experimental reports (Bose and Navrotsky, 1998; Bromiley and Pawley, 2003; Padrón-Navarta et al., 2010a; Ulmer and Trommsdorff, 1995; Wunder and Schreyer, 1997).

Table IV-2. Experimental run conditions and results of mineral assemblage.

Experiment	Dehydration stage	Time (hrs)	P (Gpa)	T (°C)	Furnace type	Silicates product phases	Metalic phases	Hematite		
								O/∑cations		Number of analysis
1275	1	5	3	580	$LaCrO_3$	Atg	Mt,Ht	1.52	(0.05)	4
1110	2	12	3	680	$LaCrO_3$	Atg, Chl, Fo, En	Sp,Chr,Mt,Ht	1.53	(0.03)	9
1111	2	3	3	690	$LaCrO_3$	Atg, Chl, Fo, En	Mt,Ht	1.57	(0.04)	4
1228	3	10	3	700	C	Chl, Fo, En	Sp,Chr,Mt	-	-	-
1224	3	10	3	770	$LaCrO_3$	Chl, Fo, En	Mt,Ht	1.53	(0.03)	11
1070	3	6	3	790	$LaCrO_3$	Chl, Fo, En	Mt,Ht	1.48	(0.03)	3
262	3	5	3	800	$LaCrO_3$	Chl, Fo, En	Sp,Chr,Mt,Ht	1.54	(0.09)	15
1273	4	5	3	900	C	Fo, En	Mt	-	-	-

IV.2 **Textural and chemical evolution during dehydration**

IV.2.1 ***Stage 1: $Atg_1 \rightarrow Atg_2 + H_2O$***

After 5 hours at 580°C, no minerals typical of dehydration assemblages (e.g. chlorite, olivine nor enstatite) is observed, except for the substantial water bubbles escaping from the capsule when pierced. The remaining antigorite matrix is homogeneous with no significant porosity (Figure IV-3.a). Nevertheless, the FeO contents of antigorite has slightly increased from to 2.60 ± 0.17 wt% in Atg_1 to 2.86 ± 0.17 wt% in $Atg_{2,}$, while the Al_2O_3 contents has remained similar (1.69 wt%, Table IV-3).

Magnetite contains approximately 98 wt% of iron (Table IV-4), similarly to the one of the starting materials (as the sum of FeO and Fe_2O_3, see Table IV-1). Hematite has appeared within the mineral assemblage and contains approximately 99 wt%.

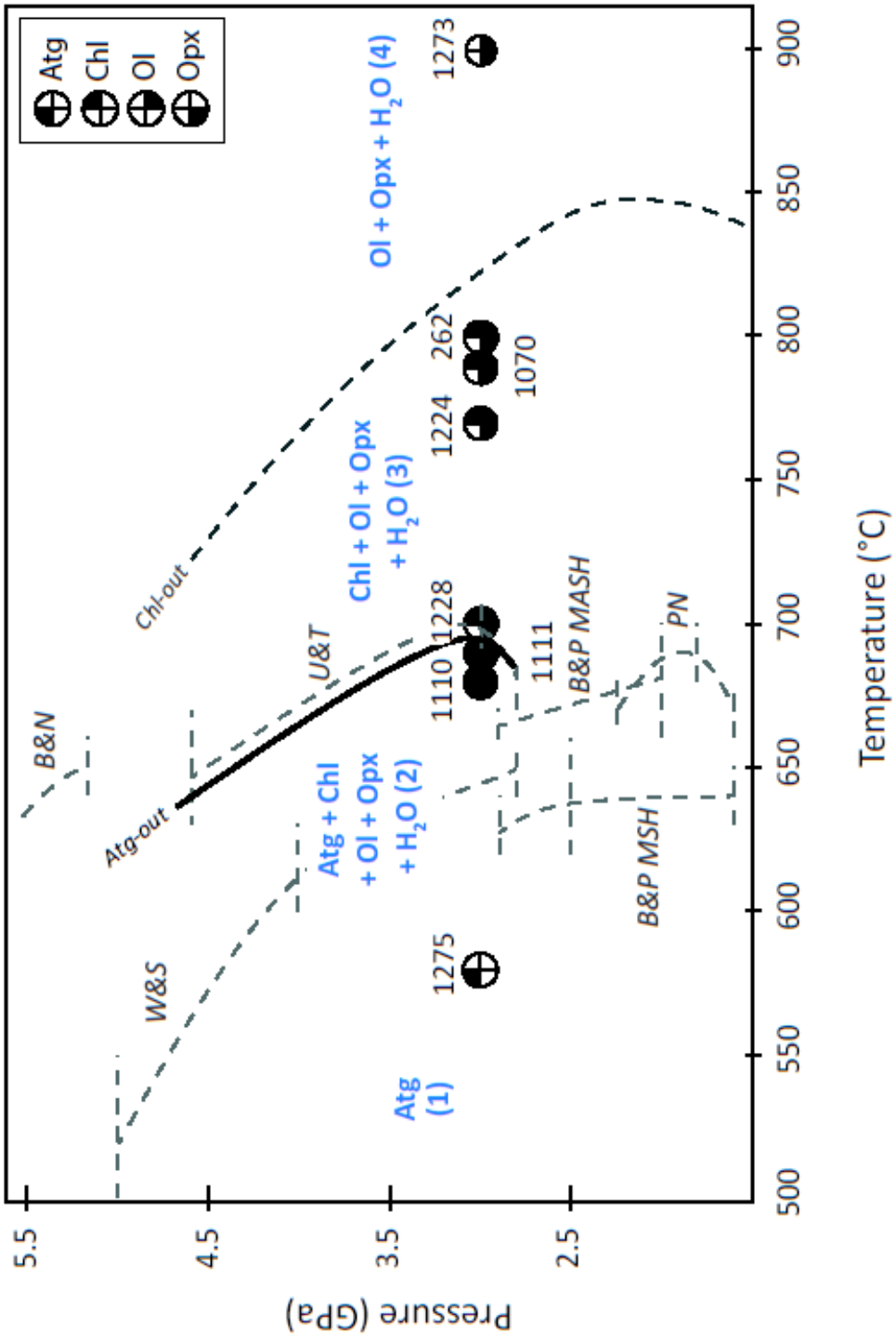

Figure IV-2 : Pressure-temperature diagram of experimental antigorite stability field. Circle symbols correspond to the conditions of experiments in this study. Mineral assemblage stability fields associated with each dehydration stage (into brackets) corresponding to this study are reported in blue. Stability fields of antigorite reported in other studies are represented by the dashed lines (Ulmer and Trommsdorff (1995) (U&T), Wunder and Schreyer (1997) (W&S), Bose and Navrotsky (1998) (B&N), Bromiley and Pawley (2003) (B&P MSH and B&P MASH) and Padrón-Navarta et al. (2009) (PN).

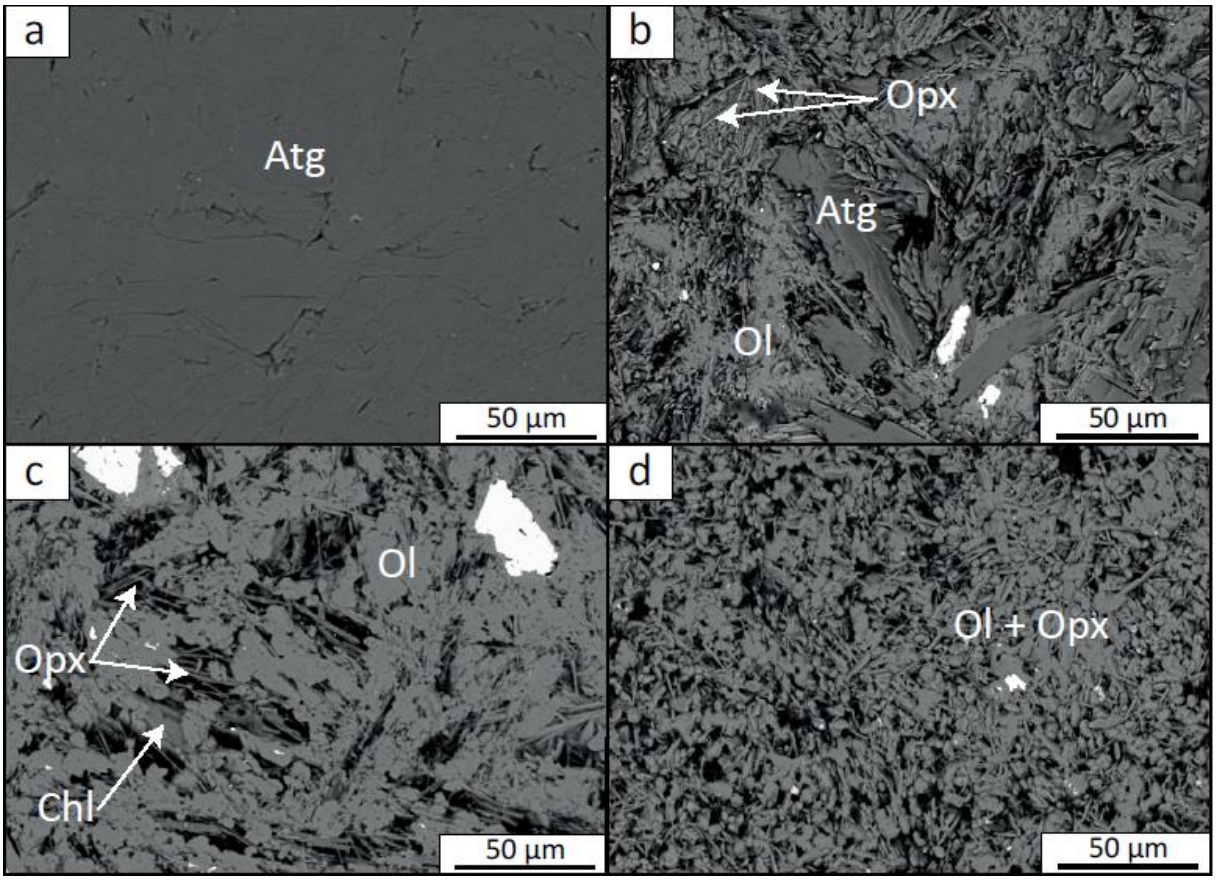

Figure IV-3 : Characteristic textures of antigorite at each stage of dehydration (SEM-BSE). (a) First stage (580°C), (b) second stage (680°C), (c) third stage (790°C), (d) final stage (900°C).

IV.2.2 ***Stage 2: $Atg_1 \rightarrow Atg_2 + Chl_1 + Ol + Opx + H_2O$***

After partial dehydration at 680 and 690°C, antigorite is replaced by a new generation of antigorite (Atg_2) co-existing with chlorite, olivine, enstatite and water. The partial dehydration has induced a texture with high porosity (10 %). Tabular Atg_2 (10 to 80 µm long) co-exists with xenomorphic chlorite + olivine + enstatite (10 µm size maximum, see Figure IV-3.b). Enstatite is characterized by dendrites either well defined or inter-grown with olivine.

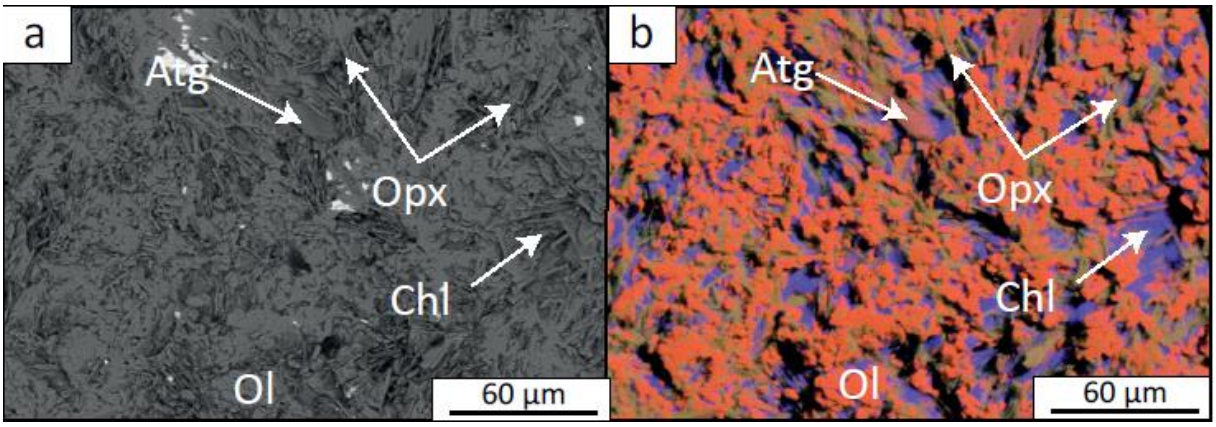

Figure IV-4: (a) SEM BSE image showing the assemblage containing secondary antigorite, chlorite, olivine and orthopyroxene at 680°C. Magnetite minerals can be observed in white color. (b) Corresponding chemical SEM map. Olivine (orange), chlorite (purple), antigorite (brown) and orthopyroxene (yellow-greenish dendrites).

Chlorite is easily identified using the chemical X-ray mapping due to its high alumina content (Figure IV-4). It crystallizes as interstitial small grains of 5-10 µm width coexisting with olivine and pyroxene. Hematite is observed as needles crossing pre-existing magnetite grains (Figure IV-5.a). Characterization of hematite and magnetite phases was confirmed by Raman spectroscopy analysis (Figure IV-5 b).

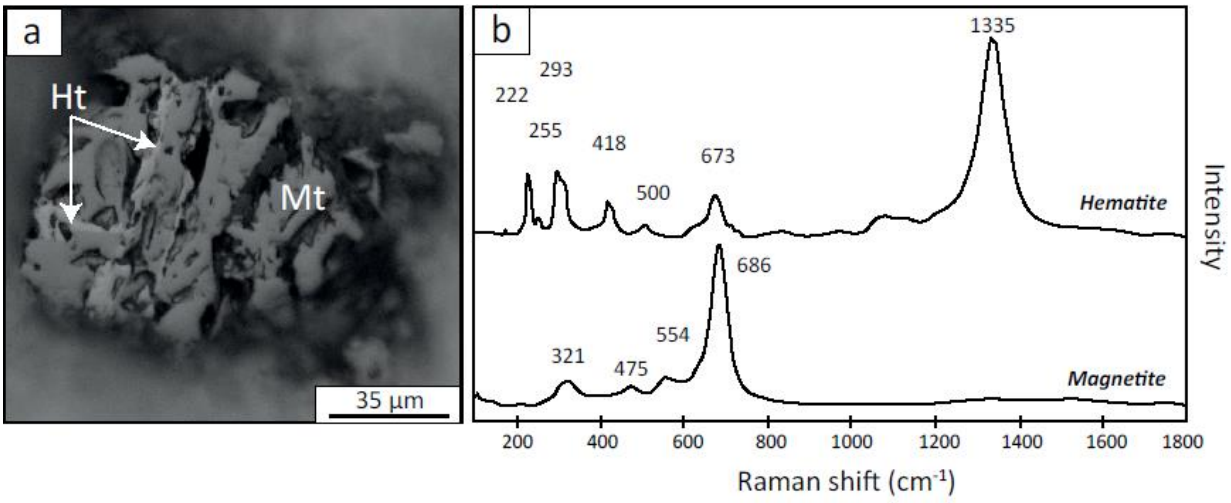

Figure IV-5. (a) Optical microscopy photograph in reflective light of well-preserved during antigorite dehydration, at 690 °C (dehydration stage 2). (b) Raman spectra of hematite and magnetite.

Similarly to Atg_2 in the first stage of dehydration, Atg_2 observed in the second stage displays higher FeO contents (2.71-3.06 wt%) compared to Atg_1 (2.62 wt%). Al_2O_3 contents have decreased to 1.06-1.47 wt% compared to the initial value of 1.66 wt% Al_2O_3 due to chlorite formation (Table IV-3). Chlorite is Al_2O_3 rich (12.43-12.86 wt%) and with similar amounts of iron as antigorite (2.62-2.83 wt% FeO) with a $Kd_{Fe\text{-}Mg}^{Atg2/Chl1}$ of 0.93-0.95, with the Mg-Fe exchange reaction:

$$1.77\ Mg_{2.82}Si_2O_{6.82}(OH)_{3.65} + Fe_5Al_2Si_3O_{10}(OH)_8 = 1.77\ Fe_{2.82}Si_2O_{6.82}(OH)_{3.65} + Mg_5Al_2Si_3O_{10}(OH)_8 \quad \text{Reaction 1}$$

(Mg) antigorite *(Fe) chlorite* *(Fe) antigorite* *(Mg) chlorite*

Yielding,

$$Kd_{Fe\text{-}Mg}^{Atg2/Chl1} = (X_{Fe}^{Atg2}.\ X_{Mg}^{Chl1})/\ (X_{Fe}^{Chl1}.\ X_{Mg}^{Atg2}) \quad \text{Eq.1}$$

FeO contents in olivine are 4.78-5.82 wt%, and orthopyroxene contains 3.22-3.68 wt% FeO, yielding $Kd_{Fe\text{-}Mg}^{Ol/Opx}$ of 1.05-1.13, according the following reaction:

$$½\ Mg_2SiO_4 + ½\ Fe_2Si_2O_6 = ½\ Fe_2SiO_4 + ½\ Mg_2Si_2O_6 \quad \text{Reaction 2}$$

(Mg) olivine *(Fe) enstatite* *(Fe) olivine* *(Mg) enstatite*

And, Eq.2

$$Kd_{Fe\text{-}Mg}^{Ol/Opx} = (X_{Fe}^{ol}.X_{Mg}^{opx}.)/\ (X_{Mg}^{ol}.\ X_{Fe}^{opx})$$

Values of $Kd_{Fe\text{-}Mg}^{Ol/Opx}$ close to 1 indicate that local equilibrium was reached.

Spinel and chromite are still present at 680°C while they have fully disappeared at 690°C. Spinel composition ($Mg_{0.39}Fe_{0.64}Al_{0.91}Cr_{0.97}O_4$) indicates a solid solution slightly shifting towards chromite endmember at the expense of Al-spinel in comparison with the starting material ($Mg_{0.52}Fe_{0.47}Al_{1.08}Cr_{0.74}O_4$). The composition of chromite ($Mg_{0.1}Fe_{1.77}Cr_{0.94}O_4$) is converging towards chromite endmember, with a decreased magnesioferrite component in comparison with the starting sample ($Mg_{0.08}Fe_{1.92}Cr_{0.76}O_4$). Magnetite and hematite are present in both runs. Their chemical compositions are close to the end member composition, despite an

enrichment in Cr at 680°C, while coexisting with Al-spinel and chromite with 3.69 wt% Cr_2O_3. Hematite is also slightly enriched in Cr at 680°C with 1.41 wt% Cr_2O_3.

IV.2.3 ***Stage 3: Atg2 → chl2 + ol + opx + H_2O***

Antigorite is completely transformed into chlorite + olivine + enstatite + H_2O in experiments performed at 700-800°C (see Table IV-2). The product assemblage exhibits a spinifex-like texture (Trommsdorff et al., 1998) with aggregates of small crystals of olivine (5-10 µm) inter-grown with dendritic enstatite (up to 30 µm long), see Figure IV-3.c. Similarly to assemblages observed in the second stage of antigorite dehydration, chlorite crystallized as interstitial small grains (5-10 µm width) coexisting with olivine and pyroxene. Al_2O_3 contents of chlorite are 13.00-15.52 wt% and FeO contents are 2.88-3.16 wt% (Table IV-3). The enrichment in aluminum of secondary chlorite (chl_2) is concomitant with consumption of the Al-bearing antigorite. As observed for the previous stages in the antigorite stability field, the iron content in chlorite increases with temperature, accompanying antigorite consumption (Figure IV-6). FeO contents in olivine range from 3.29 to 4.49 wt% (with a very high FeO content of 6.11 wt% found in olivine equilibrated in the graphite furnace) and those in orthopyroxene vary from 2.65 to 3.55 wt%, yielding a $Kd_{Fe\text{-}Mg}^{Ol/Opx}$ of 1.19 for the experiment equilibrated in the graphite furnace and 0.78 to 0.87 for the samples equilibrated in lanthanum chromite furnace. Such a deviation from $Kd_{Fe\text{-}Mg}^{Ol/Opx}$ close to 1 is addressed later in the discussion. The Al_2O_3 contents in enstatite vary between 2.41 and 3.06 wt% and increase with increasing temperature (Figure IV-6), in agreement with previous observations (Férot and Bolfan-Casanova, 2012; Gasparik, 2003).

For two experiments at 700 and 800°C, spinel minerals can be distinguished into three different solid solution types. Al-spinel is completely consumed, instead we observed magnesioferrite with varying Mg-Fe solid solutions: $Mg_{1.49}Fe_{0.88}O_4$ to $Mg_{0.70}Fe_{2.11}O_4$. Solid solution of chromite and magnesioferrite is observed with composition varying from $Mg_{0.05}Fe_{2.27}Cr_{0.56}O_4$ to $Mg_{0.24}Fe_{1.57}Cr_{0.68}O_4$. Finally, magnetite is observed in the third stage of antigorite dehydration, with a small magnesioferrite component (max. 5 wt% MgO). Hematite is observed in experiments conducted with lanthanum

chromite furnace only while it is absent in the experiment conducted with graphite furnace. It displays compositions close to the hematite endmember Fe_2O_3.

IV.2.4 ***Stage 4: Chl_2 → ol + opx + H_2O***

At 900°C antigorite is completely transformed into olivine + orthopyroxene + H_2O and chlorite is absent. The texture is fine and grain size does not exceed 10 µm (Figure IV-3.d). Olivine contains 5.55 wt% FeO, and orthopyroxene contains 4.39 wt% FeO (Table IV-3), yielding a $Kd^{Fe\text{-}Mg}_{Ol/Opx}$ =0.87. Orthopyroxene contains 3.51 wt% Al_2O_3. Probably due to the relatively low alumina content of our starting material (1.82 wt% Al_2O_3) and to the considerable Al incorporation into orthopryroxene (up to 3.51 wt% Al_2O_3), garnet is not observed in the mineral assemblage.

Spinel minerals consist only in magnetite with minor Al-spinel and chromite ($Mg_{0.41}Fe_{2.21}Al_{0.2}Cr_{0.06}O_4$). This experiment was conducted with graphite furnace and no hematite crystallized within the pre-existing magnetite.

Summary of mineral compositions and iron partitioning

The present samples are Fe-and Al-poor compared to the samples from Cerro Del Almirez studied by Debret et al. (2015), Padrón-Navarta et al. (2009) (see Table IV-1), due to the depletion of the protolith prior to subduction.

IV.2.5 ***Antigorite***

In the first and second stage of dehydration, the increase of FeO content of Atg_2 is an evidence of re-equilibration of antigorite (Figure IV-6). This has been observed by previous authors (such as Debret et al., 2014) to occur concomitantly with a decrease of magnetite mode upon serpentine dehydration and subsequent re-distribution of Fe among the silicates (Debret et al., 2014a). However, we observe no breakdown of antigorite here, except for a slight change

in analyses totals that could be interpreted as a water loss accommodated by iron redox change. Indeed, a change in the trivalent cations is evidenced by the decrease in aluminum content of antigorite.

IV.2.6 ***Chlorite***

Chlorite composition in serpentinized mantle is close to clinochlore $(Mg,Fe)_5Al(Si_3Al)O_{10}(OH)_8$. In the second stage of antigorite dehydration chlorite coexists with antigorite and contains 12.4-12.9 wt% Al_2O_3. Once antigorite is completely dehydrated, chlorite becomes richer in aluminium (up to 13-15.5 wt% Al_2O_3). Hence, for a given bulk composition evolving in a closed system, an Al_2O_3 content increase in chlorite indicates an increase in serpentinite dehydration degree.

IV.2.7 ***Olivine and Orthopyroxene***

The chemical evolution of olivine and orthopyroxene follows identical patterns at each stage of antigorite destabilization (stages 2, 3 and 4, see Figure IV-6). Concerning iron contents, three trends of evolution are observed. At stage 1, simultaneously to antigorite breakdown and chlorite crystallization, FeO increases in both olivine and orthopyroxene, with contents of 4.78 ± 0.46 to 5.82 ± 0.85 wt% for olivine and 3.22 ± 0.33 to 3.68 ± 0.17 wt% for orthopyroxene. In coexistence with chlorite, olivine and orthopyroxene display decreasing FeO contents with 6.11 ± 1.24 to 3.29 ± 0.36 wt% and 3.02 ± 0.20 to 2.65 ± 0.12 respectively. Finally, the last stage of dehydration corresponds to an increase of FeO contents in olivine to 5.55 ± 0.65 wt% and to 4.39 ± 0.38 wt% in orthopyroxene.

Al incorporation in orthopyroxene is shown in Figure IV-7. Only the Si content decreases with a slope of -1.1, when $Al^{3+}+Cr^{3+}$ increases, while the sum of divalent cations (Mg+Fe+Ni) seems to remain constant. An explanation for such chemical trend would be the substitution $Al^{3+}+H^{+} = Si^{4+}$, as graphically it displays a similar slope than our data. The present enstatite is too small to allow water content measurements; however it has been established in

the MgO-Al_2O_3-SiO_2-H_2O system, that a Hydrous Al-bearing Pyroxene (HAPY phase, up to 6.9 wt% H_2O) could be stabilized at such low temperatures (i.e about 720 °C for 5.4 GPa, see Gemmi et al., 2011).

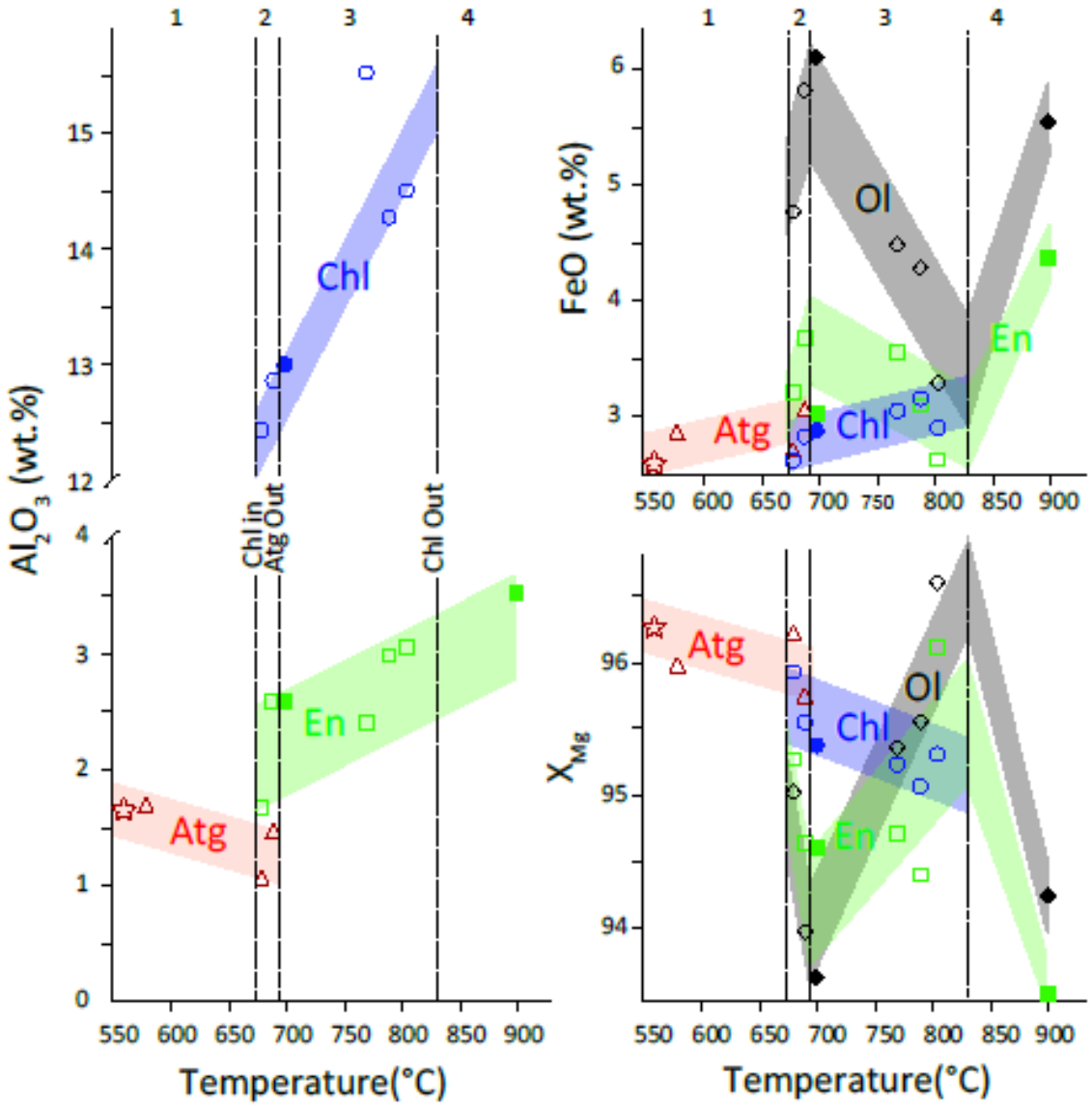

Figure IV-6 : Evolution of Al_2O_3 and FeO contents, and X_{Mg} in the silicate phases with increasing temperature. The starting antigorite (star) has been arbitrary set to 560 °C to appear on this plot. Filled symbols correspond to experiments conducted under reducing conditions and empty symbols to oxidizing conditions. Antigorite dehydration degrees are reported with the numbers 1 to 4 corresponding to the reactions 1. Atg_1= Atg_2+H_2O, 2. Atg_1= Atg_2 +Chl+Ol+Opx+H_2O, 3. Atg_2= Chl_2+Ol+Opx+H_2O, 4. Chl_2= Ol+Opx+H_2O.

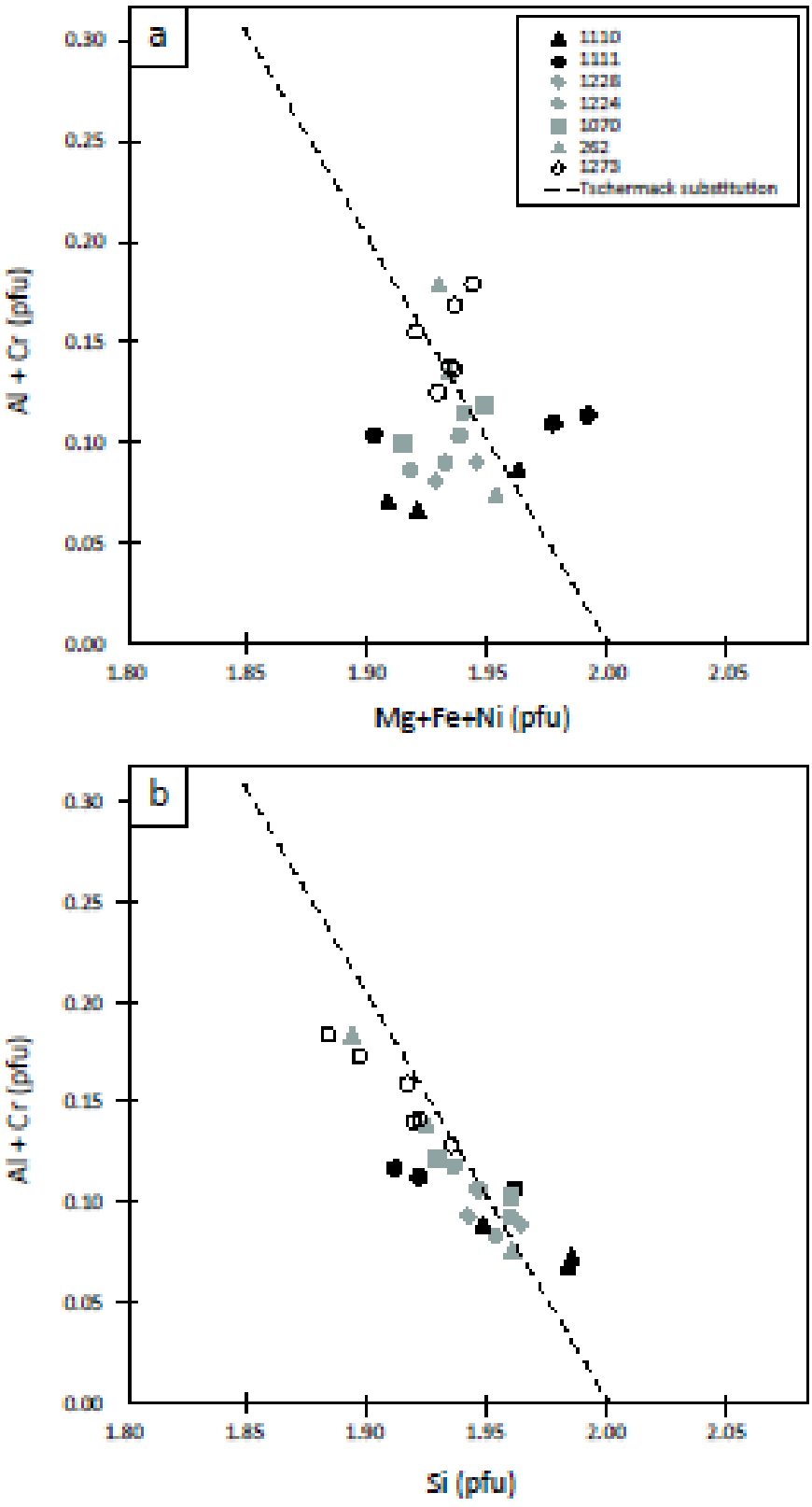

Figure IV-7 : Al content in orthopyroxene as a function of Mg and Fe or Si. The dashed line represents the Al Tschermak substitution in the octahedral site in the first plot and in the tetrahedral site in the second plot (Al+Cr = -1.1 Si +2.2).

Table IV-3. wavelength-dispersive (WDS) compositions of antigorite

Experiment	1275		1110								1111						
Dehydration	Stage 1		Stage 2								Stage 2						
Mineral	Atg		Atg		Chl		Ol		Opx		Atg		Chl	Ol		Opx	
n	14		8		3		4		4		10		1	7		3	
SiO_2	43.21	(0.46)	43.78	(0.48)	36.36	(1.29)	42.38	(1.39)	59.11	(1.22)	43.30	(0.78)	36.18	42.34	(1.03)	57.40	(1.00)
TiO_2	0.02	(0.02)	0.03	(0.04)	0.33	(0.47)	0.01	(0.01)	0.01	(0.01)	0.03	(0.04)	0.05	0.04	(0.04)	0.05	(0.06)
Al_2O_3	1.69	(0.40)	1.06	(0.35)	12.43	(0.37)	0.11	(0.07)	1.67	(0.23)	1.47	(0.76)	12.86	0.21	(0.14)	2.58	(0.16)
Cr_2O_3	0.19	(0.11)	0.24	(0.06)	0.72	(0.12)	0.16	(0.05)	0.33	(0.04)	0.15	(0.09)	0.84	0.15	(0.11)	0.24	(0.09)
FeO	2.86	(0.17)	2.71	(0.15)	2.62	(0.40)	4.78	(0.46)	3.22	(0.33)	3.06	(0.29)	2.83	5.82	(0.85)	3.68	(0.17)
NiO	0.15	(0.03)	0.17	(0.05)	0.17	(0.05)	0.29	(0.06)	0.10	(0.02)	0.16	(0.04)	0.17	0.25	(0.05)	0.11	(0.07)
MnO	0.08	(0.03)	0.09	(0.03)	0.03	(0.03)	0.15	(0.03)	0.09	(0.04)	0.06	(0.04)	0.00	0.13	(0.03)	0.09	(0.02)
MgO	38.90	(0.33)	39.24	(0.68)	35.18	(0.47)	52.02	(1.41)	36.86	(0.41)	39.15	(0.46)	34.61	51.41	(0.79)	36.79	(0.74)
CaO	0.01	(0.02)	0.01	(0.02)	0.15	(0.09)	0.00	(0.00)	0.01	(0.01)	0.01	(0.02)	0.00	0.00	(0.00)	0.03	(0.03)
Total	87.11	(1.57)	87.33	(1.01)	88.00	(0.00)	99.91	(0.55)	101.40	(1.12)	87.40	(0.81)	87.55	100.34	(0.69)	100.97	(0.39)
Ions calculated on the basis of 6.824 equivalent oxygens (polysom m=17) for antigorite, 14 for chlorite, 4 for olivine and 6 for orthopyroxene																	
Si	1.96	(0.02)	1.98	(0.01)	3.37	(0.10)	1.01	(0.03)	1.98	(0.02)	1.96	(0.03)	3.37	1.01	(0.02)	1.94	(0.03)
Ti	0.00	(0.00)	0.00	(0.00)	0.02	(0.03)	0.00	(0.00)	0.00	(0.00)	0.00	(0.00)	0.00	0.00	(0.00)	0.00	(0.00)
Al	0.09	(0.02)	0.06	(0.02)	1.36	(0.05)	0.00	(0.00)	0.07	(0.01)	0.08	(0.04)	1.41	0.01	(0.00)	0.10	(0.01)
Cr	0.01	(0.00)	0.01	(0.00)	0.05	(0.01)	0.00	(0.00)	0.01	(0.00)	0.01	(0.00)	0.06	0.00	(0.00)	0.01	(0.00)
Fe	0.11	(0.01)	0.10	(0.01)	0.20	(0.03)	0.10	(0.01)	0.09	(0.01)	0.12	(0.01)	0.22	0.12	(0.02)	0.10	(0.01)
Ni	0.01	(0.00)	0.01	(0.00)	0.01	(0.00)	0.01	(0.00)	0.00	(0.00)	0.01	(0.00)	0.01	0.00	(0.00)	0.00	(0.00)
Mn	0.00	(0.00)	0.00	(0.00)	0.00	(0.00)	0.00	(0.00)	0.00	(0.00)	0.00	(0.00)	0.00	0.00	(0.00)	0.00	(0.00)
Mg	2.63	(0.02)	2.65	(0.03)	4.86	(0.09)	1.86	(0.06)	1.84	(0.04)	2.64	(0.03)	4.81	1.83	(0.03)	1.85	(0.04)
Ca	0.00	(0.00)	0.00	(0.00)	0.01	(0.01)	0.00	(0.00)	0.00	(0.00)	0.00	(0.00)	0.00	0.00	(0.00)	0.00	(0.00)
O	6.82	(0.01)	6.82	(0.00)	14.00	(0.00)	4.00	(0.00)	6.00	(0.00)	6.82	(0.00)	14.00	4.00	(0.00)	6.00	(0.00)
X_{Mg}	0.960	(0.024)	0.963	(0.016)	0.960	(0.056)	0.951	(0.050)	0.953	(0.050)	0.958	(0.041)	0.956	0.940	(0.086)	0.947	(0.019)
X_{Fe}	0.040	(0.024)	0.037	(0.016)	0.040	(0.056)	0.049	(0.050)	0.047	(0.050)	0.042	(0.041)	0.044	0.060	(0.086)	0.053	(0.019)
$Kd_{Fe\text{-}Mg}^{ol/opx}$			1.05								1.13						
$Kd_{Fe\text{-}Mg}^{atg/chl}$			0.93								0.95						

Experiment	1228*						1224						1070					
Dehydration	Stage 3						Stage 3						Stage 3					
Mineral	Chl		Ol		Opx		Chl		Ol		Opx		Chl		Ol		Opx	
n	2		8		4		4		8		4		4		10		3	
SiO_2	36.95	(1.49)	41.60	(1.06)	58.01	(1.01)	34.01	(0.63)	42.11	(0.94)	57.46	(1.04)	34.80	(0.89)	42.50	(1.23)	56.80	(0.85)
TiO_2	0.02	(0.03)	0.03	(0.03)	0.02	(0.04)	0.01	(0.01)	0.06	(0.06)	0.01	(0.02)	0.01	(0.02)	0.03	(0.05)	0.03	(0.03)
Al_2O_3	13.00	(1.21)	0.17	(0.16)	2.59	(0.23)	15.52	(0.57)	0.14	(0.13)	2.41	(0.23)	14.27	(0.73)	0.14	(0.14)	3.00	(0.59)
Cr_2O_3	1.10	(0.17)	0.20	(0.06)	0.24	(0.06)	0.83	(0.16)	0.23	(0.06)	0.20	(0.06)	0.82	(0.09)	0.23	(0.13)	0.30	(0.10)
FeO	2.88	(0.04)	6.11	(1.24)	3.02	(0.20)	3.05	(0.19)	4.49	(1.19)	3.55	(0.26)	3.16	(0.13)	4.29	(0.63)	3.08	(0.06)
NiO	0.16	(0.00)	0.23	(0.03)	0.13	(0.03)	0.16	(0.04)	0.24	(0.06)	0.11	(0.04)	0.16	(0.11)	0.20	(0.12)	0.11	(0.06)
MnO	0.03	(0.04)	0.10	(0.03)	0.06	(0.04)	0.02	(0.03)	0.08	(0.07)	0.10	(0.02)	0.02	(0.02)	0.09	(0.04)	0.08	(0.02)
MgO	33.83	(0.41)	50.87	(1.15)	36.28	(0.95)	34.56	(0.27)	52.63	(1.11)	36.02	(0.47)	34.63	(0.51)	52.35	(0.79)	37.20	(2.50)
CaO	0.03	(0.02)	0.02	(0.02)	0.07	(0.04)	0.03	(0.02)	0.01	(0.01)	0.03	(0.01)	0.04	(0.07)	0.02	(0.02)	0.04	(0.06)
Total	88.00	(0.00)	99.32	(0.66)	100.44	(2.07)	88.18	(0.35)	99.99	(0.77)	99.90	(1.52)	87.91	(0.42)	99.86	(0.70)	100.62	(3.93)
Ions calculated on the basis of 14 oxygens for chlorite, 4 for olivine and 6 for orthopyroxene																		
Si	3.42	(0.13)	1.01	(0.02)	1.96	(0.01)	3.16	(0.05)	1.01	(0.01)	1.96	(0.01)	3.24	(0.07)	1.01	(0.02)	1.95	(0.02)
Ti	0.00	(0.00)	0.00	(0.00)	0.00	(0.00)	0.00	(0.00)	0.00	(0.00)	0.00	(0.00)	0.00	(0.00)	0.00	(0.00)	0.00	(0.00)
Al	1.42	(0.14)	0.00	(0.00)	0.09	(0.00)	1.70	(0.06)	0.00	(0.00)	0.10	(0.01)	1.57	(0.09)	0.00	(0.00)	0.10	(0.01)
Cr	0.08	(0.01)	0.00	(0.00)	0.00	(0.00)	0.06	(0.01)	0.00	(0.00)	0.01	(0.00)	0.06	(0.01)	0.00	(0.00)	0.01	(0.00)
Fe	0.22	(0.00)	0.12	(0.03)	0.10	(0.01)	0.24	(0.02)	0.09	(0.02)	0.10	(0.01)	0.25	(0.01)	0.09	(0.01)	0.11	(0.02)
Ni	0.01	(0.00)	0.00	(0.00)	0.00	(0.00)	0.01	(0.00)	0.00	(0.00)	0.00	(0.00)	0.01	(0.01)	0.00	(0.00)	0.00	(0.00)
Mn	0.00	(0.00)	0.00	(0.00)	0.01	(0.00)	0.00	(0.00)	0.00	(0.00)	0.00	(0.00)	0.00	(0.00)	0.00	(0.00)	0.00	(0.00)
Mg	4.67	(0.07)	1.84	(0.04)	1.83	(0.01)	4.79	(0.04)	1.88	(0.03)	1.83	(0.01)	4.81	(0.06)	1.86	(0.04)	1.82	(0.00)
Ca	0.00	(0.00)	0.00	(0.00)	0.00	(0.00)	0.00	(0.00)	0.00	(0.00)	0.00	(0.00)	0.00	(0.01)	0.00	(0.00)	0.00	(0.00)
O	14.00	(0.00)	4.00	(0.00)	6.00	(0.00)	14.00	(0.00)	4.00	(0.00)	6.00	(0.00)	14.00	(0.00)	4.00	(0.00)	6.00	(0.00)
X_{Mg}	0.954	(0.01)	0.937	(0.13)	0.947	(0.05)	0.953	(0.03)	0.954	(0.12)	0.948	(0.03)	0.951	(0.02)	0.956	(0.06)	0.944	(0.10)
X_{Fe}	0.046	(0.01)	0.063	(0.13)	0.053	(0.05)	0.047	(0.03)	0.046	(0.12)	0.052	(0.03)	0.049	(0.02)	0.044	(0.06)	0.056	(0.10)
$Kd_{Fe\text{-}Mg}{}^{ol/opx}$	1.19						0.87						0.78					

n number of analyses

* Experiment conducted in graphite furnace

Experiment	262						1273*			
Dehydration	Stage 3						Stage 4			
Mineral	Chl		Ol		Opx		Ol		Opx	
n	5		5		4		6		7	
SiO_2	35.73	(2.44)	42.98	(0.40)	57.38	(2.08)	42.09	(1.56)	56.22	(0.64)
TiO_2	0.00	(0.01)	0.01	(0.03)	0.01	(0.01)	0.01	(0.01)	0.04	(0.04)
Al_2O_3	14.50	(1.87)	0.22	(0.14)	3.06	(1.24)	0.22	(0.20)	3.51	(0.44)
Cr_2O_3	0.97	(0.33)	0.15	(0.10)	0.27	(0.05)	0.16	(0.08)	0.34	(0.12)
FeO	2.91	(0.27)	3.29	(0.36)	2.65	(0.12)	5.55	(0.65)	4.39	(0.83)
NiO	0.20	(0.04)	0.39	(0.16)	0.20	(0.07)	0.30	(0.03)	0.08	(0.04)
MnO	0.03	(0.03)	0.09	(0.03)	0.08	(0.02)	0.08	(0.04)	0.10	(0.03)
MgO	33.64	(0.34)	53.54	(1.40)	37.05	(0.93)	51.54	(1.47)	35.52	(0.50)
CaO	0.01	(0.01)	0.03	(0.02)	0.03	(0.03)	0.01	(0.02)	0.01	(0.01)
Total	88.00	(0.00)	100.69	(1.25)	100.72	(1.97)	99.97	(0.58)	100.23	(0.43)
Ions calculated on the basis of 14 oxygens for chlorite, 4 for olivine and 6 for orthopyroxe										
Si	3.31	(0.21)	1.01	(0.01)	1.93	(0.03)	1.01	(0.03)	1.92	(0.02)
Ti	0.00	(0.00)	0.00	(0.00)	0.00	(0.00)	0.00	(0.00)	0.00	(0.00)
Al	1.58	(0.21)	0.01	(0.00)	0.12	(0.05)	0.01	(0.01)	0.14	(0.02)
Cr	0.07	(0.02)	0.00	(0.00)	0.01	(0.00)	0.00	(0.00)	0.01	(0.00)
Fe	0.23	(0.02)	0.06	(0.01)	0.07	(0.00)	0.11	(0.01)	0.13	(0.02)
Ni	0.02	(0.00)	0.01	(0.00)	0.01	(0.00)	0.01	(0.00)	0.00	(0.00)
Mn	0.00	(0.00)	0.00	(0.00)	0.00	(0.00)	0.00	(0.00)	0.00	(0.00)
Mg	4.65	(0.07)	1.88	(0.04)	1.86	(0.02)	1.85	(0.07)	1.81	(0.02)
Ca	0.00	(0.00)	0.00	(0.00)	0.00	(0.00)	0.00	(0.00)	0.00	(0.00)
O	14.00	(0.00)	4.00	(0.00)	6.00	(0.00)	4.00	(0.00)	6.00	(0.00)
X_{Mg}	0.954	(0.04)	0.967	(0.04)	0.961	(0.02)	0.943	(0.07)	0.935	(0.12)
X_{Fe}	0.046	(0.04)	0.033	(0.04)	0.039	(0.02)	0.057	(0.07)	0.065	(0.12)
$Kd_{Fe\text{-}Mg}^{ol/opx}$	0.86						0.87			

n number of analyses

* Experiment conducted in graphite furnace

Table IV-4. Wavelength-dispersive (WDS) compositions of spinel, chromite, magnetite and hematite minerals. Distinction between magnetite and hematite endmembers is evidenced by the oxygen/Σcations ratio of (repectively close to 1.33 and and 1.50). Oxide weights were derived from atomic weight data, with the assumption that iron is in the form Fe_3O_4 for all minerals except for hematite with all iron as Fe_2O_3.

Experiment	1275		1111		1110			1228*			1070		1224		262			1273*
Dehydration	Stage 1		Stage 2		Stage 2			Stage 3			Stage 3		Stage 3		Stage 3			Stage 4
Mineral	Mt	Ht	Mt	Ht	Sp	Chr	Mt	Ht	Sp	Chr	Mt	Mt	Ht	Mt	Ht	Sp	Chr	Mt	Ht	Mt
TiO_2	0.12	0.08	0.14	0.16	0.15	1.16	0.25	0.21	0.26	2.43	0.18	0.14	0.15	0.08	0.23	0.02	4.96	0.23	0.08	0.35
Al_2O_3	0.01	0.01	0.05	0.03	18.93	0.45	0.09	0.08	0.05	0.08	0.01	0.03	0.02	0.15	0.07	0.71	0.14	0.40	0.29	3.73
Cr_2O_3	1.12	0.52	1.29	0.93	42.71	32.34	3.69	1.41	0.81	19.16	1.21	2.12	1.96	1.04	0.69	0.13	27.05	0.51	1.11	2.21
Fe_3O_4	98.36	99.19	97.10	98.57	28.33	61.06	95.17	98.18	52.35	76.59	98.26	95.40	97.52	93.53	98.92	84.53	62.39	97.06	97.40	85.23
MnO	0.07	0.08	0.09	0.04	0.99	2.94	0.28	0.04	0.07	0.76	0.12	0.17	0.06	0.13	0.02	0.00	0.48	0.10	0.12	0.14
MgO	0.31	0.13	1.33	0.27	8.90	1.88	0.52	0.09	46.45	0.97	0.21	2.14	0.30	5.07	0.08	14.61	4.98	1.71	1.01	8.35
Ti	0.00	0.00	0.00	0.00	0.00	0.03	0.01	0.00	0.00	0.06	0.01	0.00	0.00	0.00	0.00	0.00	0.11	0.01	0.00	0.01
Al	0.00	0.00	0.00	0.00	0.91	0.03	0.01	0.00	0.00	0.00	0.00	0.00	0.00	0.01	0.00	0.04	0.01	0.02	0.01	0.20
Cr	0.03	0.01	0.04	0.02	0.97	0.94	0.10	0.03	0.01	0.56	0.04	0.06	0.04	0.03	0.01	0.00	0.68	0.01	0.02	0.06
Fe	2.95	1.95	2.73	1.87	0.64	1.77	2.64	1.92	0.88	2.27	2.89	2.72	1.97	2.62	1.94	2.11	1.57	2.78	1.88	2.21
Mn	0.00	0.00	0.00	0.00	0.02	0.09	0.01	0.00	0.00	0.03	0.00	0.01	0.00	0.00	0.00	0.00	0.01	0.00	0.00	0.00
Mg	0.02	0.00	0.07	0.01	0.39	0.10	0.03	0.00	1.49	0.05	0.01	0.12	0.01	0.27	0.00	0.70	0.24	0.09	0.04	0.41
O	4.00	3.00	4.00	3.00	4.00	4.00	4.00	3.00	4.00	4.00	4.00	4.00	3.00	4.00	3.00	4.00	4.00	4.00	3.00	4.00
X_{Mg}	0.01	0.00	0.03	0.01	0.38	0.06	0.01	0.00	0.63	0.02	0.00	0.04	0.01	0.09	0.00	0.25	0.13	0.03	0.02	0.16
O/∑cations	1.33	1.52	1.40	1.57			1.43	1.53			1.36	1.38	1.48	1.37	1.53			1.37	1.54	1.38

* Experiment conducted in graphite furnace

V **Discussion**

V.1 **Comparison with natural specimens**

By performing experiments on a natural serpentinite we observe the same paragenesis as observed in Cerro del Almirez massif in Spain (Debret et al., 2014, 2015; Garrido et al., 2005; López Sánchez-Vizcaíno et al., 2005; Padrón-Navarta et al., 2010a, b, 2011; Trommsdorff et al., 1998). The massif has preserved the dehydration front between antigorite-serpentinites (atg + mgt) and chlorite-bearing harzburgites (ol + opx + chl + mgt) as a contact of transitional lithology made of atg + chl + ol + opx + mgt (and tremolite), hence allowing to compare the behavior of iron in natural samples and in our experiments. In our series of experiment, we reproduce this transitional lithology. The texture of our samples is similar to those in Almirez outcrops, especially the spinifex texture of orthopyroxene as observed in the chlorite harzburgite from this locality (Morten, L. and Puga, 1984; Padrón-Navarta et al., 2011; Trommsdorff et al., 1998). FeO enrichment in secondary antigorite and in olivine and orthopyroxene after antigorite destabilization is also in agreement with observations from natural samples (Debret et al., 2014). Moreover our experiments reproduce the formation of hematite upon antigorite dehydration as observed in the Almirez massif by Debret et al. (2015).

V.2 **Comparison with antigorite stability from previous experimental studies**

The present samples are Fe-and Al-poor compared to the samples from Cerro Del Almirez studied by Debret et al. (2015), Padrón-Navarta et al. (2009) (see Table IV-3), due to the depletion of the protolith prior to subduction. Compared to previous experimental reports we observe some variations concerning the stability of antigorite. For example, Ulmer and Trommsdorff (1995) investigated the antigorite breakdown of a material composed of a mix of 85 volume percent (vol %) of natural antigorite (1.30 wt% Al_2O_3, 2.94 wt% FeO) and 15 vol % brucite, to which was added 10 wt% of the dehydration products olivine + enstatite obtained in a preliminary experiment. Their work suggests antigorite stability up to 690°C for a pressure of

3 GPa (Figure IV-2). In their study, Wunder and Schreyer (1997) first ran dehydration experiments on a synthetic antigorite gel in the MgO-SiO_2-H_2O system, then mixed the products olivine + enstatite with natural antigorite in the proportions 1:1 and added ~ 20 wt% H_2O. These experiments constrain the stability limit of antigorite (0.68 wt% Al_2O_3, 1.66 wt% FeO in the bulk) around 640°C at 2.8 GPa and 650 °C at 3.5 GPa. Bromiley and Pawley (2003) bracketed the destabilization of antigorite at 3 GPa between 620 and 660°C for experiments in the MgO-SiO_2-H_2O (MSH) system with 0.10 wt% Al_2O_3 and 0.30 FeO (natural antigorite sample with synthetic olivine + enstatite and 20 wt% water) and between 660 and 700°C in the MgO-Al_2O_3-SiO_2-H_2O (MASH) system with 3.06 wt% Al_2O_3 and 5.47 wt% FeO (natural antigorite sample with synthetic olivine + enstatite + chlorite and 20 wt% water). Similar experiments were conducted by Padrón-Navarta et al. (2009) and show that complete dehydration of serpentine from Cerro del Almirez (3.10 wt% Al_2O_3 and 6.56 wt% FeO) occurred between 665 and 680°C for pressures of 2.5 and 1.9 GPa. These experimental studies have highlighted the thermal stabilizing effect of Al_2O_3 on antigorite. On the other hand, it has been suggested that the addition of iron reduces the thermal stability of antigorite thermal stability (Merkulova et al. (2016) concluded that the addition of 10 wt% FeO conducts in a decrease of about 25°C for antigorite breakdown, in comparison to an iron free bulk (i.e. 675°C instead of 700°C, at 2 GPa). In this study, we observe the dehydration of natural antigorite rich serpentinite containing 2.62 wt% FeO and 1.66 wt% Al_2O_3 at 680°C. This is in agreement with thermal stability limits proposed for various Al- and Fe-bearing serpentinite compositions representative of serpentinized mantle materials mentioned above (Bromiley and Pawley, 2003; Merkulova et al., 2016; Padrón-Navarta et al., 2010; Ulmer and Trommsdorff, 1995).

V.3 Ferric iron redistribution in secondary phases

Variation of iron contents in secondary phases can be related to ferric iron redistribution. During the partial breakdown of antigorite and the crystallization of olivine, orthopyroxene and

chlorite, all mineral phases display an increase of their iron content. Such a FeO content increase in the secondary silicates during antigorite dehydration is in agreement with previous studies of natural serpentinites from various localities (Debret et al., 2014, 2015) which observed a redistribution of iron associated with magnetite dissolution during the breakdown of antigorite. At the third stage, a decrease of iron content in both phases is observed, while it increases in chlorite. Antigorite is fully destabilized and its high amount of ferric iron has to be redistributed between its products. Most of this ferric iron is actually incorporated into chlorite, which owes a lower acceptance for Fe^{3+} than antigorite (Fe^{3+}/Fe_{total} of 0.47-0.69 in chlorite versus 0.48-0.75 in antigorite, see Debret et al., 2015) but still much higher than orthopyroxene. This mineral can accept up to 10% Fe^{3+}/Fe_{total} (Nimis et al., 2015), and olivine does not allow any measurable ferric iron incorporation. Such ferric iron partitioning explains FeO decrease in olivine and orthopyroxene while coexisting with chlorite. At stage 4, FeO increases again in olivine and orthopyroxene. This last stage of dehydration corresponds to the complete destabilization of chlorite and denotes a reduction of iron in mineral phases.

Iron distribution between the dehydration products olivine and orthopyroxene seems to vary following the redox environment. The exchange coefficient $Kd_{Fe\text{-}Mg}^{Ol/Opx}$ is 0.78-1.19 (see Equation 2, Figure IV-8) for our samples. This corresponds to a wider range of values than the one inferred by data from the literature, clustering mostly around 0.9-1.15 (Debret et al., 2015; Padrón-Navarta et al., 2009b; Trommsdorff et al., 1998). Note that here, since ferric iron is not measured, all X_{Fe} in Eq. 2 considers Fe_{total}. Some experiments depart from this limit and reach $Kd_{Fe\text{-}Mg}^{Ol/Opx} = 1.19$. Values for a $Kd_{Fe\text{-}Mg}^{Ol/Opx}$ of 1.0±0.2 are not correlated with Al content of pyroxene, nor annealing duration. High values of $Kd_{Fe\text{-}Mg}^{Ol/Opx}$ reflects the approach to equilibrium. The group of samples conducted under oxidizing conditions (i.e. with lanthanum chromite furnace) and the group corresponding to reducing conditions (graphite furnace) are both following a trend of decreasing $Kd_{Fe\text{-}Mg}^{Ol/Opx}$ with increasing temperature. In other terms

high temperatures favor a distribution of iron into enstatite over olivine. Such tendency has been observed especially in the case Mg-rich endmembers, typical of mantle composition (i.e. X_{Fe}^{Ol} between 0 and 0.2). Low $Kd_{Fe\text{-}Mg}^{Ol/Opx}$ might in fact be an artefact related to counting Fe^{3+} as Fe^{2+} in orthopyroxene (von Seckendorff and O'Neill, 1993). This trend is shifted to slightly higher $Kd_{Fe\text{-}Mg}^{Ol/Opx}$ in a reducing environment (i.e. lower incorporation of iron into enstatite), meaning that both high temperature and oxidizing conditions favor the distribution of iron into enstatite over olivine, probably reflecting a higher Fe^{3+}/Fe_{total} in orthopyroxene at these conditions. The redox environment control can be explained by the fact that oxidizing conditions enhance the incorporation of ferric iron in enstatite (up to 10% Fe^{3+}/Fe_{total}, Nimis et al. (2015), hence accounting for the decrease in the apparent distribution coefficient of iron between olivine and enstatite. Also, it is expected that the Fe^{3+}/Fe_{total} will increase with increasing temperature.

V.4 Influence of the redox environment on the formation of hematite during serpentinite dehydration

In this study we observe hematite formation only after the onset of antigorite dehydration. Hence, in our samples the breakdown of antigorite is intimately related to the formation of hematite. Antigorite contains a high amount of ferric iron, which cannot be incorporated in neither chlorite nor orthopyroxene or olivine. Indeed, chlorite has a lower acceptance for Fe^{3+} compared to antigorite as demonstrated by the partitioning measured on natural samples (Debret et al., 2015). Olivine and orthopyroxene are virtually Fe^{3+} free (below detection limit for olivine, and a maximum of 10% Fe^{3+}/Fe_{total} was observed in cratonic orthopyroxenes, Nimis et al., 2015). Since ferric iron cannot be hosted in the newly formed silicates, it can only be incorporated as Fe^{2+} in these new phases, inducing a decrease of the bulk Fe^{3+}/Fe_{total} during destabilization. Iron mobility in serpentinite derived fluids is relatively

restricted, as shown in Debret et al. (2016). They estimated the complexation of isotopically light Fe in the form Fe(II)-SO_4^{2-} in the fluids to be minor (i.e. ~0.1 wt% Fe for a bulk rock containing ~8 wt% Fe_2O_3) associated with atg-serpentinite dehydration. Antigorite destabilization with the concomitant dissolution of magnetite can therefore be constricted to a reaction reducing iron in the silicates and liberating oxygen (Debret et al., 2015).

Nevertheless, O_2 transfer in the fluid is known to have a relatively low efficiency, due to the low solubility of oxygen in water. In addition, Merkulova et al. (2017) calculated that the O_2 production associated with atg-serpentinite destabilization (~ 2.7 moles of O_2 for 1kg of their starting material) is too high compared the 10^{-5} ppb of O_2 contained in an aqueous fluid (at 900°C, 1.2 GPa and QFM+2, see Frost and Ballhaus, 1998). If no external reservoir (mineral or fluid) can accommodate such oxygen excess, an oxidation reaction has to take place within the considered system (i.e. within the capsule in our case) as the magnetite-hematite assemblages attest. The presence of such assemblage in our experiment allows to constrain the oxygen fugacity prevailing during the fluid pulse to be at the Fe_2O_3-Fe_3O_4 buffer. For temperatures of 600-900°C, the oxygen fugacity given by the HM (Hematite-Magnetite) buffer is of 10^{-4} to 5.10^{-2} bars. The occurrence of hematite in both experimental and natural samples (dehydrated serpentinites from meta-ophiolites in the Western Alps and from meta-peridotites in the Cerro Del Almirez massif, see Debret et al., 2016 and Debret et al., 2015 respectively) demonstrates that hematite is by no means a retrograde product in natural samples. The formation of hematite evidences saturation of O_2 in the fluid produced during atg-serpentinite breakdown. It can nevertheless be noted that we observe hematite only in experiments conducted with oxidizing conditions ($LaCrO_3$ furnace), while it is absent in assemblages equilibrated under reducing conditions (C furnace). Thus, the buffering of the oxygen fugacity by the furnace controls the stability of hematite. For instance, experiments of atg-serpentinite dehydration conducted by Merkulova et al., (2016, 2017) do not present hematite minerals in

the product assemblages. In fact, their experiments were buffered by graphite–NaCl–pyrophyllite cell assembly in piston-cylinder. Such a setup results in the permeability of the Au capsule to the hydrogen produced by the graphite furnace oxidation and sets the fO_2 between QFM-2 and QFM, below magnetite-hematite equilibrium, hence preventing hematite formation. Note also, that in their experiments magnetite is consumed very rapidly.

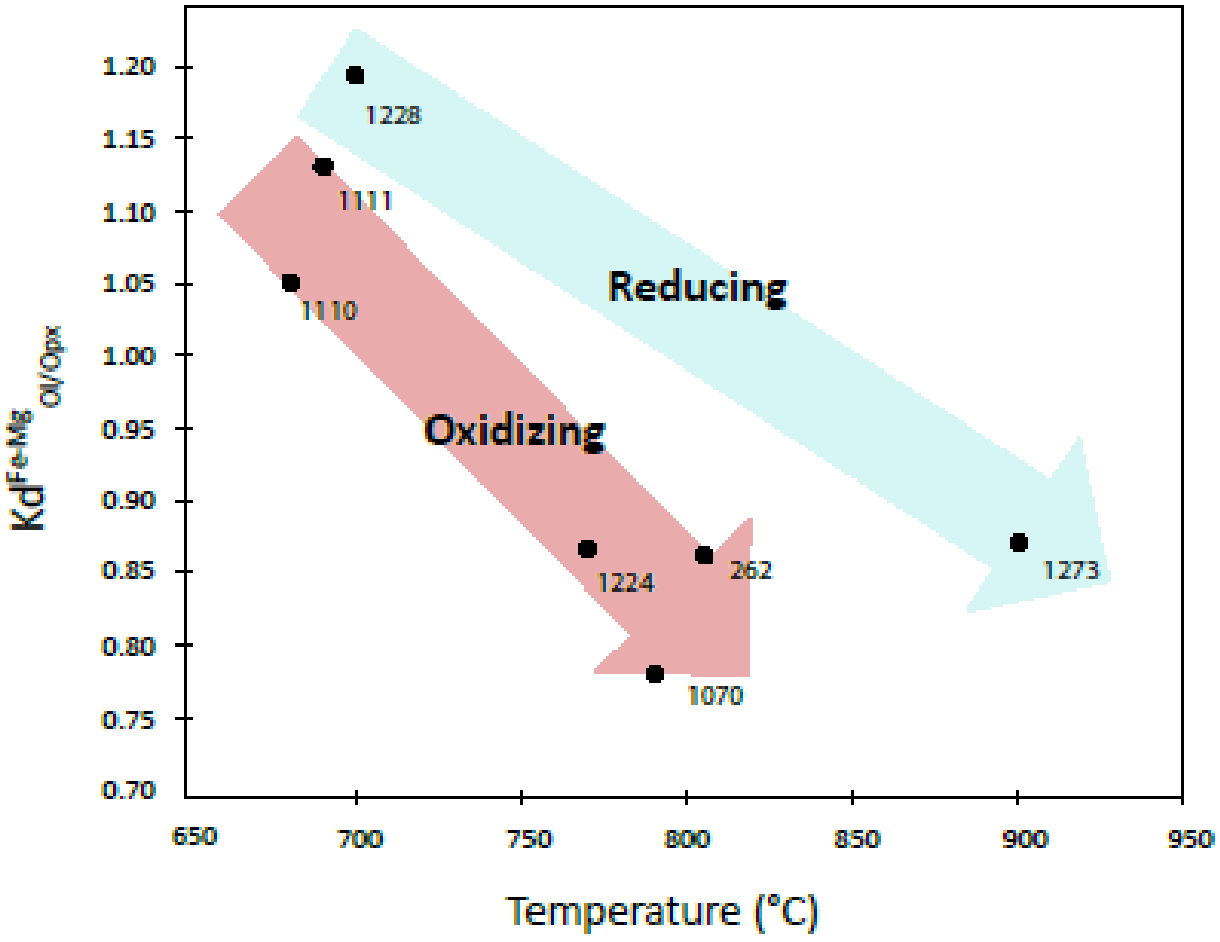

Figure IV-8 : $Kd_{Fe\text{-}Mg}^{Ol/Opx}$ as a function of temperature. The experiments under oxidized conditions were performed with lanthanum chromite furnace while the experiments under reduced conditions were performed with graphite furnace.

V.5 **Implications of high fO_2**

Hematite evidences the excess of oxygen released during antigorite dehydration in locally closed systems, as it has been described in both natural samples and the present experiments. Nevertheless, the occurrence of equilibrated hematite-magnetite assemblages in nature appears to be relatively rare, since it has only been reported in dehydrated serpentinites from meta-ophiolites in the Western Alps (Debret et al., 2016) and from meta-peridotites in the Cerro Del Almirez massif (Debret et al., 2015). This suggests that serpentinite dehydration might mostly occur in nature in an open system fashion. Such system can allow the transfer of the high oxidation degree of serpentinites by involving different O_2 consumption mechanisms. For instance, aqueous carbonates and more specifically aqueous sulfates have been proposed as potential carriers of the oxidation degree (Debret and Sverjensky, 2017). S species are indeed reported in serpentinites, up to 1wt% (Alt et al., 2013). The dehydration of sulfide-bearing serpentinites is accompanied by sulfur oxidation, allowing the production of aqueous sulfate species (Debret and Sverjensky, 2017; Merkulova et al., 2017). $SO_4^{2-}{}_{(aq)}$ species could be further mobilized in the fluids to the mantle wedge and oxidize its Fe^{2+} into Fe^{3+} the mantle wedge, hence transmitting the oxidized character of subducting serpentinites to the source of arc magmas (Debret and Sverjensky, 2017). Nevertheless, the amount of sulfides initially carried by highly oxidized serpentinites might not be sufficient to consume all O_2 produced during serpentinite dehydration, especially considering that more than 50% of the initial amount of S present in serpentinites is lost during the transition lizardite to antigorite (Debret et al., 2014b). The later could explain the crystallization of hematite in some cases. Alternatively a redox equilibration within the serpentinized layer of the lithosphere is likely to buffer the excess of oxygen, in agreement with fO_2 and serpentinization degrees heterogeneities (Debret and Sverjensky, 2017; Merkulova et al., 2017).

VI Conclusion

By performing experiments at 3 GPa and 600 to 900°C, we reproduced the different stages of prograde high-pressure transition from antigorite to enstatite-olivine rocks observed in natural samples from Cerro del Almirez. When dehydrating, atg-serpentinite sample containing ~5% magnetite produces assemblages containing secondary antigorite, chlorite, olivine, orthopyroxene and a fluid phase. Disappearance of Fe^{3+}-rich antigorite associated with progressive magnetite dissolution is accompanied by crystallization of hematite on the preexisting magnetite for experiments conducted in $LaCrO_3$ furnace. Through its oxidizing character, the $LaCrO_3$ furnace virtually reproduces a locally closed system allowing antigorite dehydration reactions to take place under natural serpentinite intrinsic redox state. It forces the local O_2 consumption via equilibrated magnetite-hematite assemblages in the capsule. Interestingly, formation of hematite during antigorite dehydration has also been noticed for example in the natural outcrop massif of Cerro del Almirez (Spain, see Debret et al., 2015). Similar observation in the present study confirms that natural hematite is not a retrograde product. This confirms that fluids released during intrinsic (i.e. closed system) antigorite dehydration are at equilibrium with magnetite and hematite. The redox state of the destabilization reaction of antigorite-bearing serpentinite can therefore be constrained to take place at FMQ+5 (i.e $\log(fO_2)$ of -10 to -12 at 700-800°C). Such a high fO_2 is in agreement with sulfur oxidation observed during destabilization of sulfide-bearing serpentinites and the production of sulfate species in both experimental and numerical models (Merkulova et al., 2017; Debret and Sverjensky, 2017). Fluids with such an oxidizing potential can have strong consequences on the mantle wedge physical and chemical properties (via $SO_4^{2-}{}_{(aq)}$ mobility) and consequently on the redox state of arc magmas. The oxidizing character of antigorite destabilization reaction could thus be, through the associated fluid phase released, a relevant explanation of the high oxidation state of arc magmas compared to Mid Oceanic Ridge Basalts.

References

Alt, J.C., Schwarzenbach, E.M., Fr??h-Green, G.L., Shanks, W.C., Bernasconi, S.M., Garrido, C.J., Crispini, L., Gaggero, L., Padr??n-Navarta, J. a., Marchesi, C., 2013. The role of serpentinites in cycling of carbon and sulfur: Seafloor serpentinization and subduction metamorphism. Lithos 178, 40–54. doi:10.1016/j.lithos.2012.12.006

Bean, V.E., Akimoto, S., Bell, P.M., Block, S., Holzapfel, W.B., Manghnani, M.H., Nicol, M.F., Stishov, S.M., 1986. Another step toward an international practical pressure scale. Phys. B+C 139–140, 52–54. doi:10.1016/0378-4363(86)90521-8

Bézos, A., Humler, E., 2005. The Fe3+/ΣFe ratios of MORB glasses and their implications for mantle melting. Geochim. Cosmochim. Acta 69, 711–725. doi:10.1016/j.gca.2004.07.026

Bose, K., Ganguly, J., 1995. Quartz-coesite transition revisited: Reversed experimental determination at 500-1200 °C and retrieved thermochemical properties. Am. Mineral. 80, 231–238.

Bose, K., Navrotsky, A., 1998. Thermochemistry and phase equilibria of hydrous phases in the system MgO-SiO2-H2O: Implications for volatile transport to the mantle. J. Geophys. Res. 103, 9713. doi:10.1029/98JB00506

Brandon, A.D., Draper, D.S., 1996. Constraints on the origin of the oxidation state of mantle overlying subduction zones: An example from Simcoe, Washington, USA. Geochim. Cosmochim. Acta 60, 1739–1749. doi:10.1016/0016-7037(96)00056-7

Bromiley, G.D., Pawley, A.R., 2003. The stability of antigorite in the systems MgO-SiO2-H2O (MSH) and MgO-Al2O3-SiO2-H2O (MASH): The effects of Al3+ substitution on high-pressure stability. Am. Mineral.

Cannat, M., Bideau, D., Hébert, R., 1990. Plastic deformation and magmatic impregnation in serpentinized ultramafic rocks from the Garrett transform fault (East Pacific Rise). Earth Planet. Sci. Lett. 101, 216–232. doi:10.1016/0012-821X(90)90155-Q

Carmichael, I.S.E., 1991. The redox states of basic and silicic magmas: a reflection of their source regions? Contrib. to Mineral. Petrol. 106, 129–141. doi:10.1007/BF00306429

Cottrell, E., Kelley, K.A., 2011. The oxidation state of Fe in MORB glasses and the oxygen fugacity of the upper mantle. Earth Planet. Sci. Lett. 305, 270–282. doi:10.1016/j.epsl.2011.03.014

de Faria, D.L.A., Venâncio Silva, S., de Oliveira, M.T., 1997. Raman microspectroscopy of some iron oxides and oxyhydroxides. J. Raman Spectrosc. 28, 873–878. doi:10.1002/(SICI)1097-4555(199711)28:11<873::AID-JRS177>3.0.CO;2-B

Debret, B., Andreani, M., Muñoz, M., Bolfan-Casanova, N., Carlut, J., Nicollet, C., Schwartz, S., Trcera, N., 2014a. Evolution of Fe redox state in serpentine during subduction. Earth Planet. Sci. Lett. 400, 206–218. doi:10.1016/j.epsl.2014.05.038

Debret, B., Bolfan-Casanova, N., Padrón-Navarta, J.A., Martin-Hernandez, F., Andreani, M., Garrido, C.J., López Sánchez-Vizcaíno, V., Gómez-Pugnaire, M.T., Muñoz, M., Trcera, N., 2015. Redox state of iron during high-pressure serpentinite dehydration. Contrib. to Mineral. Petrol. 169, 36. doi:10.1007/s00410-015-1130-y

Debret, B., Koga, K.T., Nicollet, C., Andreani, M., Schwartz, S., 2014b. F, Cl and S input via serpentinite in subduction zones: implications for the nature of the fluid released at depth. Terra Nov. 26, 96–101. doi:10.1111/ter.12074

Debret, B., Millet, M.-A., Pons, M.-L., Bouilhol, P., Inglis, E., Williams, H., 2016. Isotopic evidence for iron mobility during subduction. Geology 44, 215–218. doi:10.1130/G37565.1

Debret, B., Sverjensky, D.A., 2017. Highly oxidising fluids generated during serpentinite breakdown in

subduction zones. Sci. Rep. 7, 10351. doi:10.1038/s41598-017-09626-y

Deschamps, F., Guillot, S., Godard, M., Chauvel, C., Andreani, M., Hattori, K., 2010. In situ characterization of serpentinites from forearc mantle wedges: Timing of serpentinization and behavior of fluid-mobile elements in subduction zones. Chem. Geol. 269, 262–277. doi:10.1016/j.chemgeo.2009.10.002

Elliott, T., Plank, T., Zindler, A., White, W., Bourdon, B., 1997. Element transport from slab to volcanic front at the Mariana arc. J. Geophys. Res. Solid Earth 102, 14991–15019. doi:10.1029/97JB00788

Evans, B.W., Trommsdorff, V., 1978. Petrogenesis of garnet lherzolite, Cima di Gagnone, Lepontine Alps. Earth Planet. Sci. Lett. 40, 333–348. doi:10.1016/0012-821X(78)90158-9

Evans, K.A., 2012. The redox budget of subduction zones. Earth-Science Rev. 113, 11–32. doi:10.1016/j.earscirev.2012.03.003

Experimental insight into redox transfer by iron- and sulfur-bearing serpentinite dehydration in subduction zones, 2017. . Earth Planet. Sci. Lett. 479, 133–143. doi:10.1016/J.EPSL.2017.09.009

Férot, A., Bolfan-Casanova, N., 2012. Water storage capacity in olivine and pyroxene to 14 GPa: Implications for the water content of the Earth's upper mantle and nature of seismic discontinuities. Earth Planet. Sci. Lett. 218–230. doi:10.1016/j.epsl.2012.06.022

Frost, B.R., Ballhaus, C., 1998. Comments on "Constraints on the origin of the oxi-dation state of mantle overlying subduction zones: an example from Simcoe, Washington, USA." Geochim. Cosmochim. Acta 62, 329–331. doi:10.1016/S0016-7037(98)00008-8

Gaetani, G.A., Grove, T.L., 1998. The influence of water on melting of mantle peridotite. Contrib. to Mineral. Petrol. 131, 323–346. doi:10.1007/s004100050396

Garrido, C.J., López Sánchez-Vizcaíno, V., Gómez-Pugnaire, M.T., Trommsdorff, V., Alard, O., Bodinier, J.-L., Godard, M., 2005. Enrichment of HFSE in chlorite-harzburgite produced by high-pressure dehydration of antigorite-serpentinite: Implications for subduction magmatism. Geochemistry, Geophys. Geosystems 6, n/a-n/a. doi:10.1029/2004GC000791

Gasparik, T., 2003. Phase Diagrams for Geoscientists: An Atlas of the Earth's Interior.

Gemmi, M., Fischer, J., Merlini, M., Poli, S., Fumagalli, P., Mugnaioli, E., Kolb, U., 2011. A new hydrous Al-bearing pyroxene as a water carrier in subduction zones. Earth Planet. Sci. Lett. 310, 422–428. doi:10.1016/j.epsl.2011.08.019

Gill, J.B., 1981. Orogenic Andesites and Plate Tectonics, Minerals a. ed. Springer Berlin Heidelberg.

Grove, T.L., Chatterjee, N., Parman, S.W., Médard, E., 2006. The influence of H2O on mantle wedge melting. Earth Planet. Sci. Lett. 249, 74–89. doi:http://dx.doi.org/10.1016/j.epsl.2006.06.043

Guillot, S., Hattori, K.H., de Sigoyer, J., 2000. Mantle wedge serpentinization and exhumation of eclogites: Insights from eastern Ladakh, northwest Himalaya. Geology 28, 199. doi:10.1130/0091-7613(2000)28<199:MWSAEO>2.0.CO;2

Hattori, K.H., Guillot, S., 2007. Gechemical character of serpentinites associated with high- to ultahigh-pressure metamorphic rocks in the Alps, Cuba, and the Himalayas: Recycling of elements in subduction zones. Geochemistry, Geophys. Geosystems 8.

Kelley, K.A., Cottrell, E., 2012. The influence of magmatic differentiation on the oxidation state of Fe in a basaltic arc magma. Earth Planet. Sci. Lett. 329–330, 109–121. doi:10.1016/j.epsl.2012.02.010

Kelley, K.A., Cottrell, E., 2009. Water and the oxidation state of subduction zone magmas. Science 325, 605–607. doi:10.1126/science.1174156

Laubier, M., Grove, T.L., Langmuir, C.H., 2014. Trace element mineral/melt partitioning for basaltic

and basaltic andesitic melts: An experimental and laser ICP-MS study with application to the oxidation state of mantle source regions. Earth Planet. Sci. Lett. 392, 265–278. doi:10.1016/j.epsl.2014.01.053

Lee, C.-T.A., Luffi, P., Le Roux, V., Dasgupta, R., Albaréde, F., Leeman, W.P., 2010. The redox state of arc mantle using Zn/Fe systematics. Nature 468, 681–685. doi:10.1038/nature09617

Lee, C.T.A., Leeman, W.P., Canil, D., Li, Z.X.A., 2005. Similar V/Sc systematics in MORB and arc basalts: Implications for the oxygen fugacities of their mantle source regions. J. Petrol. 46, 2313–2336.

López Sánchez-Vizcaíno, V., Trommsdorff, V., Gómez-Pugnaire, M.T., Garrido, C.J., Müntener, O., Connolly, J.A.D., 2005. Petrology of titanian clinohumite and olivine at the high-pressure breakdown of antigorite serpentinite to chlorite harzburgite (Almirez Massif, S. Spain). Contrib. to Mineral. Petrol. 149, 627–646. doi:10.1007/s00410-005-0678-3

Mallmann, G., O'Neill, H.S.C., 2009. The Crystal/Melt Partitioning of V during Mantle Melting as a Function of Oxygen Fugacity Compared with some other Elements (Al, P, Ca, Sc, Ti, Cr, Fe, Ga, Y, Zr and Nb). J. Petrol. 50, 1765–1794. doi:10.1093/petrology/egp053

Merkulova, M., Muñoz, M., Vidal, O., Brunet, F., 2016. Role of iron content on serpentinite dehydration depth in subduction zones: Experiments and thermodynamic modeling. doi:10.1016/j.lithos.2016.09.007

Merkulova, M.V., Muñoz, M., Brunet, F., Vidal, O., Hattori, K., Vantelon, D., Trcera, N., Huthwelker, T., 2017. Experimental insight into redox transfer by iron- and sulfur-bearing serpentinite dehydration in subduction zones. Earth Planet. Sci. Lett. 479, 133–143. doi:10.1016/J.EPSL.2017.09.009

Mevel, C., 2003. Serpentinization of abyssal peridotites at mid-ocean ridges. Geomaterials.

Morten, L. and Puga, E., 1984. Blades of olivines and ortho- dissolved lithium in the oceans. Geochim. Cosmochim. pyroxenes in ultramafic rocks from the Cerro del Almirez, Acta, 48: 859-872. Sierra Nevada Complex, Spain: relics of quench-textured Strong, D.F. and Dostal, J., 1980. Dyna. Neues Jahrb. Miner. Monatsh. 5:211-218.

Muñoz, M., Vidal, O., Marcaillou, C., Pascarelli, S., Mathon, O., Farges, F., 2013. Iron oxidation state in phyllosilicate single crystals using Fe-K pre-edge and XANES spectroscopy: Effects of the linear polarization of the synchrotron X-ray beam. Am. Mineral. 98, 1187–1197. doi:10.2138/am.2013.4289

Nimis, P., Goncharov, A., Ionov, D.A., McCammon, C., 2015. Fe3+ partitioning systematics between orthopyroxene and garnet in mantle peridotite xenoliths and implications for thermobarometry of oxidized and reduced mantle rocks. Contrib. to Mineral. Petrol. 169, 6. doi:10.1007/s00410-014-1101-8

Padrón-Navarta, J.A., Hermann, J., Garrido, C.J., López Sánchez-Vizcaíno, V., Gómez-Pugnaire, M.T., 2010a. An experimental investigation of antigorite dehydration in natural silica-enriched serpentinite. Contrib. to Mineral. Petrol. 159, 25–42. doi:10.1007/s00410-009-0414-5

Padrón-Navarta, J.A., Lopez Sanchez-Vizcaino, V., Garrido, C.J., Gomez-Pugnaire, M.T., 2011. Metamorphic Record of High-pressure Dehydration of Antigorite Serpentinite to Chlorite Harzburgite in a Subduction Setting (Cerro del Almirez, Nevado-Filabride Complex, Southern Spain). J. Petrol. 52, 2047–2078. doi:10.1093/petrology/egr039

Padrón-Navarta, J.A., Tommasi, A., Garrido, C.J., Sanchez-Vizcaino, V.L., Gomez-Pugnaire, M.T., Jabaloy, A., Vauchez, A., 2010b. Fluid transfer into the wedge controlled by high-pressure hydrofracturing in the cold top-slab mantle. Earth Planet. Sci. Lett. 297, 271–286. doi:10.1016/j.epsl.2010.06.029

Parkinson, I.J., Arculus, R.J., 1999. The redox state of subduction zones: insights from arc-peridotites. Chem. Geol. 160, 409–423. doi:10.1016/S0009-2541(99)00110-2

Plank, T., Langmuir, C.H., 1998. The chemical composition of subducting sediment and its consequences for the crust and mantle. Chem. Geol. 145, 325–394.

Ranero, C.R., Morgan, J.P., McIntosh, K., Reichert, C., 2003. Bending-related faulting and mantle serpentinization at the Middle America trench. Nature 425, 367–373.

Savov, I.P., Ryan, J.G., D'Antonio, M., Fryer, P., 2007. Shallow slab fluid release across and along the Mariana arc-basin system: Insights from geochemistry of serpentinized peridotites from the Mariana fore arc. J. Geophys. Res. 112, B09205. doi:10.1029/2006JB004749

Scambelluri, M., Tonarini, S., 2012. Boron isotope evidence for shallow fluid transfer across subduction zones by serpentinized mantle. Geology 40, 907–910. doi:10.1130/G33233.1

Schwartz, S., Guillot, S., Reynard, B., Lafay, R., Debret, B., Nicollet, C., Lanari, P., Auzende, A.L., 2013. Pressure–temperature estimates of the lizardite/antigorite transition in high pressure serpentinites. Lithos 178, 197–210. doi:10.1016/j.lithos.2012.11.023

Tatsumi, Y., 1986a. Formation of the volcanic front in subduction zones. Geophys. Res. Lett. 13, 717–720. doi:10.1029/GL013i008p00717

Tatsumi, Y., 1986b. Formation of the volcanic front in subduction zones. Geophys. Res. Lett. 13, 717–720. doi:10.1029/GL013i008p00717

Trommsdorff, V., Sánchez-Vizcaíno, V.L., Gómez-Pugnaire, M.T., Müntener, O., 1998. High pressure breakdown of antigorite to spinifex-textured olivine and orthopyroxene, SE Spain. Contrib. to Mineral. Petrol. 132, 139–148. doi:10.1007/s004100050412

Ulmer, P., Trommsdorff, V., 1995. Serpentine stability to mantle depths and subduction-related magmatism. Science 268, 858–861. doi:10.1126/science.268.5212.858

von Seckendorff, V., O'Neill, H.S.C., 1993. An experimental study of Fe-Mg partitioning between olivine and orthopyroxene at 1173, 1273 and 1423 K and 1.6 GPa. Contrib. to Mineral. Petrol. 113, 196–207. doi:10.1007/BF00283228

Wunder, B., Schreyer, W., 1997. Antigorite: High-pressure stability in the system MgO-SiO2-H2O (MSH). Lithos 41, 213–227. doi:10.1016/S0024-4937(97)82013-0

Zhang, J., Li, B., Utsumi, W., Liebermann, R., 1996. In situ X-ray observations of the coesite-stishovite transition: reversed phase boundary and kinetics. Phys. Chem. Miner. 23, 1–10. doi:10.1007/BF00202987

.

Chapter V - Antigorite phase relations for a natural system up to 11 GPa and 850 °C: Implications for slab related water transfer to the deep mantle

This chapter deals with phase relations for a natural antigorite bulk composition containing iron and alumina at high pressure: between 6.5 and 11 GPa and for temperatures between 400 and 850°C. Here are presented, the products of antigorite breakdown, consisting in assemblages containing the hydrous minerals Mg-sursassite (Mg-S) balangeroite (bal) and the Dense Hydrous Magnesium Silicates (DHMS) phases A and Al-rich phase E. The role of such minerals in transporting H_2O back into the mantle, is exanimated using experimental results and thermodynamic modelling. In particular, our experiments on phase equilibria at high pressure and high temperature for the natural antigorite-serpentinite bulk composition allowed us to constrain hydrous phase stability domains. These data can allow constructing a petrogenetic grid displaying phase stability. We present in this chapter the details concerning the Shreinemakers analysis. Finally, a comparison with simplified chemical systems allows to identify the limitation of computational modelling, given the limited available thermodynamic properties of hydrous minerals suitable for natural environments. In order to avoid repetitions, some of the data and figures will be referred as those in the second article manuscript presented in this thesis, in the next chapter. This publication has been submitted to Contribution to Mineralogy and Petrology after the defense and is intimately related to this chapter.

I The role of post antigorite minerals in deep water transfer

Water is most efficiently transported from the Earth surface into the deep mantle by hydrous minerals in the subducting lithosphere. The serpentinized oceanic lithosphere, and in particular the high-pressure form of serpentine, namely antigorite ($Mg_{48}Si_{34}O_{85}(OH)_{62}$), is considered as a significant water carrier (Fumagalli and Klemme, 2015; Schmidt and Poli, 2014, 1998; Ulmer and Trommsdorff, 1995). Serpentine forms by hydrothermal alteration of peridotite at the ocean floor and contains about 13 weight percent (wt %) of water, which fate depends on the phase diagram of hydrated mantle as well as on the slab gradient (Komabayashi, 2006). In the case of a relatively hot slab path antigorite breakdown releases water in the mantle wedge through a series of dehydration reactions, forming first olivine + enstatite + chlorite + H_2O and then olivine + enstatite + garnet + H_2O (Padrón-Navarta et al., 2013; Ulmer and Trommsdorff, 1995). For a lower temperature slab path, the antigorite to phase A reaction has been long considered to be the path of water survival in the subducting slab. Liu (1987), identified the "water-line" corresponding to the liberation of aqueous fluid by the reaction phase A + enstatite = forsterite + water (inverse here). It is commonly accepted that the fate of water in descending peridotite depends on whether temperatures are low enough (below 660°C) to allow phase A crystallization after antigorite breakdown. Indeed, in the case of a relatively cold slab (such as Honshu subduction zone), antigorite destabilization produces the assemblage phase A + enstatite. On the other hand, in the case of a relatively hot slab (Peru subduction zone for example) antigorite dehydration produces the anhydrous assemblage olivine + enstatite + H_2O, rendering water transfer to greater depth not efficient. Still, up to date, the investigation of antigorite stability is not known at high pressures since most studies have been conducted in simplified systems.

Two lines of evidence indicate that new investigations of the phase stability of antigorite stability are needed. First, recent studies have emphasized the role of aluminum in stabilizing hydrous phases such as phase D and phase H to extreme temperatures and pressures, hence rendering water transfer to the deep mantle possible at most slab conditions (Pamato et al., 2014; Nishi et al., 2014). This shows that phase diagrams established in simplified systems may not be relevant to constrain the fate of water during deep subduction. While phase A barely incorporates any aluminum, it has been shown that phase E incorporates substantial amounts of aluminum (Kawamoto, 1995, 2004), that probably influences greatly its domain of stability. Determination of the P-T stability of post-antigorite phases in a natural system is thus crucial in order to determine the fate of water in subduction zones. Secondly, hydrous ringwoodite containing ~1-2 wt% H_2O has been discovered in a diamond originating from the Transition Zone (Pearson et al., 2014). This unique sample shows that efficient subduction of water is possible to high-pressure beyond the stability field of antigorite.

Here, we report results from experiments on a natural antigorite with the aim of investigating the stability of hydrous minerals (such as phase A, phase E, balangeroite and Mg-sursassite) in order to understand water transfer modality in the deep mantle using realistic composition.

II Experimental procedure

Experiments were conducted using cores drilled in a natural serpentinite from the Iron Mountain, North Cascades, Washington USA. This sample has also been used for the study at 3 GPa presented in Chapter IV. More details about its composition can be found in the section concerning our starting antigoritite sample in Chapter III. The detailed experimental methods and characterization of run products can be found in the next chapter in the methods section of the article manuscript related to this study.

Characterization of mineral assemblages in our samples allowed us to define the total number of mineral phases P=8. We identified antigorite, olivine, enstatite, phase A, phase E, balangeroite, garnet and a fluid phase. We chose to not include brucite minerals nor Mg-sursassite in the analysis, as explained in more details in the section IV.2 of this chapter (brucite) and in the next chapter (Mg-sursassite). These experiments involve dehydration reactions, and the presence of an aqueous phase coexisting with post-antigorite assemblages is confirmed by running mass balance calculations. This will also be discussed in more details in the following paragraphs.

Before going in further details with the phase assemblages and their significance regarding water transfer, we will present the theory of the Shreinemakers' analysis and explain how we used it to better understand phase equilibria in the complex natural system here investigated.

III Shreinemakers analysis

III.1 The phase rule: generalities

Schreinemakers' method is a geometric approach suitable for establishing the network of univariant reaction curves and invariant points that involve phases in a multicomponent system. Phase equilibria are here examined in a system that we assume closed. As no matter exchange takes place, the only exchange with the system is energy. This geometric method uses the phase rule (derived by Gibbs 1961, see also Spear, 1993)

$$P+F=C+2$$

Where P is the number of *phases*, F the *degree of freedom*, and C the minimum number of *components*. The phases are either solid minerals or fluids present in the considered system. The minimum of components refers to the minimum number of independent chemical constituents (elements oxides, such as SiO_2, Al_2O_3, etc.) that are necessary and sufficient to

describe all phases compositions studied. The degree of freedom is also called *variance* and represents the minimum number of parameters that needs to be fixed to describe the state of the system. In other words, F can be seen as the maximum number of parameters that are allowed to vary without causing any changes on the number of phases (P) or their chemical composition. In the frame of phase equilibria studies, and in particular for geological purposes, these parameters correspond to temperature and pressure. For example, in a Pressure-Temperature (P-T) phase diagram, F refers to a P-T domain where a mineral assemblage containing P phases of a composition that can be described by C components is stable. This domain can be materialized by 3 types of geometries: a point, a line or a bi-dimensional space (field or domain). If varying the pressure and the temperature independently does not imply a phase appearance/disappearance, that means that 2 degrees of freedom are allowed (F=2). In this particular case, the corresponding domain is a bi-dimensional field. If P and T cannot vary independently, i.e., if P is changed, T must change and vice versa, then F=1 and the corresponding domain is a line or univariant curve, separating two fields. F=0 corresponds to an invariant point, where neither P nor T are allowed to vary in order to keep the phases existing at given conditions. For a given system with *n* components, we can deduce the number of phases associated with each geometric feature of phase equilibria diagram using the phase rule.

- at an invariant point F=0, P=n+2
- along a univariant curve F=1, P=n+1
- in a divariant field F=2, P=n

III.2 Definition of the system

III.2.1 Chemistry of the starting sample

By choosing the composition of the starting material for performing phase equilibria experiments, we constrain the chemical system, i.e. the number of components. The system

experimentally investigated during this work is indeed defined by the composition of our starting sample of serpentinite (see chapter III, section I.1.starting materials). Chemical analyses of this sample states that our system is defined by the following components: SiO_2, TiO_2, Al_2O_3, Cr_2O_3, FeO, NiO, MnO, MgO, CaO and H_2O. Nevertheless, an important number of varying parameters adds complexity in establishing a phase diagram. Hence, we chose to simplify the system for more clarity, based on the following assumptions.

- For instance, components such as TiO_2, NiO, MnO and CaO represent a negligible amount in the composition of the starting material (0.03, 0.25, 0.09, 0.02 wt% respectively). Therefore, these elements do not control phase's stability and do not interfere with the phase rule. Hence, the chemical system can be first reduced to the Cr-FMASH system (Cr_2O_3-FeO-MgO-Al_2O_3-SiO_2-H_2O).
- An additional way to simplify the system is to group elements that occupy the same structural site in minerals, without interfering with the phase rule. For example, the substitution MgO ↔ FeO is very commonly observed in ultramafic minerals and favors solid solutions over creating new phases. We can therefore set MgO = MgO+FeO.
- As well, Cr_2O_3 is considered together with Al_2O_3 (leading to Al_2O_3 = Al_2O_3 + Cr_2O_3). As a result, a graphical representation of our system can be established in the quaternary MASH system.

  By assuming that the components MgO, Al_2O_3, SiO_2 and H_2O are enough to describe the composition of minerals existing in our experiments, that brings the number of components to 4 (C=4).

III.2.2 Iron and magnetite in the starting sample

The starting sample is composed to about 95 % by an antigorite matrix scattered by iron oxides (magnetite mostly, chapter III, section I.1.starting materials). For a matter of simplicity and to reduce the number of varying parameters we chose to not consider magnetite and other iron oxides (spinel, chromite) in mineral assemblages observed in both the starting material and the recovered samples. Indeed, as these opaque minerals display zonation and uncomplete equilibration, taking these species in account for mass balance calculation would add complexity to interpretation of modal abundances results. In fact, it is assumed that the oxides from the starting sample are partly consumed through antigorite destabilization. Observations on natural sample from Cerro Del Almirez allowed to propose that antigorite dehydration at low pressure (in the chlorite stability field) is accompanied by magnetite dissolution (Debret et al., 2015), according to the reaction:

Antigorite 1 + magnetite = olivine + antigorite 2 + chlorite + SiO_2 $_{(aq)}$ + H_2O $_{(aq)}$ + O_2 (reaction V.1)

The contribution of these opaque minerals mostly results in increasing the concentration in iron from 2.6 in the antigorite to 7.8 wt% FeO in the bulk (Chapter III, Table III-1). Displacement of the bulk composition towards the magnetite endmember composition can be observed on chemographic representation of phases in the MASH (**Erreur ! Source du renvoi introuvable.**) tetrahedral space and in the MAS triangular projection (**Erreur ! Source du renvoi introuvable.**). Representation of spinel, magnetite and chromite in MAS or MASH systems is based on the projection through Cr_2O_3 and Fe_2O_3. As FeO is reported on the MgO site, the increase of iron content in the bulk due to magnetite results in a virtual increase of the

MgO content in these chemical systems compared to the SiO_2, Al_2O_3 and H_2O pure endmembers.

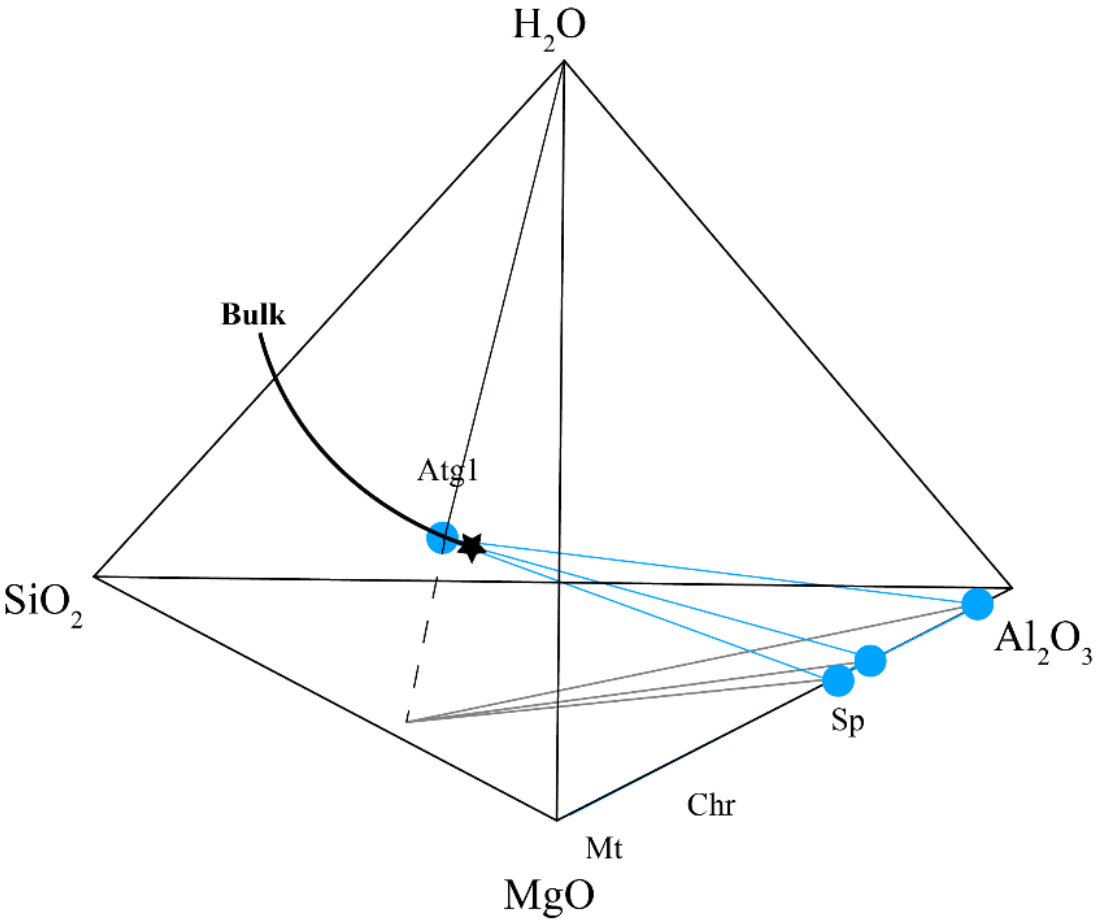

Figure V-1 : Representation of mineral assemblage of the starting sample in the MASH system.

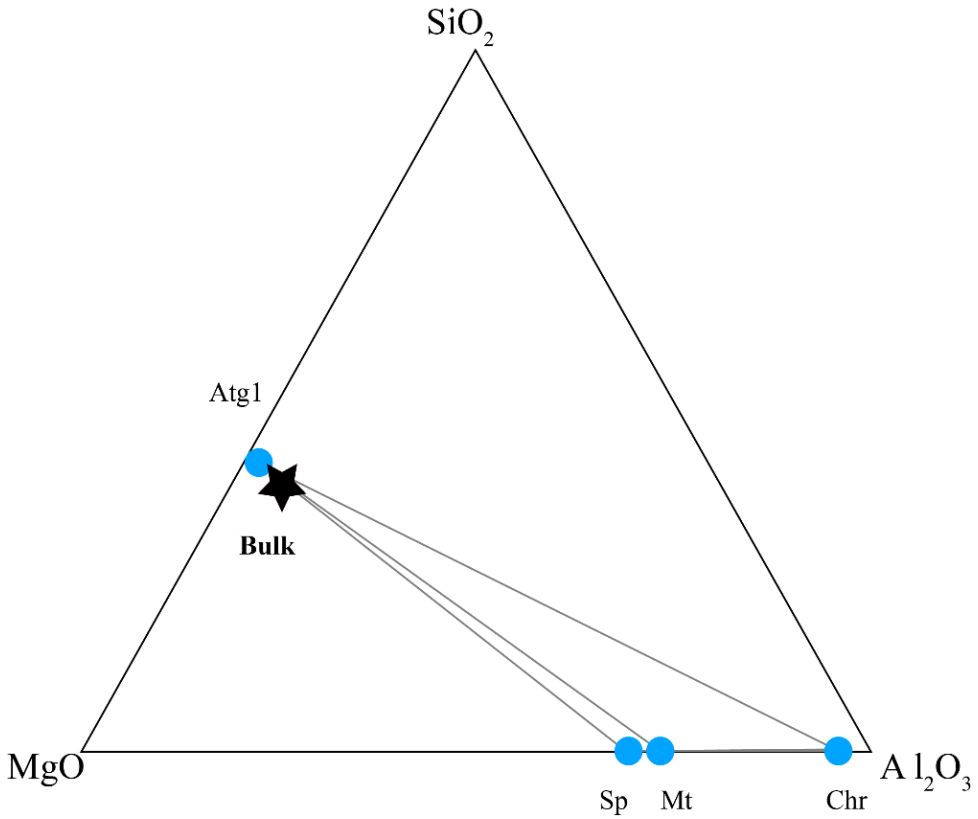

Figure V-2. Representation of mineral assemblage of the starting sample in the MAS system

Nevertheless, this displacement is particularly weak and does not affect significantly the location of the bulk compared to that of antigorite minerals in the starting sample. Therefore, we chose to approach the geometric representation of phase equilibria and the associated reaction by assuming that the bulk location in the MASH space is that of pure antigorite mineral. This is consistent with defining a mineral system free from iron oxides (magnetite, chromite and spinel) for the following geometric analysis. On the opposite, iron bulk displacement associated with iron oxides is considered in running the mass balance calculation on the bulk rock composition rather than the single antigorite minerals. In other words, the significant amount of iron of the serpentinite sample is still considered in the numerical constraints of the system (bulk composition and mass balance calculation).

IV Results

IV.1 Run products versus phase rule

Table V-1. Experimental conditions and mineral assemblages observed.

	P (GPa)	T(°C)	t(h)	phases
M453	6.5	700	8	Ol, En, Grt
M448	8	400	4	Atg
M638	8	550	24	Ol, En, Mg-S
M447	8	650	10	PhE, En, Ol
M473	8	700	26	PhE, En, Bal
M450	8	750	10	PhE, En, Ol
M452	8	800	8	Ol, En, Grt
M451	8	850	8	Ol, En, Grt
M474	8.5	650	25	PhE, En, Bal
M472	8.5	700	25	PhE, En, Ol
M471	9	730	23	PhE, PhA, En
M639	10	550	23	PhE, PhA, En
M467	10	700	28	PhE, PhA, En
M640	11	780	23	Ol, En, Grt

According to the phase rule, in the 4 components system MASH, invariant points allow 6 phases to interact along 5 univariant curves. Since our experiments revealed a total of 8 stable phases (without considering Mg-sursassite most likely related to garnet stability, see discussion in article 2, nor brucite), in a system in which no degeneracy occurs, we should be expecting combinations of 6 phases out of 8 per invariant point, i.e. $\binom{8}{6} = \frac{8!}{6!(8-6)!}$ = 28 invariant points at maximum. As water is present as a fluid phase in excess in our experiments, we chose to project mineral phases in the MASH tetrahedron onto the MAS plan. Therefore, the fluid cannot be represented in the MAS system, which is reduced to 3 components and 7 phases. At each invariant point (21 at maximum, if no degeneracies), 5 phases are involved. Each reaction (5 at maximum – if no degeneracy) should involve 4 phases and separate divariant fields composed

of 3 phases. As it can be observed in the phase assemblage present in our experiments, more than the 3 phases predicted by the phase rule can coexist. In some experiments, we actually observe 4 phases. Indeed, the natural chemical system here investigated, includes FeO and Al_2O_3, and most univariant reactions become divariant and trivariant. In fact, from all the reactions (and invariant points) that could be predicted using the phase rule, only few are stable in a given system. In theory, predicting which reaction is stable or metastable could be done using Gibbs free energy minimization. This is however not achievable in the chemical system here investigated, because the thermodynamic properties of hydrous phases are not available. Despite this limitation in constraining phase reactions in the natural serpentinite composition using a quantitative thermodynamic analysis, comparing observation from our experiments with well constrained reactions in simplified systems such as the MSH from the literature is possible. This comparison represents a first step to understand phase equilibria in a more realistic composition for the subducting hydrated lithosphere.

IV.2 Phase assemblages

The aim of the following section is to establish a first outline of the possible stability fields and associated mineral reactions in the natural hydrous peridotite system corresponding to our experimental conditions (6.5-11 GPa, 400-850°C). This first hint on the phase diagram is based on the geometric analysis, from a qualitative point of view.

The chemical composition of the minerals observed in our experiments is represented on Figure V-3, (as well as on Figure VI-2, in the second article, see chapter VI, with different projection vectors representations). Average composition of phases is plotted for each experiment, in the MASH space (a). It can be noted that compositions are quite consistent from one experiment to the other and that they fall in a restricted area, except for phase E that displays a more variable composition (Frost, 1999). The overall experiments average for each mineral

composition is also reported in the MAS + excess H_2O (b). Atg_1 corresponds to the composition of the starting antigorite while atg_2 represents the average composition of antigorite observed in M448 and M447.

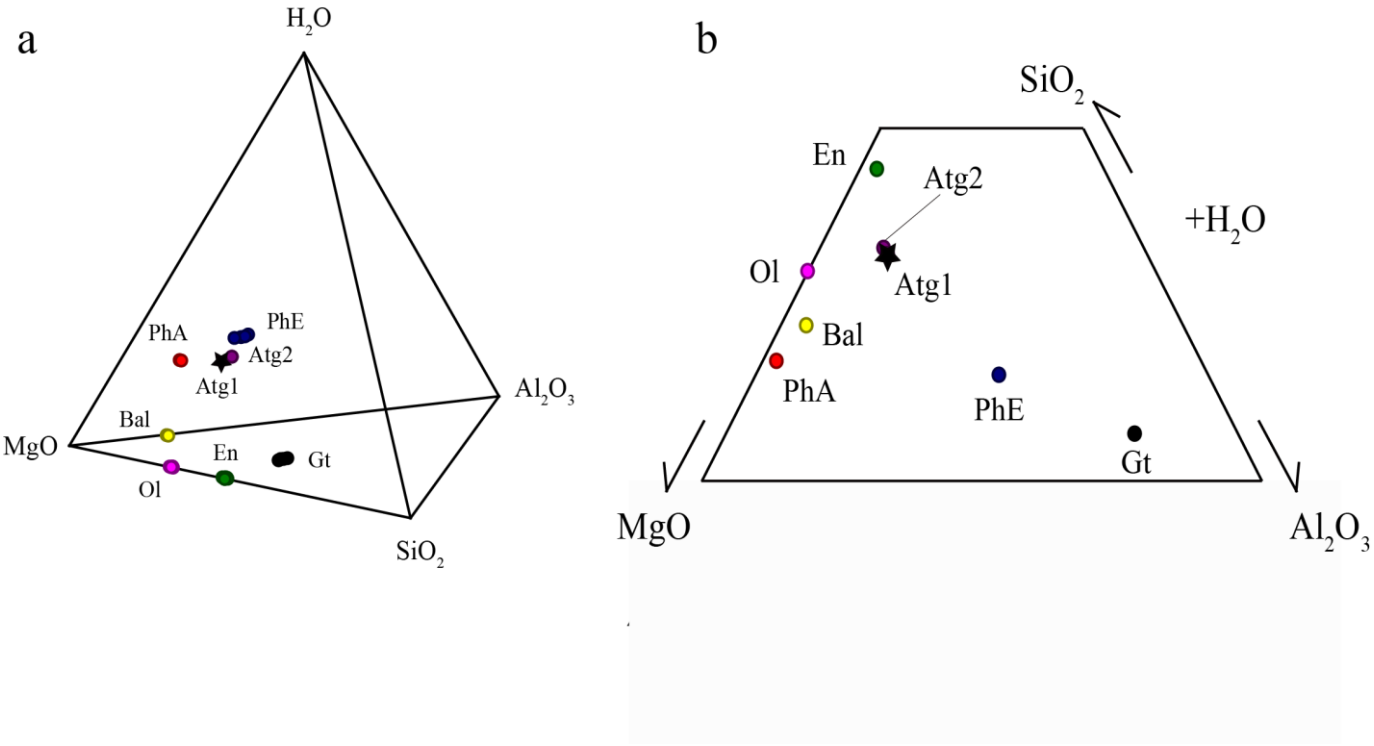

Figure V-3 : Mineral composition represented in the MASH system, and b. in the MAS system with excess water.

Chemical compositions are presented in 3 separate tables in the second article presented in chapter VI (Table VI-3: olivine and enstatite composition – MAS system; Table VI-4: balangeroite and phase A – MSH system; Table VI-5: Mg sursassite, garnet and Al-phase E – MASH system). Description of mineral chemistry and detailed discussion about compositions, can also be found in the same article manuscript. Phase assemblages have been located in the Shreinemakers grid using chemographic representation (Figure V-3). Mineral assemblages from our experiments and those that were established from the Shreinemakers' analysis is

reported in Table V-2. Figures V-4, V-5, V-6 and V-7 show the experimental textures. The distinction between mineral assemblages that were actually observed in the experiments (named A_0 to A_6) and those that were deduced from the phase rule for our system (B_1 to B_5) is made using color symbols versus grey symbols for minerals.

Table V-2. Observed assemblages in the experiments (A_0 to A_6) with associated pressure and temperature conditions. Theoretically predicted assemblages (B_1 to B_5) were established based on the Schreinemakers' analysis

Assemblage	Phases	P (GPa)	T (°C)
A_0	atg	8	400
$A_1(B_2 + B_4)$	atg + ol + en + Al-PhE + H_20	8	650
A_2	en + bal + Al-PhE + H_20 (+Br)	8.5	650
$A_3(A_2 + B_4)$	ol + en + bal + Al-PhE + H_20 (+Br)	8	700
$A_4(B_4 + A_5)$	ol + en + bal + grt + H_20 (+Br)	6.5-8.5	600-650
A_5	ol + en + grt + H_20	8-11	800-850
A_6	en + phA + Al-PhE + H_20 (+Br)	9-10	700-730
B_1	atg + bal + Al-PhE + H_20	-	-
B_2	atg + ol + Al-PhE + H_20	-	-
B_3	atg + phA + Al-PhE + H_20	-	-
B_4	ol + en + Al-PhE + H_20	-	-
B_5	phA + en + grt + H_20	-	-

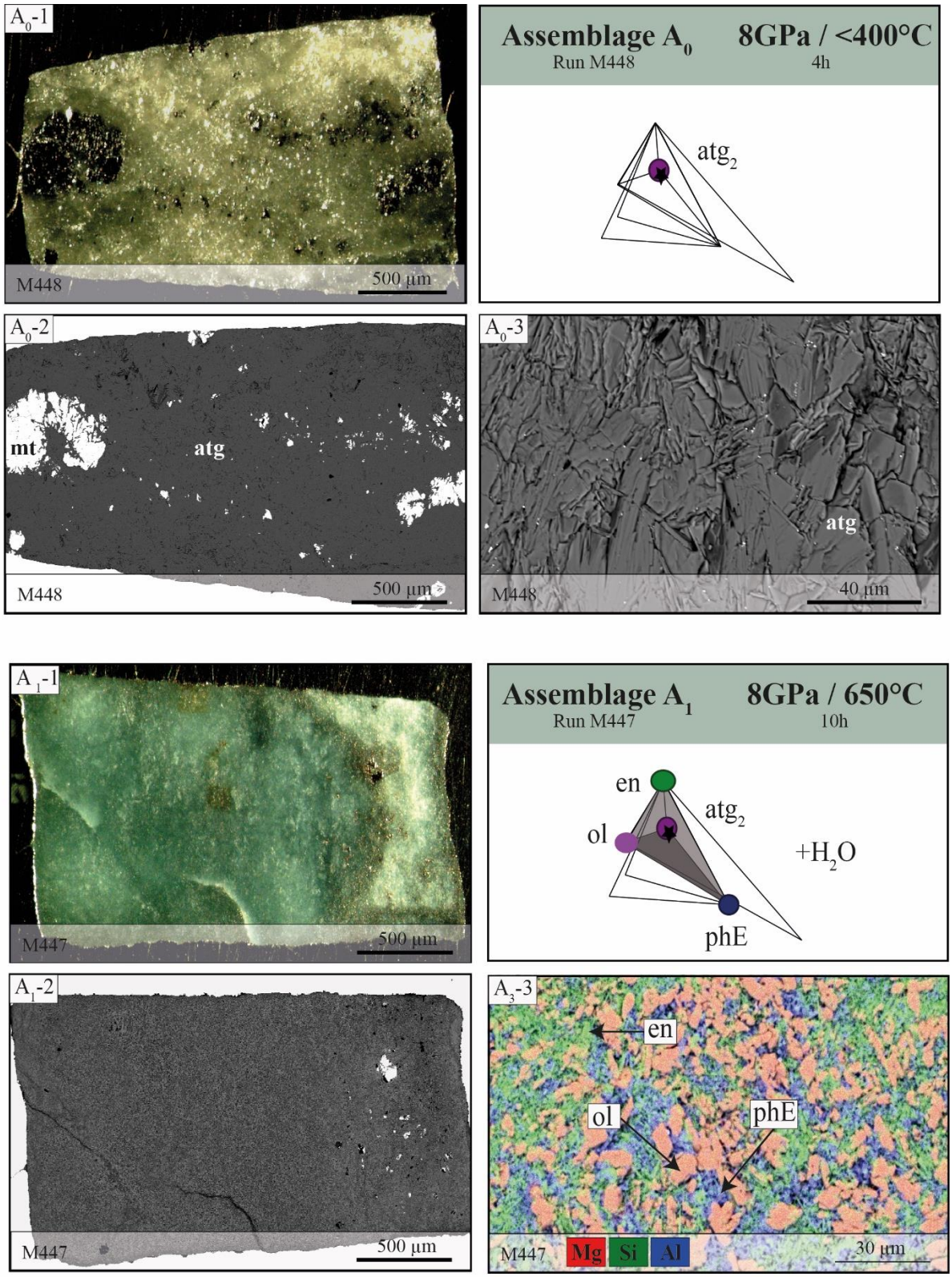

Figure V-4 : Optical microscopy, and back-scattered electron images for mineral assemblage A_0 and A_1.

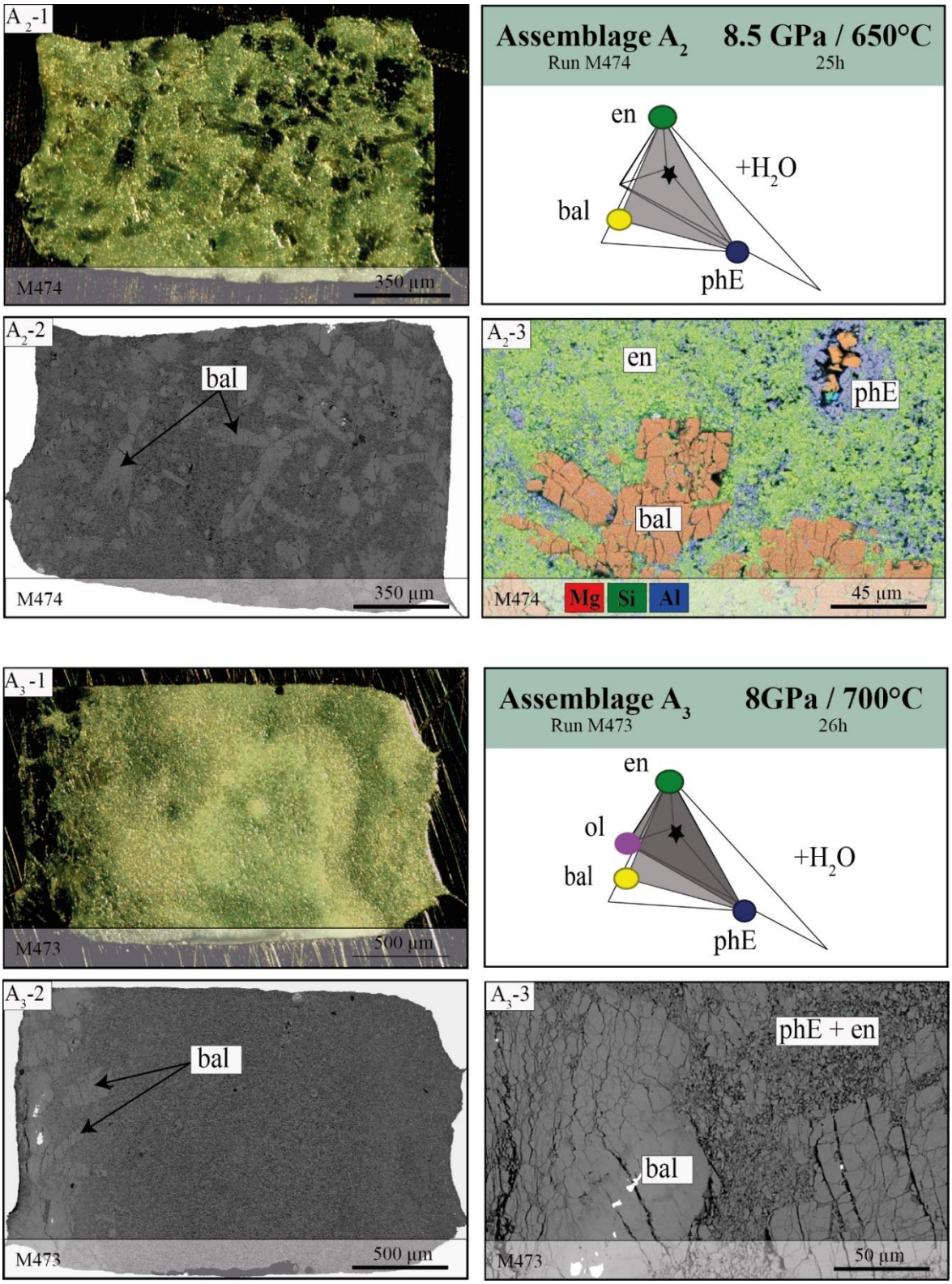

Figure V-5 : Optical microscopy, and back-scattered electron images for mineral assemblage A_2 and A_3.

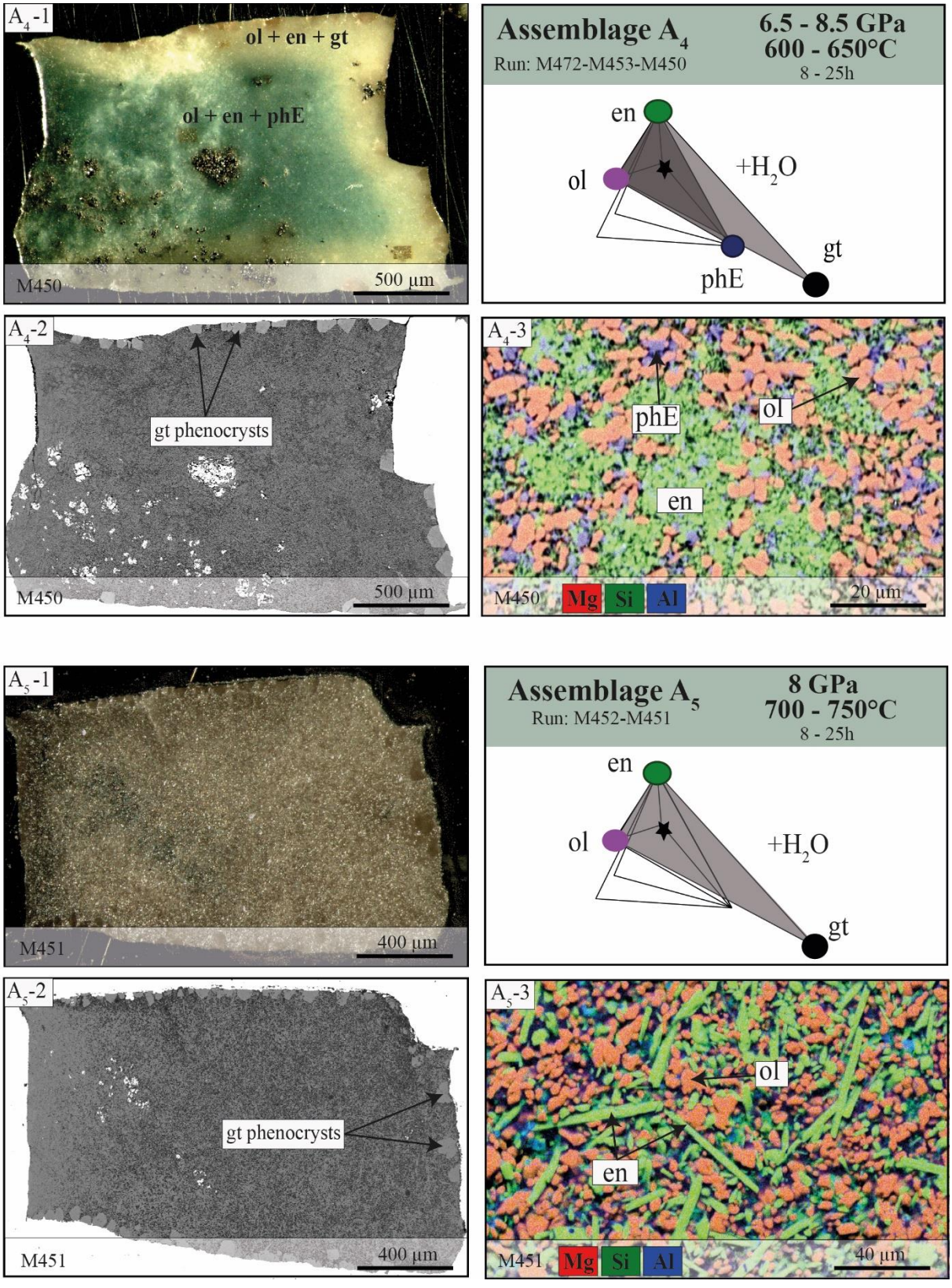

Figure V-6 : Optical microscopy, and back-scattered electron images for mineral assemblage A_4 and A_5.

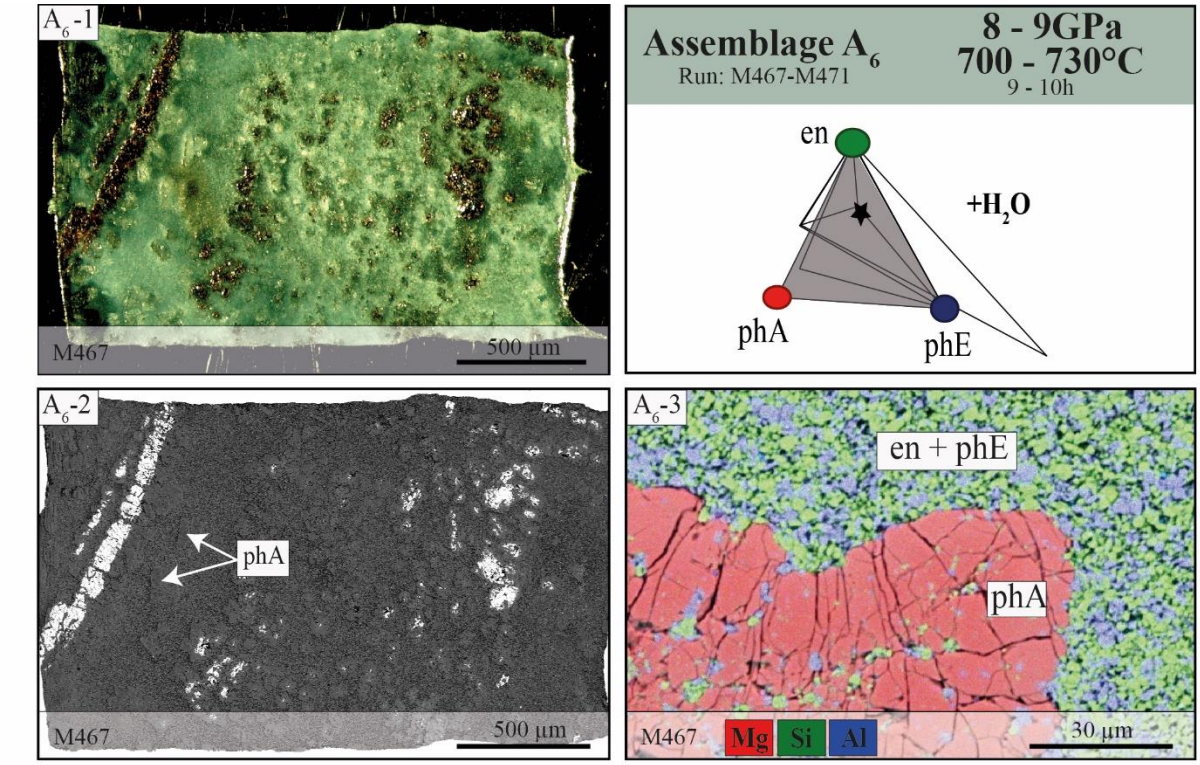

Figure V-7 : Optical microscopy, and back-scattered electron images for mineral assemblage A_6.

IV.3 Dehydration reactions

Few dehydration reactions are highlighted from mineral assemblages observed in our experiments. Except for the run M448 (8 GPa, 400°C) corresponding to unreacted antigorite, all the assemblages contain a free fluid phase (H_2O). The unreacted character of antigorite minerals observed in the experiment M448 is supported by the lack of iron content increase, usually observed for secondary antigorite (it contains 2.76 wt% FeO while the starting antigorite contains 2.62 wt% FeO).

As described earlier, phase assemblages observed in our experiments are not systematically composed of the 3 different mineral species predicted by the phase rule. The occurrence of 4 mineral species assemblages can be explained by divariant reactions due to the

presence of iron. Hence, these 4-phases assemblages allow us to locate reactions, and we can differentiate 2 “sub” assemblages made of 3 phases.

For instance, the first step of antigorite dehydration encountered in our experiments corresponds to the assemblage antigorite + olivine + enstatite + phase E + H_2O (A_1, M447) at 650°C and 8 GPa. This experiment describes the divariant reaction antigorite = olivine + enstatite + phase E + H_2O. As a result, two 3-phases assemblages can be considered (**Erreur ! Source du renvoi introuvable.**): on the low temperature side of the reaction, the assemblage antigorite + olivine + phase E (B_2) and on the low temperature side, the assemblage olivine + enstatite + phase E (B_4). In addition, to be in agreement with the phase rule, separating 4-phases assemblages into two assemblages made of 3 phases is supported by textural observations. Another evidence for the two sub assemblages can be deduced from optical images of M450, with the crystallization of the assemblage olivine + enstatite + phase E (B_4) in the center of the capsule and that of olivine + enstatite + garnet (A_5) at the hotter borders.

At 8.5 GPa and 650°C, antigorite breaks down according to the reaction antigorite = balangeroite + phase E + enstatite (reaction V.2) produced a 3-phases assemblage A_2 (run M474), with very large balangeroite crystals.

With increasing temperature, we observe the assemblage A_3 composed of olivine + enstatite + phase E + balangeroite (M473; 8 GPa and 700°C). This experiment locates the divariant reaction V.3: enstatite + balangeroite = phase E + olivine + H_2O that occurs between the assemblage A_2 and the predicted assemblage olivine + enstatite + phase E (B_4).

The assemblage A_4 composed of olivine + enstatite + phase E + garnet has been observed for 6.5 to 8.5 GPa and for the temperature range of 650-700°C (M472-M450-M453) while at 8 GPa and higher temperatures (800-850°C) we observed the assemblage A_5 composed of the anhydrous minerals olivine + enstatite + garnet (M452-M451-M640). Destabilization of

phase E is here suggested, passing from assemblage A_4 to A_5 by the reaction V.4: phase E = olivine + garnet + H_2O.

At higher pressures of 9 and 10 GPa, and temperatures of 730 and 700°C, the assemblage A_6 containing phase A + phase E + enstatite + H_2O (M467- M471- M639) suggest the occurrence of reaction V.5: olivine + phase E + H_2O = phase A + enstatite.

Table V-3. I, II and III are the invariant points involving phase equilibria in the MASH system, with MgO' = MgO + FeO. Their name corresponds to missing phases in mineral assemblages and reactions associated with each point. Dehydration curves experimentally investigated are reactions 1 to 5 while reactions 6 to 10 are theoretical prediction using Shreinemakers analysis.

Invariant points	
garnet, phase A	I
Balangeroite, garnet	II
antigorite, Balangeroite	III
Reactions	
0.018 antigorite = 0.103 olivine + 0.27 enstatite + 0.05 phase E + H_2O	V.1
0.0214 antigorite = 0.04 Balangeroite + 0.102 phase E + 0.22 enstatite + H2O	V.2
0.81 enstatite + 0.95 Balangeroite = 0.37 Phase E + 4.84 olivine + H2O	V.3
0.41 phase E = 0.48 olivine + 0.0048 garnet+ H_2O	V.4
0.35 Phase A + 0.002 enstatite = 0.92 olivine + 0.46 phase E+ H_2O	V.5
0.033 Antigorite = 0.14 phase A + 0.103 phase E + 0.84 enstatite+ H_2O	V.6
0.032 phase A + 0.016 antigorite = 0.5 Olivine + 0.79 phase E+ H_2O	V.7
0.18 Balangeroite + 0.016 antigorite = 1.02 olivine + 0.14 phase E + H2O	V.8
0.17 Phase A + 0.22 enstatite = 0.79 olivine + 0.0046 garnet + H_2O	V.9
0.76 Phase E = 0.14 phase A + 0.12 enstatite + 0.13 garnet+ H_2O	V.10

In addition to the reactions V.1 to V.5 that we were able to bracket with assemblages A_1 to A_6 observed in our experiments, a Schreinemakers analysis has been constructed to match our observations and provide a more detailed petrogenetic grid. This web for phase equilibria in the natural antigorite system involves 3 connected invariant points of particular interest at

our experimental conditions. Additional assemblages were deduced from the phase rule (B_1 to B_5). They are represented on the petrogenetic grid together with observed assemblages.

The reactions were balanced using the atomic per formula unit data for each mineral, estimated from the average chemical composition obtained via electron probe micro-analyses to insure the consistency of balancing reactions with the definition of phase equilibria in the ternary MAS system, alumina (+ chromium in the same site) appears on the structural formula. The iron content of each mineral also appears on the formula. It was nevertheless reported on the magnesium site for balancing calculations.

IV.4 Mass balance calculations

Mass balance calculations were run using chemical composition of minerals for our chemical system the bulk composition and assuming that the fluid is pure H_2O.

Table V-4. Structural formula of the mineral phases observed in the natural serpentinite system compared to the MSH system.

	This study Natural antigoritite bulk	**MgO-SiO_2-H_2O**
Phase E	$Mg_{1.67}Fe_{0.37}Al_{0.27}Si_{1.21}O_{3.55}(OH)_{2.6}$	$Mg_{2.33}Si_{1.26}O_{3.55}(OH)_{2.6}$
Phase A	$Mg_{6.3}Fe_{0.47}Al_{0.01}Si_{2.09}O_8(OH)_6$	$Mg_7Si_2O_8(OH)_6$
Balangeroite	$Mg_{34.4}Fe_{6.1}Al_{0.3}Si_{16.4}O_{54}$ $(OH)_{40}$	$Mg_{42}Si_{16}O_{54}(OH)_{40}$
Antigorite1	$Mg_{44.6}Fe_{1.7}Al_{1.5}Si_{33.5}O_{85}(OH)_{62}$	$Mg_{48}Si_{34}O_{85}(OH)_{62}$
Antigorite2	$Mg_{44.37}Fe_{1.79}Al_{1.39}Si_{33.71}O_{85}(OH)_{62}$	$Mg_{48}Si_{34}O_{85}(OH)_{62}$
Forsterite	$Mg_{1.88}Fe_{0.12}SiO_4$	Mg_2SiO_4
Enstatite	$Mg_{1.88}Fe_{0.12}Al_{0.02}Si_{1.99}O_6$	$Mg_2Si_2O_6$
Garnet	$Mg_{2.5}Fe_{0.7}Al_{1.7}Si_{3.1}O_{12}$	$Mg_3Al_2Si_3O_{12}$

The approach adopted for mass balance calculations concerning 4-phases assemblages consists in running two calculations on the 3-phases “sub” assemblages. For instance, mass

balance linear regression on the 4-phases assemblage A_1 observed in M447 leads to the following modal abundances:

fluid	en	phE	ol	atg
0.24	0.70	0.34	0.86	-1.15

This approach leads to an over-estimation of the amount of fluid (indeed the bulk rock contains only a maximum of 13 wt% H_2O) and a negative amount of one phase, here antigorite. Indeed, the bulk water content (measured by loss on ignition) is of about 11.40 wt%. Therefore, even if antigorite and phase E were not holding water, the starting sample is not providing as much as 24% of the total mass of the bulk.

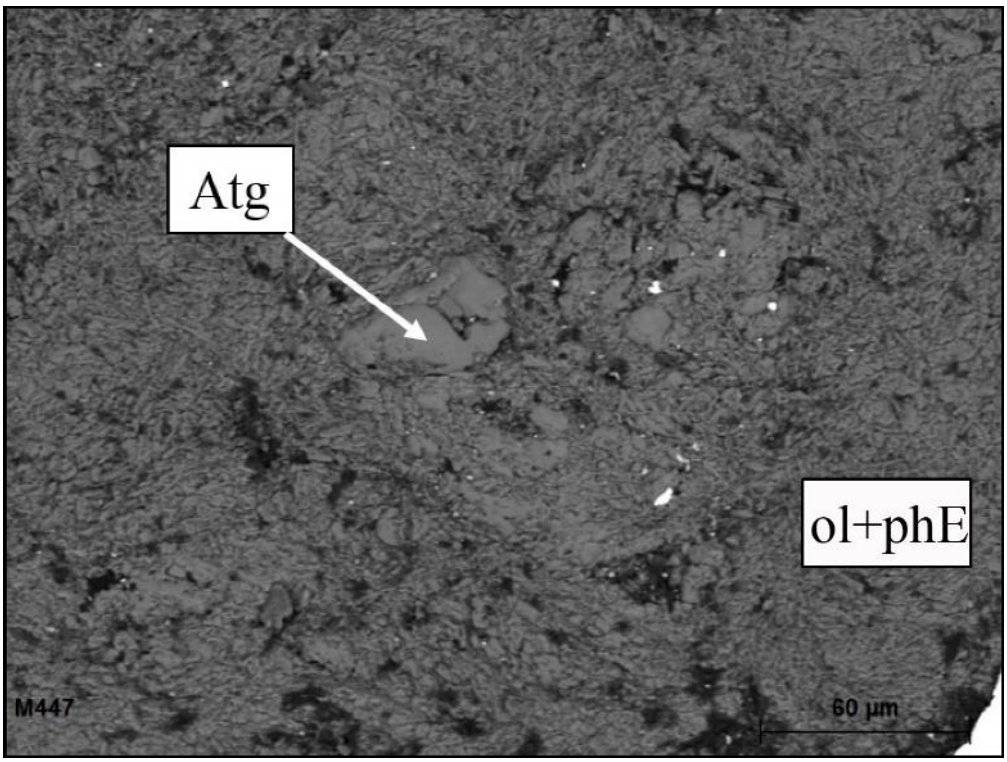

Figure V-8 : Phase assemblage containing antigorite + olivine + phase E (B_2) observed in M447 at 8 GPa and 650°C at the lateral border of the capsule.

Now, when mass balance calculations are conducted separately on the two sub-mineral assemblage, antigorite + olivine + phase E + fluid (assemblage B_2) and olivine + enstatite + phase E + fluid (assemblage B_4), the following mass balance calculations is produced:

B2	fluid	ol	atg	phE
	0.04	0.25	0.35	0.36
B4	fluid	ol	en	phE
	0.09	0.39	0.20	0.32

Based on the extremely low amount of antigorite found in the capsule, it seems reasonable to estimate that the assemblage B_2 composes the sample to 10 % at maximum. The combination of 90 % of B_4 and 10% of B_2 provides more realistic phase proportions than the first one based on 4-phases assemblage:

fluid	ol	en	phE	atg
0.08	0.37	0.18	0.32	0.03

This experiment helps us to locate the divariant reaction antigorite = olivine + enstatite + phase E + H_2O. In particular the low amount of remaining antigorite is an evidence for the high temperature boundary of this domain. The antigorite was observed very close to the capsule border, and analyzed after the first step of polishing. The capsule was only slightly opened by polishing, and no more antigorite has been found once fully opened at the center.

On one hand, the fact that these antigorite minerals were observed in very small amount gives rise to the question about antigorite metastability at these pressure and temperature conditions (Figure V-8). On the other hand, kinetics of antigorite dehydration related to the reaction antigorite = forsterite + "talc-like" phase + H_2O at 4.1 GPa and 530°C (Perrillat et al., 2005) indicates that equilibrium is established after 200 min of heating (Figure V-9**Erreur ! Source du renvoi introuvable.**) which is satisfied by the run duration of 10 hours for this experiment. Moreover, because of the reduced thermal gradient produced by the stepped

furnace (Figure III-5) lateral sides are the hottest part of the capsule. For these reasons, the remaining antigorite cannot be unreacted antigorite associated with colder part of the capsule and belongs to the phase assemblage for such conditions.

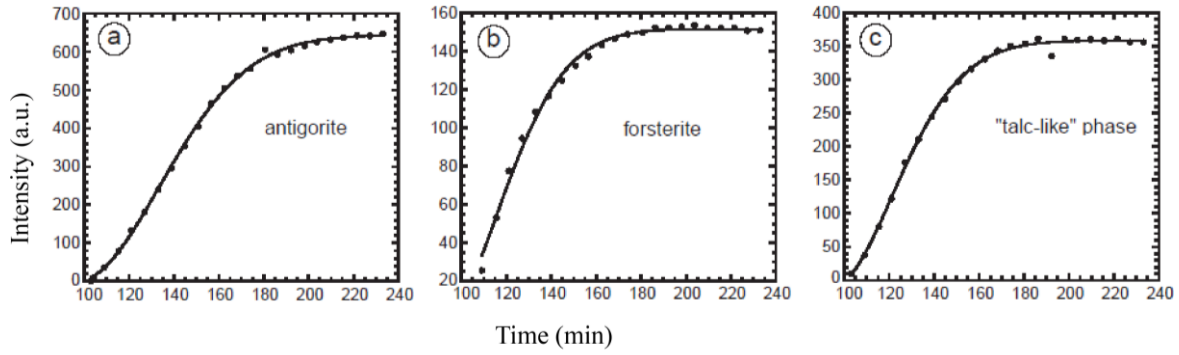

Figure V-9 : Kinetics of antigorite dehydration from Perrillat et al. (2005). (a) shows the destabilization of antigorite, while (b) and (c) show the appearance of the products forsterite and the „talk-like“ phase. The stabilization of arbitrary unit of intensity on the y-axis corresponds to the achievement of reaction equilibrium and occurs at about 200 mins.

The same mass balance calculation procedure has been applied for each experiment. This method allowed us to estimate the modal amount of all the minerals and in particular of the fluid phase present in the experiments. Moreover, we could estimate the amount of structurally bound water associated with each experiment (Table V-5). These results will be presented in more details in section IV of this chapter, when discussing estimations of the water budget.

Table V-5. Modal abundances corresponding to mineral assemblages in our experiments after mass balance calculation. Mineral water budget is expressed as H_2O stored in the hydrous minerals atg (antigorite), PhE (phase E), PhA (phase A) and Bal (balangeroite). Estimation built by balancing water content of minerals (respectively 12.4, 9, 12 and 11 wt% H_2O) with the modal amount of each phase given by the mass balance.

Phase	mt	Fluid	Atg1	Atg2	PhE	PhA	Bal	En	Ol	Gt	
H_2O wt%			12.05	12.00	11.90	11.30	11.10				
Mass balance	**mt**	**Fluid**	**Atg1**	**Atg2**	**PhE**	**PhA**	**Bal**	**En**	**Ol**	**Gt**	**Assemblage H_2O wt%**
Start. Sample	0.05	-	0.95		-	-	-	-	-	-	**11.45**
M453	0.04	0.11	-	-	-	-	-	0.25	0.53	0.07	**0.00**
M448	0.05	-	-	0.95	-	-	-	-	-	-	**11.40**
M447	0.04	0.09	-	0.06	0.17	-	-	0.24	0.41	-	**2.75**
M473	0.02	0.08	-		0.18	-	0.10	0.26	0.36	-	**3.26**
M450	0.03	0.09	-		0.15	-	-	0.26	0.45	0.01	**1.75**
M452	0.04	0.11	-		-	-	-	0.24	0.54	0.07	**0.00**
M451	0.03	0.11	-		-	-	-	0.21	0.57	0.08	**0.00**
M474	0.01	0.04	-		0.15	-	0.45	0.35	-	-	**6.76**
M472	0.02	0.10	-		0.14	-	-	0.23	0.50	0.02	**1.66**
M467	0.00	0.05	-		0.28	0.30	-	0.37	-	-	**6.68**
M471	0.02	0.05	-		0.23	0.30	-	0.40	-	-	**6.07**

Figure V-10 : Qualitative diagram of phase relation in the natural antigorite system (P-T dependency is not respected). Reactions 1 to 10 are detailed in table 5. Mineral assemblages experimentally observed are reported with colourful phases while those predicted from the Schreinemakers' analysis is indicated in grey. The thick black lines corresponds to the reaction curves directly bracketed through our experiments (reactions 1 to 5), while the curves deduced using Shreinemakers' analysis are the thin black lines (reactions 6 to 10).

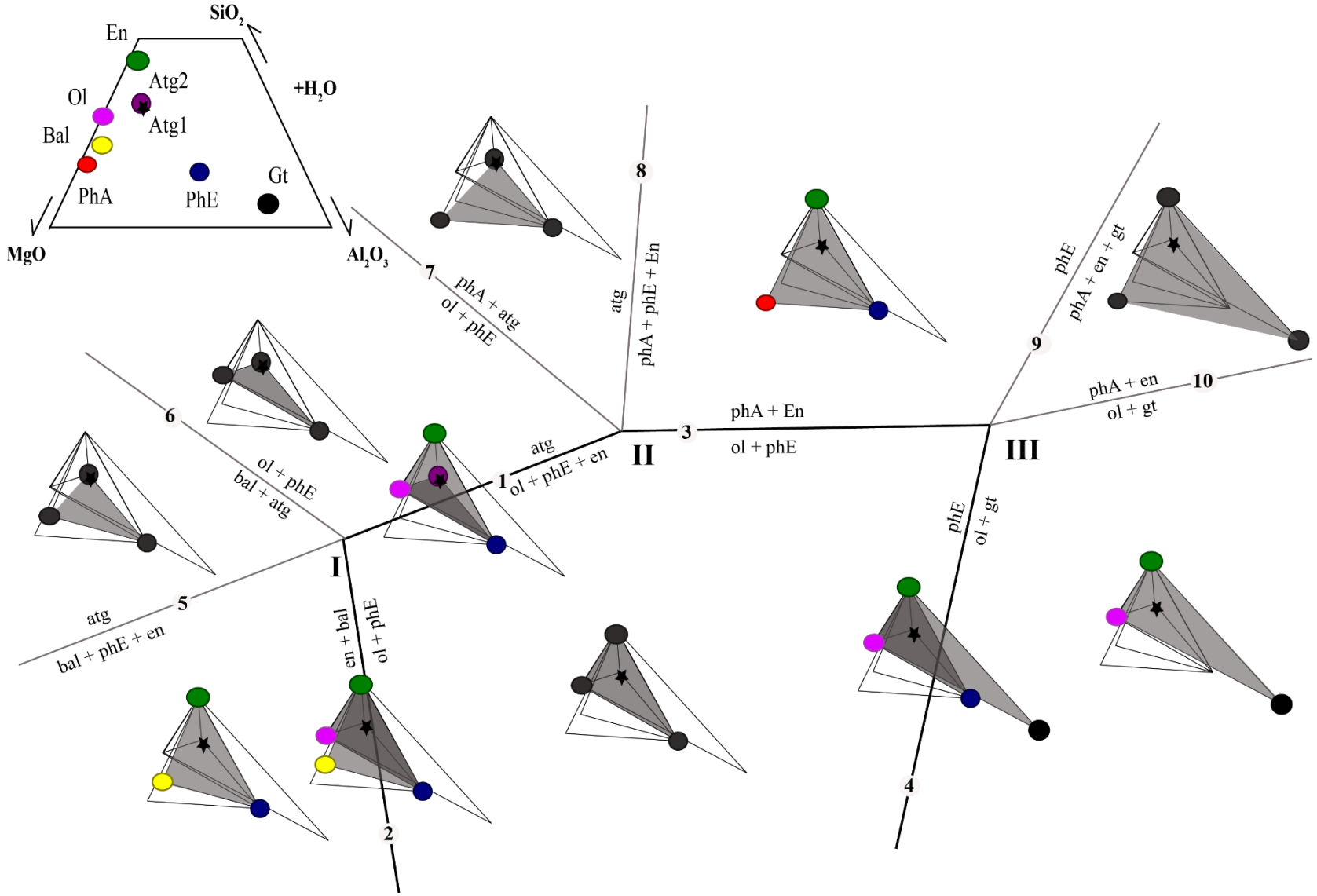

An extended indicative phase diagram (Figure V-10) can be assessed through the Shreinemakers geometric analysis articulated around 3 invariant points of interest for our experimental conditions and the reactions displayed in Table V-5. In order to simplify the reading of this Schreinemakers web (Figure V-10), the divariant reactions have nevertheless been represented as univariant lines. In complex natural systems, invariant points and dehydration curves do not occur as they do in the simplified MSH system, due to solid solutions. In addition, the thermodynamic parameters of phase A and E being unknown for the natural system, the Clapeyron slopes of reactions could not be calculated. Therefore, only the reactions directly observed through mineral assemblages within our experiments can be more precisely located. Comparison of the phase assemblages found in our experiments with predictions in the MSH system calculated with perplex displays many differences, the first one being the absence of course of the aluminous phases, namely garnet and phase E, and secondly the occurrence of different reactions.

IV.5 Phase diagram: comparison with other studies

IV.5.1 About the stabilization of antigorite to higher pressures

We observe in this study that the stability of antigorite is expanded by 3 GPa in pressure and 100°C in temperature (up to 8 GPa and 650°C) compared to previous experimental observations in the MSH system (Figure V-11). Indeed, Komabayashi et al. (2005) proposed that the "water line" (Fo + H_2O = phA + En) would intersect the dehydration curve of antigorite at an invariant point located at 5.1 GPa and 550°C (their Figure 8). Even though antigorite breakdown at HP-LT conditions has not been investigated in their study, it was suggested that antigorite would not remain stable at temperatures higher than 500°C for pressures above 6 GPa (i.e. 180 km depth).

Investigations on antigorite stability using thermodynamic modelling have led to contrasting results. In the MSH system, calculations based on previous experimental data on the join antigorite – phase A at high pressure show both expanded pressure and thermal stabilization of antigorite to about 9 GPa at 500°C and to 750 °C at low pressure (Bose and Ganguly, 1995a). Bose and Navrotsky (1998) later used combined calorimetry, phase equilibria and in situ equation of state data in the MSH system to revise the antigorite stability to lower values of 8 GPa for 500°C, more in agreement with Ulmer and Trommsdorff (1995). Still Perplex models in the MSH emphasize the importance of the bulk modulus value chosen on the calculation of the antigorite stability domain (Hilairet et al., 2006).

According to our results, it appears that Al and Fe- rich antigorite in the natural system is stabilized to higher pressures than previously experimentally reported, since we observe it at 8 GPa and 650°C. In particular, this is in disagreement with the data from Ulmer and Trommsdorff (1995), who reported stability to >700°C below 3 GPa and < 550°C at about 8 GPa for a natural antigorite containing of 1.3 wt % Al_2O_3 and 3.1 wt % FeO. Hence, we propose that the iron content is the factor controlling antigorite stability at high-pressure.

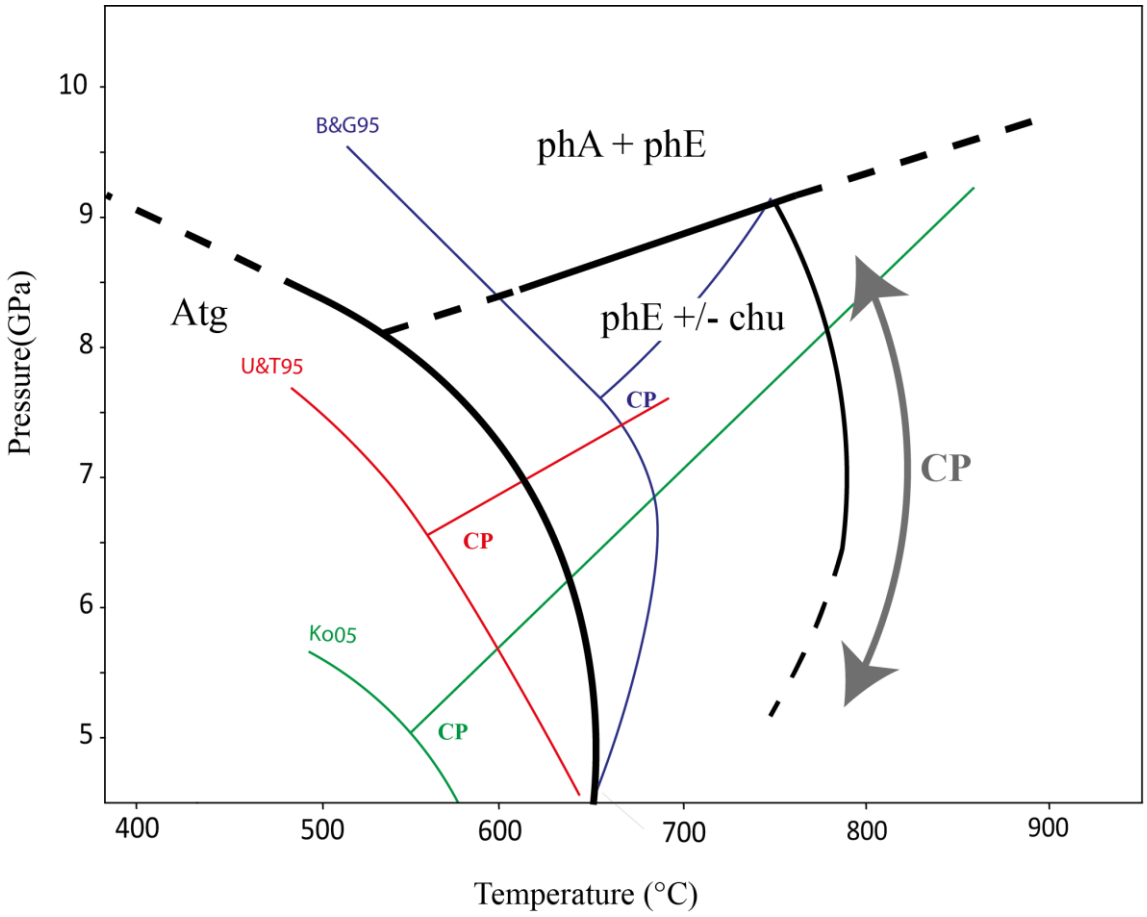

Figure V-11. Summary of location ot the antigorite-phase A join. Stability domains related to hydrous phases for this study are represented with the thick black curves. B&G95: Bose and Ganguly (1995) – thermodynamic calculations in the MSH system; U&T95: Ulmer and Trommdorff (1995) – starting sample derived from natural antigorite with 1.30 Al_2O_3 and 3.1 FeO; Ko95: Komabayashi et al. (2005) – synthetic starting sample, in the MSH system. Locations of the Choke Point (CP) associated with each study is reported on the anhydrous mineral assemblage side of the antigorite-phase A triple junction. The Choke Point location suggested by this study depends on phE dehydration at low pressure.

IV.5.2 About the stabilization of Phase E to lower pressures

The singularity of our results is that phase E appears at lower pressure (from 8 GPa and 650°C) than phase A (9 and 10 GPa, 730 and 700°C) while it has systematically been established in previous investigations that phase A is the DHMS that is stable at low pressure (Frost, 1999) after antigorite dehydration. For instance, phase E has not been observed below 900°C for 9 GPa (Kawamoto et al., 1995), 850°C for 12 GPa (Stalder and Ulmer, 2001) and

below 1110°C for 10 GPa (Luth, 1995). In addition, in our experiments, phase A appears at higher pressure compared to other studies in simplified antigorite bulk composition (Bromiley and Pawley, 2002; Komabayashi et al., 2005; Luth, 1995; Wunder, 1998). On Figure V-12 the location of the invariant point involving phase A, phase E and the anhydrous assemblage olivine + enstatite (+ garnet in the natural system) is represented for different bulk composition. It is worth noting that the invariant point is shifted towards lower temperatures compared to the studies of Irifune et al. (1998) in the FMSH system (825°C for 10.5 GPa) and Luth (1995) in the MSH system (>1000°C, 11 GPa, see Figure V-12).

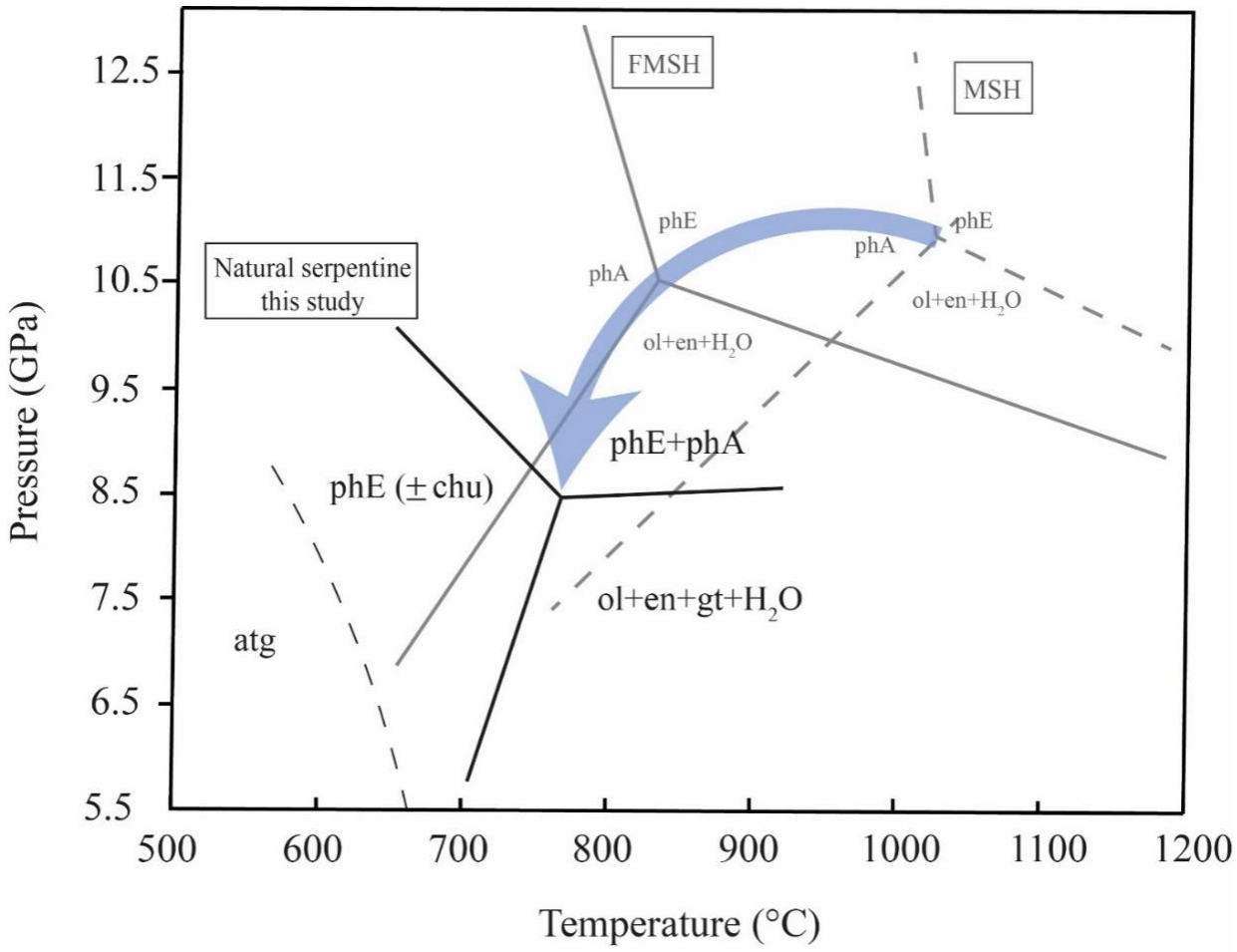

Figure V-12. Comparison of the different location for the invariant point involving phase A, Phase E and anhydrous assemblage with olivine and enstatite. Results from this study are shown by the black lines and stability fields while data associated with other chemical systems are in grey. FMSH: Irifune et al., 1998; MSH Luth 1995. The antigorite destabilization curve is located on the basis of this study experimental data.

Few hypotheses can be considered to explain this exchange of stability fields:

(1) Phase E has been described as a metastable phase, based on a decrease in modal amount with run duration (Luth, 1995). Also, based on its lack of compositional trend as well as disordered crystal structure, Frost (1999) discusses the possibility that phase E may be a quenched phase. In our experiments, phase E appears as very small crystals (below 10 µm) mixed with enstatite crystals of the same texture in a fine and porous matrix. Based

on this texture (which is similar to that after antigorite dehydration in most experiments), we suggest that phase E is in equilibrium with the following assemblages at 8 GPa: olivine + enstatite and 650°C, balangeroite + enstatite + olivine at 700°C, olivine + enstatite + garnet at 750°, enstatite + garnet at 800-850°C and phase A + enstatite at 9-10 GPa and 700-730°C. Instead, we propose that it might have been missed in previous studies due to its very fine grain size.

(2) The distribution of alumina among hydrous phases is also a critical factor for their stability. Al_2O_3 is mainly incorporated into antigorite (1.5 wt %), garnet (15-20 wt %) and phase E (5-9 wt %) while phase A contains less than 0.2 wt % alumina. Therefore, in phase assemblages after antigorite destabilization and before garnet stability phase E is the only hydrous mineral that can host alumina after antigorite destabilization. This agrees with its crystallization in our experiments at lower pressures than phase A, in the garnet free field.

(3) FeO partitioning is an important parameter that can influence the stability field of minerals, an effect known as the chemical pressure (arising from the fact that Fe^{2+} is a much larger ion than Mg^{2+}). Also, iron-loving phases can be stabilized at lower temperatures, and this can counteract the thermal stabilizing effect of alumina. The preferential partitioning of iron into phase E over phase A in our experiments with $Kd_{Fe\text{-}Mg}{}^{phE/PhA}$ of 2.1 to 3.9, and $Kd_{Fe\text{-}Mg}{}^{phE/phA} = (X_{Fe}{}^{phE} \cdot X_{Mg}{}^{phA}) / (X_{Fe}{}^{phA} \cdot X_{Mg}{}^{phE})$, X being the atomic fractions, is therefore favoring a stabilization of phase E at lower pressures at the expense of phase A.

IV.5.3 About the Choke Point definition and location

IV.5.3.a The antigorite-phase A join

The P-T domain intimately related to the join antigorite-phase A (i.e. on the high temperature side of antigorite stability and low-pressure side of phase A stability) was defined

as a “Choke Point” where water transfer to deeper levels via hydrous minerals is impossible. This particular join has been investigated in the MSH, yielding substantial differences with the invariant point occurring at 4.4 GPa at 570°C (Wunder and Schreyer, 1997), 5.5 GPa at 550°C (Komabayashi et al., 2005), 6.5 GPa at 560°C (Ulmer and Trommsdorff, 1995), to 7 GPa at 700°C (Bose and Ganguly, 1995a) (Figure V-12). Phase E is stable continuously from antigorite breakdown, and in coexistence with balangeroite and phase A (this study) to the transition zone (Kawamoto, 2004). Therefore, the domain of stability of hydrous minerals is extended on the HT side of antigorite dehydration curve, suggesting that the Choke Point location would rather depend on the P-T conditions of the antigorite-phase E join in the natural serpentinite system than the antigorite-phase A join in the simplified systems, and therefore could be displaced to higher temperatures.

IV.5.3.b The role of the intermediate-pressure hydrous phases

Recently, the stability of other intermediate-pressure hydrous phases such as the 10Å phase, the hydrous Al-bearing pyroxene (HAPY phase), Mg-sursassite, the 11.5Å and the 23Å phases, have been the subject of a growing number of studies, suggesting their potential importance as water carrier in subduction zones (Bromiley and Pawley, 2002; Cai et al., 2015; Fumagalli et al., 2014, 2001; Gemmi et al., 2011; Omori et al., 2004). Stability domains of these intermediate-pressure hydrous phases overlap the low-pressure stability of phase E observed in this study (5-7.5 GPa, for 650-800°C approximately). Despite the fact that these phases were not observed in the mineral assemblages at our run conditions, the consequences in displacing the Choke Point to higher temperatures are in agreement (Figure V-13). Explanations on the absence of these minerals in our phase assemblages include differences in composition but also starting material as we used natural, ungrounded sample. Indeed, the 10Å phase was described as an important water carrier after antigorite destabilization in the MSH system (Fumagalli et

al., 2001) while the rest of the aluminous hydrous phases listed here were observed in MASH systems with bulk Al contents significantly higher (3.95 to 28 wt % Al, here reported for anhydrous bulk composition) than the one displayed by our starting serpentinite (0.97 Al wt % for the anhydrous bulk).

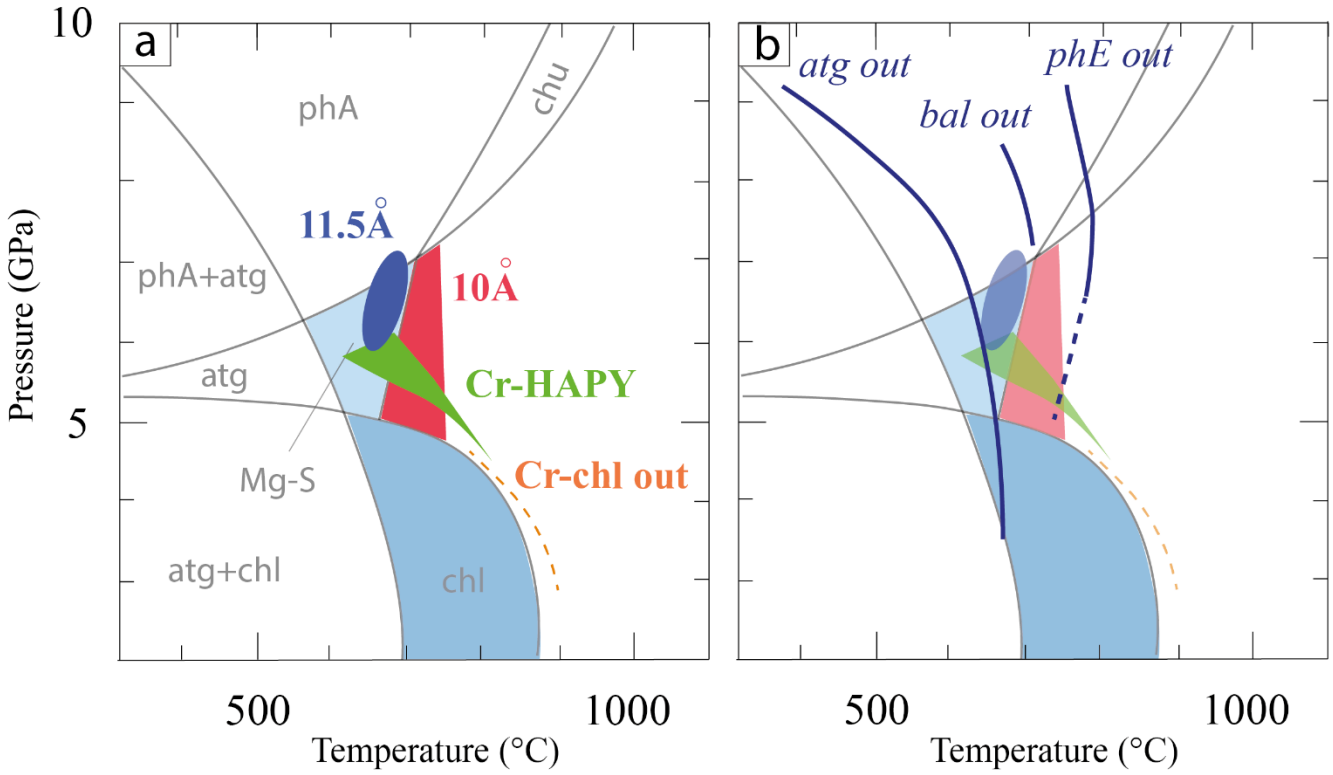

Figure V-13. a. Summary of intermediate-pressure hydrous minerals stability. Cr-HAPY, Cr-chl and 11.5Å data are from Fumagalli et al. (2014), 10 Å from Fumagalli et al. (2001) and Mg-sursassite from Bromiley and Pawley (2002). Stability boundaries involving atg, chl, chu and phase A are from the consistent summary proposed by Iwamori (2004) for the water saturated peridotite system (grey lines). b. Stability boundaries for hydrous phases encountered in our study (antigorite, balangeroite and phase E) are reported.

V The role of hydrous minerals in water recycling in the mantle

V.1 Water budget estimations from the literature

V.1.1 Water budget of the crust

Lawsonite and chlorite are the two mineral phases with the higher water storage capacity within the basaltic crust. They contain 11.2 and 12 wt% H_2O respectively, and their modal amount is estimated to 7 to 15 % for lawsonite and 12 % for chlorite. Their contribution for water transfer via the subducted oceanic crust is therefore not negligible. Nevertheless, because of its higher modal amount in basaltic crust (20 to 60 %) and despite its lower water content (2.1 wt. %), amphibole represents the major water carrier mineral in the MORB component.

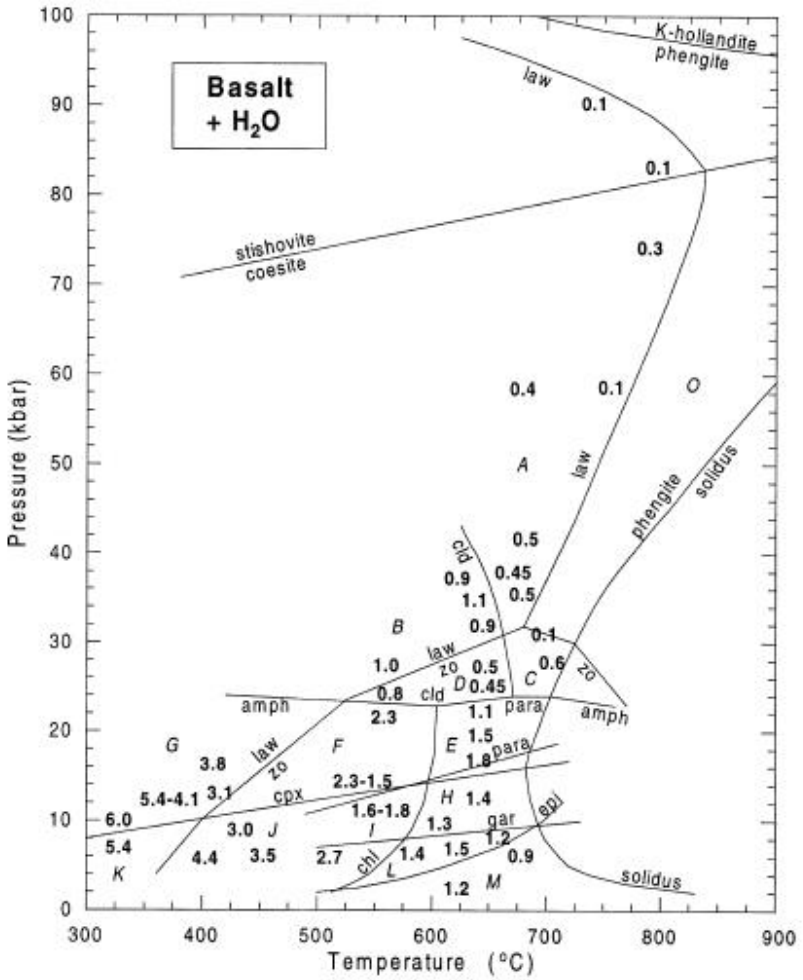

Figure V-14. Phase diagram for H_2O-saturated MORB composition. Numbers indicate the maximum water content stored in hydrous minerals (Schmidt and Poli, 1998).

The detailed analysis of water budget brought in the subduction zone by the basaltic component established in Schmidt and Poli (1998) (Figure V-14) is based on experimentally investigated hydrous mineral stability domains compared to their modal amounts in the bulk and their water contents They established that the total water budget brought in subduction zone by the oceanic crust represents 5 to 6 wt% before any dehydration reaction occurs. It is assumed to decrease to 3 wt% in the low-grade blue schist facies, to 2-2.5 wt. % at intermediate temperature and to 1-1.5 wt. % at higher temperature in the amphibole eclogite facies. At higher pressures, it corresponds to about 1 to 0.5 wt % in the zoisite eclogite facies and 0.5 to 0.12 in the highest pressure metamorphic facies i.e. lawsonite amphibolite (Schmidt and Poli, 1998). The contribution of phengite in the case of a potassium rich basalt can be assumed adding 0.5 wt. % H_2O per 1 wt. % of K_2O entering the system, which corresponds to 8-9 % phengite in the bulk. Figure V-14 represents the bulk water content of the MORB investigated.

V.1.2 Structurally bound water in peridotite mineral assemblages

Because most of hydrous minerals in the crust dehydrate at shallow depth (REF) the fate of structurally bound water in the down going slab is strongly controlled by phase relation in the hydrous peridotite layer of the slab. The nature of phase assemblage depends on the chemical composition of the peridotite and also on the thermal path followed by the subducting lithosphere. In particular, these two crucial parameters control the amount of water than can survive while the slab is sinking into the mantle.

As it has been discussed in the previous chapters of this thesis, one can define at given pressure and temperature conditions a Choke Point. This point is of particular interest in the frame of water transportation in the mantle: any rock equilibrated at higher temperature consists in an assemblage of nominally anhydrous minerals. As a consequence, a slab that would enter this area, would not carry anymore hydrous phases and would not allow water transfer at greater

depths in the mantle. This notion was first introduced by Kawamoto (1996) and describes the domain after antigorite high temperature destabilization at about 5-6 GPa and 550-600°C and before the low-pressure stability of the phase A. Locating precisely this domain is therefore of crucial interest. This point has later been bracketed in few experimental studies and remains in the MSH stystem related to the position of the antigorite-phase A join. On the other hand, in more complex systems, other intermediate pressure hydrous phases are involved (Chapter II-II.3). Stability domains for most relevant hydrous phases in the range of the PT conditions investigated in this study are shown in Figure V-15.

In the MSH system, the stability of hydrous phases forming after antigorite destabilization has been well constrained through the description of dense hydrous magnesium silicates, also known as the alphabet phases A, E, B, super hydrous B, D and H (Kanzaki, 1991; Kudoh et al., 1993; Liu, 1987; Nishi et al., 2014; Ohtani et al., 1995, 1997; Ringwood and Major, 1967; Yamamoto and Akimoto, 1974) , the 10Å phase, chondrodite and clinohumite (Yamamoto and Akimoto, 1977). The 10Å phase does not appear in this diagram because its stability field is particularly restricted and actually correspond to the precise Choke Point location (Fumagalli et al., 2001) and overlaps the stability domain of Mg-sursassite, existing in aluminum-rich compositions.

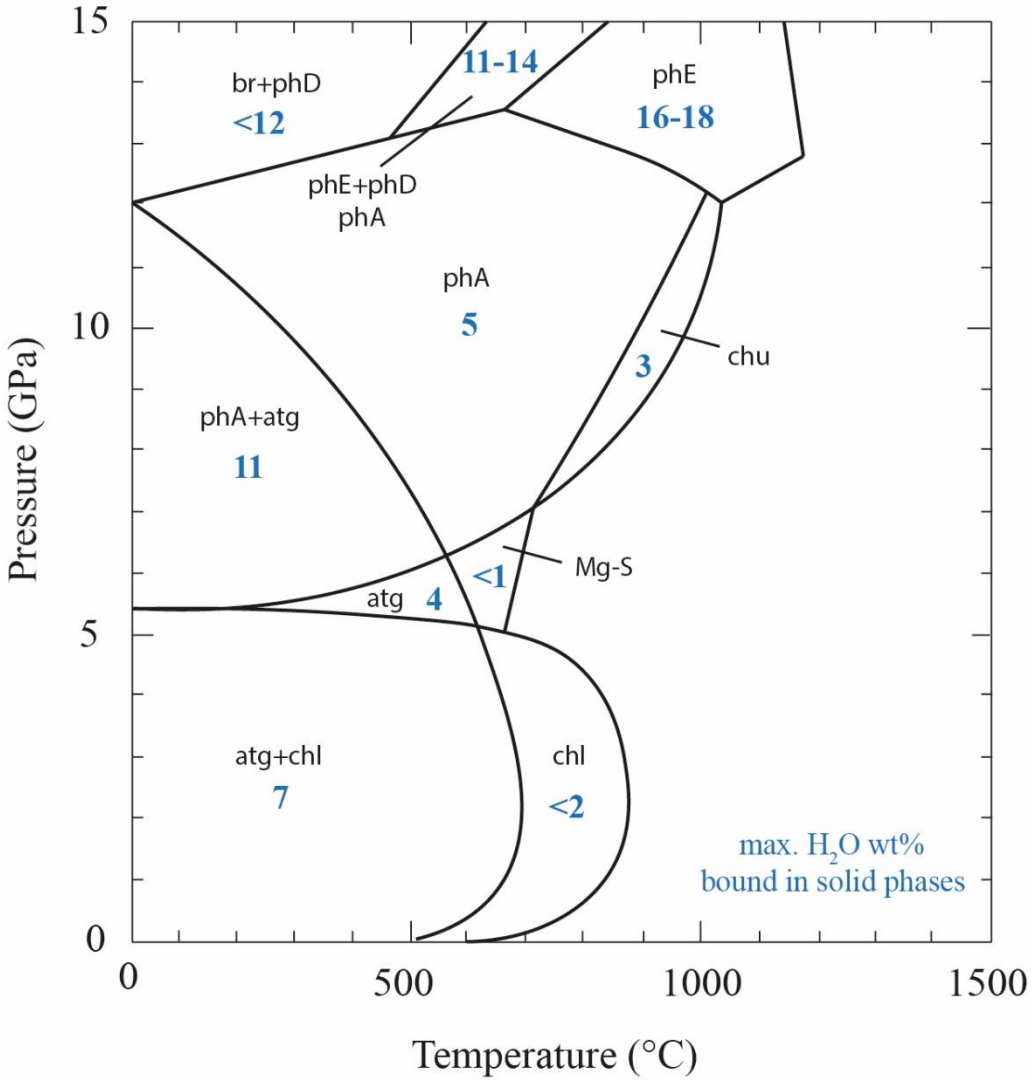

Figure V-15. Simplified phase diagram of the H_2O saturated peridotite rocks for the MSH system, modified after Iwamori 2004. Numbers reported in blue correspond to the maximum value of water storage in hydrous mineral assemblages.

Few studies have more recently brought up the interest of constraining hydrous phases stability in the MASH system. The addition of aluminum in to the MSH system is not only changing the nature of mineral assemblages crystallizing in the hydrous peridotite composition but expands their thermal stability. For instance, Al-rich chlorite plays an important role in water storage in the MASH system: it persists to about 150-200°C beyond antigorite breakdown below 5 GPa (Fumagalli and Poli, 2005; Pawley, 2003; Ulmer and Trommsdorff, 1995) to 6

GPa (Bromiley and Pawley, 2002). Moreover, like antigorite, chlorite displays a high H_2O storage capacity with about 13 wt% water hold in its structure. From a mass balance calculation based on the hypothesis of about 4 wt% Al_2O_3 in a fertile peridotite, Luth (2003) inferred that chlorite-bearing assemblage could provide up to 2.8 wt. % H_2O. Estimation from Iwamori (2004) and Schmidt and Poli (1998) provide a slightly decreased water budget associated to chlorite with 2.1 wt. % H_2O. An additional hydrous phase, Mg-sursassite specific to the MASH system has also been observed after the high-pressure destabilization of chlorite. As it is represented on Figure V-16, a displacement to higher temperature of the Choke Point due to Mg-sursassite could be considered. It should be noted that the high temperature stability of Mg-sursassite proposed in the pure endmember (Fockenberg, 1998) might not be as relevant as that one presented for more realistic peridotite assemblage compositions (Bromiley and Pawley, 2002). In addition, Mg-sursassite-bearing assemblages represent a maximum water content significantly smaller than chlorite, antigorite or phase A-bearing assemblages with only 0.4 to 0.7 wt. % H_2O. Hence, Iwamori (2004) suggested the location of the Choke Point to be at 6.2 GPa and 550°C.

In more complex systems, such as the NCFMASH (Fumagalli and Poli, 2005, 1999), the 10Å phase stability field slightly extends to higher temperatures compared to that of Mg-Sursassite (Bromiley and Pawley, 2002). Mineral assemblages containing the 10Å phase are expected to provide about 0.8 wt.% H_2O (Fumagalli and Poli, 1999), which is similar to the water budget brought by Mg-sursassite-bearing assemblages.

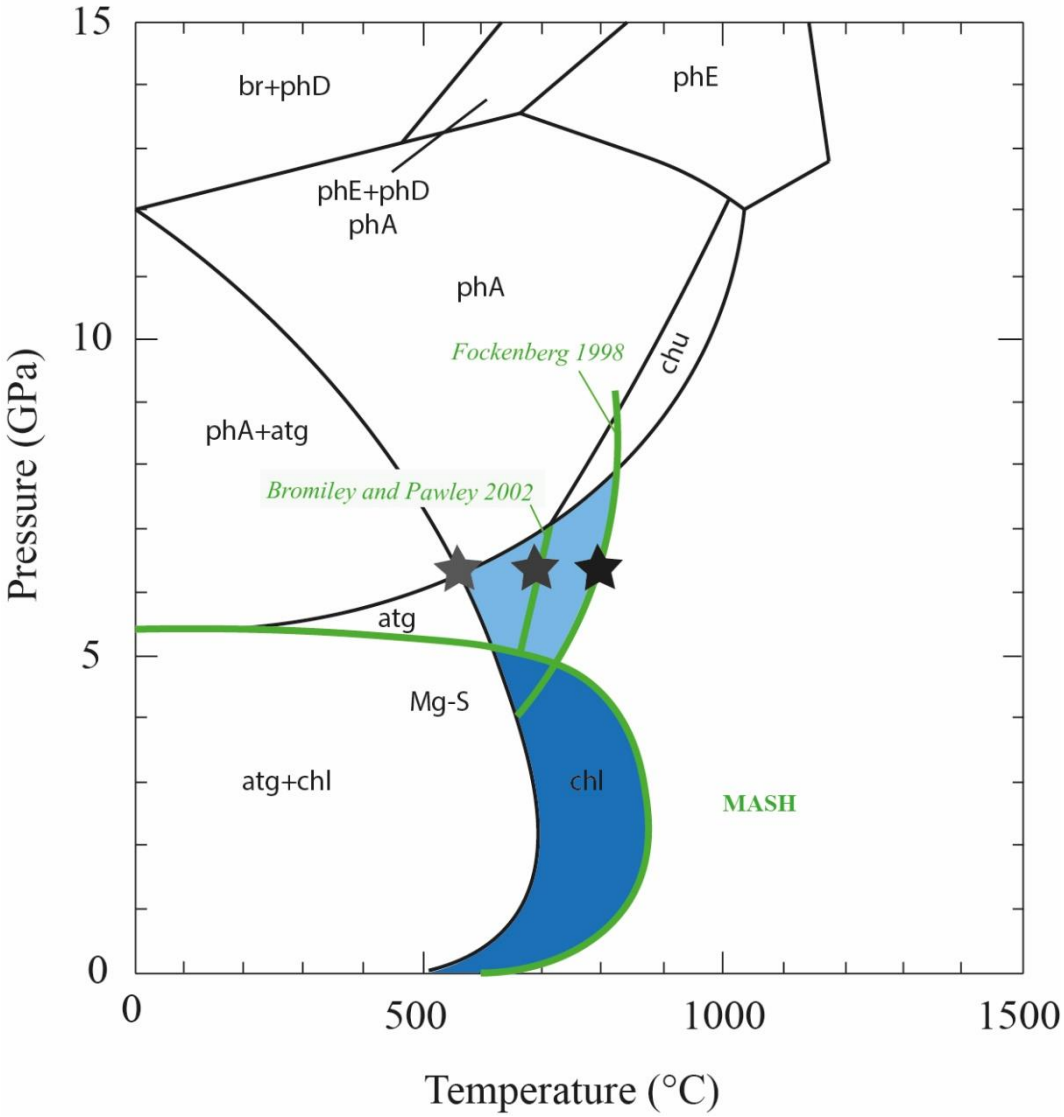

Figure V-16. Simplified phase diagram of the H_2O saturated peridotite rocks for the MASH system, modified after Iwamori 2004. The addition of chlorite and Mg-sursassite creates new domains (respectively in dark and light blue) of potential water reservoirs compared to the MSH system. This leads to a displacement of the Choke Point to higher temperature.

More recently, the experimental investigation in the Cr-MASH conducted by Fumagalli et al. (2014), confirmed the existence of the hydrous Al-bearing pyroxene (phase HAPY – 7 wt% H_2O) in the precise location of the Choke Point area. This hydrous mineral has first been discovered at 5.4 GPa and 720°C in the MASH (Gemmi et al., 2011). Likewise, a new hydrous phase, the 11.5Å (14 to 15 wt% H_2O) was encountered on the same region, at slightly higher

pressure (Figure V-16). Despite their restricted stability fields, these two hydrates are candidates for H_2O storage in the mantle and can play a pivotal role in water transfer to the deep mantle, because of their high water content and the particular location of their stability domains. Indeed, they can allow the transfer of water beyond chlorite high pressure destabilization to phase A. For instance, phase HAPY-bearing assemblages are expected to allow conservation of about 2.6 wt% H_2O after chlorite destabilization. While this hypothesis is built upon modal abundances of the HAPY phase retrieved by mass balance calculation on its chemistry, such information is not available for the 11. 5Å phase. It is worth noting that in this chemical system, Cr-chlorite is stabilized to slightly higher conditions.

V.2 Water transfer associated with phase assemblages of this study

V.2.1 Nature of the fluid phase

At our run conditions, the fluid phase consists in an aqueous fluid, in coexistence with minerals (Hermann et al., 2006). Moreover, it is more likely that the fluid phase is not pure H_2O but that it contains some dissolved MgO and SiO_2. Assessing the composition of the fluid phase in water-saturated experiments is challenging. Indeed, at high pressure, an aqueous fluid phase is not quenchable into one phase but rather occurs as a mixture of quenched crystals, glass and almost pure water (Schneider and Eggler, 1986). It has nevertheless been estimated using different experimental methods. For example, aqueous fluid in the MSH has been trapped using diamond aggregates and analyzed (Stalder et al., 2001), it has been approached via the study of run product phase equilibrium in the Na_2O-Al_2O_3-SiO_2-H_2O (Mysen and Wheeler, 2000), or determined chemographically in the MSH system (Mibe et al., 2002). As a result, it seems undeniable that both silicate component solubility and Mg/Si ratio increases with pressure (in the MSH system). Consistency in the proposed values for silicate component dissolved in the fluid as a function of pressure is nevertheless lacking. For instance, it has been inferred that an

aqueous fluid in coexistence with forsterite and enstatite minerals contains about 30 wt% SiO_2 at 3 GPa, up to 70 wt% at 8 GPa, and that silica content will no more increase at higher pressures. Likewise, Mg/Si ratio in the fluid is found to increase from 1.2 to 1.4 as pressure increases (3 to 8 GPa) and remains constant above 8 GPa (Mibe et al., 2002). Stalder et al. (2001) found a much lower value for silicate component in the aqueous fluid phase, of about 20 wt% at 9 GPa and 1000°C. Komabayashi et al. (2005) retrieved the activity of H_2O in coexistence with high-pressure phases in the MSH system, using calculated dehydration boundaries deduced from their experimental results. In agreement with previous works, they found that the activity of water, a (H_2O), decreases with increasing pressure but their results suggest a water activity of unity at 9 GPa, 0.68 at 12.5 GPa, 0.6 at 13.5 GPa and down to 0.58 above 13.5 GPa. That leads to more than 55 wt% of silicate component dissolved in the fluid phase but only at pressures higher than 12.5 GPa, while it would not dissolve silicates below this pressure. According to the incongruent dissolution behavior of enstatite observed by Kawamoto et al. (2004) at 0.5–5.8 GPa and 800–1000°C, our experiments are close to the boundary where Mg/Si=1 in the fluid. Most of the above studies have been performed in the MSH system and we should expect that the addition of incompatible elements will have a great influence as shown by the comparison of the different behavior of the silicate-H_2O system in the MSH or MASH and MFASH systems (Bali et al., 2008; Férot and Bolfan-Casanova, 2012).

Therefore, in this work no attempt has been made in obtaining the composition of the aqueous phase. Even though establishing the exact composition of the fluid phase present in our experiments is analytically not possible, it is more likely at these conditions that it would not be a pure H_2O phase. Evidence for such fluids can be observed through chemical zoning in experimental samples. For instance, MgO preferential dissolution in the aqueous fluid phase resulting in a chemical zoning and related to separation of the fluid from the solids by interfacial energy forces has been noticed in experiments performed between 5 and 14 GPa and 800 to

1200°C in a system close to the MSH (Stalder and Ulmer, 2001b). Komabaysahi et al. (2005) also observed zoned textures in their high PT experiments, (12 GPa and 1100°C) while it did not occur in their lower PT experiments (7-9 GPa, T<800°C). In our experiments, in the natural composition, brucite crystallization has been observed, only at the edges of the capsule

This chemical zoning is in agreement with migration of a MgO rich fluid phase in these areas. Also, because the amount of brucite is negligible, and in order to be in agreement with the phase rule in our 3 components system, we chose to neglect it in phase equilibria analysis. The fluid composition remains unknown for our experiments; therefore, we chose to consider it as pure H_2O phase, although as established before it might be containing significant amounts of Mg and Si. Given these observations, mineral assemblages stable at run conditions are composed of 3 to 4 phases plus excess H_2O.

V.2.2 Estimation of structurally bound water available in the mineral assemblages

Considering the fluid as pure H_2O, the water budget related to mineral assemblages at given PT conditions could be estimated using mass balance. The same procedure as used in the previous section on the example of the sample M447 has been used (see Table V-5 for modal abundances details). It consists in estimating the modal amount of the 3 mineral phases + the fluid phase present in each sub-assemblage when the experiment is made of 4 minerals. For each hydrous phase occurring in our run products (antigorite, Mg-sursassite, balangeroite, phase A and phase E), the water content was estimated from the stoichiometric calculation based on molar composition of the hydrous phases (12.31, 8, 11.1, 11.3 and 11.9 wt% H_2O respectively) obtained from microprobe data.

The starting sample contains about 12.31 wt % H_2O stored in antigorite mineral (Table V-5). At 8 GPa and for T ~ 400°C (M448- assemblage A_0), antigorite was still stable, and its

chemistry is very close to that of the starting antigorite. No reaction seems to have occurred except for some magnetite dissolution in antigorite. The unreacted character of antigorite is questionable. Indeed, the slight increase of Fe total content in this antigorite (2.76 ± 0.17 wt% FeO) compared to that of the starting material (2.62 ± 0.18 wt% FeO) could be considered as negligible while considering the standard deviation. Moreover, a slight decrease of the microprobe totals seems to indicate minimal dehydration (86.46 ± 0.49 wt% total in #448 compared to the starting 86.64 ± 0.60 wt% total). Therefore, we assume that it contains the same amount of water as the starting material, before reaction, i.e. 12.31 wt% of structurally bound H_2O in the mineral phase antigorite, despite the eventuality that a weak and not quantifiable dehydration could have been initiated.

At higher temperature, (M447-A_1; 8 GPa, 650°C) some minor antigorite was observed coexisting with phase E, enstatite, olivine and a fluid phase. Given the water content of antigorite and phase E of respectively 12.31 and 11.9 wt%, and their modal abundances estimated to 0.06 and 0.17 by mass balance calculation, this mineral assemblage allows the storage of 2.77 wt% H_2O, structurally bound in the solid phases. The associated fluid phase is then assumed to represent 9 wt% of the bulk charge, and to be pure H_2O. The same procedure has been used for the rest of the experiments, considering 11.3 wt% water stored in phase A and 11.10 wt% in balangeroite. With increasing temperature, a gradual decrease of water stored in mineral phases is accompanied by an increase of the fluid phase modal amount. This process occurs with distinct efficiency at low pressure (≤ 8.5 GPa) or high pressure (between 8.5 and 10 GPa). On the low-pressure domain, after antigorite destabilization, between 650 and 700°C, water structurally bound in mineral phases (balangeroite and phase E) decreases down to 6.76 - 3.26 wt %, while the fluid phase reaches 8 %. With increasing temperature, dehydration of balangeroite leads to 1.75 - 2.77 wt % H_2O, carried by phase E only, and beyond 750-800°C, all the structurally bound water is expelled from the minerals phases: the (nominally) anhydrous

mineral assemblage ol + en + grt coexists with 11% of the bulk as a fluid phase. Compared to the 11.4 wt% of water contained in the bulk starting sample (considering also magnetite minerals) and the calculation approximations, this is in very good agreement with bulk water preservation within the sample and the low permeability of the capsule. At higher pressure, up to ~ 6.68 wt% water is preserved in minerals, by the phase assemblage phase A + phase E + enstatite displaying a higher water storage capacity than the other assemblages observed. These conditions correspond to about 5 % of fluid coexisting with mineral phases.

Our experimental investigation in the natural serpentinite bulk concludes to different mineral assemblages at the PT conditions of the Choke Point compared to all previous studies. Based on mass balance calculation and hydrous mineral average water content that we could estimate different water budgets for the subducted hydrous peridotite are suggested by our results. First, an important feature that leads to strong modifications in water budget estimations is the stabilization to higher conditions of antigorite. Indeed, we estimated that a non-reacted antigorite assemblage can transfer about 12.31 wt% H_2O, or 11.40 wt% H_2O for the bulk rock. In our system, beyond antigorite breakdown, balangeroite and Al-phase E are coexisting over a limited temperature range of about 100 to 150 °C. Given their respective water contents of 11.1 wt% and 11.90 wt%, this type of mineral assemblage provides storage and potential transfer up to 6.76 wt% H_2O. The stability domain for this assemblage overlaps that of phase A inferred from previous diagrams, which was reported to carry about 5 wt % H_2O. Hence, phase E + balangeroite-bearing assemblages in the natural system is actually describing a reduced amount of water that can be transported to the deep mantle on this particular area, in comparison to other studies. On the other hand, our experiments suggest phase E stabilization to < 800°C, providing the potential water storage and transfer up to 2.77 wt%. Phase E-bearing assemblages were found to overlap the former depicted domain for the 10 Å phase, the HAPY phase and the 11.5 Å phase. Despite the different nature of hydrous minerals composing our

system in this PT area of interest, estimation of water budget is rather consistent with the maximum of 2.6 wt% H_2O brought by the HAPY phase. At higher pressure, we found the assemblage composed of phase A and phase E in coexistence to be stable beyond antigorite breakdown. This assemblage corresponds to a potential water transfer to the deep mantle of about 6.07 to 6.68 wt% H_2O. This is about 2 wt % higher than what was thought to be carried via the subducted water saturated peridotite component. As a result, it could dramatically increase the amount of water dragged down, in particular in the case of relatively cold slabs, such as Honshu subduction zone, after the thermal model from Syracuse et al. 2010. However, such an increase of water storage capacity in phase assemblages is to be considered with caution because this relies on available water from antigorite-bearing assemblage, and a slow dehydration of the primary antigorite into a less hydrous secondary antigorite is to take into consideration.

According to our results in the natural serpentine system, water transfer is enhanced by the continuous stability of highly hydrated minerals antigorite, and phase E + phase A. Moreover, phase E stability is expected to be stable to much higher pressure and temperature. It has actually been observed in the H_2O-saturated KLB-1 between 9 and 16 GPa and for temperatures between 800 and 1400 °C (Kawamoto et al., 1995), and at 14 GPa, 1000°C in the CaO-Al_2O_3 enriched pyrolite composition (L. Martinek, personal communication). Such high conditions for phase E stability in Al_2O_3 and FeO rich compositions and in particular its continuous character promotes the efficiency of water transfer to the deep mantle in considerable amount. Nevertheless, the limitation of possible water transfer according to the relatively low temperature stability for the hydrous phases observed in our chemical system is to be exanimated. A more detailed discussion about such low-T stability fields in comparison to those depicted in the literature and the implications for descending slab water carriage potential is addressed in the second article presented in this thesis manuscript.

VI Conclusions

Our experiments show that in a natural system composition, phase E is stable at lower PT conditions than previously reported and, especially it occurs before phase A, which in turn appears at higher pressures than reported in earlier studies. Therefore, the location of the "water line" as defined by Liu (1987) should be reconsidered. We also observe that antigorite is stabilized to higher pressure and temperature compared to the study of Ulmer and Trommsdorf (1995) and we attribute this difference to the bulk iron content being twice larger in our study (7.8 wt% FeO here vs 3.1 wt%). Here, in the natural system, antigorite stability is extended to 8 GPa and 650 °C. Using the thermal structure of slabs presented in Syracuse et al. (2010), antigorite could persist in intermediate temperature slab (such as the Philippines) down to 240 km depth. This is 90 km deeper than for the synthetic MSH composition, according to the location of the univariant point involving antigorite and phase A as determined in Komabayashi et al. (2005).

Compared to hydrous mineral stability previously reported (Bromiley and Pawley, 2002; Komabayashi et al., 2005; Luth, 1995; Ulmer and Trommsdorff, 1995; Wunder, 1998; Wunder and Schreyer, 1997), only a relatively cold slab (such as Kermadec, Tonga) could allow the reaction of antigorite to phase A to occur and a transfer of water to the deep mantle via DHMS. On the contrary, a hot slab, would cross the antigorite-out curve and release water in the mantle wedge. The recent discovery of hydrous ringwoodite in a diamond originating from the Transition Zone from Juina, Brazil (Pearson et al., 2014) demonstrates that water can be carried until at least 520 km depth by subduction. The subducted character of the related fluids is evidenced by the crustal chemical signature of inclusions (Eu anomalies in Ca-Mg perovskite and majoritic garnet; Harte, 2010) and the occurrence of Ca-Mg-Fe rich carbonates derived from oceanic sediments.

Serpentine dehydration has experimentally been demonstrated to be the cause of subduction deep seismicity (Meade and Jeanloz, 1991; Dobson et al., 2002). Antigorite dehydration is believed to be the cause of double seismic zones (Brudzinski et al., 2007; Omori et al., 2002; Peacock, 2001). Although the direct link between dehydration embrittlement due to serpentine destabilization and subduction deep seismicity is controversial Chernak and Hirth, 2011, 2010; Proctor and Hirth, 2015, Brantut et al., 2012), it remains clear that serpentine dehydration is triggering mechanisms at the onset of deep earthquakes. The displacement of antigorite breakdown to higher P-T conditions than previously reported is therefore in agreement with double seismic zones noted as deep as 180 km beneath northeast Japan and Aleutian for example, as suggested in Komabayashi et al (2005) but even in the case of hotter subduction zones. Omori et al. (2004) introduced the extended dehydration-induced earthquake (EDIE) hypothesis, according to which any dehydration event would potentially trigger earthquake in the slab. It would therefore be possible that seismicity between 200 and 300 km would be related to balangeroite and phase E dehydration.

Chapter VI - The stability of hydrous phases beyond antigorite breakdown for a magnetite-bearing natural serpentinite between 6.5 and 11 GPa

J. MAURICE [1], N. BOLFAN-CASANOVA[1], J.A. PADRÓN-NAVARTA[2], G. MANTHILAKE[1] , T. HAMMOUDA[1], J.M. HENOT[1], D. ANDRAULT[1]

[1] Laboratoire Magmas et Volcans, Campus des Cézeaux , 6 Avenue Blaise Pascal , TSA60026 - CS60026 , 63178 AUBIERE CEDEX France

[2] Géosciences Montpellier, CNRS & Université Montpellier, Place E. Bataillon, 34095 Cedex 5, Montpellier, France

This chapter corresponds to an article manuscript submitted to Contributions to Mineralogy and Petrology. It refers at the study detailled in the previous chapter with emphasis on mineral chemistry and comparison with previously and experimentally determined phase diagrams.

I Abstract

Phase relations for a natural serpentinite containing 5 wt% of magnetite have been investigated using a multi-anvil apparatus between 6.5-11 GPa and 400-850°C. Post antigorite hydrous phase assemblages comprise the Dense Hydrous Magnesium Silicates (DHMSs) phase A (11.3 wt% H_2O) and the aluminous phase E (Al-PhE, 11.9 wt% H_2O). In addition, a ferromagnesian hydrous silicate (11.1 wt% H_2O) identified as balangeroite $(Mg,Fe)_{42}Si_{16}O_{54}(OH)_{40}$, typically described in low pressure natural serpentinite, was found coexisting with Al-PhE between 650 and 700°C at 8 GPa. In the natural antigorite system, phase E stability is extended to lower pressures (8 GPa) than previously reported in simple chemical systems. The reaction Al-phase E = garnet + olivine + H_2O is constrained between 750-800°C between 8 and 11 GPa as the terminal boundary between hydrous mineral assemblages and nominally anhydrous assemblages, hence restricting water transfer into the deep mantle to the coldest slabs. The water storage capacity of the assemblage Al-PhE + enstatite (high-clinoenstatite) + olivine, relevant for realistic hydrated slab composition along a relatively cold temperature path is estimated to be ca. 2 wt% H_2O. Attempts to mass balance run products emphasizes the role of magnetite in phase equilibria, and suggests the importance of ferric iron in the stabilization of hydrous phases such as balangeroite and aluminous phase E.

Keywords: Hydrous phases stability; natural serpentinite; water transfer; subduction.

II **Introduction**

Water is transported from the Earth's surface into the deep mantle by hydrous minerals present in the subducting lithosphere. The serpentinized oceanic lithosphere, and in particular the high-pressure form of serpentine, namely antigorite ($Mg_{48}Si_{34}O_{85}(OH)_{62}$), is considered as a significant water carrier (Ulmer and Trommsdorff 1995; Schmidt and Poli 1998, 2014; Capitani and Mellini 2004; Fumagalli and Klemme 2015). Serpentinites are mainly formed by

hydrothermal alteration of peridotite in the oceanic lithosphere and might contain up to 13 weight percent (wt%) of water, the fate of this water budget during subduction and high pressure metamorphism depends on the water content of the phases in the prograde mineral assemblages as well as on the slab thermal structure (Komabayashi 2006). In the case of a relatively hot slab path antigorite breakdown releases water in the mantle wedge through a series of dehydration reactions, forming first olivine + enstatite + chlorite + H_2O and then olivine + enstatite + garnet + H_2O at higher temperatures (Ulmer and Trommsdorff 1995; Padrón-Navarta et al. 2011, 2013). For cold slab paths, the antigorite to phase A reaction has been long considered to be the unique possibility to retain water in hydrous phases in the subducting slab. Liu (1987) defined the "water-line" corresponding to the liberation of aqueous fluid by the reaction: phase A + enstatite = olivine + H_2O. It is commonly accepted that the fate of water in the subducting hydrated peridotite depends on whenever temperatures are low enough (below 660°C) to allow phase A crystallization after antigorite breakdown (Komabayashi et al. 2005a). Indeed, in the case of a relatively cold slab, such as Honshu or the Marianas subduction zones (Syracuse et al. 2010; van Keken et al. 2011), antigorite breakdown likely results in the assemblage phase A + enstatite. On the other hand, in the case of a relatively hot slab, such as Peru subduction zone (Syracuse et al. 2010) antigorite dehydration produces the nominally anhydrous assemblage olivine + enstatite + H_2O, rendering water transfer to greater depth less efficient (see also Padrón-Navarta and Hermann 2017). Phase relations involving the breakdown of natural antigorite (or natural antigorite mixed with synthetic materials) have been intensively investigated at relatively low pressures, below 7 GPa (Ulmer and Trommsdorff 1995; Wunder and Schreyer 1997; Bromiley and Pawley 2003; Padrón-Navarta et al. 2010; Merkulova et al. 2016; Padrón-Navarta and Hermann 2017). Nevertheless, the investigation of hydrous phase stability beyond antigorite breakdown in a natural system is only poorly constrained at higher pressures since most experimental studies have been conducted in simplified chemical systems

(Yamamoto and Akimoto 1974, 1977; Kawamoto et al. 1995; Luth 1995; Wunder 1998; Stalder and Ulmer 2001; Komabayashi et al. 2005a; Gemmi et al. 2011; Fumagalli et al. 2014; Cai et al. 2015).

Two lines of evidence indicate that new investigations of the phase relations beyond antigorite stability are of special interest. Firstly, recent studies have emphasized the role of aluminum in stabilizing hydrous phases such as phase D and phase H to extreme temperatures and pressures, hence promoting the possibility of water transfer from the hydrated lithosphere to lower mantle conditions (Nishi et al. 2014; Pamato et al. 2014). The stabilization of antigorite at higher temperature has also been related to aluminum substitution, as well as other trivalent cations such as Fe^{3+} (Bromiley and Pawley 2003; Padrón-Navarta et al. 2010, 2013). The role of ferric iron incorporation in hydrous phase assemblages is to be taken into consideration in the framework of phase equilibria, since natural antigorite displays moderate to high $Fe^{3+}/\sum Fe$ ratios (0.48-0.75 Debret et al. 2015) in addition to relatively widespread occurrence of magnetite. The above observations indicate that phase diagrams established in simplified systems might not be suitable to constrain the fate of water during deep subduction. While phase A barely incorporates any aluminum, it has been shown that phase E incorporates substantial amounts of aluminum (Kawamoto et al. 1995; Kawamoto 2004), potentially influencing its domain of stability. Determination of the P-T stability of post-antigorite phases in a natural system is thus crucial in order to better constrain the deep-water cycle in subduction zones. Secondly, hydrous ringwoodite containing ~1.5 wt% H_2O has been discovered in a diamond originating from the Transition Zone (Pearson et al. 2014). This unique sample shows that efficient subduction of water is at least locally possible beyond the stability field of antigorite.

Antigorite exhibits a complex sinusoidal structure due to the inversion in polarity of the tetrahedral sheet over a certain wavelength or polysome (*m*). This periodic parameter has been shown to play a role on the phase stability of antigorite (Wunder et al. 2001). It is likely that it

plays also a role on its crystal chemistry, in particular through the incorporation of trivalent cations such as Al^{3+} and Fe^{3+}. In addition, natural samples of serpentinized oceanic lithosphere have shown the presence of magnetite (Hattori and Guillot 2007; Deschamps et al. 2013; Schwartz et al. 2013). Such complex structure and texture would be difficult to reproduce synthetically. Hence, in order to investigate water transfer under realistic compositions, experiments were conducted in this study on a natural antigorite sample that originally contains magnetite thus allowing to constrain phase equilibria for a composition and redox conditions both representative of the serpentinized oceanic lithosphere.

III **Methods**

III.1 Starting material

Experiments were conducted using a natural serpentinite from the Iron Mountain, North Cascades, Washington USA. It is composed of a matrix of antigorite and magnetite (Fig. 1) which occasionally shows unreacted cores of chromite and minor spinel. Neither olivine nor calcium phases (diopside or tremolite) have been observed in the investigated sample. In order to avoid H_2O and CO_2 absorption by using a grinded material, our starting sample was prepared by drilling a cylindrical core from the rock. Additionally, this has the advantage of preserving a heterogeneous distribution on the modal amount of magnetite (see below), and thus reproducing better natural conditions.

The composition of antigorite $Mg_{2.62}Fe^{2+}_{0.08}Fe^{3+}_{0.02}Al_{0.09}Cr_{0.01}Si_{1.97}O_{6.82}(OH)_{3.65}$ was obtained by means of an electron probe micro-analyzer and its water content (12.05 wt% H_2O) by calculation from its structural formula corresponding to an assumed polysome m = 17 (Capitani and Mellini, 2004). Samples from the same locality (IM3) were investigated by Evans et al. (2012) using Mössbauer spectroscopy. They estimated a $Fe^{3+}/\sum Fe$ ratio of 0.23 for this

sample and the same is assumed in this work. Bulk analyses were performed using Inductively Coupled Plasma Atomic Emission Spectroscopy on 5 distinct batches of about 100 mg, separately grinded, in order to test the homogeneous distribution of magnetite grains within the bulk rock. The average bulk rock composition (BR_1) is reported in Table VI-1, as well as the standard deviation calculated on the 5 analyses. A slightly higher amount of chromium can be noted in BR_1 (0.27 wt% Cr_2O_3) in comparison to antigorite (0.22 wt% Cr_2O_3) indicating the very minor proportion of chromite and associated spinel. Therefore, the ferric and ferrous iron in the bulk rock is mostly controlled by the modal amount of magnetite.

Table VI-1. Average chemical compositions of starting material minerals (EPMA) and standard deviation Bulk Rock (BR1) composition from ICP-AES measurements and Bulk Rock composition calculated for 94.5% antigorite and 5.5% magnetite (BR2).

	Antigorite	Magnetite	BR_1	BR_2
n	17	7	5	-
SiO_2	43.17 (0.51)	-	40.04 (0.30)	40.79
TiO_2	0.03 (0.03)	0.22	0.03 (0.01)	0.04
Al_2O_3	1.66 (0.36)	0.02	1.63 (0.11)	1.57
Cr_2O_3	0.22 (0.08)	1.26	0.27 (0.00)	0.28
FeO_{Total}	2.60 (0.17)	91.32	7.79 (0.48)	7.48
FeO	2.00 (0.13)	30.44	- -	3.57
Fe_2O_3	0.66[(a)] (0.04)	67.65[(b)]	- -	4.35
NiO	0.16 (0.03)	-	0.25 (0.00)	0.15
MnO	0.07 (0.04)	0.12	0.09 (0.00)	0.07
MgO	38.56 (0.41)	0.22	38.94 (0.40)	36.45
CaO	0.02 (0.02)	-	0.02 (0.02)	0.02
Total	86.55 (0.59)	99.93	88.64 (0.39)	87.28
H_2O	12.05 [(c)]	-	11.4[(d)]	11.39 [(e)]
FeO/Fe_2O_3 (wt%)	3.01	0.45		2.87
Cations calculated on the basis of 6.824 equivalent oxygens (polysom *m* =17) for antigorite, 4 oxygens for magnetite.				
Si	1.968	-	1.844	1.891
Ti	-	0.006	0.001	0.001
Al	0.089	-	0.088	0.086
Cr	0.008	0.022	0.010	0.010
Fe^{2+}	0.076	0.980	0.300	0.138
Fe^{3+}	0.023	1.960	-	0.152
Ni	0.006	-	0.010	0.010
Mn	-	-	0.004	0.003
Mg	2.620	0.010	2.673	2.519
Ca	-	-	0.001	0.001
O	6.820	4.000	6.824	6.824
OH	3.647	-	-	-
∑cat.	4.791	2.978	4.931	4.812
X_{MgO}	-	-	0.833 [(f)]	0.911[(g)]
X_{Mg}	0.972	0.010	0.9 [(f)]	0.95 [(g)]

n Number of measurements

[(a)] Fe_2O_3 estimated from $\sum Fe^{3+}/Fe_{total}$ of 0.23 (cf.sample IM3, Evans et al., 2012)

[(b)] Fe_2O_3 estimated from $\sum Fe^{3+}/Fe_{total}$ of 2/3, from Magnetite stoichiometry

[(c)] H_2O content calculated from structural formula

[(d)] H_2O content from loss on ignition

[(e)] H_2O content estimated from modal amount of antigorite in BR

[(f)] $X_{MgO}=MgO/(MgO+FeO_{Total})$; $X_{Mg}=Mg/(Mg+Fe_{Total})$

[(g)] $X_{MgO}=MgO/(MgO+Fe^{2+}O)$; $X_{Mg}=Mg/(Mg+Fe^{2+})$

Mass balance calculation based on total iron content of the bulk and of magnetite and antigorite (with a $Fe^{3+}/\sum Fe$ ratios of 0.23) already suggests that the sample contains up to 5.5 wt% magnetite in average, in agreement with analyses of back-scattered electron images (Figure VI-1). This results in a ratio of FeO/Fe_2O_3 of 2.87 in the bulk rock (BR_2 in Table VI-1). The water content of the bulk (11.40 wt% H_2O) measured by loss on ignition is also in agreement with 5.5 wt. % magnetite (Table VI-1).

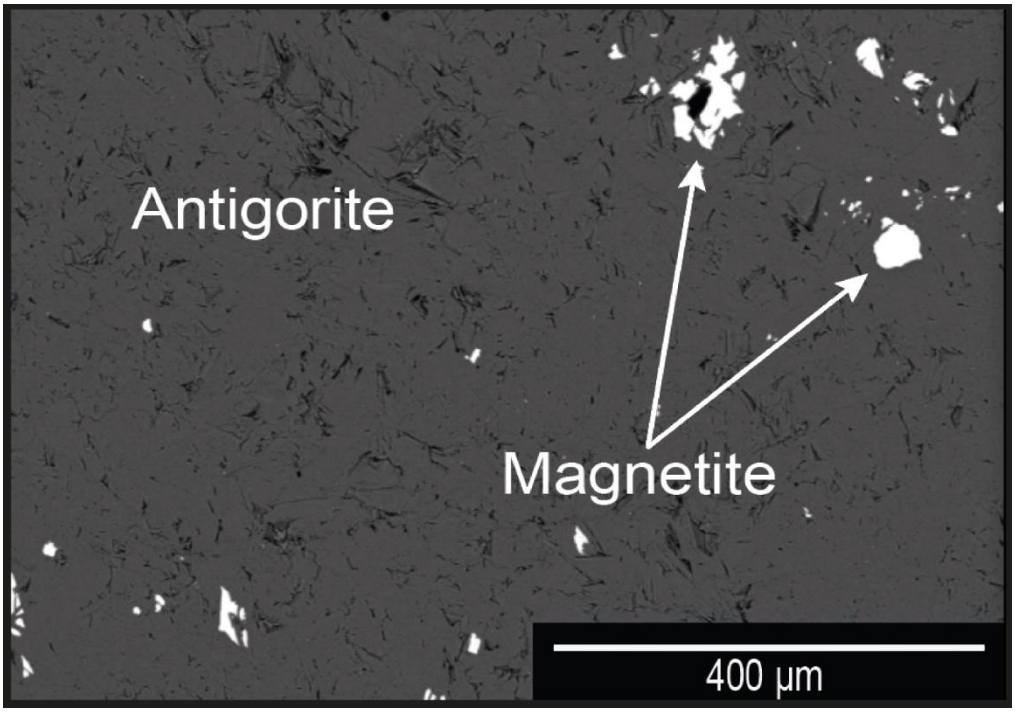

Figure VI-1. Representative back-scattered image of the serpentinite used as starting material, showing the distribution of the magnetite crystals in the antigorite matrix. Magnetite modal amount is estimated to be about 5.5 wt. % in the starting sample (c.f. Bulk Rock composition BR_2 in Table VI-1)

III.2 Experimental procedure

The experiments were performed in a 1500-tons multi-anvil press at Laboratoire Magmas et Volcans (Clermont-Ferrand, France) at pressures between 6.5-11 GPa, for temperatures ranging from 400 to 850°C. The experiments were conducted using the 18/11 assembly configuration, with an 18 mm edge length Cr_2O_3-doped MgO octahedral pressure medium and 11 mm WC

anvil truncation. The calibration of sample pressure was based on Bi I-II and Bi III-V phase transitions at 2.55 and 7.7 GPa (Bean et al. 1986) at room temperature and the quartz to coesite phase transition at 3.2 GPa at 1200°C (Bose and Ganguly 1995) and coesite to stishovite transition at 9 GPa at 1200°C (Zhang et al. 1996). A stepped graphite furnace is used in order to reduce the temperature gradient in the axial direction. Using this configuration the temperature gradient is believed to be less than 40 °C/mm at 1200 °C and less than 11°C/mm at 700°C based on the modelling of the thermal gradient in the 18M assembly using finite element analysis (Hernlund et al. 2006). Sample temperature during the experiments was monitored using a $W_{95}Re_5$–$W_{74}Re_{26}$ (C-type) thermocouple inserted within an alumina sleeve. The thermocouple junction was in contact with the top of the sample capsule. No pressure correction was made for the emf (voltage) of the thermocouple. The serpentinite core was encapsulated in a AuPd capsule of 2.0 mm diameter, no additional water was added. Oxygen fugacity was not controlled during the high-pressure experiments but is expected to be high due to the presence of magnetite in the starting material for the relatively short run duration (< 28 hours).

III.3 Characterization of run products

Identification of run products was obtained using back-scattered images in combination with chemical maps using energy-dispersive X-ray spectroscopy (EDS). Mineral chemistry was measured by means of a Cameca SX100 electron microprobe, using an accelerating voltage of 15 kV, a beam current of 15 nA for olivine and 8 nA for hydrous minerals with a focused beam (1 μm). The counting time was set to 10 seconds for all elements except for Ni (20 s). False color maps were generated based on the relative intensity of Al, Mg and Si peaks, using a Jeol JSM-5910 LV scanning electron microprobe. Additionally, three samples (containing phase A

and phase E - M467 and M471 and containing balangeroite – M474) were hand-polished with colloidal silica suspension to improve the quality of the surface to allow for electron backscattered diffraction (EBSD) analyses. The crystallization of phase A and E and balangeroite was further confirmed by using Raman spectroscopy. Raman spectra were collected at LMV using an InVia confocal Raman micro-spectrometer manufactured by Renishaw and equipped with a 532nm diode laser (200mW output power), a Peltier-cooled CCD detector, a motorized XY stage and a Leica DM 2500M optical microscope. Scattered light was collected by a backscattered geometry. Laser power on the sample was reduced by filters in order to operate at 8 mW in order to avoid thermal damaging. A 100× microscope objective and 20 μm slit aperture were used along with a 2400 grooves/mm grating, which resulted in a spectral resolution better than 1 cm^{-1}. Daily calibration of the spectrometer was performed based on a Si 520.5 cm^{-1} peak. The spectra were recorded from 100 to 1350 cm^{-1} (alumino-silicate network domain) and from 3100 to 3900 cm^{-1} (water domain) using Wire 4.2 software. Acquisition times were set to 5 s with 20 accumulating cycles for balangeroite and 15 s with 8 accumulating cycles for phase A and phase E, for both alumino-silicate and water domains. Single crystal X-ray diffraction of balangeroite was performed on a specimen of approximate dimensions 0.145 mm x 0.184 mm x 0.236 mm, at the Institut de Chimie de Clermont-Ferrand, using a Bruker ApexII single crystal diffractometer with a 4 circles Kappa-CCD (a detail account of this study will be presented elsewhere)

IV **Results**

IV.1 **Phase relations and textures**

Experimental conditions are presented in Table VI-2. Mineral compositions are reported in the simplified systems MgO-SiO_2-H_2O (MSH), MgO-Al_2O_3-SiO_2-H_2O (MASH) and FeO-MgO-SiO_2-H_2O (FMSH) after projection from several exchange vectors in Figure VI-2. The aim of these projections was to reduce the dimensionality of the natural system to effective ternary diagrams that can be then treated by conventional Schreinemaker analyses. For instance, the exchanges of Mg for Fe, Ni and Mn are considered through exchange vectors $Fe_{-1}Mg_1$, $Ni_{-1}Mg_1$ and $Mn_{-2}Mg_1$, modifying the original MgO vertex into MgO+FeO+NiO+MnO. As a consequence, any influence of these exchange vectors on phase relations is not further considered. Although Cr is known to affect phase relations in the ultramafic system (e.g. Fumagalli et al. 2014) it is assumed here as a first approximation that it plays a similar role than Al by treating it through the exchange vector $Cr_{-1}Al_1$ (Figure VI-2).

Table VI-2. Experimental run conditions and results of mineral assemblages

	P (GPa)	T(°C)	t(h)	phases	Comments
M453	6.5	700	8	Ol, En, Grt	
M448	8	400	4	Atg	No reaction observed
M638	8	550	24	Ol, En, Mg-S	
M447	8	650	10	PhE, En, Ol	Scarce antigorite remaining
M473	8	700	26	PhE, En, Bal	Scarce olivine; brucite*
M450	8	750	10	PhE, En, Ol	Olivine+enstatite+garnet**
M452	8	800	8	Ol, En, Grt	
M451	8	850	8	Ol, En, Grt	
M474	8.5	650	25	PhE, En, Bal	Brucite*
M472	8.5	700	25	PhE, En, Ol	Olivine+enstatite+garnet**; brucite*
M471	9	730	23	PhE, PhA, En	Brucite*
M639	10	550	23	PhE, PhA, En	Balangeroite**
M467	10	700	28	PhE, PhA, En	Brucite*
M640	11	780	23	Ol, En, Grt	

* Close to one end of the capsule

** Close to the capsule walls

Mineral abbreviation after Whitney and Evans (2010), except for ballangeroite (Bal) and phase E (PhE)

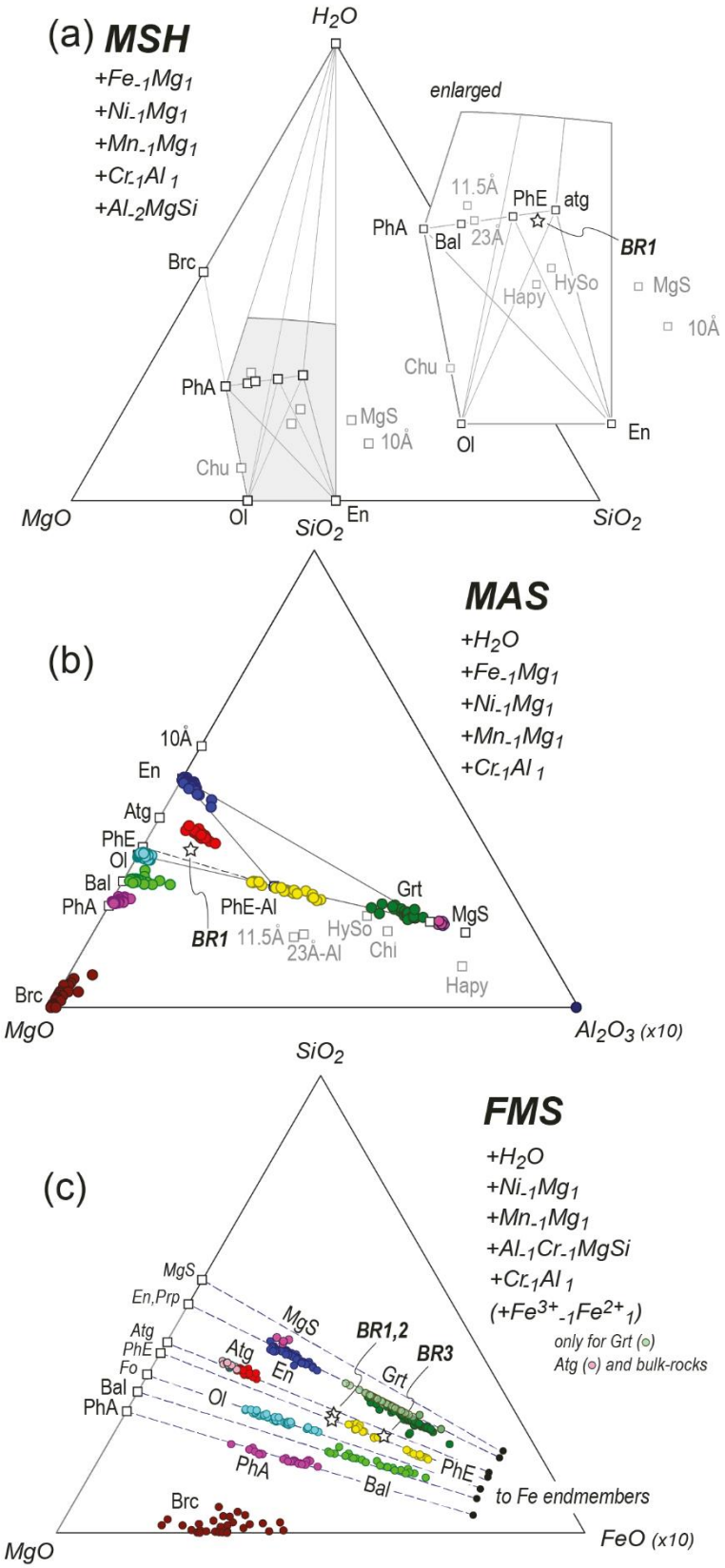
(a) MSH
+Fe-1Mg1
+Ni-1Mg1
+Mn-1Mg1
+Cr-1Al1
+Al-2MgSi
H2O
enlarged
11.5Å
PhE
atg
PhA
Bal
23Å
BR1
Brc
Hapy
HySo
MgS
10Å
Chu
PhA
MgS
10Å
Ol
En
Chu
MgO
Ol
En
SiO2
SiO2
(b)
MAS
+H2O
+Fe-1Mg1
+Ni-1Mg1
+Mn-1Mg1
+Cr-1Al1
10Å
En
Atg
PhE
Ol
Bal
PhA
PhE-Al
Grt
MgS
BR1
11.5Å
HySo
23Å-Al
Chi
Hapy
Brc
MgO
Al2O3 (x10)
SiO2
(c)
FMS
+H2O
+Ni-1Mg1
+Mn-1Mg1
+Al-1Cr-1MgSi
+Cr-1Al1
(+Fe3+-1Fe2+1)
only for Grt (⊙)
Atg (⊙) and bulk-rocks
MgS
En,Prp
Atg
PhE
Fo
Bal
PhA
MgS
BR1,2
BR3
Atg
En
Grt
Ol
PhA
PhE
Bal
to Fe endmembers
Brc
MgO
FeO (x10)

Figure VI-2. Compositional diagrams for different systems using projections according to several exchange vectors. The exchange vectors used for these projections are reported for each diagram, for instance the original MgO vertex is modified in condensing MgO+FeO+NiO+MgO, as indicated by the vectors $Fe_{-1}Mg_1$; $Ni_{-1}Mg_1$; $Mn_{-1}Mg_1$ in the $MgO-Al_2O_3-SiO_2-H_2O$ system projected from H_2O. (a) Compositional diagram in the $MgO-SiO_2-H_2O$ (MSH) system projected from several exchange vectors involving Fe, Ni, Mn, Al and Cr. For a matter of comparison, endmembers projected in the MSH system not observed in the PT range investigated in this work are indicated in grey. The star represents the bulk rock composition (BR1, Table VI-1). (b) Compositional diagram in the $MgO-Al_2O_3-SiO_2-H_2O$ system projected from H_2O and indicated exchange vectors. Compositions of mineral phases found in the present study are reported in colors and with labels following the mineral abbreviation after Whitney and Evans (2010), except for Mg-sursassite (Mg-S), balangeroite (Bal) and phase E (PhE). (c) Compositional diagram in the $FeO-MgO-SiO_2-H_2O$ system projected from H_2O and indicated exchange vectors showing the variation on $FeMg_{-1}$ exchange between the observed phases. Light colors for antigorite and garnet correspond to analyses where Fe^{3+} is estimated based on stoichiometry (garnet) or assuming an atomic ratio $Fe^{3+}/(Fe^{2+}+Fe^{3+}) = 0.23$ for antigorite (c.f. Table VI-1). In all other phases the whole of iron is assumed to be ferrous. All projection units are molar oxides and were generated using the program CSpace, Torres-Roldán et al. (2000).

These ternary diagrams allow for better visualizing the phase relations and phase compositional variability. Phase assemblages and experimentally derived phase relations are reported in Figure VI-3. Antigorite remains stable up to 8 GPa and 400°C, with no observed reaction after 8h of run duration. At all other investigated conditions antigorite fully reacted, resulting in mineral assemblages comprising hydrous (phase A, phase E and balangeroite, minor Mg-sursassite) and nominally anhydrous phases (olivine, garnet and enstatite) and a fluid phase inferred by a high porosity of the run products. The first hydrous phase occurring after antigorite breakdown is Mg-sursassite (8 GPa, 550°C). At higher temperatures the appearance of balangeroite is observed together with phase E (8.5 GPa, 650°C and 8 GPa 700°C). Mineral assemblages containing only phase E as a hydrous phase are found for slightly higher temperatures at similar pressure conditions. Indeed, we observed phase E at 8.5 GPa, 700°C and at 8 GPa, 750°C. The occurrence of phase E at 8 GPa and 650°C in the run M447 is reported with a question mark on Figure VI-3, as Schreinemakers analyses later conducted (presented in the discussion section) suggests that the temperature of this run is likely overestimated by at

least 50°C. Phase A is present together with phase E between 9 and 10 GPa and below 800°C. Anhydrous assemblages containing garnet are observed at the highest investigated temperatures (800°C at 8 and 11 GPa, 850°C at 8 GPa and 700°C at 6.5 GPa).

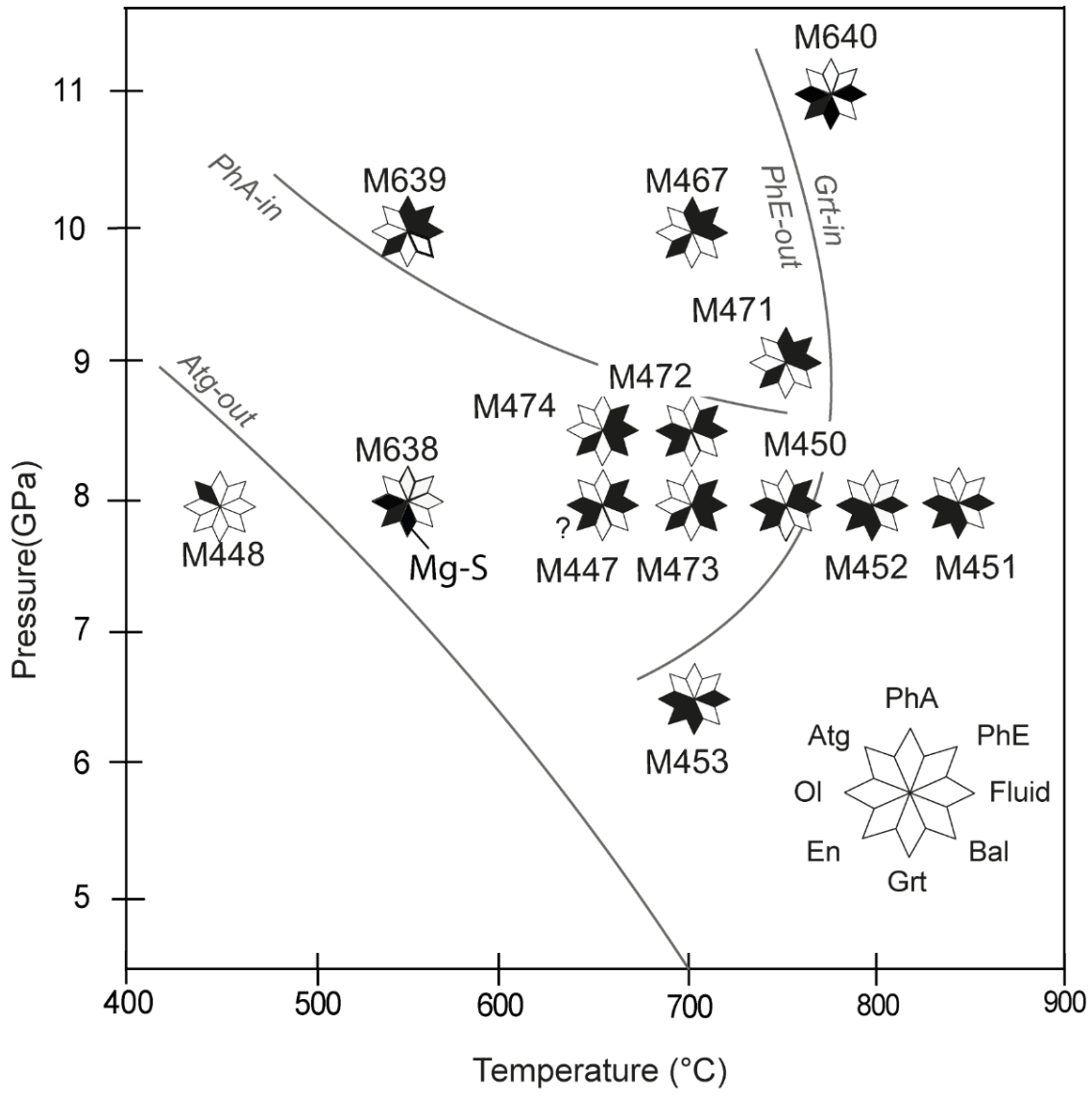

Figure VI-3. Observed mineral assemblages in the experimental runs (Table VI-2) for the investigated natural serpentine composition. Boundaries were established based on appearance and disappearance of phases observed from the recovered samples, with the exception of the antigorite-out curve, connecting our experimental constraints at 8 GPa with the P-T location of the antigorite destabilization reaction presented in Ulmer and Trommsdorff 1995 at lower pressure.

Mg-sursassite is observed at 8 GPa and 550°C in an assemblage of olivine and enstatite (Figure VI-4. a, b). Enstatite in all runs is most likely high-clinoenstatite (Ulmer and Stalder 2001). At 9 and 10 GPa, for temperatures ranging between 550 and 730°C, the mineral assemblage is composed of phase E, phase A and enstatite. Phase A occurs as large crystals of approx. 20 to 150 µm size (Figure VI-4.c, d). These crystals show fractures filled with minerals from the matrix (enstatite and phase E as small crystals < 5 µm). At 8 GPa, 700°C and 8.5 GPa, 650°C (Figure VI-4.e,f) the mineral assemblage is composed of phase E, enstatite and a ferromagnesian hydrous silicate identified as balangeroite (see below), with a general formula $(Mg,Fe)_{42}Si_{16}O_{54}(OH)_{40}$ (Deriu et al. 1994). It occurs in a fine-grained matrix (grain size < 10 µm in length) of enstatite and phase E. Although balangeroite in this work displays acicular textures (up to 150 µm long, Figure VI-4.f), similar to textural description in natural samples (Bonaccorsi et al. 2012), it also occurs as sub-idiomorphic prisms (Fig. 4e). Brucite is found close to one end of the capsule in most runs at temperatures below 730°C, its occurrence is examined in more detail in the discussion part of this study. The phase assemblage containing phase E, enstatite and olivine (Figure VI-4.g) is found at 8 GPa, 650°C and 750°C, and at 8.5 GPa, 700°C. At higher temperatures phase E breaks down to the assemblage olivine, enstatite and garnet (6.5 GPa, 700°C; 8 GPa, 800°C and 850°C). Poikilitic garnets of various sizes (ca. 20 µm to 100 µm) with olivine inclusions are located close to the capsule walls (Figure VI-4.h).

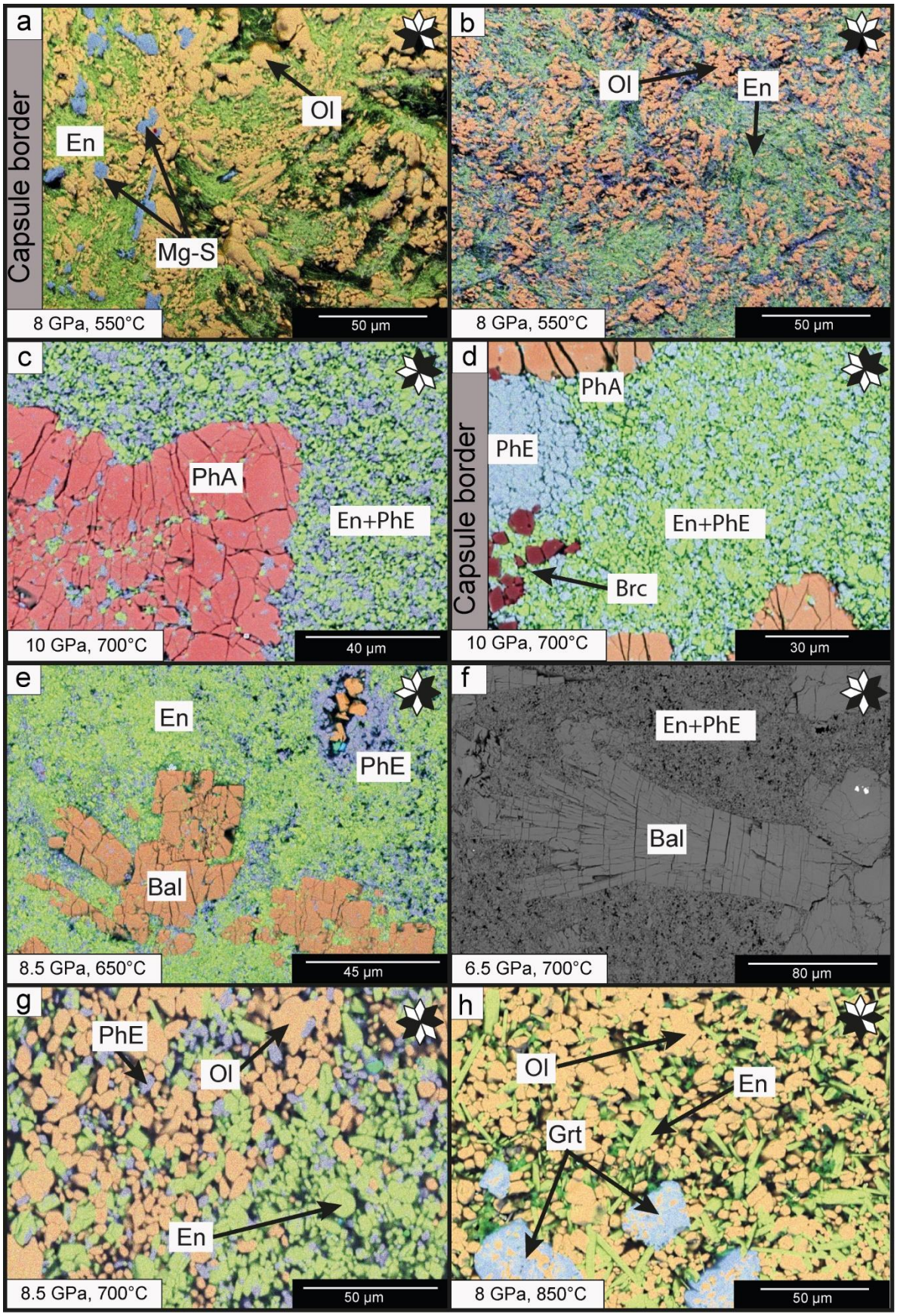
a
Capsule border
Ol
En
Mg-S
8 GPa, 550°C
50 µm
b
Ol
En
8 GPa, 550°C
50 µm
c
PhA
En+PhE
10 GPa, 700°C
40 µm
d
Capsule border
PhA
PhE
En+PhE
Brc
10 GPa, 700°C
30 µm
e
En
PhE
Bal
8.5 GPa, 650°C
45 µm
f
En+PhE
Bal
6.5 GPa, 700°C
80 µm
g
PhE
Ol
En
8.5 GPa, 700°C
50 µm
h
Ol
En
Grt
8 GPa, 850°C
50 µm

Figure VI-4. EDS chemical maps showing (a, b) the assemblage Mg-sursassite + orthopyroxene + olivine). (c, d) Assemblage composed of phase A, phase E, orthopyroxene, note the dissimilar grain size between PhA and the homogenous mixture of En + PhE. Brucite crystals occurs only close to the capsule walls. EDS chemical map (e) and and backscattered image (f) showing the assemblage balangeroite + phase E + orthopyroxene, note the acicular texture of balangeroite. (g) The assemblage olivine + enstatite + phase E with a homogenous grain size distribution. (h) Nominally anhydrous assemblage composed of poikilitic garnet preferentially occurring along the capsule wall, olivine and enstatite. l. For all chemical maps, relative amounts of Si, Al and Mg are respectively represented with the colors green, blue and red.

IV.2 **Mineral composition**

IV.2.1 ***Olivine and enstatite***

Olivine has a X_{Mg} ($Mg/(Mg+Fe^{2+})$ in atoms per formula unit) ranging from 0.92 to 0.95 (Table VI-3). Enstatite (high-clinoenstatite) is also correspondingly rich in magnesium displaying X_{Mg} between 0.92 and 0.95. The Fe-Mg distribution coefficient between olivine and enstatite plots along the $K_d = 1.0$ line, (Figure VI-5.a), where K_d is defined as:

$$K_{d\ Fe\text{-}Mg}{}^{\varphi 1/\varphi 2} = (X_{Fe}{}^{\varphi 1}.\ X_{Mg}{}^{\varphi 2})/\ (X_{Mg}{}^{\varphi 1}.\ X_{Fe}{}^{\varphi 2})$$

with X the atomic ratio of Fe or Mg in a given phase (φ1 or φ2). The aluminum content in enstatite is quite low (up to. 0.95±0.37 wt% Al_2O_3) in agreement with the high pressures of this study.

Table VI-3. Chemical composition of olivines and enstatites (EPMA)

	Olivine								Enstatite					
Run	M453	M638	M447	M450	M452	M451	M472	M640	M452	M451	M474	M472	M471	M467
P(Gpa)	6.5	8	8	8	8	8	8.5	11	8	8	8.5	8.5	9	10
T(°C)	700	550	650	750	800	850	700	780	800	850	650	700	730	700
n	*7*		*7*	*9*	*8*	*7*	*9*		*8*	*9*	*6*	*14*	*11*	*10*
SiO_2	41.98 (0.46)	41.87 (0.31)	41.58 (0.52)	41.53 (0.45)	41.29 (0.21)	41.80 (0.59)	41.69 (0.46)	42.04 (0.85)	57.56 (1.05)	59.19 (0.30)	56.73 (2.54)	58.55 (0.93)	58.74 (1.54)	59.14 (0.98)
TiO_2	0.03 (0.02)	0.02 (0.01)	0.05 (0.03)	0.02 (0.02)	0.02 (0.02)	0.01 (0.01)	0.02 (0.03)	0.01 (0.02)	0.00 (0.01)	0.00 (0.00)	0.03 (0.02)	0.03 (0.02)	0.02 (0.02)	0.02 (0.03)
Al_2O_3	0.22 (0.08)	0.02 (0.02)	0.18 (0.13)	0.10 (0.15)	0.06 (0.10)	0.01 (0.02)	0.03 (0.04)	0.02 (0.03)	0.33 (0.11)	0.25 (0.08)	0.95 (0.37)	0.41 (0.33)	0.12 (0.10)	0.19 (0.18)
Cr_2O_3	0.28 (0.04)	0.30 (0.09)	0.23 (0.04)	0.13 (0.09)	0.13 (0.18)	0.05 (0.04)	0.11 (0.11)	0.05 (0.04)	0.21 (0.07)	0.22 (0.04)	0.14 (0.07)	0.20 (0.06)	0.05 (0.05)	0.11 (0.07)
FeO	4.75 (0.53)	4.71 (0.39)	5.34 (0.93)	5.73 (0.81)	5.55 (0.47)	6.52 (0.28)	7.87 (0.86)	5.07 (0.36)	3.65 (0.19)	4.29 (0.08)	3.82 (0.50)	4.92 (0.35)	4.25 (0.38)	5.44 (0.65)
NiO	0.33 (0.11)	0.34 (0.05)	0.09 (0.03)	0.49 (0.17)	0.36 (0.06)	0.54 (0.06)	0.04 (0.12)	0.49 (0.05)	0.14 (0.02)	0.14 (0.02)	0.00 (0.00)	0.00 (0.00)	0.00 (0.00)	0.00 (0.00)
MnO	0.10 (0.01)	0.07 (0.02)	0.02 (0.02)	0.08 (0.03)	0.07 (0.03)	0.06 (0.02)	0.03 (0.03)	0.05 (0.03)	0.06 (0.04)	0.08 (0.02)	0.07 (0.03)	0.09 (0.03)	0.09 (0.05)	0.08 (0.06)
MgO	52.01 (0.82)	53.06 (1.32)	52.27 (0.91)	52.06 (0.73)	52.13 (0.40)	51.04 (0.37)	50.25 (0.56)	52.93 (1.00)	36.78 (0.81)	36.57 (0.23)	37.29 (1.61)	36.53 (0.57)	36.48 (1.38)	36.70 (0.41)
Total	99.70 (0.76)	100.40 (0.84)	100.07 (0.67)	100.17 (0.67)	99.64 (0.40)	100.06 (0.73)	100.08 (0.86)	100.57 (1.38)	98.76 (1.74)	100.74 (0.44)	99.04 (3.78)	100.74 (1.17)	99.76 (2.90)	101.71 (1.61)
Si	1.01 (0.01)	1.00 (0.01)	1.00 (0.01)	1.00 (0.01)	1.00 (0.00)	1.01 (0.01)	1.01 (0.01)	1.00 (0.01)	1.98 (0.01)	2.00 (0.00)	1.95 (0.02)	1.99 (0.01)	2.00 (0.01)	1.99 (0.01)
Ti	0.00 (0.00)	0.00 (0.00)	0.00 (0.00)	0.00 (0.00)	0.00 (0.00)	0.00 (0.00)	0.00 (0.00)	0.00 (0.00)	0.00 (0.00)	0.00 (0.00)	0.00 (0.00)	0.00 (0.00)	0.00 (0.00)	0.00 (0.00)
Al	0.01 (0.00)	0.00 (0.00)	0.01 (0.00)	0.00 (0.00)	0.00 (0.00)	0.00 (0.00)	0.00 (0.00)	0.00 (0.00)	0.01 (0.00)	0.01 (0.00)	0.04 (0.02)	0.02 (0.01)	0.00 (0.00)	0.01 (0.01)
Cr	0.01 (0.00)	0.01 (0.00)	0.00 (0.00)	0.00 (0.00)	0.00 (0.00)	0.00 (0.00)	0.00 (0.00)	0.00 (0.00)	0.01 (0.00)	0.01 (0.00)	0.00 (0.00)	0.01 (0.00)	0.00 (0.00)	0.00 (0.00)
Fe	0.10 (0.01)	0.09 (0.01)	0.11 (0.02)	0.12 (0.02)	0.11 (0.01)	0.13 (0.01)	0.16 (0.02)	0.10 (0.01)	0.11 (0.00)	0.12 (0.00)	0.11 (0.02)	0.14 (0.01)	0.12 (0.01)	0.15 (0.02)
Ni	0.01 (0.00)	0.01 (0.00)	0.00 (0.00)	0.01 (0.00)	0.01 (0.00)	0.01 (0.00)	0.00 (0.00)	0.01 (0.00)	0.00 (0.00)	0.00 (0.00)	0.00 (0.00)	0.00 (0.00)	0.00 (0.00)	0.00 (0.00)
Mn	0.00 (0.00)	0.00 (0.00)	0.00 (0.00)	0.00 (0.00)	0.00 (0.00)	0.00 (0.00)	0.00 (0.00)	0.00 (0.00)	0.00 (0.00)	0.00 (0.00)	0.00 (0.00)	0.00 (0.00)	0.00 (0.00)	0.00 (0.00)
Mg	1.86 (0.02)	1.89 (0.03)	1.87 (0.02)	1.87 (0.02)	1.88 (0.01)	1.84 (0.01)	1.81 (0.02)	1.88 (0.01)	1.89 (0.02)	1.84 (0.01)	1.91 (0.01)	1.85 (0.01)	1.86 (0.02)	1.84 (0.01)
O	4.00 (0.00)	4.00 (0.00)	4.00 (0.00)	4.00 (0.00)	4.00 (0.00)	4.00 (0.00)	4.00 (0.00)	4.00 (0.00)	6.00 (0.00)	6.00 (0.00)	6.00 (0.00)	6.00 (0.00)	6.00 (0.00)	6.00 (0.00)
∑cat.	2.99 (0.01)	3.00 (0.01)	2.99 (0.00)	3.00 (0.00)	3.00 (0.00)	2.99 (0.01)	2.99 (0.01)	3.00 (0.01)	4.01 (0.01)	3.99 (0.00)	4.02 (0.02)	4.00 (0.01)	3.99 (0.01)	4.00 (0.01)
XMg	0.95 (0.01)	0.95 (0.00)	0.95 (0.01)	0.94 (0.01)	0.94 (0.00)	0.93 (0.00)	0.92 (0.01)	0.95 (0.00)	0.95 (0.00)	0.94 (0.00)	0.95 (0.01)	0.93 (0.01)	0.94 (0.01)	0.92 (0.01)

n Number of measurements

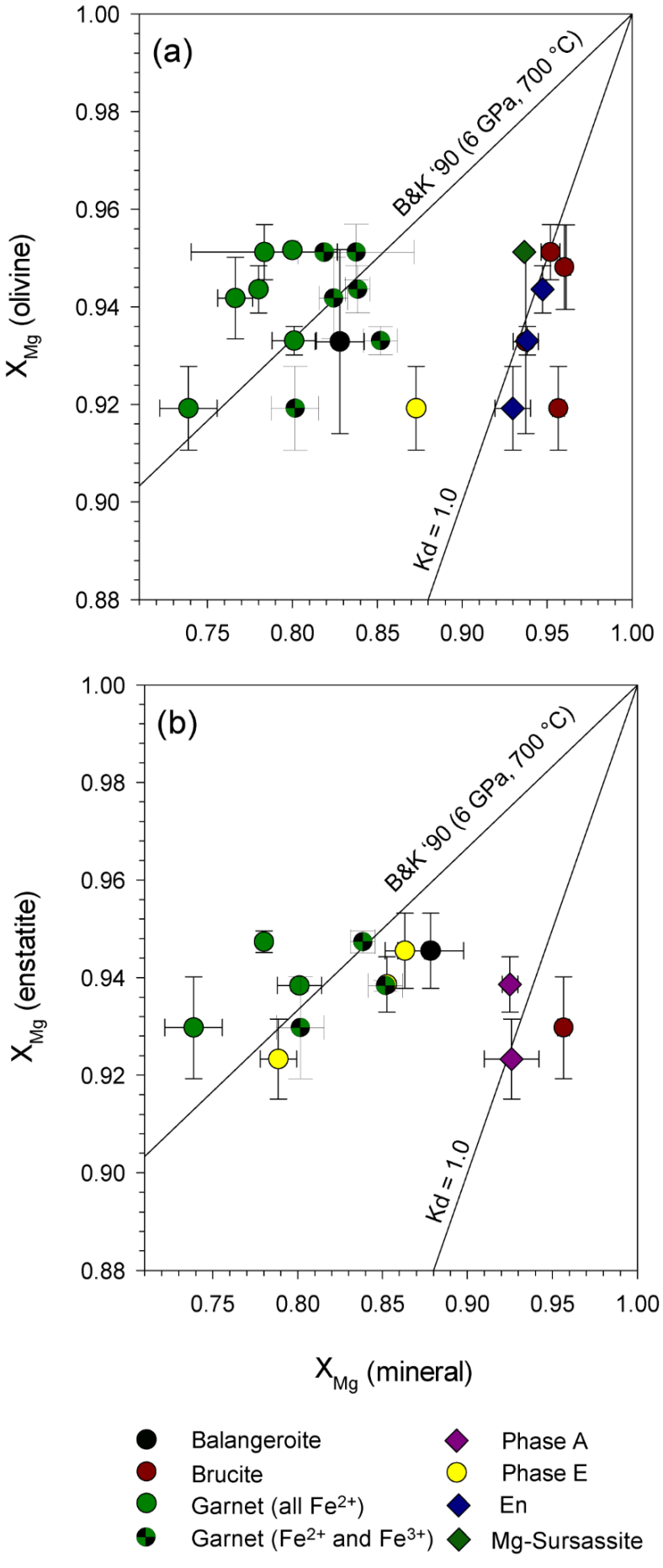
(a)
(b)
B&K '90 (6 GPa, 700 °C)
Kd = 1.0
X_Mg (olivine)
X_Mg (enstatite)
X_Mg (mineral)
1.00
0.98
0.96
0.94
0.92
0.90
0.88
0.75
0.80
0.85
0.90
0.95
1.00
Balangeroite
Brucite
Garnet (all Fe2+)
Garnet (Fe2+ and Fe3+)
Phase A
Phase E
En
Mg-Sursassite

Figure VI-5. (a) Fe-Mg distribution between olivine and other ferromagnesian minerals, and (b) between enstatite and other ferromagnesian minerals X_{Mg} = Mg/(Mg+Fe^{2+}+Mn+Ni) where all Fe is assumed to be ferrous (except from garnet). Both ferrous and ferric iron-rich garnets are represented. For the Fe^{3+}-rich garnet, Fe used in the calculation of X_{Mg} is Fe^{2+} only, since Fe^{3+} is mainly assumed to occupy the octahedral site with Al^{3+}. As a consequence, X_{Mg} corrected for Fe^{3+} is displaced to higher values compared to a garnet endmember containing only Fe^{2+}. Olivine and enstatite distribution follows a 1:1 line indicating that chemical equilibrium was reached. Whereas the other ferromagnesian silicates are significantly richer in iron approximately following the experimental data for Fe-Mg distribution between olivine and garnet at 6 GPa and 700°C from (B&K' 90: Brey and Köhler, 1990).

IV.2.2 *Balangeroite*

Balangeroite is an asbestiform mineral closely related to the serpentine structure (Compagnoni et al., 1983). It was first reported in veins from natural serpentinite samples from the Piemonte Zone, Western Alps in Italy (Compagnoni et al. 1983). Its composition in the present study follows the formula $(Mg_{34.4}Fe_{6.1}Mn_{0.1}Al_{0.3}Cr_{0.1})_{\sum 41.0}Si_{16.4}O_{54}(OH)_{40}$ with X_{Mg} of 0.82-0.88 (Table VI-4). It contains about 11.1 wt% H_2O. Water contents for hydrous phases observed in our experiments were estimated after calculation from electron probe micro analyzes derived stoichiometry. Balangeroite from the type locality is known to contain Fe^{3+} based on ^{57}Fe Mössbauer spectroscopy, with a $Fe^{3+}/\sum Fe$ ratio of 0.20 (Deriu et al. 1994). The specific speciation of iron in balangeroite observed in this study remains unknown. Raman spectra obtained on our sample displays peaks at 283, 478, 692, 983, 1070 cm^{-1} in agreement with data collected on natural Balangeroite from the type locality (Groppo and Compagnoni 2007).

Table VI-4. Chemical composition (EPMA) of balangeroites and phases A (system MgO-SiO_2-H_2O)

	Balangeroite		Balangeroite	Phase A		
Run	M473	M474	*Ref*[1]	M471	M639	M467
P(Gpa)	8	8.5	-	9	10	10
T(°C)	700	650	-	730	550	700
n	*9*	*14*	*-*	*12*	*12*	*13*
SiO_2	29.87 (0.51)	31.16 (0.77)	28.32	25.51 (0.49)	26.67 (0.84)	26.99 (0.82)
TiO_2	0.06 (0.04)	0.02 (0.02)	0.06	0.02 (0.03)	0.03 (0.03)	0.03 (0.03)
Al_2O_3	0.35 (0.32)	0.43 (0.39)	0.00	0.07 (0.03)	0.44 (0.20)	0.19 (0.13)
Cr_2O_3	0.25 (0.14)	0.23 (0.06)	0.00	0.13 (0.07)	0.18 (0.06)	0.15 (0.09)
FeO_{Total}	15.81 (1.51)	11.08 (1.64)	-	7.52 (0.37)	5.45 (0.65)	6.48 (1.63)
FeO	-	-	19.43	-	-	-
Fe_2O_3	-	-	5.40	-	-	-
MnO	0.18 (0.04)	0.11 (0.04)	0.67	0.09 (0.04)	0.08 (0.02)	0.10 (0.07)
MgO	40.97 (1.43)	44.93 (1.72)	35.62	52.07 (1.46)	54.17 (0.99)	53.91 (1.32)
Total	87.55 (1.15)	87.98 (0.83)	89.49	85.45 (1.74)	87.02 (0.77)	87.87 (1.14)
H_2O[(a)]	10.96 (0.14)	11.32 (0.16)	10.07	11.07 (0.23)	11.46 (0.12)	11.48 (0.18)
Si	16.35 (0.20)	16.50 (0.30)	16.00	2.07 (0.02)	2.09 (0.05)	2.11 (0.04)
Ti	0.03 (0.02)	0.01 (0.01)	0.02	0.00 (0.00)	0.00 (0.00)	0.00 (0.00)
Al	0.23 (0.20)	0.27 (0.24)	0.00	0.01 (0.00)	0.04 (0.02)	0.02 (0.01)
Cr	0.11 (0.06)	0.09 (0.02)	0.00	0.01 (0.00)	0.01 (0.00)	0.01 (0.01)
Fe^{2+}	7.24 (0.73)	4.91 (0.79)	9.18	0.51 (0.03)	0.36 (0.05)	0.43 (0.11)
Fe^{3+}	-	-	2.29	-	-	-
Mn	0.09 (0.02)	0.05 (0.02)	0.32	0.01 (0.00)	0.01 (0.00)	0.01 (0.00)
Mg	33.41 (1.00)	35.47 (1.03)	29.99	6.31 (0.06)	6.34 (0.11)	6.29 (0.12)
O	54.00 (0.00)	54.00 (0.00)	54.00	11.00 (0.00)	11.00 (0.00)	11.00 (0.00)
OH	40.00 (0.00)	40.00 (0.00)	40.00	6.00 (0.00)	6.00 (0.00)	6.00 (0.00)
∑cat.	57.47 (0.28)	57.31 (0.34)	55.51	8.92 (0.02)	8.88 (0.06)	8.87 (0.04)
XMg	0.82 (0.02)	0.88 (0.02)	0.77	0.93 (0.00)	0.95 (0.01)	0.94 (0.02)

n Number of measurements

[(a)] Calculated H_2O content (wt%) from stoechimetry

Ref[1]. Balangeroite average composition from Bonaccorsi et al. (2012), Fe^{2+} and Fe^{3+} calculated from Fe^{2+}/Fe^{3+} ratio from Mössbauer of 4:1 (Deriu et al., 1994)

IV.2.3 *Phase A*

The average chemical composition of phase A formed in the natural system in this study (Table VI-4) is $Mg_{6.3}Fe_{0.5}Si_{2.1}O_8(OH)_6$, close to the MSH endmember $Mg_7Si_2O_8(OH)_6$ first reported by Yamamoto and Akimoto (1974). It contains about 11.3 wt% H_2O. The observed X_{Mg} of phase A (0.93 Table VI-4, Figure VI-5.b) is close to the K_d = 1.0, between PhA and enstatite. Phase A contains almost no aluminum (less than 0.19 wt% Al_2O_3). The Raman spectra of Phase A (Figure VI-6) exhibits characteristic peaks at 178, 220, 550, 807 and 845 cm^{-1} and

the two main broad OH-bands at 3400 and 3517 cm^{-1} , similar to previous reports (Liu et al. 1997a; Komabayashi et al. 2005a; Holl et al. 2006; Kleppe and Jephcoat 2006). The presence of phase A has been further confirmed by EBSD analyses. The diffraction patterns related to phase A crystal structure fit within 50-68% with that used in the American Mineralogist Crystal Structure Database, corresponding to the crystallographic data presented in Holl et al. (2006) for iron-bearing phase A (see Supplementary Fig.1).

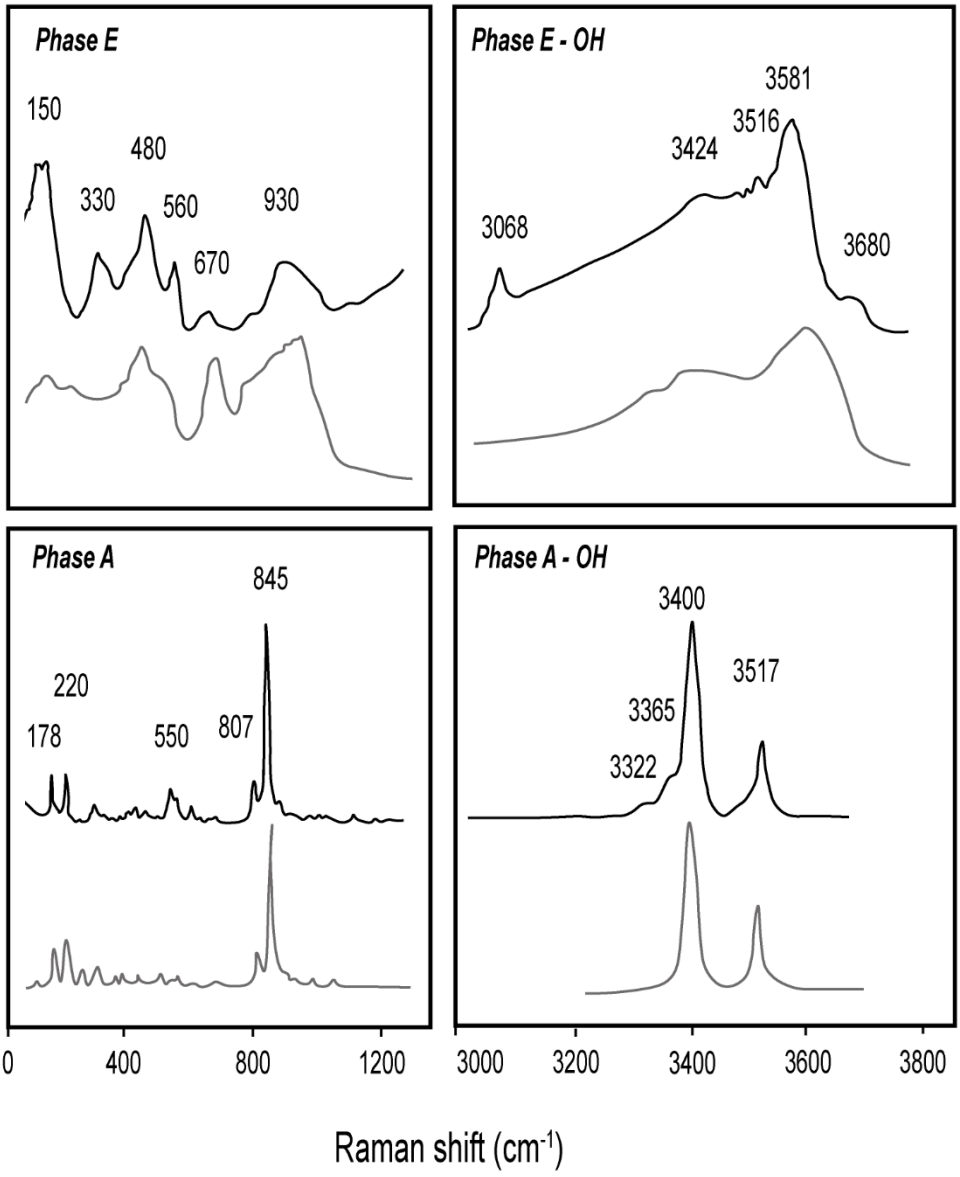

Figure VI-6. Raman spectra for phase E and phase A in the present study (top lines). Spectra from previous studies are represented as references in bottom lines. Phase E and phase A references are from Kleppe and Jephcoat (2006).

IV.2.4 *Phase E*

Phase E in the MSH system has the formula $Mg_{2.33}Si_{1.26}O_{3.55}(OH)_{2.6}$ (Komabayashi et al. 2005b), and contains 11.9 wt% H_2O. In the natural system from this study it contains substantial amounts of iron (X_{Mg}=0.79-0.87 see Table VI-5) and aluminum (up to 8.9 wt% Al_2O_3). Its chemical composition is homogeneous within each experiment, but varies as a function of pressure and temperature, with an average formula $Mg_{1.67}Fe_{0.31}Al_{0.27}Si_{1.21}O_{3.55}(OH)_{2.60}$. In our experiments, phase E displays a range of X_{Mg} values and Al_2O_3 contents of 0.79-0.87 and 5.5-8.9 wt% respectively. This is in agreement with the chemical variability of phase E reported by Kawamoto et al. (1995) in the KLB-1 hydrous peridotite system (1.5 to 9 wt% Al_2O_3). More specifically, we observe that X_{Mg} values decrease with increasing pressure from 0.87 at 8.5 GPa, to 0.79 at 10 GPa. Likewise, Al_2O_3 contents also decrease with increasing pressure, from 7-9 wt% at 8.5 GPa to 5.5 wt% at 10 GPa (Figure VI-7.a). Such decrease of aluminum content in phase E with pressure was also previously reported for the pressure ranges of 12-13.8 GPa (Stalder and Ulmer 2001), 10.3-15.5 GPa (Kawamoto et al. 1995) and 14-17 GPa (Kawamoto 2004). Our data at low pressures confirms that the aluminum substitution in Phase E does not follow a Tschermak substitution $^{[6]}M^{2+} + {}^{[4]}Si^{4+} = {}^{[6]}Al^{3+} + {}^{[4]}Al^{3+}$. In particular, Mg and Al contents in phase E are linearly anti-correlated with a coefficient equal to -0.7. The silicon content does not seem to vary with aluminum content if we consider our data as a whole. However, if we divide the data in pressure subsets, we observe trivalent cations versus Si trends that are parallel to the Tschermak substitution (linearly correlated with a -1 coefficient) as observed by Kawamoto et al. (1995) (Figure VI-7.b). Hence, we propose a substitution mechanism as following:

$$20\ Mg_{Mg}^{X} + 20\ Si_{Si}^{X} + 9\ O_o^{X} + 17\ Al_2O_3 = 14\ Al_{Mg}^{\cdot} + 20\ Al_{Si}' + 6\ V_{Mg}'' + 9\ VO^{\cdot\cdot}$$

$$+ 20\ MgSiO_3$$

with Mg = Mg + Fe^{2+} + Mn + Ni (divalent cations) and Al = Al + Cr + Fe^{3+} (trivalent cations). The Kröger-Vink notation used for this mechanism allows to specify the sites of occupancy (subscript) and the excess negative charge ('), excess positive charge (˙) or neutral balance of charge (^{x}) (superscript). While the Si site can be fully occupied by Al, this substitution is accompanied by vacancies on the Mg site. This is in agreement with the structural observation from Kudoh et al. (1993) highlighting the cation disordered crystal structure of phase E. Their study evidenced the impossibility of Mg octahedral sites on the brucite-like intra layer to be occupied when facing inter layered Si tetrahedra, hence causing vacancies.

Table VI-5. Chemical composition (EPMA) of Mg-Sursassite, garnets and phases E (system MgO-Al_2O_3-SiO_2-H_2O)

	Mg-Sursassite	Garnet						Phase E						
Run	M638	M453	M638	M450	M452	M451	M472	M474	M472	M471	M467	Ref[2]	Ref[3]	
P(Gpa)	8	6.5	8	8	8	8	8.5	8.5	8.5	9	10	9.3	-	
T(°C)	550	700	550	750	800	850	700	650	700	730	700	800	-	
n	*7*	*6*	*9*	*14*	*12*	*10*	*6*	*5*	*7*	*4*	*10*	-	-	
SiO_2	40.78 (0.91)	44.01 (1.37)	43.22 (0.36)	42.72 (1.00)	42.69 (0.24)	43.71 (0.70)	41.93 (0.48)	36.57 (0.73)	37.98 (0.96)	36.32 (0.47)	36.44 (0.57)	35.51	40.10	
TiO_2	0.01 (0.01)	0.09 (0.05)	0.02 (0.02)	0.02 (0.02)	0.04 (0.03)	0.03 (0.02)	0.03 (0.04)	0.02 (0.02)	0.01 (0.03)	0.04 (0.05)	0.02 (0.03)	0.00	0.00	
Al_2O_3	24.36 (0.83)	18.89 (0.94)	19.86 (0.42)	20.10 (0.83)	19.88 (0.35)	19.39 (0.93)	20.29 (0.45)	7.11 (0.57)	8.93 (0.81)	6.88 (0.28)	5.53 (0.55)	4.41	0.00	
Cr_2O_3	0.43 (0.09)	1.30 (0.62)	1.91 (0.42)	1.88 (0.33)	1.80 (0.44)	1.74 (0.48)	1.67 (0.20)	1.48 (0.72)	1.31 (0.23)	0.91 (0.10)	0.38 (0.23)	0.00	0.00	
FeO_{Total}	2.66 (0.18)	11.64 (2.01)	10.90 (0.57)	12.62 (0.44)	11.65 (0.45)	10.92 (0.63)	13.57 (0.57)	9.12 (0.78)	9.00 (0.23)	10.58 (0.07)	15.80 (0.82)	8.51	0.00	
FeO	2.66 (0.18)	9.79 (3.77)	8.43 (0.97)	9.18 (0.96)	8.30 (0.65)	7.89 (1.14)	11.09 (2.38)	-	-	-	-	-	-	
Fe_2O_3 [(a)]	-	2.06 (3.24)	2.75 (0.97)	3.83 (1.05)	3.71 (0.57)	3.36 (1.28)	2.76 (2.23)	-	-	-	-	-	-	
NiO	0.09 (0.02)	0.01 (0.01)	0.00 (0.00)	0.02 (0.02)	0.01 (0.01)	0.01 (0.03)	0.00 (0.00)	0.02 (0.02)	0.00 (0.00)	0.00 (0.00)	0.00 (0.00)	0.00	0.00	
MnO	0.26 (0.03)	0.44 (0.05)	0.41 (0.03)	0.44 (0.05)	0.44 (0.09)	0.38 (0.06)	0.61 (0.07)	0.02 (0.03)	0.04 (0.04)	0.05 (0.02)	0.08 (0.06)	0.00	0.00	
MgO	24.03 (0.81)	23.78 (2.25)	24.48 (0.32)	23.23 (0.57)	23.72 (0.43)	24.66 (0.80)	21.56 (1.02)	34.72 (0.74)	34.70 (1.10)	34.33 (0.68)	33.07 (0.79)	41.14	48.50	
Total	100.80 (0.74)	100.37 0.90	101.09 (0.44)	101.40 (1.89)	100.59 (0.50)	101.17 (0.72)	99.92 (0.44)	89.11 (2.31)	92.02 (2.24)	89.11 (1.32)	91.35 (1.25)	89.57	88.60	
H_2O*	8.17 (0.08)	-	-	-	-	-	-	11.81 (0.24)	12.27 (0.30)	11.74 (0.18)	11.71 (0.19)	10.51	11.40	
Si	5.24 (0.08)	3.12 (0.07)	3.04 (0.01)	3.01 (0.02)	3.02 (0.01)	3.06 (0.05)	3.02 (0.04)	1.21 (0.01)	1.21 (0.02)	1.21 (0.01)	1.21 (0.01)	1.16	0.95	
Ti	0.00 (0.00)	0.00 (0.00)	0.00 (0.00)	0.00 (0.00)	0.00 (0.00)	0.00 (0.00)	0.00 (0.00)	0.00 (0.00)	0.00 (0.00)	0.00 (0.00)	0.00 (0.00)	0.00	0.00	
Al	3.69 (0.10)	1.58 (0.10)	1.64 (0.03)	1.67 (0.05)	1.66 (0.03)	1.60 (0.07)	1.72 (0.04)	0.28 (0.03)	0.33 (0.03)	0.27 (0.01)	0.22 (0.02)	0.17	0.00	
Cr	0.04 (0.01)	0.07 (0.04)	0.11 (0.02)	0.10 (0.02)	0.10 (0.02)	0.10 (0.03)	0.09 (0.01)	0.04 (0.02)	0.03 (0.01)	0.02 (0.00)	0.01 (0.01)	0.00	0.00	
Fe2+	0.29 (0.02)	0.58 (0.23)	0.50 (0.06)	0.54 (0.05)	0.49 (0.04)	0.46 (0.07)	0.67 (0.14)	0.25 (0.02)	0.24 (0.01)	0.29 (0.00)	0.44 (0.03)	0.23	0.00	
Fe^{3+} [(b)]	-	0.11 (0.17)	0.15 (0.05)	0.20 (0.06)	0.20 (0.03)	0.18 (0.07)	0.15 (0.12)	-	-	-	-	-	-	
Mn	0.03 (0.00)	0.03 (0.00)	0.02 (0.00)	0.03 (0.00)	0.03 (0.01)	0.02 (0.00)	0.04 (0.00)	0.00 (0.00)	0.00 (0.00)	0.00 (0.00)	0.00 (0.00)	0.00	0.00	
Mg	4.60 (0.19)	2.51 (0.21)	2.56 (0.04)	2.44 (0.05)	2.50 (0.03)	2.57 (0.08)	2.31 (0.11)	1.71 (0.01)	1.64 (0.03)	1.70 (0.01)	1.64 (0.02)	2.00	1.64	
∑cat.	13.90 (0.09)	8.00 (0.00)	8.02 (0.03)	8.00 (0.00)	8.00 (0.00)	8.00 (0.00)	8.00 (0.00)	3.49 (0.01)	3.46 (0.01)	3.50 (0.01)	3.52 (0.01)	3.52	3.52	
O	21.00 (0.00)	12.00 (0.00)	12.00 (0.00)	12.00 (0.00)	12.00 (0.00)	12.00 (0.00)	12.00 (0.00)	4.85 (0.00)	4.85 (0.00)	4.85 (0.00)	4.85 (0.00)	4.80	3.60	
OH	7.00 (0.00)	-	-	-	-	-	-	2.60 (0.00)	2.60 (0.00)	2.60 (0.00)	2.60 (0.00)	2.40	2.40	
$Fe^{3+}/\sum Fe$ [(c)]	-	0.17 (0.26)	0.23 (0.08)	0.27 (0.07)	0.29 (0.04)	0.28 (0.10)	0.19 (0.15)	-	-	-	-	-	-	
Lβ/Lα	-		-	0.87 (0.04)	0.88 (0.00)	0.76 (0.02)	-	-	-	-	-	-	-	
$Fe^{3+}/\sum Fe$ [(d)]	-	-	-	0.20 (0.00)	0.12 (0.00)	0.17 (0.00)	-	-	-	-	-	-	-	
X_{Mg}	0.94 (0.00)	0.81 [(e)] (0.07)	0.84 [(e)] (0.02)	0.82 [(e)] (0.02)	0.84 [(e)] (0.01)	0.85 [(e)] (0.02)	0.78 [(e)] (0.04)	0.87 [(f)] (0.01)	0.87 [(f)] (0.00)	0.85 [(f)] (0.00)	0.79 [(f)] (0.01)	0.89 [(f)]	0.79 [(f)]	

n Number of measurements

* Calculated H_2O content (wt%) from stoechimetry

[(a)] Fe_2O_3 calculated from

[(b)] $Fe^{3+} = 24*(1\text{-}8/\sum cations)$, see equation in Droop et al. (1987)

[(c)] $Fe^{3+}/\sum Fe$ calculated from $Fe^{3+(b)}$

[(d)] $Fe^{3+}/\sum Fe$ calculated using the Flank method after Hofer and Brey (2007)

[(e)] $X_{Mg}=Mg/(Mg+Fe^{2+})$

[(f)] $X_{Mg}=Mg/(Mg+Fe_{total})$

Ref[2]. Phase E in the FMASH from Kawamoto et al. (1995); their run #14

Ref[3]. Phase E in the MSH from Kanzaki (1991)

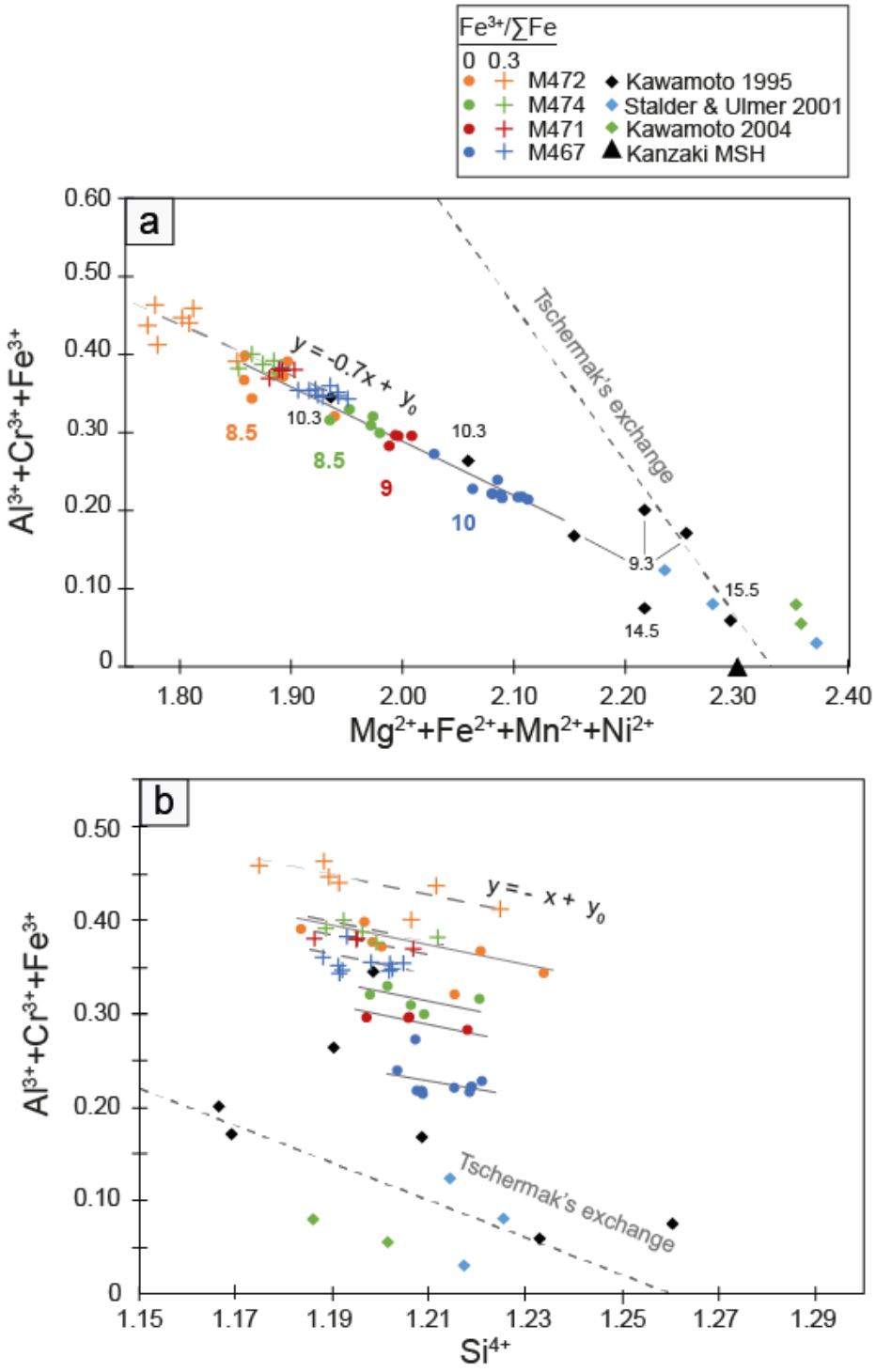

Figure VI-7. Substitution mechanism for Al in phase E. Data from this study are reported with the filled color dots ($Fe^{3+}/\sum Fe = 0$) and color crosses ($Fe^{3+}/\sum Fe = 0.3$). Data from previous experimental works appear with the colored diamonds. Phase E endmember in the MSH system ($Mg_{2.3}Si_{1.3}H_{2.4}O_6$) is reported with the black triangle (Kanzaki 1991). Pressures of experiments are reported in colors for this study, and in grey for previous experimental works. The Tschermak's exchange vector $^{[6]}M^{2+} + {}^{[4]}Si^{4+} = {}^{[6]}Al^{3+} + {}^{[4]}Al^{3+}$ for phase E is plotted along the dashed line for the structural formula $Mg_{2.33}Si_{1.26}O_{3.55}(OH)_{2.6}$ (Komabayashi et al., 2005b).

The Raman spectra of phase E is shown in Figure VI-6. The bands are quite broad and suggest cation disorder and lack of long range ordering (Kudoh et al. 1993; Frost and Fei 1998). Here, the spectra are characterized by broad bands at 150, 330, 480, 560, 670 and 930 cm^{-1}. Compared to the data published in Liu et al. (1997b), Frost and Fei (1998), Stalder and Ulmer (2001) and Kleppe and Jephcoat (2006) we observe bands at slightly lower frequencies, but the spacing between the main broad bands remains in agreement with our observations. Likewise, the position of the broad OH-band for phase E is not in agreement between the different studies, with positions varying between 3190 and 3631 cm^{-1}. Here we observe bands at 3068, 3424, 3516, 3581 (main peak) and 3680 cm^{-1}.

Similarly to phase A, phase E has been further confirmed by EBSD. Fitting of the diffraction patterns was based on the crystallographic data from Kudoh et al. (1993) available in the American Mineralogist Crystal Structure Database. Nevertheless, due to the porous and very fine-grained nature of the matrix containing phase E (Figure VI-4.c, d, e) was more challenging, but still provides confirmation of the nature of this phase, together with chemical microprobe data and Raman spectra.

IV.2.5 *Garnet*

Garnet is mostly pyrope ($Mg_3Al_2Si_3O_{12}$) with minor khoharite ($Mg_3Fe^{3+}{}_2Si_3O_{12}$), majorite ($Mg_3(Fe^{2+},Si,Al)_2Si_3O_{12}$) and knorringite ($Mg_3Cr^{3+}{}_2Si_3O_{12}$) components, and it has the average formula $(Mn_{0.03}Mg_{2.47}Fe_{0.55})^{2+}(Fe_{0.17}Al_{1.64}Cr_{0.09})^{3+}Si_{3.04}O_{12}$. The $Fe^{3+}/\sum Fe$ ratio of garnets has been estimated between 0.17 and 0.29 based on microprobe data using the general equation from Droop (1987) for stoichiometric minerals (Fe^{3+}= 24*(1-8/∑cations, see Table VI-5). The flank method, which is based on the correlation between FeLα/FeLβ X-ray emission and total FeO content with iron speciation (Höfer and Brey 2007) indicates marginally lower values of the $Fe^{3+}/\sum Fe$ ratio, ranging between 0.12 and 0.20. Both methods used for the estimation of the $Fe^{3+}/\sum Fe$ ratio in garnets lead to values ranging between 0.12 and 0.29, in agreement with the

maximum value of 0.3 found at 4.8 GPa, 680°C by Fumagalli and Poli (2005). When all the iron in garnet is assumed to be Fe^{2+}, X_{Mg} varies between 0.74 and 0.80, whereas the X_{Mg} corrected for the ferric iron varies between 0.78 and 0.85 (Figure VI-5). There is an increase in X_{Mg} in garnet from 0.78-0.81 to 0.85 for an increase in temperature from 700°C to 850°C.

IV.2.6 *Mg-sursassite*

On the hottest part of the capsule (close to the lateral walls) Mg-sursassite displays sub idiomorphic crystals of approximately 15 µm, while it is intimately mixed with enstatite in a fine-grained fibrous matrix in the center of the capsule. Its average composition follows the formula $Mg_{4.6}Fe_{0.3}Al_{3.7}Si_{5.2}O_{21}(OH)_7$, with approximately 8 wt% H_2O.

V **Discussion**

V.1 **Attainment of equilibrium**

The attainment of equilibrium in complex systems is difficult to constrain using reversal experiments, especially due to the continuous character of the reactions. Therefore, no attempt in bracketing phase boundaries has been made. However, several lines of evidence point out that equilibrium was reasonably attained in our experiments:

(1) Agreement with the phase rule. The chemical system here studied can be reduced to the MASH system after projection from several exchange vectors (cf. Figure VI-2). Divariant fields therefore should contain three solid phases. Commonly the ferric iron component is regarded as non-reacting (but see later discussion) thus adding magnetite as an extra (but inert) phase. All experiments conducted beyond the antigorite stability field contain 3 solid phases suggesting that the approximation to the MASH system is correct. Occasionally two different assemblages are found (one at the center of the capsule and the other close to the capsule walls). This is related to thermal gradients in the capsule estimated to be approximately 11°C/mm at

our experimental conditions (see Table VI-2). In many experiments performed below 750°C, traces of brucite $Mg(OH)_2$ are observed (Table VI-2). Brucite stability has been described in the MSH system from 5 GPa, 600°C (Yamamoto and Akimoto, 1974) to 15.5 GPa, 1200°C. Brucite occurrence only at the edge of the capsule that is opposite to the thermocouple, hence the coldest end (Figure VI-4.d) could also suggest a chemical zoning most likely induced by MgO dissolution in the fluid phase, as discussed by Stalder and Ulmer (2001). These authors described a strong chemical layering in their experiments conditions (800-1200°C and 5-14 GPa) most probably related to a separation of the fluid from the solids by surface forces, then inducing a chemical gradient by MgO preferential dissolution. At these conditions, the fluid phase might indeed contain some dissolved MgO and SiO_2 (Kawamoto and and Holloway 1997; Stalder and Ulmer 2001; Mibe et al. 2002; Komabayashi et al. 2005a). Even if in our experiments we do not observe layered structures, the experimental capsules are quite long (up to 2.5 mm) and we cannot exclude that fluctuations as little as 11°C/mm could have contributed to brucite stabilization. As suggested in the case of low-temperature zones within experiments performed in the MASH system (Cai et al. 2015), such minor amounts of brucite can be considered as disequilibrium products. Finally, water budgets are not affected by its minute occurrence in our samples (<0.5‰ according to the estimation based on the SEM chemical map of M467, see Figure VI-4.d). Therefore, brucite is no further considered in the phase equilibria addressed in the present study.

(2) Textural observation. Subhedral textures of small crystals (olivine, enstatite and phase E (see Figure VI-4.g) prismatic to acicular textures of balangeroite (Figure VI-4.c, d) and chemical homogeneity of these minerals (see below) suggests the approach to equilibrium. Some chemical zonation can nevertheless be noted. Poikilitic textures of garnets evidences a local textural disequilibrium inferred by its slower kinetics of crystallization compared to other

minerals. This is often observed in experiments containing growing garnets (Hammouda 2003; Auzanneau et al. 2006) and seems difficult to avoid.

(3) Chemical equilibrium. Except for some chemical zonation (mostly Fe-Mg exchange) observed on the 10-15 µm rim of the larger crystals of phase A (>100 µm large), with variations of 1.63 wt% FeO and 1.32 wt% MgO, mineral composition is homogenous within the capsule. Additionally, the systematic variation of Al in phase E with pressure further suggests that chemical equilibrium is attained. Fe-Mg distribution between phases is furthermore in agreement with chemical equilibrium. Olivine and enstatite typically display K_d close to 1.0 (Figure VI-5) in agreement with previous observations of dehydration product of antigorite in nature (e.g. Trommsdorff et al., 1998) and in experiments (Taylor and Green 1988; Brey and Köhler 1990; Niida and Green 1999; Fumagalli and Poli 2005; Padrón-Navarta et al. 2010a). Fe-Mg distribution coefficient in garnet from this study is also in good agreement with Brey and Köhler (1990) at 6 GPa and 700°C (Figure VI-5), even when calculated with $Fe^{3+}/\sum Fe$ ratio up to 0.29. Similarly, a K_d of 1 is found between enstatite and Phase A, in agreement with the data from Fumagalli and Poli (2005) concerning Mg-Fe distribution between other ferromagnesian hydrous phases (amphibole, chlorite and the 10 Å phase) and olivine.

V.2 **The role of magnetite**

A significant decrease in X_{Mg} is observed between the starting antigorite mineral (X_{Mg}=0.97) and the ferromagnesian silicate products, especially in the case of garnet, phase E and balangeroite minerals (X_{Mg}=0.82-0.85) (note that such behavior is also observed in dehydrated serpentinites at lower pressure from subduction settings, e.g. Trommsdorff et al. 1998, Padrón-Navarta et al. 2011, Debret et al., 2015). The amount of iron observed in the different phases is displayed in the FeO-MgO-SiO_2-H_2O ternary diagram projected from H_2O (Figure VI-2.c). The reaction involving exclusively antigorite (without magnetite) cannot explain the decrease in

X_{Mg} in the newly formed ferromagnesian silicates, without violating the mass balance. This indicates that magnetite plays an important role in the studied phase equilibria here, and indeed in natural samples magnetite is observed to decrease in amount with increasing degree of dehydration (Debret et al. 2015). This is particularly critical in the case of the mineral assemblage composed of enstatite, phase E and balangeroite, displaying the lowest X_{Mg}: any starting material with a composition characterized by a higher X_{Mg} than the one depicted by the enstatite-balangeroite join is not in agreement with the observed phase assemblages. Starting material containing 5 wt% of magnetite (BR_2) can explain the composition of the assemblages observed. X_{Mg} values for balangeroite and phase E are to be taken into consideration with particular attention, since these two phases most likely incorporate Fe^{3+}, probably as much as garnet ($Fe^{3+}/\sum Fe$ of 0.2 for natural balangeroite, see Deriu et al. 1994). Such ferric iron contents would nevertheless not drastically change the previous conclusion.

V.3 **Previous experimental studies on DHMS close to antigorite breakdown**

Phase equilibria beyond antigorite stability have been addressed by several experimental studies in various chemical systems. Relevant experimental data for this study have been reported in Figure VI-8.a. At low temperature and low pressure (below 7.5 GPa and 700 °C), data involving the stability of the 10 Å phase, phase A and olivine are in good agreement between different studies (Yamamoto and Akimoto 1977; Fumagalli and Poli 1999, 2005). Other intermediate-pressure hydrous phases have been reported in various chemical systems for conditions relevant to the boundary with nominally anhydrous phases. For instance, Mg-sursassite (Bromiley and Pawley 2002), the hydrous Al-bearing pyroxene or HAPY phase (Gemmi et al. 2011), the hydrated dense layered sorosilicate HySo phase and the 11.5 Å phase (Fumagalli et al. 2014; Gemmi et al. 2016), the 23 Å phase (Cai et al. 2015), have been the

subject of a growing number of studies, suggesting their potential importance as water carrier in subduction zones.

At higher temperature and pressure conditions phase relations involving phase A, phase E, enstatite and olivine are more controversial. For instance, the panel of experimental investigations on the stability of dense hydrous magnesium silicates (DHMS) between 700-1200°C and 7-13 GPa offers the possibility of comparing different chemical systems. In particular, experiments were conducted using synthetic reagent oxides or gels in the MSH system (Luth 1995; Wunder 1998), natural antigorite mixed with synthetic MgO, $Mg(OH)_2$ and amorphous SiO_2 in serpentine stoichiometry in the FMSH system (Irifune et al. 1998) and synthetic gel of KLB-1 peridotite composition in the FMASH system (Kawamoto et al. 1995). All these studies agree in the relative location of the stability field of phase A + enstatite on the low temperature side (<800-1000°C), phase E + enstatite on the high pressure and high temperature domain (10-11 GPa and >800-1000°C) and the nominally anhydrous assemblages (olivine and enstatite) on the low pressure and high temperature conditions. In the MSH system all these phases are related to the invariant point containing PhA+PhE+En+Ol+H_2O. In FMSH and FMASH systems this point becomes uni- and divariant respectively but based on previous experiments it can be still bracketed between 9-11 GPa and 850-1000°C (Figure VI-8.a). Moreover, it can be noted that all experimental works suggest consistent geometry and slopes of phase boundaries. Still, in comparison to the MSH system, a reduced temperature stability of phase A can be observed in the FMSH system, to the benefit of phase E while in the FMASH system the pressure stability of phase A is reduced again to the benefit of phase E. Indeed, aluminum seems to stabilize phase E to lower pressures (Kawamoto et al. 1995), while FeO is acknowledged to decrease the thermal stability of hydrous ferromagnesian silicates (Trommsdorff and Evans 1974) and in particular hydrous phases such as antigorite and chlorite (Padrón-Navarta et al. 2010, 2011; Merkulova et al. 2016). In iron-rich system, the lowering of

chlorite thermal stability in favor to garnet has been observed with respect to MASH system, as related to the preferential partitioning of iron into garnet in comparison to chlorite (Fumagalli et al. 2005). Likewise, for a preferential partitioning of iron into garnet with respect to Mg-Sursassite (or MgMgAl-pumpellyite), the destabilization reaction of Mg-sursassite forming garnet is displaced to lower temperature when compared to iron free system (Artioli et al. 1999). Such observations are in agreement with the preferential incorporation of iron into garnet with respect to phase A, together with the displacement of phase A breakdown to lower temperatures in the FMASH system (Kawamoto et al, 1995) in comparison to observations in the MSH system (Luth, 1995), as evidenced in Figure VI-8a. Hydroxyl-clinohumite has been observed in some previous works conducted on starting mixtures with Mg/Si > 1. This hydrous phase is found in assemblages close to the invariant point mostly on the high temperature (700-1100°C) and low pressure domains (7-10 GPa), (Yamamoto and Akimoto 1977; Kawamoto et al. 1995; Luth 1995; Wunder 1998). However, if clinohumite is stable in the MSH system the above mentioned invariant point becomes metastable and other three invariant points arise, with respectively one missing phase, [PhA], [PhE] and [Ol]. Such topology (Figure VI-8.b) has been presented by Komabayashi et al. (2005b) based on thermodynamic grounds using an internally consistent database for DHMS derived from experiments at higher pressures (15.5-21.5 GPa). Clinohumite has also been observed to be stabilized to a wider P-T area by titanium and fluorine (Ulmer and Trommsdorff 1999; Stalder et al. 2001; Grützner et al. 2017). However, in this study we do not observe clinohumite, and instead observe balangeroite.

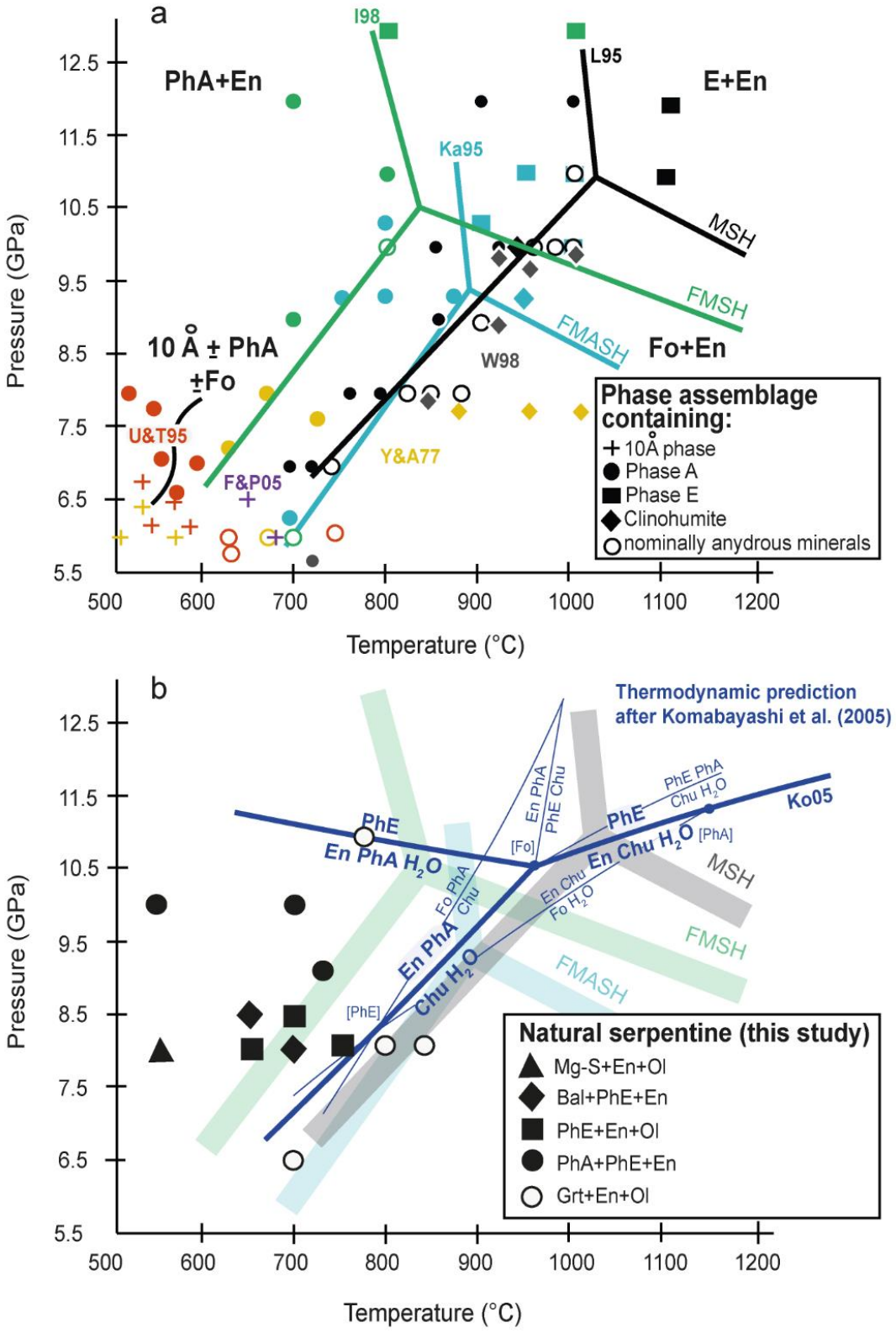
a
I98
L95
Ka95
PhA+En
E+En
MSH
FMSH
FMASH
Fo+En
W98
10 Å ± PhA
±Fo
U&T95
F&P05
Y&A77
Phase assemblage containing:
10Å phase
Phase A
Phase E
Clinohumite
nominally anydrous minerals
Pressure (GPa)
Temperature (°C)
b
Thermodynamic prediction after Komabayashi et al. (2005)
PhE
En PhA H2O
En PhA
Chu H2O
En Chu H2O
Ko05
[Fo]
[PhA]
[PhE]
MSH
FMSH
FMASH
Natural serpentine (this study)
Mg-S+En+Ol
Bal+PhE+En
PhE+En+Ol
PhA+PhE+En
Grt+En+Ol
Pressure (GPa)
Temperature (°C)

Figure VI-8. (a) Summary of previous experimental data for hydrous phases beyond antigorite breakdown at high pressure. Experiments conducted in the system MgO-SiO_2-H_2O (MSH): L95, Luth (1995); Y&A77, Yamamoto and Akimoto (1977); W98, Wunder (1998). FeO-MgO-SiO_2-H_2O system: I98, Irifune et al. (1998). MgO-Al_2O_3-SiO_2-H_2O system: Ka0, Kawamoto et al. (1995). Lherzolite model composition in the Na_2O-CaO-FeO-MgO-Al_2O_3-SiO_2-H_2O system (NCFMASH): F&P05, Fumagalli and Poli (2005). Natural antigorite + brucite + synthetic forsterite and enstatite mix: U&T95, Ulmer and Trommsdorff (1995). (b) Thermodynamic prediction of hydrous phases stability in the MSH system from Komabayashi et al. (2005b) (Ko05, bold blue line) versus experimentally determined reactions (in grey: Luth,1995; in green: Irifune et al., 1998; in blue: Kawamoto et al. 1995). Note the discrepancy in slope of reaction En + PhA + H_2O = PhE between the thermodynamic prediction (sub-horizontal) and experimental studies (sub vertical). Phases assemblages for this study, in the natural antigoritite composition are represented with the black symbols according to the corresponding P-T run conditions.

It is worth noting that with the exception of the common univariant reaction PhA + En = Ol + H_2O, there is an important disagreement between the thermodynamic prediction of the database from Komabayashi et al. (2005b) and all previous experimental studies concerning all other reactions expected. An extreme case is the reaction En + PhA + H_2O = PhE, which displays a near-vertical Clapeyron slope in experimental P-T diagrams but a near-horizontal slope in the thermodynamic model of Komabayashi et al. (2005b). More importantly, in the reactions of the later model, the fluid phase controlling the stability of PhE is located in the low-pressure/low-temperature side of the reaction, which is at odds with expected negative Clapeyron slope of dehydration reactions.

V.4 DHMS phase relations in the MASH system derived from this study

Our experiments show that in a natural system composition, phase E is stable at lower PT conditions than previously reported. In addition, we report its stability at lower pressures than phase A. Few hypotheses can be considered to explain such observations:

(1) The distribution of alumina among hydrous phases is a critical factor for their stability. Al_2O_3 is mainly incorporated into antigorite (1.5 wt%), garnet (15-20 wt%) and phase E (5-9 wt%) while phase A contains less than 0.2 wt% Al_2O_3. Therefore, Al-PhE is the only hydrous mineral that can host alumina beyond the stability of antigorite (and chlorite) and when garnet is not stable. This is in agreement with its crystallization in our experiments at lower pressures than phase A, in the garnet free field. An exception is Mg-sursassite that we observed in one experiment performed at 8 GPa and 550°C, containing 24 wt% Al_2O_3.

(2) FeO incorporation is also an important parameter that can influence the stability field of minerals, an effect known as the chemical pressure (arising from the fact that the Fe^{2+} ion is larger than Mg^{2+}). Also, phases that preferably partition iron can be stabilized at lower pressures, and this can counteract the thermal stabilizing effect of Al_2O_3. The preferential distribution of iron into phase E over phase A in our experiments with $Kd_{Fe\text{-}Mg}^{PhE/PhA}$ of 2.1 to 3.9, is therefore favoring a stabilization of phase E at lower pressures at the expense of phase A.

(3) Finally, phase E has been described with specific crystal features in the literature. For instance, it is characterized by its long-range cation disordered structure, as evidenced by the broad bands in its Raman spectrum (Kleppe and Jephcoat 2006). Phase E is a non-stoichiometric phase displaying variable composition (Kanzaki 1991; Kudoh et al. 1993). Based

on such particular features it has been discussed, whether phase E may be a quenched phase (Frost 1999, Stalder and Ulmer 2001). Phase E has been described as a metastable phase, based on a decrease in modal amount with run duration (Luth, 1995). Instead, we propose that it might have been missed in previous studies due to its very fine grain size. Indeed, in our experiments Al-bearing phase E appears as very small crystals (below 10 μm) mixed with enstatite in a fine and porous matrix (Figure VI-4). Based on this texture (which is similar to the one found in most experiments after antigorite breakdown), we suggest that phase E is in equilibrium with the following assemblages at 8 GPa: balangeroite + enstatite below 700°C, olivine + enstatite between 700 and 800°C, and phase A + enstatite at 9-10 GPa and 700-730°C.

The complex nature of the starting material addressed in this study allows depicting more realistic phase relations occurring beyond the antigorite stability, hence directly applicable to the slab dehydration in nature. In order to evaluate to a wider extent phase relations inferred by our experiments, we conducted a Schreinemakers analysis in the MASH system involving balangeroite and garnet in addition the other MSH phases (PhA, PhE, Ol and En). The presence of aluminum implies that garnet or Al-bearing phase E participate to the reactions. The Schreinemakers projection (Figure VI-9) has been constructed based on experimental results, together with the known stability of the invariant point at the lowest pressure with phase E + balangeroite as missing phases, designated as [PhE, Bal], and the invariant point [PhA,Grt] at the highest temperature and pressure (see also Komabayashi et al. 2005b). Phase relations involving balangeroite are degenerated as they plot in the tie-line joining phase A and phase E, thus reducing the number of reactions around invariant points from 5 to 4. Because among the DHMS aluminum is incorporated mainly in phase E, its stability field is displaced toward lower pressures making possible its coexistence with PhA + En, Bal + En, Grt + En and Ol + En. For instance, the terminal MSH univariant reaction of PhE,

$$PhE = En + Ol + H_2O \quad (1)$$

is displaced to lower pressure and transformed into the MASH univariant reaction (Fig. 9),

$$\text{Al-PhE} = \text{Grt} + \text{Ol} + H_2O \quad (2)$$

In between these two reactions the divariant assemblage Al-PhE + En + Ol + H_2O is stable.

Because Al-phase E is also approximately colinear with garnet and olivine (see Figure VI-2 and Figure VI-9), reaction (2) can be considered degenerated in the MASH system, thus involving 4 phases as in the MSH system. At the lower temperature side, when olivine is not stable the terminal reaction is not degenerated, and becomes,

$$\text{PhA} + \text{En} + \text{Grt} + H_2O = \text{Al-PhE} \quad (3)$$

The slope of reactions involving phase E are chosen to be intermediate between previous experiments and the thermodynamic predictions, although the thermodynamic parameters of Al-phase E are unknown. The coexistence of PhE + PhA + En at 10 GPa, 550°C and at 9 GPa, 730°C from this study is consistent with a pressure dependent negative Clapeyron slope of reaction 3 (as suggested by the equivalent MSH reaction PhA + En + H_2O = PhE, modeled by Komabayashi et al. 2005b).

Despite the prediction of assemblage PhA + En + Grt +H_2O on the low temperature side of reaction (3), we observe the assemblage composed of Mg-sursassite, enstatite and olivine in the experiment M638. The presence of Mg-sursassite at 8 GPa and 550°C is in agreement with its stability field of 6-9 GPa, up to 730°C reported in the MASH system (Bromiley and Pawley 2002) and at 6 GPa, 650°C reported in the Cr-MASH system (Fumagalli et al. 2014). Mg-sursassite could have crystallized in our samples as breakdown product of garnet. Such occurrence has indeed been observed from Mg-sursassite (MgMgAl-Pumpellyite, see Fockenberg, 1998) intergrowth with pyrope in natural samples. Moreover, the presence of olivine instead of phase A at these conditions, suggests the proximity of the invariant point [PhE, Bal]. As a consequence, the stability field of nominally anhydrous phases En + Ol + Grt

+H_2O is most likely extended to low temperatures and low pressures (below 8 GPa and 650°C, see Figure VI-9).

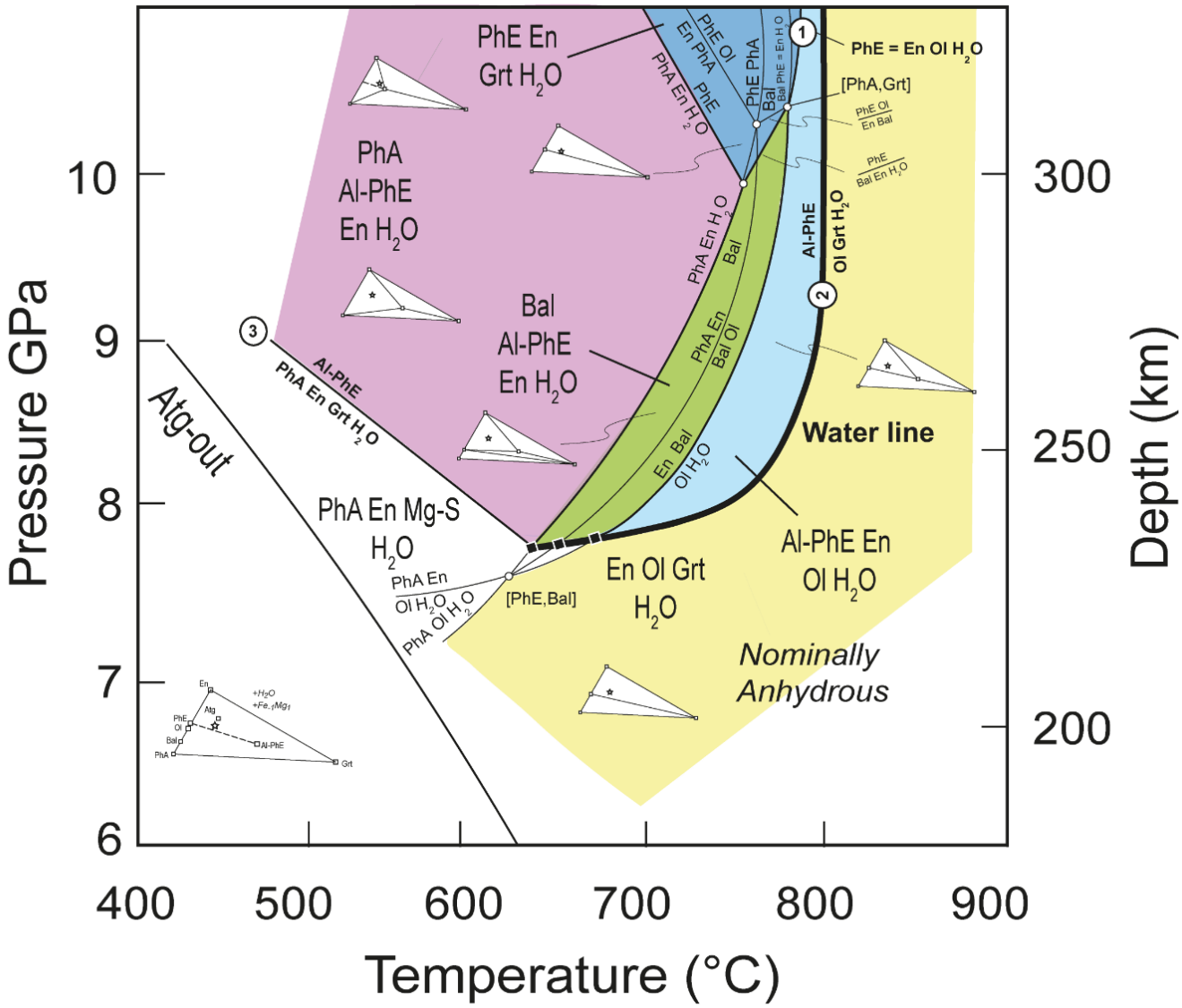

Figure VI-9. Qualitative phase diagram showing the stability field of phase assemblages for the natural serpentinite system based on the experimental results combined with a potential solution of the Schreinemaker's projection for the MgO-Al_2O_3-SiO_2-H_2O (MASH) system beyond the antigorite (Atg) stability at high-pressure. Phase considered involve the MSH phases, olivine (Ol), enstatite (En), Phase A (PhA), Phase E (PhE), Balangeroite (Bal) and aqueous fluid (H_2O), the MASH phase aluminum-bearing Phase E (Al-PhE) and the MAS phase garnet (Grt). Univariant reactions and invariant points are represented as thin lines and empty dots respectively. A part of the chemography relevant for the serpentinite bulk composition (white star) is shown in each stability field (cf.Figure VI-2.b).

Addressing the role of Cr is beyond the scope of this study, despite its undeniable contribution in affecting phase relations in complex chemical systems (Fumagalli et al., 2014). It can nevertheless be noted that the chromium content from the starting material (0.27 wt% Cr_2O_3, corresponding to a X_{Cr} of 0.1, with X_{Cr}=Cr/(Cr+Al)) is redistributed among the product phases in various amounts. Olivine, enstatite, phase A and balangeroite display relatively low Cr_2O_3 contents (<0.25 wt%). Likewise, Mg-sursassite contains small amounts of chromium, with less than 0.5 wt% Cr_2O_3. Garnet hosts higher amounts of chromium, with an average of 1.72 ± 0.22 wt% Cr_2O_3. Incorporation of chromium in Al-phase E seems to be pressure dependent, with contents decreasing from 1.48 ± 0.72 wt% Cr_2O_3 at 8.5 GPa to 0.38 ± 0.23 wt% Cr_2O_3 at 10 GPa. This suggests that similarly to Al, Cr could favor the stability of Al-phase E to lower pressures.

V.5 Implications for water transport

The boundary between structurally bound water and anhydrous assemblages was traditionally marked in the MSH system by the reaction PhA + En = Ol + H_2O, also defined as the "water line" by Liu (1987). In MgO enriched compositions, hydroxyl-clinohumite minerals are suggested to play an important role on water transfer in the mantle, after antigorite high-pressure destabilization and phase A high-temperature destabilization (Yamamoto and Akimoto 1977; Iwamori 2004). However, our results suggest that the water line in the MASH system is related to the aluminous phase E. We constrain that for temperatures higher than 750-800°C between 8 and 11 GPa, Al-PhE is no longer stable and the assemblage composed of nominally anhydrous minerals (olivine, enstatite and garnet) is found, in agreement with stability fields for nominally anhydrous mineral assemblages in the MSH system (Luth 1995; Komabayashi et al. 2005b) and in the MASH system (Kawamoto et al. 1995). Therefore, the

water line can be described with the final dehydration reaction (3) Al-PhE = Ol + Grt + H_2O, as it marks the boundary between structurally bound water and anhydrous assemblages for increasing PT (Figure VI-9). At high pressure, the location of the water line based on reaction (3) in the present study (see black line A on Figure VI-10) is displaced to approximately 250°C lower temperatures (i.e. 800°C) for pressures between 8 to 11 GPa, in comparison to the reaction involving the breakdown of clinohumite (black line B, Figure VI-10). This displacement to lower temperatures is also remarkable compared to the maximum thermal stability of the 23 Å phase, located between 8-12 GPa at 1000-1100°C (Cai et al. 2015). In our phase assemblages, the absence of clinohumite, the 23 Å phase and other lower pressure hydrous phases (i.e. intermediate pressure hydrous phases observed in various chemical compositions) can be related to differences in bulk composition, especially concerning Al and Fe^{3+}. For instance, the 10 Å phase was described as an important water carrier after antigorite breakdown in the MSH system (Fumagalli et al. 2001) while the other phases (HAPY, 11.5 Å, HySo) were observed in MASH and Cr-MASH systems with bulk Al contents significantly higher (3.95 to 28 wt% Al_2O_3, for anhydrous bulk composition) than the one displayed by the present starting natural serpentinite (0.97 Al_2O_3 wt% for the anhydrous bulk). These intermediate-pressure hydrous phases have been described at 5-7.5 GPa, for 650-800°C approximately. In our system, this domain covers mainly the low-temperature and low-pressure region of the stability field of nominally anhydrous minerals. Indeed, only garnet, enstatite and olivine are found at 6.5 GPa and 700°C. As a consequence, the hydrous versus nominally anhydrous phases boundary (i.e. the water line) appears to be displaced to lower PT while comparing to the stability domains of intermediate pressure hydrous phases mentioned above. On the other hand, our results are in agreement with the location of the 'choke point' traditionally described in MSH systems, based on the antigorite-phase A join, as the intersection of the PT path of the slab with the "water line".

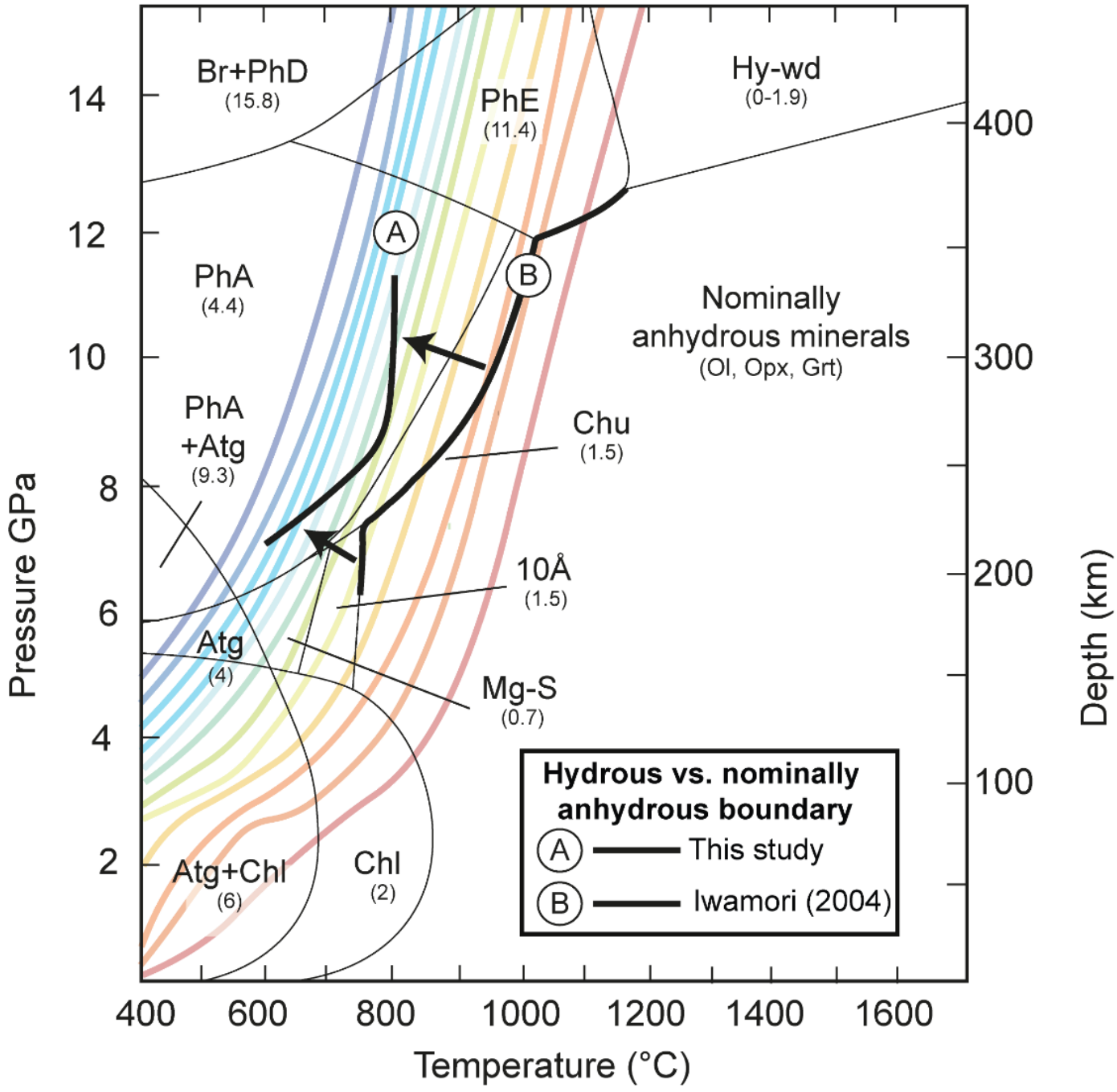

Figure VI-10. Phase diagram depicting the hydrous phases stability fields relevant for the hydrated peridotite composition (both MSH and MASH systems, see Iwamori, 2004). Colored lines represent most of the thermal range covered by slabs, after models in Syracuse et al. (2010) and van Keken et al. (2011). The "water line" defined for the natural antigorite system between 6.5 and 11 GPa is represented with the thick black line A, while the one corresponding to the hydrated peridotite from previous studies is shown with the line B. The boundaries of hydrous phases corresponds to experimental results: chlorite (Pawley, 2003); antigorite (Bromiley and Pawley, 2003); clinohumite (Yamamoto and Akimoto, 1977; Wunder, 1998;

Stalder and Ulmer, 2001); Mg-sursassite (Bromiley and Pawley, 2003); 10Å phase (Yamamoto and Akimoto, 1977; Fumagalli et al., 2001); phase A (Bose and Ganguly, 1995; Luth, 1995; Pawley and Wood, 1996); phase E (Kudoh et al., 1993; Kawamoto et al., 1995; Stalder and Ulmer, 2001), phase D (Frost and Fei, 1995; Shieh et al., 1995) and also from thermodynamic modelling for the high pressure stability of antigorite (Bose and Ganguly, 1995).

The initial water content (12.31 wt% H_2O) held by the starting antigorite material in the present experiments is mainly redistributed between balangeroite (11.1 wt% H_2O), phase A (11.3 wt% H_2O), Al-phase E (11.9 wt% H_2O) and an aqueous fluid phase. Based on the average water content calculated from stoichiometry for the hydrous phases and modal amounts of minerals in phase assemblages, water storage capacities have been calculated in both MSH and MASH systems. Such values are here reported as a theoretical maximum storage capacity (H_2O wt%) of a given phase assemblage. Nevertheless, the actual amount of water held by hydrous assemblages in a slab are limited by the field of minimum storage capacity crossed during descent. When antigorite breaks down at high pressure, the water storage capacities in the MASH system varies with increasing PT conditions according to the following sequence (H_2O wt%): 3.67 (PhA + En + Grt/Mg-S) / 4.89 (PhA + Al-PhE + En) / 5.69 (Bal+ Al-PhE + En) / 2.05 (Al-PhE + En + Ol). At higher temperature, the nominally anhydrous assemblage enstatite + olivine + garnet stability field marks the end of potential paths for slab containing H_2O structurally bound in hydrous minerals. In this field, water capacity is controlled by the solubility of hydrogen as point defects in nominally anhydrous minerals (Demouchy and Bolfan-Casanova 2016; Padrón-Navarta and Hermann 2017). It is worth noting that water storage capacity is higher in the MASH system due to lower pressure stability of PhE in comparison to the MSH system: 3.67 (PhA + En + Grt/Mg-S) / 3.67 (PhA + Al-PhE + En) / 4.30 (Bal+ Al-PhE + En). This suggests a possible underestimation of the amount of recycled water to the deep mantle from experiments or computation models performed in MSH systems.

It is worth noting that our results are based on the contribution of the hydrated ultramafic part of the slab only, which corresponds to the serpentinite layer of the slab. While the basalts and sediments in the upper crust are expected to dehydrate at relatively shallow depth in response to the high temperature experienced by the top of the slab, the lower units can allow water transfer to about 200 km depths, especially due to the survival of lawsonite and phengite present in the gabbro section in the deep crust layer (van Keken et al., 2011). While confronting the water line location established here at relatively low temperatures with the thermal models proposed in Syracuse et al. (2010) and in van Keken et al. (2011), water transfer in the mantle related to the serpentinite composition here investigated appears to be restricted only to the coldest slabs (Figure VI-10). Based on the phase relations observed in the present study, it is unlikely that a slab of intermediate to hot temperature would allow the transfer of water to depth. More precisely, a slab entering the >600°C region between 6-7 GPa is expected to dehydrate and could no longer transfer water to hydrated phase assemblages stables at higher pressures. Therefore, the terminal dehydration reaction Al-PhE = Grt + Ol + H_2O is unlikely to be crossed by a slab, preventing any important water release to happen into the mantle wedge between 8 and 11 GPa (i.e. between 250 and 350 km depth). On the other hand, cold slabs could allow water transfer to depth from antigorite high pressure domain and most efficiently via phase assemblages containing Mg-sursassite, phase A and Al-phase E. The successive stability of assemblages PhA + En + Grt/Mg-S and PhA + Al-PhE + En (below 650°C approximately) would permit the transfer of 3.7 wt% H_2O at maximum (limited by the water storage capacity of PhA + En + Grt/Mg-S). If non-fully dehydrated slabs enter the stability domains of assemblages Bal + Al-PhE + En and PhE + En + Grt (below 700-750°C) and Al-PhE + En + Ol (below 800°C), 2.0-3.7 wt% H_2O at maximum can be carried to deeper depths (Figure VI-9). Additionally, the hydrated deep crust layer of the slab most likely contributes to the water

transfer budget to depth with about 0.7 wt% bound H_2O in gabbro except in the case of the hottest subduction zones (van Keken et al., 2011).

As suggested by previous experimental studies, in the case of Si-enriched environments, water transfer could be possible for slabs of higher temperatures than inferred from our results, in the 5-7 GPa region (120-200 km) with the 10Å phase stability domain (Fumagalli and Poli 1999; Fumagalli et al. 2001). Likewise, in aluminum enriched environments, the stability of the HAPY, 11.5 Å or HySo phases could allow water transfer to higher pressure hydrous phases (Gemmi et al. 2011, 2016). Such Al- and Si-enriched compositions are particularly relevant in the context of "hybrid" rocks associated with subduction mélange zones (Spandler et al., 2008; Padrón-Navarta et al., 2010; Marchesi et al. 2013; Gemmi et al. 2001, 2016) and can at least locally have an impact on water transfer modalities in the deep mantle. Finally, the release of water in the case of relatively hot slabs occurs at shallower depth than those related to previous hydrous phases (i.e 100-130 km depth) and depends on Al-rich chlorite maximum thermal stability (Ulmer and Trommsdorff 1995; Bromiley and Pawley 2003; Till et al. 2012; Fumagalli et al. 2014). The water line at low pressure then relies on chlorite stability rather than hydrous phases such as antigorite or other DHMS.

Despite the restriction of water transfer in the deep mantle to the coldest slabs inferred by the present study, the recent discovery of hydrous ringwoodite in a diamond from Juina, Brazil (Pearson et al. 2014) demonstrates that water can still efficiently be carried (at least locally) by subduction to 520 km depth, corresponding to the transition zone. Indeed, the subducted character of the related fluids is evidenced by the crustal chemical signature of the inclusions (Eu anomalies in Ca-Mg perovskite and majoritic garnet; Harte, 2010) and the occurrence of Ca-Mg-Fe rich carbonates derived from oceanic sediments (Bulanova et al. 2010). In addition, this suggests that the down going hydrated lithosphere might not be limited to the pure serpentinite system. For example, natural occurrences of Si-enriched serpentinites

have been locally observed in the massif of Cerro del Almirez (Padrón-Navarta et al. 2010, 2011; Marchesi et al. 2013). Indeed, mixing at the slab-mantle interface can produce hybrid rocks (Bebout et al., 2002), allowing the formation of silica or alumina enriched serpentinites depending on interactions with talc or chlorite for example (Spandler et al., 2008). Despite the difficulty to precisely constrain heterogeneities in serpentinite compositions, the existence of local Si- or Al-rich systems associated with mélange zones can explain the possibility of deeper water transfer than inferred from the present study.

VI **Conclusions**

The stability of hydrous phase beyond antigorite breakdown in the natural system has been experimentally constrained. When compared to previous works, our experimental results show different locations for phase A and phase E stability fields, with the stabilization of aluminum rich phase E to lower pressure. The role of magnetite is also further confirmed in post antigorite phase relations. The presence of magnetite is required to mass balance iron contents of phase assemblages in the natural system. In particular, it could play an important role stabilizing phase E and balangeroite. Investigation in the natural antigorite composition allows for constraining the reaction Al-PhE = Ol + Grt + H_2O as a novel characterization of the "water line", that cannot be observed in the MSH system. Indeed, the particularity of this natural system is that Al-rich phase E replaces phase A in the terminal reaction involved in the thermal boundary with nominally anhydrous mineral domain. Related to the extension of phase E stability to lower pressure conditions, a higher water storage capacity has been demonstrated in the MASH system compared to the MSH system. The "water line" established based on the present experiments is however located at lower temperatures compared to previous experimental studies conducted in simplified MSH ($\pm Al_2O_3$) systems (Kawamoto et al. 1995;

Luth 1995). As a consequence, water transfer to the deep mantle is restricted to the coldest slabs. The present "water line" depicts a positive slope below 8 GPa, between 600°C and 800°C, continued in a sub-vertical fashion at 800° between 8 and 11 GPa. This geometry defines a region of anhydrous phase assemblages' stability for the natural serpentinite. This domain is of similar nature than the "choke point" defined in (Kawamoto et al. 1995). Such a "choke point" implies the dehydration of phase assemblages for slabs of cold to intermediate temperatures, before entering the stability field of assemblages containing balangeroite and Al-phase E, and limits efficient water transfer to the very low portion of cold slabs, via assemblages containing Mg-sursassite + Phase A and Phase A + Al-Phase E.

Acknowledgements

We gratefully acknowledge constructive reviews by R. Stalder, P. Fumagalli and K. Iacovino and the editorial handling. We thank D. Mainprice for providing us with the natural sample of serpentinite that was used for our experiments. This study is part of J. Maurice PhD financed by the ANR HYDEEP "Hydrogen in the Deep Earth" project to N. Bolfan-Casanova and the ANR OxyDeep project to Denis Andrault. We also thank J.-L. Devidal (Laboratoire Magmas et Volcans, Clermont-Ferrand) for his assistance during microprobe analysis, F. Schiavi (LMV, Clermont-Ferrand) for Raman analyses support, P. Bouilhol (CRPG, Nancy) for instructive discussions and assistance during garnets Fe^{3+} measurements using the flank method. We thank L. Jouffret (Institut de Chimie, Clermont-Ferrand) for providing balangeroite X-Ray single crystal structure refinement. This is Laboratory of Excellence Clervolc contribution number XXX.

References

Andreani M, Muñoz M, Marcaillou C, Delacour A (2013) μXANES study of iron redox state in serpentine during oceanic serpentinization. Lithos 178:70–83

Artioli, G, Fumagalli, P & Poli, S (1999) The crystal structure of $Mg_8Mg_2Al_2Al_8Si_{12}(O,OH)_{56}$ pumpellyite and its relevance in ultramafic systems at high pressure. Am Mineral 84:1906–1914.

Auzanneau E, Vielzeuf D, Schmidt MW (2006) Experimental evidence of decompression melting during exhumation of subducted continental crust. Contrib to Mineral Petrol 152:125–148.

Bean VE, Akimoto S, Bell PM, Block S, Holzapfel WB, Manghnani MH, Nicol MF, Stishov SM (1986) Another step toward an international practical pressure scale: 2nd AIRAPT IPPS task group report. Phys B+C 139–140:52–54

Bebout GE, Barton MD (2002) Tectonic and metasomatic mixing in a high-T, subduction-zone mélange-insights into the Geochemical evolution of the slab–mantle interface. Chem Geol 187:79–106

Bonaccorsi E, Ferraris G, Merlino S (2012) Crystal structure of 2M and 1A polytypes of balangeroite. Zeitschrift für Krist 227:460–467

Bose K, Ganguly J (1995) Quartz-coesite transition revisited: Reversed experimental determination at 500-1200 °C and retrieved thermochemical properties. Am Mineral 80:231–238

Brey GP, Köhler T (1990) Geothermobarometry in Four-phase Lherzolites II. New Thermobarometers, and Practical Assessment of Existing Thermobarometers. J Petrol 31:1353–1378

Bromiley GD, Pawley AR (2002) The high-pressure stability of Mg-sursassite in a model hydrous peridotite: a possible mechanism for the deep subduction of significant volumes of H_2O. Contrib to Mineral Petrol 142:714–723

Bromiley GD, Pawley AR (2003) The stability of antigorite in the systems MgO-SiO_2-H_2O (MSH) and MgO-Al_2O_3-SiO_2-H_2O (MASH): The effects of Al^{3+}substitution on high-pressure stability. Am Mineral 88:99–108

Bulanova GP, Walter MJ, Smith CB, Kohn SC, Armstrong LS, Blundy J, Gobbo L (2010) Mineral inclusions in sublithospheric diamonds from Collier 4 kimberlite pipe, Juina, Brazil: subducted protoliths, carbonated melts and primary kimberlite magmatism. Contrib to Mineral Petrol 160:489–510

Cai N, Inoue T, Fujino K, Ohfuji H, Yurimoto H (2015) A possible new Al-bearing hydrous Mg-silicate (23 Å phase) in the deep upper mantle. Am Mineral 100:2330–2335

Capitani G, Mellini M (2004) The modulated crystal structure of antigorite: the m = 17 polysome. Am Mineral 89:147–158

Compagnoni R, Ferraris G, Fiora L (1983) Balangeroite, a new fibrous silicate related to gageite from Balangero, Italy. Am Mineral 68:214-219

Connolly JAD (2009) The geodynamic equation of state: What and how. Geochemistry, Geophys Geosystems 10:10

Debret B, Bolfan-Casanova N, Padrón-Navarta JA, Martin-Hernandez F, Andreani M, Garrido CJ, López Sánchez-Vizcaíno V, Gómez-Pugnaire MT, Muñoz M, Trcera N (2015) Redox state of iron during high-pressure serpentinite dehydration. Contrib to Mineral Petrol 169:36

Demouchy S, Bolfan-Casanova N (2016) Distribution and transport of hydrogen in the lithospheric mantle: A review. Lithos 240–243:402–425

Deriu A, Ferraris G, Belluso E (1994) ^{57}Fe Mössbauer study of the asbestiform silicates balangeroite and carlosturanite. Phys Chem Miner 21:222-227

Deschamps F, Godard M, Guillot S, Hattori K (2013) Geochemistry of subduction zone serpentinites: A review. Lithos 178:96-127

Droop GTR (1987) A general equation for estimating Fe^{3+} concentrations in ferromagnesian silicates and oxides from microprobe analyses, using stoichiometric criteria. Mineral Mag 51:431–5

Evans BW, Dyar MD, Kuehner SM (2012) Implications of ferrous and ferric iron i antigorite. Am Mineral 97:184–196

Fockenberg T (1998) An experimental study of the pressure-temperature stability of MgMgAl-pumpellyite in the system MgO-Al_2O_3-SiO_2-H_2O. Am Mineral 83:220–227

Frost DJ, Fei Y (1998) Stability of phase D at high pressure and high temperature. J Geophys Res Solid Earth 103:7463–7474

Frost DJ (1999) The stability of dense hydrous magnesium silicates in earth's transition zone and lower mantle. In: Geochemical Society Special Publication, Houston T (ed) Mantle Petrology: Field observations and High-pressure Experimentation, Geochemica. Y. fei, C.M. Bertka, and B.O. Mysen, Eds., pp 283–296

Fumagalli P, Poli S (1999) Phase relationships in hydrous peridotites at high pressure: preliminary results of multi-anvil experiments. Period di Mineral 68:275–286

Fumagalli P, Stixrude L, Poli S, Snyder D (2001) The 10Å phase: a high-pressure expandable sheet silicate stable during subduction of hydrated lithosphere. Earth Planet Sci Lett 186:125–141

Fumagalli P, Poli S (2005) Experimentally Determined Phase Relations in Hydrous Peridotites to 6.5 GPa and their Consequences on the Dynamics of Subduction Zones. J Petrol 46:555–578

Fumagalli P, Poli S, Fischer J, Merlini M, Gemmi M (2014) The high-pressure stability of chlorite and other hydrates in subduction mélanges: experiments in the system Cr_2O_3–MgO–Al_2O_3–SiO_2–H_2O. Contrib to Mineral Petrol 167:979

Fumagalli P, Klemme S (2015) 2.02 – Mineralogy of the Earth: Phase Transitions and Mineralogy of the Upper Mantle. In: Treatise on Geophysics. pp 7–31

Gemmi M, Fischer J, Merlini M, Poli S, Fumagalli P, Mugnaioli E, Kolb U (2011) A new hydrous Al-bearing pyroxene as a water carrier in subduction zones. Earth Planet Sci Lett 310:422–428

Gemmi M, Merlini M, Palatinus L, Fumagalli P, Hanfland M (2016) Electron diffraction determination of 11.5 Å and HySo structures: Candidate water carriers to the Upper Mantle. Am Mineral 101:2645–2654

Groppo C, Compagnoni R (2007) Metamorphic veins from the serpentinites of the Piemonte Zone, western Alps, Italy: a review. Period di Mineral 76:95–124

Grützner T, Klemme S, Rohrbach A, Gervasoni F, Berndt J (2017) The role of F-clinohumite in volatile recycling processes in subduction zones. *Geology 45*: 443–446

Hammouda T (2003) High-pressure melting of carbonated eclogite and experimental constraints on carbon recycling and storage in the mantle. Earth Planet Sci Lett 214:357–368

Harte B (2010) Diamond formation in the deep mantle: the record of mineral inclusions and their distribution in relation to mantle dehydration zones. Mineral Mag 74:189–215

Hattori KH, Guillot S (2007) Geochemica acter of serpentinites associated with high- to ultahigh-pressure metamorphic rocks in the Alps, Cuba, and the Himalayas: Recycling of elements in subduction zones. Geochemistry, Geophys Geosystems 8, pp.Q09010l char

Hernlund J, Leinenweber K, Locke D, Tyburczy JA (2006) A numerical model for steady-state temperature distributions in solid-medium high-pressure cell assemblies. Am Mineral 91:295-305

Höfer HE, Brey GP (2007) The iron oxidation state of garnet by electron microprobe: Its determination with the fl ank method combined with major-element analysis. Am Mineral 92:873–885.

Holl CM, Smyth JR, Manghnani MH, Amulele GM, Sekar M, Frost DJ, Prakapenka VB, Shen G (2006) Crystal structure and compression of an iron-bearing Phase A to 33 GPa. Phys Chem Miner 33:192–199

Holland TJB, Powell R (2011) An improved and extended internally consistent thermodynamic dataset for phases of petrological interest, involving a new equation of state for solids. J Metamorph Geol 29:333–383

Inoue T (1994) Effect of water on melting phase relations and melt composition in the system Mg_2SiO_4-$MgSiO_3$-

H_2O up to 15 GPa. Phys Earth Planet Inter 85:237–263

Irifune T, Kubo N, Isshiki M, Yamasaki Y (1998) Phase transformations in serpentine and transportation of water into the lower mantle. Geophys Res Lett 25:203–206

Iwamori H (2004) Phase relations of peridotites under H_2O-saturated conditions and ability of subducting plates for transportation of H_2O. Earth Planet Sci Lett 227:57-71

Kanzaki M (1991) Stability of hydrous magnesium silicates in the mantle transition zone. Phys Earth Planet Inter 66:307–312

Kawamoto T, Leinenweber K, Hervig RL, Holloway JR (1995) Stability of hydrous minerals in H_2O-saturated KLB-1 peridotite up to 15 GPA. In: AIP Conference Proceedings. AIP, pp 229–239

Kawamoto T, and Holloway JR (1997) Melting Temperature and Partial Melt Chemistry of H_2O-Saturated Mantle Peridotite to 11 GPa. Science (80) 276:240–243

Kawamoto T (2004) Hydrous phase stability and partial melt chemistry in H_2O-saturated KLB-1 peridotite up to the uppermost lower mantle conditions. Phys Earth Planet Inter 143144:387–395

Kleppe AK, Jephcoat AP (2013) Raman Spectroscopic Studies of Hydrous and Nominally Anhydrous Deep Mantle Phases. In: Geophysical Monograph Series. pp 69–93

Komabayashi T, Hirose K, Funakoshi K, Takafuji N (2005a) Stability of phase A in antigorite (serpentine) composition determined by in situ X-ray pressure observations. Phys Earth Planet Inter 151:276–289

Komabayashi T, Omori S, Maruyama S (2005b) Experimental and theoretical study of stability of dense hydrous magnesium silicates in the deep upper mantle. Phys Earth Planet Inter 153:191–209

Komabayashi T (2006) Phase relations of hydrous peridotite: Implications for water circulation in the Earth's mantle. American Geophysical Union, pp 29–43

Kudoh Y, Finger LW, Hazen RM, (1993) Phase E: A high pressure hydrous silicate with unique crystal chemistry. Phys Chem Miner 19:357-360

Liu L (1987) Effects of H_2O on the phase behaviour of the forsterite-enstatite system at high pressures and temperatures and implications for the Earth. Phys Earth Planet Inter 49:142–167

Liu L, Lin CC, Mernagh TP, Irifune T (1997a) Raman spectra of phase A at various pressures and temperatures. J Phys Chem Solids 58:2023–2030

Liu L, Mernagh TP, Lin CC, Irifune T (1997b) Raman spectra of phase E at various pressures and temperatures with geophysical implications. Earth Planet Sci Lett 149:57–65

Luth RW (1995) Is phase A relevant to the Earth's mantle? Geochim Cosmochim Acta 59:679–682

Marchesi, C., Garrido, C.J., Padrón-Navarta, J.A., López Sánchez-Vizcaíno, V., Gómez-Pugnaire, M.T., 2013. Element mobility from seafloor serpentinization to high-pressure dehydration of antigorite in subducted serpentinite: Insights from the Cerro del Almirez ultramafic massif (southern Spain). Lithos 15, 128–142.

Merkulova M, Muñoz M, Vidal O, Brunet F (2016) Role of iron content on serpentinite dehydration depth in subduction zones: Experiments and thermodynamic modeling. Lithos 254: 441-452

Mibe K, Fujii T, Yasuda A (2002) Composition of aqueous fluid coexisting with mantle minerals at high pressure and its bearing on the differentiation of the Earth's mantle. Geochim Cosmochim Acta 66:2273–2285

Niida K, Green DH (1999) Stability and chemical composition of pargasitic amphibole in MORB pyrolite under upper mantle conditions. Contrib to Mineral Petrol 135:18–40

Nishi M, Irifune T, Tsuchiya J, Tange Y, Nishihara Y, Fujino K, Higo.Y (2014) Stability of hydrous silicate at high pressures and water transport to the deep lower mantle. Nat Geosci 7:224–227

Padrón-Navarta JA, Hermann J, Garrido CJ, et al (2010) An experimental investigation of antigorite dehydration in natural silica-enriched serpentinite. Contrib to Mineral Petrol 159:25–42

Padrón-Navarta JA, López Sánchez-Vizcaíno V, Garrido CJ, Gómez-Pugnaire MT (2011) Metamorphic Record of High-pressure Dehydration of Antigorite Serpentinite to Chlorite Harzburgite in a Subduction Setting

(Cerro del Almirez, Nevado-Filabride Complex, Southern Spain). J Petrol 52:2047–2078

Padrón-Navarta JA, Sánchez-Vizcaíno VL, Hermann J, Connolly JAD, Garrido CJ, Gómez-Pugnaire MT, Marchesi C (2013) Tschermak's substitution in antigorite and consequences for phase relations and water liberation in high-grade serpentinites. Lithos 178:186–196

Padrón-Navarta JA, Hermann J (2017) A Subsolidus Olivine Water Solubility Equation for the Earth's Upper Mantle. J Geophys Res Solid Earth 122:9862–9880

Pamato MG, Myhill R, Boffa Ballaran T, Frost DJ, Heidelbach F, Miyajima N (2014) Lower-mantle water reservoir implied by the extreme stability of a hydrous aluminosilicate. Nat Geosci 8:75–79

Pawley AR, Wood BJ (1996) The low-pressure stability of phase A, $Mg_7Si_2O_8(OH)_6$. Contrib to Mineral Petrol 124:90–97

Pawley A (2003) Chlorite stability in mantle peridotite: the reaction clinochlore + enstatite = forsterite + pyrope + H_2O Contrib to Mineral Petrol 144:449–456

Pearson DG, Brenker FE, Nestola F, McNeill J, Nasdala L, Hutchison MT, Matvee S, Mather K, Silversmit G, Schmitz S, Vekemans B, Vincze L (2014) Hydrous mantle transition zone indicated by ringwoodite included within diamond. Nature 507:221–4

Schmidt MW, Poli S (2014) Devolatilization During Subduction. In: Treatise on Geochemistry. Elsevier, pp 669–701

Schmidt MW, Poli S (1998) Experimentally based water budgets for dehydrating slabs and consequences for arc magma generation. Earth Planet Sci Lett 163:361–379

Schwartz S, Guillot S, Reynard B, Lafay R, Debret B, Nicollet C, Lanari P, Auzende AL (2013) Pressure–temperature estimates of the lizardite/antigorite transition in high pressure serpentinites. Lithos 178:197–21

Shieh SR, Mao Hk, Hemley RJ, Ming LC (1998) Decomposition of phase D in the lower mantle and the fate of dense hydrous silicates in subducting slabs, Earth Planet Sci Lett 159:13–23

Spandler C, Hermann J, Faure K, Mavrogenes J, Arculus R (2008) The importance of talc and chlorite ''hybrid'' rocks for volatile recycling through subduction zones; evidence from the high-pressure subduction mélange of New Caledonia. Contrib Mineral Petrol 155:181–198

Stalder R, Ulmer P (2001) Phase relations of a serpentine composition between 5 and 14 GPa: significance of clinohumite and phase E as water carriers into the transition zone. Contrib to Mineral Petrol 140:670–679

Stalder R, Ulmer P, Thompson A, Günther D (2001) High pressure fluids in the system $MgO–SiO_2–H_2O$ under upper mantle conditions. Contrib to Mineral Petrol 140:607–618

Syracuse EM, van Keken PE, Abers GA (2010) The global range of subduction zone thermal models. Phys Earth Planet Inter 183:73–90

Taylor WR, Green DH (1988) Measurement of reduced peridotite-C-O-Hsolidus and implications for redox melting of the mantle. Nature 332:349–352

Till CB, Grove TL, Withers AC (2012) The beginnings of hydrous mantle wedge melting. Contrib to Mineral Petrol 163:669–688

Torres-Roldán, R.L., García-Casco, A., García-Sanchez, P.A., 2000. CSpace: an integrated workplace for the graphical and algebraic analysis of phase assemblages on 32-bit wintel platforms. Comput. Geosci. 26, 779-793.

Trommsdorff V, Evans BW (1974) Alpine metamorphism of peridotitic rocks. Schweizerische Mineral und Petrogr Mitteilungen 54:333–354

Trommsdorff V, Sánchez-Vizcaíno VL, Gómez-Pugnaire MT, Müntener O (1998) High pressure breakdown of antigorite to spinifex-textured olivine and orthopyroxene, SE Spain. Contrib to Mineral Petrol 132:139–148

Ulmer P, Trommsdorff V (1995) Serpentine stability to mantle depths and subduction-related magmatism. Science 268:858–861

Ulmer P, Trommsdorff V (1999) Phase relations of hydrous mantle subducting to 300 km. In: Fei Y-W, Bertka C, Mysen BO (eds) Mantle petrology: field observations and high pressure experimentation: a Tribute to Francis R. (Joe) Boyd. Geochem Soc Spec Publ 6:259–281

Ulmer, P. and Stalder, R. (2001) The $Mg(Fe)SiO_3$ orthoenstatite-clinoenstatite transitions at high pressures and temperatures determined by Raman-spectroscopy on quenched samples. Am Mineral 86:1267–1274

van Keken PE, Hacker BR, Syracuse EM, Abers GA (2011) Subduction factory: 4. Depth-dependent flux of H_2O from subducting slabs worldwide. J Geophys Res 116:B01401

Whitney DL, Evans BW (2010) Abbreviations for names of rock-forming minerals. Am Mineral 95:185–187

Wunder B (1998) Equilibrium experiments in the system MgO-SiO_2 -H_2O (MSH): stability fields of clinohumite-OH [$Mg_9Si_4O_{16}(OH)_2$], chondrodite-OH [$Mg_5Si_2O_8(OH)_2$] and phase A ($Mg_7Si_2O_8(OH)_6$). Contrib to Mineral Petrol 132:111–120

Wunder B, Schreyer W (1997) Antigorite: High-pressure stability in the system MgO-SiO_2-H_2O (MSH). Lithos 41:213–227

Wunder B, Wirth R, Gottschalk M (2001) Antigorite: Pressure and temperature dependence of polysomatism and water content. Eur J Mineral 13:485–495

Yamamoto K, Akimoto SI (1974) High pressure and high temperature investigations in the system MgO-SiO_2-H_2O. J Solid State Chem 9:187–195

Yamamoto K, Akimoto S (1977) The system MgO-SiO_2-H_2O at high pressures and temperatures; stability field for hydroxyl-chondrodite, hydroxyl-clinohumite and 10Å-phase. Am J Sci 277:288–312

Zhang J, Li B, Utsumi W, Liebermann R (1996) In situ X-ray observations of the coesite-stishovite transition: reversed phase boundary and kinetics. Phys Chem Miner 23:1–10

Chapter VII - Discussion

I Comparison with simple system models and the importance of accurate thermodynamic properties

I.1 Why using thermodynamic models in addition to experimentally deduced phase diagrams?

I.2 Development of database for minerals thermodynamic properties

I.3 Computation of models in simple systems using Perplex versus phase relations experimentally observed in this study

I Comparison with simple system models and the importance of accurate thermodynamic properties

I.1 Why using thermodynamic models in addition to experimentally deduced phase diagrams?

The results from our experimental investigation allowed us to constrain the stability of mineral assemblages in the natural serpentinite system at a given pressure and temperature conditions. Together with the Schreinemakers analysis conducted in the simplified MASH system, experimentally determined phase assemblages were used to develop a petrogenetic grid. This approach is used to understand phase relations in a more comprehensive way, but remains qualitative. Constraining more precisely phase boundaries as a function of pressure and temperature for a given composition can nonetheless be performed using thermodynamic calculations. Indeed, bracketing precisely phase boundaries solely via experimentation can represent a tedious task for few reasons. For instance, the extremely slow kinetics for low temperature reactions and the difficulty of establishing reversal of reactions when solid solutions and continuous reactions are involved justify the use of a complementary approach based on calculations. Nevertheless, our experiments showed a good quality of texture (for instance, see optical microscopy, and back-scattered electron images (see Figure VI-4 for example) and local equilibrium was achieved. These two particularities (kinetics and solid solutions) are actually participating in the challenging character of phase equilibria study in the complex chemical system investigated here. Indeed, in the down going slab, dehydration reactions occur at relatively low temperature for equilibration kinetics (below 700-900°C). Moreover, in a natural rock sample, the complexity of the chemical system implies solid solutions, especially between Mg and Fe end-members but also in phase E, which displays complex solid solution involving Al (Frost, 1999). Needless to say that ferric iron is never

accounted for in the thermodynamic calculations performed on such systems (see Merkulova et al., 2016) and rarely measured (except for some exceptions on natural samples: Debret et al., 2014; 2015) given the small grain sizes involved.

I.2 Development of database for minerals thermodynamic properties

Perplex (Connolly, 2005) like other software packages (Theriak-Domino, by de Capitani and Petrakakis, 2010) offers the possibility of calculating equilibrium phase assemblages relying on thermodynamic databases and activity models for solid solutions, which are obtained via experimental methods. Since the 80's the interest in constructing such database greatly increased, supported by advances in computational modelling using softwares and experimental studies of phase equilibria. For instance, works from Holland and Powell and coworkers (but not only) in this topic have largely contributed to improve databases of minerals, aqueous, and silicate fluids thermodynamic properties. The thermodynamic databases consist of a compilation of calorimetrically derived data and tabulations based on analyses of phase equilibria. The latter are assessed on the basis of experimentally retrieved parameters for mineral species as well as natural mineral partitioning. Evaluation of phase reactions relies on the calculation of the Gibbs free energy for each mineral species knowing the enthalpy, entropy, volume, heat capacity, thermal expansion and compressibility of each phase. The method used in models developed by Holland and Powell (Holland and Powell, 2004, 1998, 1991), among others, consists in obtaining the enthalpy of formation of mineral end-members by using the center value of reaction brackets enthalpy (from experiments) weighted by a least squares approach (cumulative enthalpy). A large end-members database further enables the estimation of solid solution thermodynamic parameters. Prediction of mineral equilibria for reactions that have not been experimentally determined can be deduced from calorimetric measurements. Unlike enthalpy quantities, those of entropy, volume, heat capacity, thermal expansion and

compressibility are not derived by regressions from experimentally bracketed reactions but taken directly from measurements. For instance, Holland and Powell (1989) used heat capacity experimental determination to conduct direct integration of entropy for mineral end-members. When appropriate, entropy was adjusted by regressions to improve agreement with experimentation. Despite the vast number of thermodynamically based models for phase equilibria, a convergence of dataset proposed can be observed. As a result, phase diagram constructions based on available data are conceivable. Even though thermodynamic calculation is of undeniable help in extrapolating experimental observation, assessing the thermodynamic quantities necessary for this purpose also rely on experimental data. Unfortunately, no such information is yet available for complex chemical system such as that one studied in this thesis.

I.3 Computation of models in simple systems using Perplex versus phase relations experimentally observed in this study

A Shreinemakers grid has been computed for the MSH system using the database proposed by Holland and Powell for the mineral species (1998, updated in 2002) and the CORK EoS for H_2O (Holland and Powell, 1991) between 5 and 10 GPa and temperatures ranging from 400 to 900°C (**Erreur ! Source du renvoi introuvable.**Figure VII-1.a). Equilibria involving quartz polymorphs are not shown. **Erreur ! Source du renvoi introuvable.**.Figure VII-1.b displays a refined petrogenetic grid for a pure antigorite bulk composition $Mg_{48}Si_{34}O_{85}(OH)_{62}$. For both models, phases encountered are antigorite, phase A, balangeroite, brucite, forsterite, enstatite and a fluid phase. Garnet is not present in this model because it is an aluminium-bearing phase. Although Phase E can exist in the MSH system, its thermodynamic properties are not existing in the database used to build these models. On one hand, the Schreinemakers petrogenetic grid for the MSH system evaluates all possible compositions and displays all the associated mineral combinations (a). On the other hand, the pseudo-section computed in the

antigorite bulk composition (b) refines the possible combinations to those corresponding specifically to the antigorite composition.

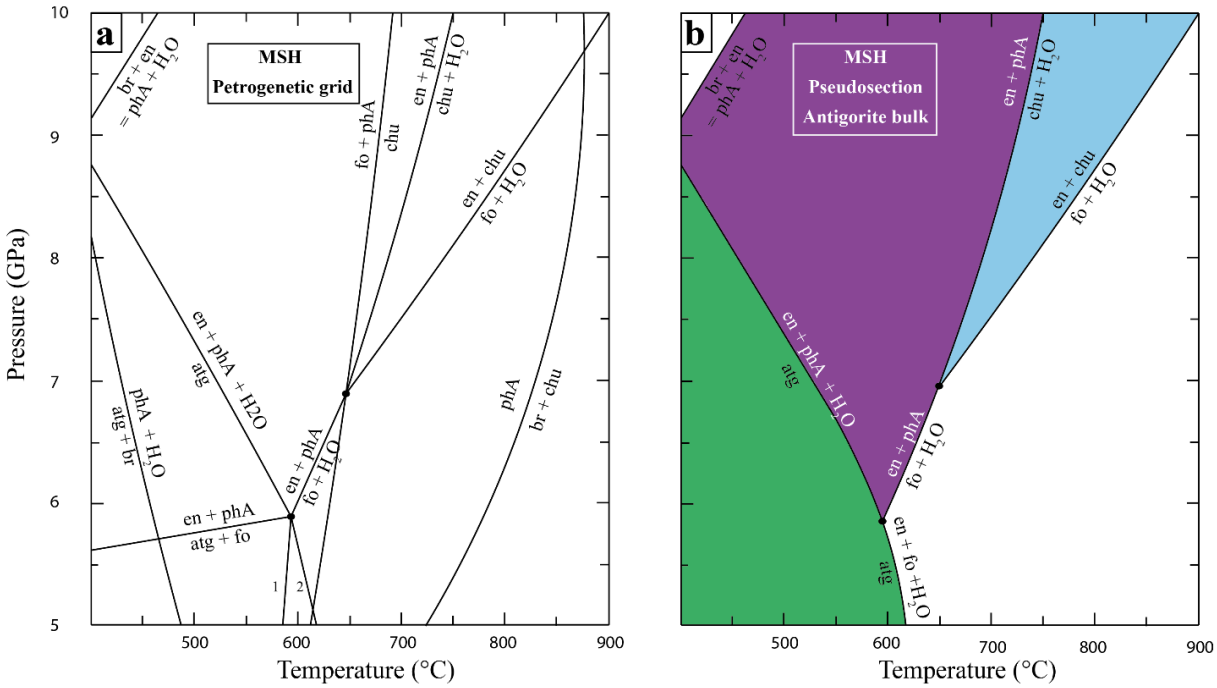

Figure VII-1 : a. Schreinemaker's grid in the MSH system. Phase boundaries were established using the database from Holland and Powell (1998, updated in 2002) and the CORK EoS for H_2O from Holland and Powell (1991). Reaction 1: atg + phA = fo +H_2O. Reaction 2: atg = en + fo + H_2O. b. Pseudo-section in the MSH for a pure antigorite bulk of the composition $Mg_{48}Si_{34}O_{85}(OH)_{62}$.

Differences exist between phase assemblages experimentally produced in the natural system and those predicted in the MSH system (Figure VII-2). First, it is worth noting that out of 11 experiments, 7 are in agreement with the predicted stability fields, if not considering garnet and phase E, absent from the model. The main differences are that we did not observe phase A at 650 (8-8.5 GPa) and 700°C (8.5 GPa), while it is expected in the computation. Likewise, balangeroite is produced after antigorite dehydration at 8.5 GPa and 650°C while it is not expected in the MSH system. Also, in our experiments antigorite remains until 8 GPa and

650°C, possibly locating the maximum thermal boundary for antigorite while in the MSH system it disappears at 450°C.

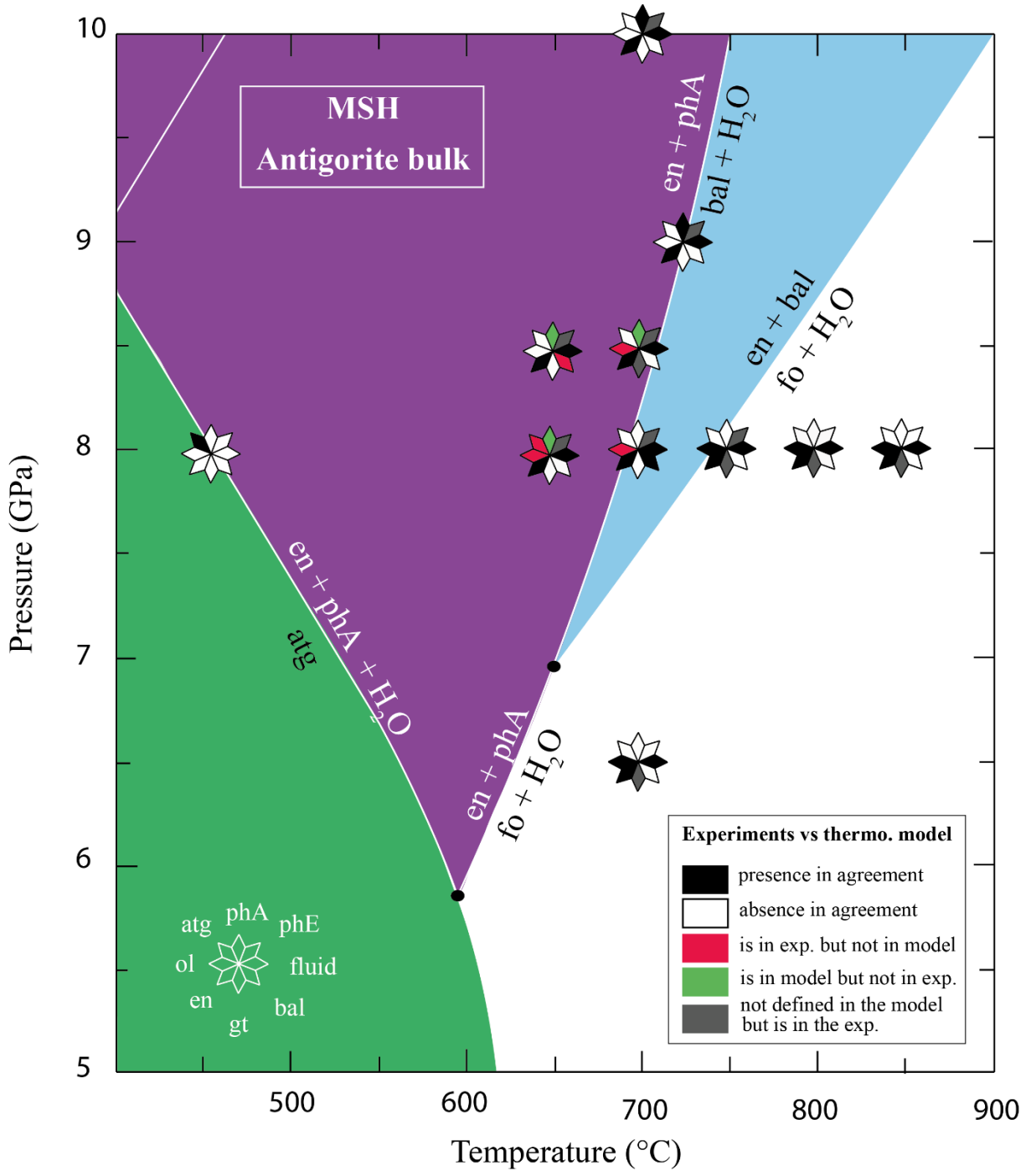

Figure VII-2. Pseudo-section produced in the MSH system for the antigorite composition and comparison with experimental phase assemblages observed in this study (flowers symbols). Black petals correspond to minerals that were both observed in the experimental products and predicted by the thermodynamic calculation using Perplex. White petals correspond to minerals that are not expected from the model and that we don't observe experimentally. In red are the phases that appeared in the experiment while not being

predicted in the model, while green petals correspond to the reverse situation. Grey petals describe minerals that we observed but that do not belong to the MSH system (garnet and phase E).

In order to understand the effect of Fe on phase stability, a pseudosection has been constructed, using a similar composition to the one of our starting material (Figure VII-3.a). The two bulk compositions investigated correspond to $Mg_{46.56}Fe_{1.44}Si_{34}O_{85}(OH)_{62}$, equivalent to an X_{Mg} of 0.97, and $Mg_{46.08}Fe_{1.92}Si_{34}O_{85}(OH)_{62}$ corresponding to X_{Mg} = 0.96. In comparison to the MSH system phase relations for the antigorite bulk in the FMSH system present some discrepancies with our experimental observations. The introduction of Fe-Mg solid solutions, induces new stability domains. In particular, we observe the appearance of divariant and trivariant fields. The stability field of phase A + enstatite + H_2O assemblage is considerably reduced, down to 7.5 GPa at < 500°C and > 9.5 GPa at 900°C, the brucite-bearing assemblage gaining stability at lower temperatures. In the FMSH system, antigorite destabilization occurs at lower pressure and temperature conditions of approximately 1 GPa and 100°C compared to the MSH system. The invariant point atg-phaseA-en-fo-H_2O has not moved.

In order to evaluate the variations of phase boundaries locations that are directly related to those of the iron bulk content a second pseudo-section in the FMSH system has been produced with a different iron content (Figure VII-3.b). Even the small increase in iron concentration from an X_{Mg} of 0.97 to 0.96 can affect phase stability. For instance, the clinohumite-bearing assemblage enstatite + olivine + clinohumite + H_2O is expanded towards higher temperature by about 150 degrees at around 8 GPa, with decreasing iron content from X_{Mg}=1.00 to X_{Mg}=0.96. This allows to quantify the effect of iron on clinohumite stability: 37.5°C / 0.01 X_{Mg}. It is also interesting to observe that while antigorite is stabilized of 100°C at 8 GPa by the simple addition of iron, its thermal stability is not changed by further addition of Fe.

Antigorite stability is displaced to higher pressure of about 0.5 GPa, at the expense of the divariant fields antigorite+ enstatite + brucite + H_2O, antigorite + enstatite + phase A + H_2O and antigorite+ enstatite + olivine + H_2O. Such a modification can have important effect on

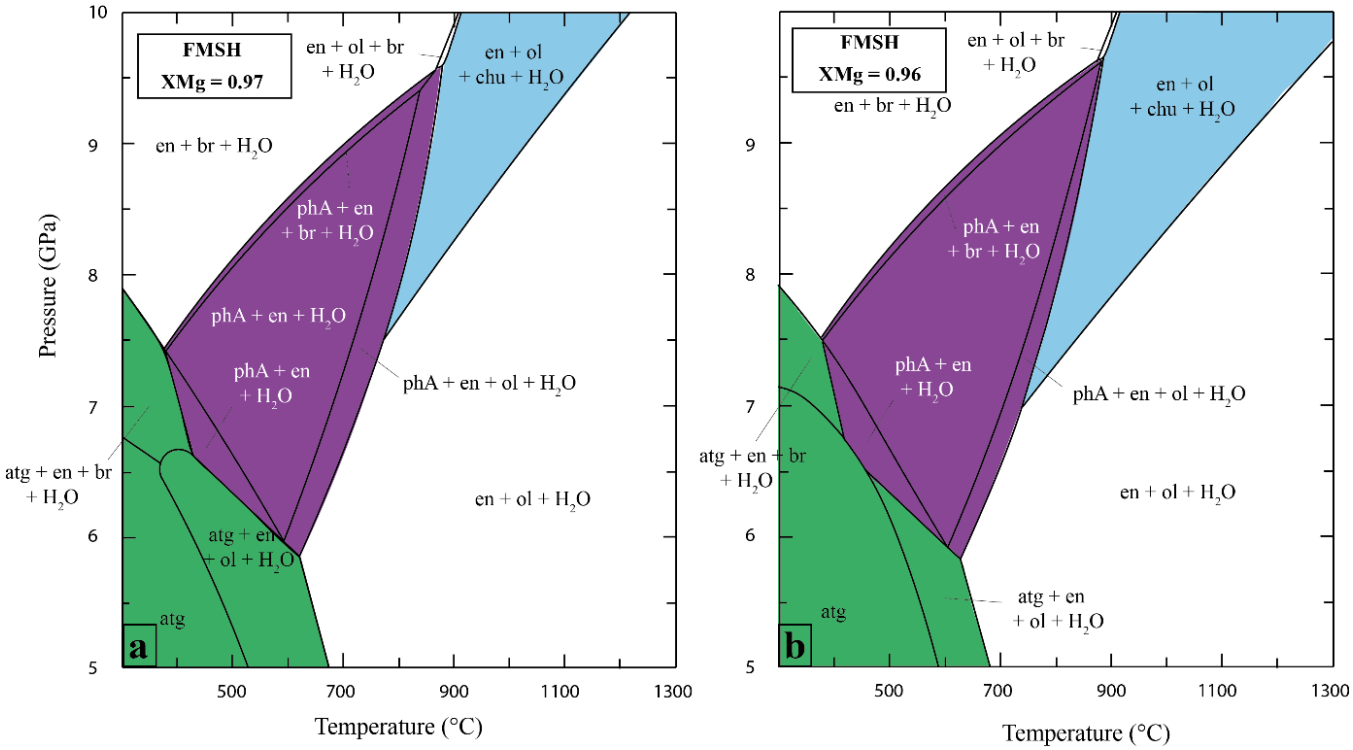

structurally bound water mobility, since a pure antigorite mineral assemblage would carry more water than an assemblage of antigorite + nominally anhydrous minerals. The final antigorite-out curve is however not displaced.

Figure VII-3. Pseudo-section in the FMSH system, showing the effect of different amount of iron on phases boundaries. a. The bulk composition is $Mg_{46.56}Fe_{1.44}Si_{34}O_{85}(OH)_{62}$, equivalent to an X_{Mg} of 0.97 and b. $Mg_{46.08}Fe_{1.92}Si_{34}O_{85}(OH)_{62}$ (X_{Mg} = 0.96).

Ferric iron is very common in natural antigorite: their $Fe^{3+}/Fe_{(total)}$ ratio is actually very high. For instance, it ranges between 0.46 and 0.57 for Atg-serpentinites in transitional lithologies from the Cerro del Almirez massif (Spain) and alpine ophiolites (Debret et al., 2015, 2014). Fully serpentinized peridotites display ratios up to 0.7 (oceanic settings, Andreani et al.

(2013)). Fe_2O_3 incorporation in antigorite structure would lead to an X_{Mg} variation, hence modifying stability domains of antigorite dehydration products. Such as incorporation of Al^{3+} cations in antigorite, we could expect a thermal stabilizing effect of Fe^{3+} incorporation. Ferric iron partitioning into other hydrous phases such as clinohumite, phase A and phase E is nevertheless not yet known, as well as its potential effect on their stability domains. This dependence of phase relations on the redox state of the starting sample highlights the importance of using a natural sample for dehydration experiments rather than synthetic gels or mixtures.

The addition of aluminum to the simple MSH system adds new mineral species to consider such as pyrope or chlorite (below 5 GPa, see Figure VII-4). Aluminum incorporation is also known to have a thermal stabilizing effect on antigorite (Bromiley and Pawley, 2003; Padrón-Navarta et al., 2013).

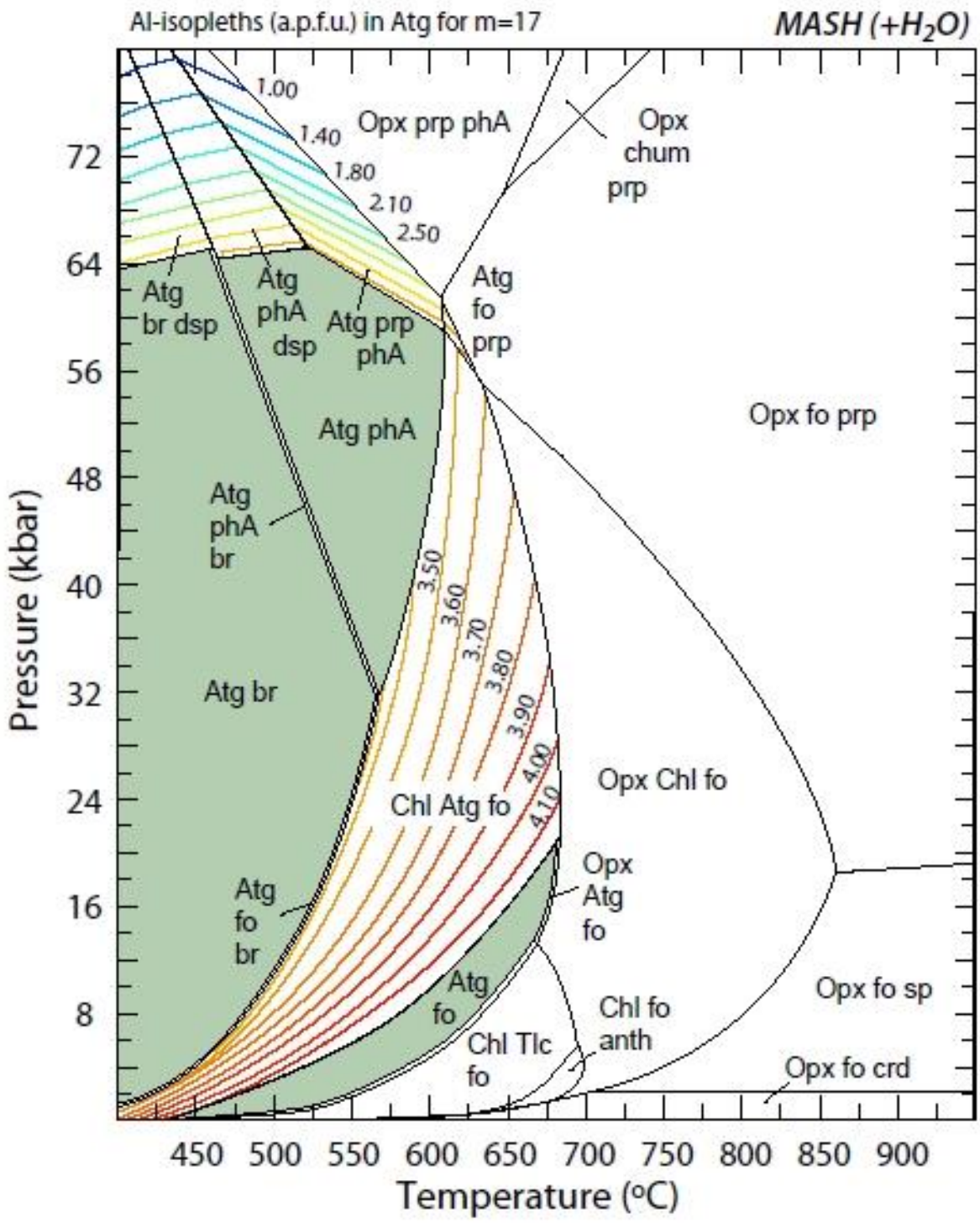

Figure VII-4. Pseudo-section in the MASH for antigorite composition, Padrón-Navarta (personal communication, 2016)

Moreover, we observed that alumina seems to play an important role in stabilizing the Al_2O_3-rich phase E in our experiments (discussed in chapter V). Testing this effect with numerical modelling is not possible, because thermodynamic data for DHMS do not exist for aluminous compositions. A pseudo-section in the MSH system, can nevertheless be constructed using the thermodynamic database from Komabayashi (2006), which includes phase A and phase E thermodynamic properties (Figure VII-5). They retrieved thermodynamic properties of DHMS from experimentally determined fluid-absent relations. In comparison to the MSH system investigated with the database from Holland and Powell (1998, revised in 2002), the latter proposes different Clapeyron slopes for dehydration reactions as well as different stability fields. For instance, on Figure VII-5 antigorite does not appear in any phase assemblages, even at 5 GPa. The reaction phase A = brucite + clinohumite is moved to lower pressures, and an additional phase (stishovite) takes part in the predicted reactions. Phase E appears in the system for pressures beyond 10 GPa only.

Comparing our results in the natural system to the phase assemblages predicted by Peplex in the MSH system (with the database from Komabayashi, 2006), it appears clearly that the stability of hydrous phases is very different (Figure VII-6). For example, antigorite is stable at 8 GPa below 500°C and to 650°C at maximum in our experiments while it is not even there in the model. We observe phase E from 6.5 to 10 GPa for the temperature range of 650 to 750 °C while it is predicted only above 10 GPa and at relatively higher temperatures in the model. Also, the stability field of clinohumite is restricted to a very narrow area in our experimental phase assemblages compared to the Perplex prediction.

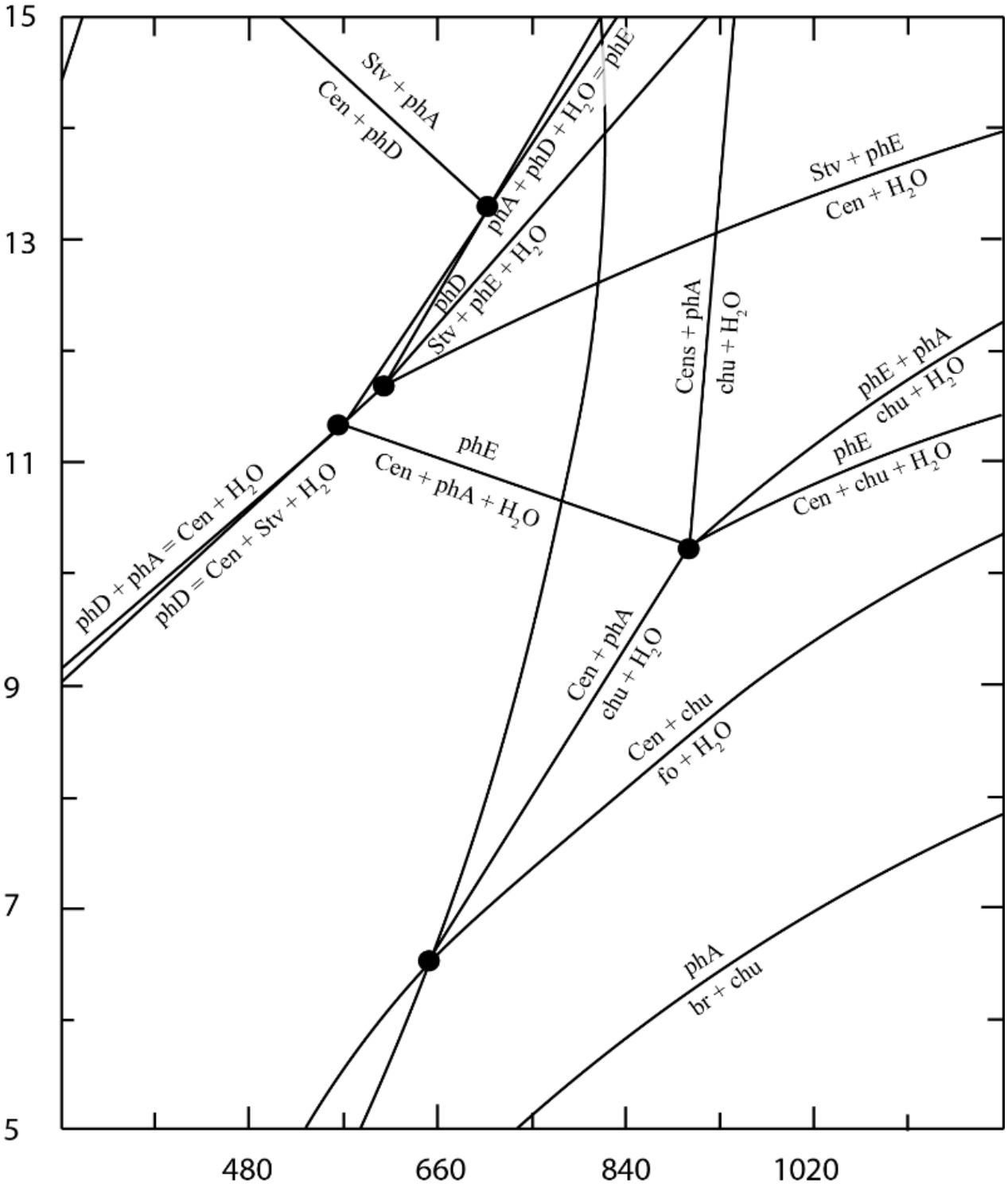

Figure VII-5. Pseudosection in the MSH system according to the thermodynamic database from Komabaysahi et al. (2006).

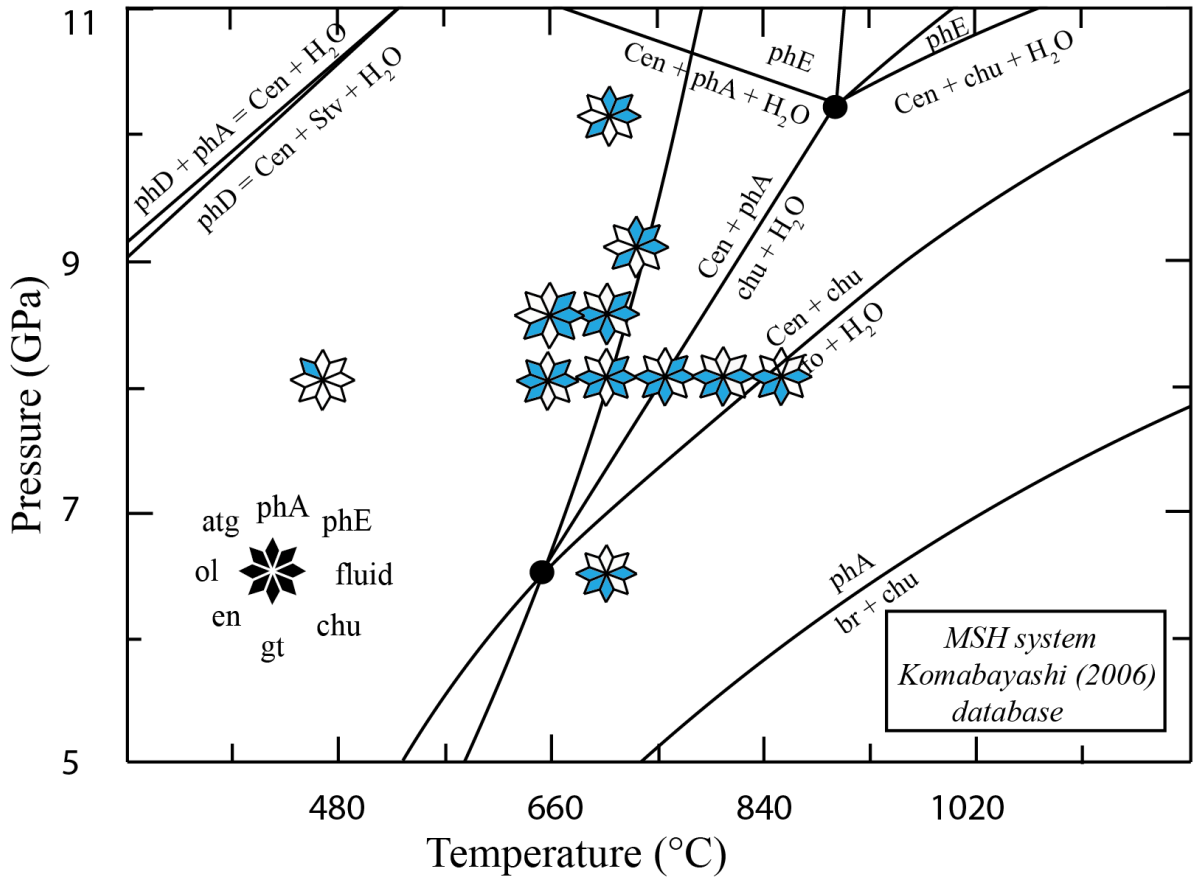

Figure VII-6. Phase diagram in the MSH system constructed using Perplex with the database from Komabayashi (2006). Phase assemblages observed in our experiments are reported for comparison.

Conclusions and perspectives

By conducting experiments on a natural serpentinite sample, we were able to examine antigorite dehydration reactions and its products at conditions relevant to subduction processes. The first experimental study was conducted at 3 GPa, and between 600 and 900°C, to constrain modalities of antigorite dehydration at the conditions of fluid release-induced mantle wedge melting. Our results suggest an oxygen fugacity corresponding to FMQ+5 (Fayalite-Magnetite-Quartz buffer) for the fluids released at antigorite breakdown. This oxidizing character could explain the higher Fe^{3+}/Fe_{total} ratios observed in arc magmas, compared to Mid-Oceanic-Ridge-Basalts (MORB) and Oceanic-Island Basalts (OIB).

Evidence for oxidized mantle sources related to arc magmatism (Brandon and Draper, 1996; Carmichael, 1991; Parkinson and Arculus, 1999) and the role of slab derived fluids (Evans, 2012; Kelley and Cottrell, 2012; Frezzotti et al., 2011; Tumiati et al., 2015) were clearly established. Nevertheless, mechanisms of ferric iron incorporation in the mantle wedge from these fluids needs to be better understood. In addition, Fe^{3+} partitioning between residual minerals and primary melts still remains unknown. These data are needed in order to assess whether or not an oxidized character of the source (as we support in this study, based on the oxidizing potential of antigorite breakdown related fluids) could be transmitted to arc magmas.

The second study conducted in this thesis aimed at constraining the ability of structurally bound water to survive at greater depth via hydrous minerals, existing beyond antigorite stability. We conducted high pressure experiments on the same natural serpentinite sample and investigated phase relations between 6.5 and 10 GPa and for <500 to 850 °C. In particular, our results suggest that the presence of aluminum and iron in the system leads to important

modifications on the phase diagram of hydrated peridotite, mostly on antigorite, phase A and phase E boundaries and stability domains.

By combining experimental observations with a phase equilibria geometric approach (Schreinemakers analysis), we were able to correlate stability of hydrous phases in the natural serpentine composition and water quantity that can be transferred to the deep mantle. Despite the different phase relations observed in the natural serpentinite system compared to previous studies in simplified systems, maximum amounts of water that could be held by hydrous mineral assemblages in the slab suggested by our results is consistent with previous estimations from the literature. Our results suggest the transfer of a maximum of 12 wt% H_2O by antigorite-bearing assemblages that can be transmitted through cold slabs (Honshu) to phase E- and phase A- bearing assemblages up to about 7 wt% H_2O. For a slab of intermediate temperature (Aleutians), phase E- and clinohumite-bearing assemblages can store up to 3.4 wt% H_2O. In the case of a hot subduction (Peru), the mineral assemblages are composed of nominally anhydrous minerals only.

Constraining phase relations in system relevant for natural subduction conditions is a challenging task, because of the complexity of chemical systems involved. This can be executed using an experimental and/or a thermodynamic empirical method. Previous experimental works resulted in some discrepancies on antigorite stability limits, attributed to different experimental procedures but also to variations in the starting material composition. Moreover, differences in chemical systems investigated such as the addition of aluminum in comparison to the MgO-SiO_2-H_2O system creates new mineral assemblages, with the appearance of garnet for example. Likewise, thermodynamic computations of phases boundaries can produce quite different phases relationships depending on the mineral thermodynamic models. Because antigorite is a hydrous phase, its molar volume is expected to be affected by pressure and temperature increase. Therefore, it is crucial to use the most precise and accurate Equation of State (EoS)

refinement. The importance of accurate thermodynamic parameters to produce petrological models on phases stabilities has been illustrated in Hilairet et al. (2006) for example. They were able to refine the bulk modulus value for a natural antigorite sample and emphasized its control on the pressure and temperature conditions of its destabilization. In particular, they found that varying the bulk modulus from their measured value of 67.27 GPa to the value in Holland and Powell (1998) database of 54.5 GPa leads to the computation of a smaller stability field for antigorite (it is decreased of about 200 °C at 7 GPa). It results in shifting antigorite destabilizations to lower conditions.

Updated thermodynamic properties for antigorite are now available. Thermodynamic properties of the Tschermak-antigorite endmember were retrieved and can be used in ideal solution models in the FMASH system (Padrón-Navarta et al., 2013). The parameters of the ferrous antigorite endmember are also available (Merkulova et al., 2016). However, accurate thermodynamic properties of the DHMS are not yet know. These data are required to compute models of phase equilibria in the hydrated ultramafic system. Such a modelling would be of a great help, in addition to our experimental results, to better understand what the options of water transfer by the slab are in the deep mantle. In particular, they would help to constrain more precisely the P-T location of phases boundaries. This would further provide a more precise evaluation of water budgets while comparing the conditions for hydrous phases stability to the slab thermal structures available in the literature.

References

A

Ahrens, T.J., 1972. The mineralogic distribution of iron in the upper mantle. Phys. Earth Planet. Inter. 5, 267–281. doi:10.1016/0031-9201(72)90097-0

Andreani, M., Muñoz, M., Marcaillou, C., Delacour, A., 2013. μXANES study of iron redox state in serpentine during oceanic serpentinization. Lithos 178, 70–83. doi:10.1016/j.lithos.2013.04.008

Arcay, D., Tric, E., Doin, M.-P., 2007. Slab surface temperature in subduction zones: Influence of the interplate decoupling depth and upper plate thinning processes, Earth and Planetary Science Letters. doi:10.1016/j.epsl.2006.12.027

Artioli G, Fumagalli P, Poli S (1999) The crystal structure of $Mg_8(Mg_2Al_2)Al_8Si_{12}(O,OH)_{56}$ pumpellyite and its relevance in ultramafic systems at high pressure. Am Mineral 84:1906–1914

B

Bali, E., Audétat, A., Keppler, H., 2010. The mobility of U and Th in subduction zone fluids: an indicator of oxygen fugacity and fluid salinity. Contrib. to Mineral. Petrol. 161, 597–613. doi:10.1007/s00410-010-0552-9

Bebout, G.E., 1996. Volatile Transfer and Recycling at Convergent Margins: Mass-Balance and Insights from High-P/T Metamorphic Rocks. pp. 179–193. doi:10.1029/GM096p0179

Bean, V.E., Akimoto, S., Bell, P.M., Block, S., Holzapfel, W.B., Manghnani, M.H., Nicol, M.F., Stishov, S.M., 1986. Another step toward an international practical pressure scale. Phys. B+C 139–140, 52–54. doi:10.1016/0378-4363(86)90521-8

Bézos, A., Humler, E., 2005. The Fe3+/ΣFe ratios of MORB glasses and their implications for mantle melting. Geochim. Cosmochim. Acta 69, 711–725. doi:10.1016/j.gca.2004.07.026

Bliss, N.W., MacLean, W.H., 1975. The paragenesis of zoned chromite from central Manitoba. Geochim. Cosmochim. Acta 39, 973–990. doi:10.1016/0016-7037(75)90042-3

Boillot, G., Winterer, E.L., 1988. 41. Rifting of the Galicia margin: crustal thinning and emplacement of mantle rocks on the seafloor.

Bose, K., Ganguly, J., 1995a. Experimental and theoretical studies of the stabilities of talc, antigorite and phase A at high pressures with applications to subduction processes. Earth

Planet. Sci. Lett. 136, 109–121. doi:10.1016/0012-821X(95)00188-I

Bose, K., Ganguly, J., 1995b. Quartz-coesite transition revisited: Reversed experimental determination at 500-1200 °C and retrieved thermochemical properties. Am. Mineral. 80, 231–238.

Bose, K., Navrotsky, A., 1998. Thermochemistry and phase equilibria of hydrous phases in the system MgO-SiO 2 -H 2 O: Implications for volatile transport to the mantle. J. Geophys. Res. 103, 9713. doi:10.1029/98JB00506

Brandon, A.D., Draper, D.S., 1996. Constraints on the origin of the oxidation state of mantle overlying subduction zones: An example from Simcoe, Washington, USA. Geochim. Cosmochim. Acta 60, 1739–1749. doi:10.1016/0016-7037(96)00056-7

Brantut, N., Schubnel, A., David, E.C., Héripré, E., Guéguen, Y., Dimanov, A., 2012. Dehydration-induced damage and deformation in gypsum and implications for subduction zone processes. J. Geophys. Res. Solid Earth 117. doi:10.1029/2011JB008730

Bromiley, G.D., Pawley, A.R., 2003. The stability of antigorite in the systems MgO-SiO_2-H_2O (MSH) and MgO-Al_2O_3-SiO_2-H_2O (MASH): The effects of Al^{3+} substitution on high-pressure stability. Am. Mineral.

Bromiley, G.D., Pawley, A.R., 2002. The high-pressure stability of Mg-sursassite in a model hydrous peridotite: a possible mechanism for the deep subduction of significant volumes of H2O. Contrib. to Mineral. Petrol.

Brudzinski, M.R., Thurber, C.H., Hacker, B.R., Engdahl, E.R., 2007. Global Prevalence of Double Benioff Zones.

C

Cai, N., Inoue, T., Fujino, K., Ohfuji, H., Yurimoto, H., 2015. A possible new Al-bearing hydrous Mg-silicate (23 Å phase) in the deep upper mantle. Am. Mineral. 100, 2330–2335. doi:10.2138/am-2015-5148

Cannat, M., Bideau, D., Hébert, R., 1990. Plastic deformation and magmatic impregnation in serpentinized ultramafic rocks from the Garrett transform fault (East Pacific Rise). Earth Planet. Sci. Lett. 101, 216–232. doi:10.1016/0012-821X(90)90155-Q

Capitani, G., Mellini, M., 2004. The modulated crystal structure of antigorite: The m = 17 polysome. Am. Mineral. doi:10.2138/am-2004-0117

Carmichael, I.S.E., 1991. The redox states of basic and silicic magmas: a reflection of their source regions? Contrib. to Mineral. Petrol. 106, 129–141. doi:10.1007/BF00306429

Charlou, J.L., Donval, J.P., Fouquet, Y., Jean-Baptiste, P., Holm, N., 2002. Geochemistry of high H 2 and CH 4 vent fluids issuing from ultramafic rocks at the Rainbow hydrothermal field (36j14VN, MAR).

Connolly, J.A.D., 2005. Computation of phase equilibria by linear programming: A tool for geodynamic modeling and its application to subduction zone decarbonation. doi:10.1016/j.epsl.2005.04.033

Cottrell, E., Kelley, K.A., 2011. The oxidation state of Fe in MORB glasses and the oxygen fugacity of the upper mantle. Earth Planet. Sci. Lett. 305, 270–282. doi:10.1016/j.epsl.2011.03.014

D

Danyushevsky, L. V., Eggins, S.M., Falloon, T.J., Christie, D.M., 2000. H2O Abundance in Depleted to Moderately Enriched Mid-ocean Ridge Magmas; Part I: Incompatible Behaviour, Implications for Mantle Storage, and Origin of Regional Variations. J. Petrol. 41, 1329–1364. doi:10.1093/petrology/41.8.1329

Davies, J.H., Stevenson, D.J., 1992. Physical model of source region of subduction zone volcanics. J. Geophys. Res. Solid Earth 97, 2037–2070. doi:10.1029/91JB02571

De Capitani, C., Petrakakis, K., 2010. The computation of equilibrium assemblage diagrams with Theriak/Domino software. Am. Mineral. 95.

De Faria, D.L.A., Venâncio Silva, S., de Oliveira, M.T., 1997. Raman microspectroscopy of some iron oxides and oxyhydroxides. J. Raman Spectrosc. 28, 873–878. doi:10.1002/(SICI)1097-4555(199711)28:11<873::AID-JRS177>3.0.CO;2-B

Debret, B., Andreani, M., Muñoz, M., Bolfan-Casanova, N., Carlut, J., Nicollet, C., Schwartz, S., Trcera, N., 2014. Evolution of Fe redox state in serpentine during subduction. Earth Planet. Sci. Lett. 400, 206–218. doi:10.1016/j.epsl.2014.05.038

Debret, B., Bolfan-Casanova, N., Padrón-Navarta, J.A., Martin-Hernandez, F., Andreani, M., Garrido, C.J., López Sánchez-Vizcaíno, V., Gómez-Pugnaire, M.T., Muñoz, M., Trcera, N., 2015. Redox state of iron during high-pressure serpentinite dehydration. Contrib. to Mineral. Petrol. 169, 36. doi:10.1007/s00410-015-1130-y

Deschamps, F., Guillot, S., Godard, M., Chauvel, C., Andreani, M., Hattori, K., 2010. In situ characterization of serpentinites from forearc mantle wedges: Timing of serpentinization and behavior of fluid-mobile elements in subduction zones. Chem. Geol. 269, 262–277. doi:10.1016/j.chemgeo.2009.10.002

Dobson, D.P., Meredith, P.G., Boon, S.A., 2002. Simulation of Subduction Zone Seismicity by Dehydration of Serpentine. Science (80-.). 298.

Domanik, K.J., Holloway, J.R., 1996. The stability and composition of phengitic muscovite and associated phases from 5.5 to 11 GPa: Implications for deeply subducted sediments. Geochim. Cosmochim. Acta 60, 4133–4150. doi:10.1016/S0016-7037(96)00241-4

E

Ellis, D.E., Wyllie, P.J., 1980. Phase relations and their petrological implications in the system MgO-SiO2-H2O-CO2 at pressures up to lfi) kbar. Am. Mineral. 65, 540–556.

Evans, B.W., Trommsdorff, V., 1978. Petrogenesis of garnet lherzolite, Cima di Gagnone, Lepontine Alps. Earth Planet. Sci. Lett. 40, 333–348. doi:10.1016/0012-821X(78)90158-9

Evans, B.W., Guggenheim, S., 1988. Talc, pyrophyllite, and related minerals. Rev. Mineral. Geochemistry 19.

Evans, K.A., 2012. The redox budget of subduction zones. Earth-Science Rev. 113, 11–32. doi:10.1016/j.earscirev.2012.03.003

F

Falloon, T.J., Green, D.H., 1990. Solidus of carbonated fertile peridotite under fluid-saturated conditions. Geology 18, 195. doi:10.1130/0091-7613(1990)018<0195:SOCFPU>2.3.CO;2

Férot, A., Bolfan-Casanova, N., 2012. Water storage capacity in olivine and pyroxene to 14 GPa: Implications for the water content of the Earth's upper mantle and nature of seismic discontinuities. Earth Planet. Sci. Lett. 218–230. doi:10.1016/j.epsl.2012.06.022

Fockenberg, T., 1998. An experimental study of the pressure-temperature stability of MgMgAl-pumpellyite in the system MgO-Al_2O -SiO_2-H_2O. Am. Mineral. 83, 220–227.

Frezzotti, M.L., Selverstone, J., Sharp, Z.D., Compagnoni, R., 2011. Carbonate dissolution during subduction revealed by diamond-bearing rocks from the Alps. Nat. Geosci. 4, 703–706. doi:10.1038/ngeo1246

Frohlich, C., 1989. The Nature of Deep-Focus Earthquakes. Annu. Rev. Earth Planet. Sci. 17, 227–254. doi:10.1146/annurev.ea.17.050189.001303

Frost, D.J., 1999. The stability of dense hydrous magnesium silicates in earth's transition zone and lower mantle, in: Geochemical Society Special Publication, Houston, T. (Ed.), Mantle Petrology: Field Observations and High-Pressure Experimentation. Y. fei, C.M. Bertka, and B.O. Mysen, Eds., pp. 283–296.

Frost, D.J., Fei, Y., 1998. Stability of phase D at high pressure and high temperature. J. Geophys. Res. Solid Earth 103, 7463–7474. doi:10.1029/98JB00077

Früh-Green, G.L., Plas, A., Lécuyer, C., 1996. 4. Petrologic and stable isotope constraints on

hydrothermal alteration and serpentinization of the EPR shallow mantle at hess deep (site 895)1 147.

Fumagalli, P., Klemme, S., 2015. 2.02 – Mineralogy of the Earth: Phase Transitions and Mineralogy of the Upper Mantle, in: Treatise on Geophysics. pp. 7–31. doi:10.1016/B978-0-444-53802-4.00052-X

Fumagalli, P., Poli, S., 2005. Experimentally Determined Phase Relations in Hydrous Peridotites to 6.5 GPa and their Consequences on the Dynamics of Subduction Zones. J. Petrol. 46, 555–578.

Fumagalli, P., Poli, S., 1999. Phase relationships in hydrous peridotites at high presssure: Preliminary results of multi-anvil experiments 68, 275–286.

Fumagalli, P., Poli, S., Fischer, J., Merlini, M., Gemmi, M., 2014. The high-pressure stability of chlorite and other hydrates in subduction mélanges: experiments in the system Cr_2O_3–MgO–Al_2O_3–SiO_2–H_2O. Contrib. to Mineral. Petrol. 167, 979. doi:10.1007/s00410-014-0979-5

Fumagalli, P., Stixrude, L., Poli, S., Snyder, D., 2001. The 10A phase: a high-pressure expandable sheet silicate stable during subduction of hydrated lithosphere. Earth Planet. Sci. Lett. 186, 125–141.

Furukawa, Y., 1993. Magmatic processes under arcs and formation of the volcanic front. J. Geophys. Res. Solid Earth 98, 8309–8319. doi:10.1029/93JB00350

G

Garrido, C.J., López Sánchez-Vizcaíno, V., Gómez-Pugnaire, M.T., Trommsdorff, V., Alard, O., Bodinier, J.-L., Godard, M., 2005. Enrichment of HFSE in chlorite-harzburgite produced by high-pressure dehydration of antigorite-serpentinite: Implications for subduction magmatism. Geochemistry, Geophys. Geosystems 6, n/a-n/a. doi:10.1029/2004GC000791

Gasparik, T., 2003. Phase Diagrams for Geoscientists: An Atlas of the Earth's Interior.

Gemmi, M., Fischer, J., Merlini, M., Poli, S., Fumagalli, P., Mugnaioli, E., Kolb, U., 2011. A new hydrous Al-bearing pyroxene as a water carrier in subduction zones. Earth Planet. Sci. Lett. 310, 422–428. doi:10.1016/j.epsl.2011.08.019

Gibbs, J.., 1961. No Title, in: The Scientific Papers of J. Willard Gibbs, Vol. 1: Thermodynamics.

Grove, T.L., Chatterjee, N., Parman, S.W., Médard, E., 2006. The influence of H2O on mantle wedge melting. Earth Planet. Sci. Lett. 249, 74–89. doi:http://dx.doi.org/10.1016/j.epsl.2006.06.043

Gudmundsson, G. and Holloway, J.R., 1990. Pressure effect of the Fe3+/Fe2+ ratio. Terra Abstr. 2, 14.

Guillot, S., Hattori, K.H., de Sigoyer, J., 2000. Mantle wedge serpentinization and exhumation of eclogites: Insights from eastern Ladakh, northwest Himalaya. Geology 28, 199. doi:10.1130/0091-7613(2000)28<199:MWSAEO>2.0.CO;2

H

Hacker, B.R., 2008. H_2O subduction beyond arcs. Geochem. Geophys. Geosyst 3613. doi:10.1029/2007GC001707

Hacker, B.R., Abers, G.A., Peacock, S.M., 2003. Subduction factory 1. Theoretical mineralogy, densities, seismic wave speeds, and H_2O contents. J. Geophys. Res. Solid Earth 108. doi:10.1029/2001JB001127

Harte, B., 2010. Diamond formation in the deep mantle: the record of mineral inclusions and their distribution in relation to mantle dehydration zones. Mineral. Mag. 74, 189–215. doi:10.1180/minmag.2010.074.2.189

Hattori, K.H., Guillot, S., 2007. Gechemical character of serpentinites associated with high- to ultahigh-pressure metamorphic rocks in the Alps, Cuba, and the Himalayas: Recycling of elements in subduction zones. Geochemistry, Geophys. Geosystems 8.

Hattori, K.H., Guillot, S., 2003. Volcanic front form as a consequence of serpentinite dehydration in the forearc mantle wedge.

Hempelmann, R., 1984. Diffusion of hydrogen in metals. J. Less Common Met. 101, 69–96. doi:10.1016/0022-5088(84)90088-2

Hermann, J., 2002. Experimental constraints on phase relations in subducted continental crust. Contrib. to Mineral. Petrol. 143, 219–235. doi:10.1007/s00410-001-0336-3

Hermann, J., Spandler, C., Hack, A., Korsakov, A. V., 2006. Aqueous fluids and hydrous melts in high-pressure and ultra-high pressure rocks: Implications for element transfer in subduction zones. Lithos 92, 399–417. doi:10.1016/j.lithos.2006.03.055

Hernlund, J., Leinenweber, K., Locke, D., Tyburczy, J.A., 2006. A numerical model for steady-state temperature distributions in solid-medium high-pressure cell assemblies. Am. Mineral. doi:10.2138/am.2006.1938

Hilairet, N., Daniel, I., Reynard, B., 2006. Equation of state of antigorite, stability field of serpentines, and seismicity in subduction zones. Geophys. Res. Lett. 33, L02302. doi:10.1029/2005GL024728

Hirose, K., Kawamoto, T., 1995. Hydrous partial melting of lherzolite at 1 GPa: The effect of H2O on the genesis of basaltic magmas. Earth Planet. Sci. Lett. 133, 463–473. doi:10.1016/0012-821X(95)00096-U

Holland, T.J.B., Powell, R., 2004. An internally consistent thermodynamic data set for phases of petrological interest. J. Metamorph. Geol. 16, 309–343. doi:10.1111/j.1525-1314.1998.00140.x

Holland, T.J.B., Powell, R., 1998. An internally consistent thermodynamic data set for phases of petrological interest. J. Metamorph. Geol. 16, 309–343. doi:10.1111/j.1525-1314.1998.00140.x

Holland, T.J.B., Powell, R., 1991. A Compensated-Redlich-Kwong (CORK) equation for volumes and fugacities of CO_2 and H_2O in the range 1 bar to 50 kbar and 100-1600°C. Contrib. to Mineral. Petrol. 109, 265–273. doi:10.1007/BF00306484

Howe, H., Pawley, A., Droop, G., 2016. The effect of Fe-Mg solid solution on the stability of talc and the 10 Å phase, in: EMPG.

I

Inoue, T., 1994. Effect of water on melting phase relations and melt composition in the system Mg_2SiO_4-$MgSiO_3$-H_2O up to 15 GPa. Phys. Earth Planet. Inter. 85, 237–263. doi:10.1016/0031-9201(94)90116-3

Ito, E., Harris, D.M., Anderson, A.T., 1983. Alteration of oceanic crust and geologic cycling of chlorine and water. Geochim. Cosmochim. Acta 47, 1613–1624. doi:10.1016/0016-7037(83)90188-6

J

Jenkins, D.M., Chernosky Jr, J. V, 1986. Phase equilibria and crystallochemical properties of Mg-chlorite. Am. Mineral. 71, 924–936.

Johnson, M.C., Anderson, A.T., Rutherford, M.J., 1994. Pre-eruptive volatile contents of magmas. Rev. Mineral. Geochemistry 30.

K

Kanzaki, M., 1991. Stability of hydrous magnesium silicates in the mantle transition zone. Phys. Earth Planet. Inter. 66, 307–312. doi:10.1016/0031-9201(91)90085-V

Kawamoto, T., and Holloway, J.R., 1997. Melting Temperature and Partial Melt Chemistry of H2O-Saturated Mantle Peridotite to 11 GPa. Science (80). 276, 240–243. doi:10.1126/science.276.5310.240

Kawamoto, T., Hervig, R.L., Holloway, J.R., 1996. Experimental evidence for a hydrous

transition zone in the early Earth's mantle. Earth Planet. Sci. Lett. 142, 587–592. doi:10.1016/0012-821X(96)00113-6

Kawamoto, T., Leinenweber, K., Hervig, R.L., Holloway, J.R., 1995. Stability of hydrous minerals in H2O-saturated KLB-1 peridotite up to 15 GPA, in: AIP Conference Proceedings. AIP, pp. 229–239. doi:10.1063/1.48731

Kelemen, P.B., Hirth, G., 2007. A periodic shear-heating mechanism for intermediate-depth earthquakes in the mantle. Nature 446, 787–790. doi:10.1038/nature05717

Kelley, K.A., Cottrell, E., 2012. The influence of magmatic differentiation on the oxidation state of Fe in a basaltic arc magma. Earth Planet. Sci. Lett. 329–330, 109–121. doi:10.1016/j.epsl.2012.02.010

Kelley, K.A., Cottrell, E., 2009. Water and the oxidation state of subduction zone magmas. Science 325, 605–607. doi:10.1126/science.1174156

Kincaid, C., Sacks, I.S., 1997. Thermal and dynamical evolution of the upper mantle in subduction zones. J. Geophys. Res. Solid Earth 102, 12295–12315. doi:10.1029/96JB03553

Khisina, N.R., Wirth, R., 2002. Hydrous olivine (Mg 1− y Fe 2+ y) 2− x v x SiO 4 H 2 x - a new DHMS phase of variable composition observed as nanometer-sized precipitations in mantle olivine. Phys. Chem. Miner. 29, 98–111. doi:10.1007/s002690100205

Kleppe, A.K., Jephcoat, A.P., 2006. Raman spectroscopic studies of hydrous and nominally anhydrous deep mantle phases. pp. 69–93. doi:10.1029/168GM07

Komabayashi, T., 2006. Phase relations of hydrous peridotite: Implications for water circulation in the Earth's mantle. pp. 29–43. doi:10.1029/168GM04

Komabayashi, T., Hirose, K., Funakoshi, K., Takafuji, N., 2005. Stability of phase A in antigorite (serpentine) composition determined by in situ X-ray pressure observations. Phys. Earth Planet. Inter. 151, 276–289. doi:http://dx.doi.org/10.1016/j.pepi.2005.04.002

Kudoh, Y., Finger, L.W., Hazen, R.M., Prewitt, C.T., Kanzaki, M., Veblen, D.R., 1993. Phase E: A high pressure hydrous silicate with unique crystal chemistry. Phys. Chem. Miner. 19. doi:10.1007/BF00202972

L

Laubier, M., Grove, T.L., Langmuir, C.H., 2014. Trace element mineral/melt partitioning for basaltic and basaltic andesitic melts: An experimental and laser ICP-MS study with application to the oxidation state of mantle source regions. Earth Planet. Sci. Lett. 392, 265–278. doi:10.1016/j.epsl.2014.01.053

Lécuyer, C., Ricard, Y., 1999. Long-term fluxes and budget of ferric iron: implication for the redox states of the Earth's mantle and atmosphere. Earth Planet. Sci. Lett. 165, 197–211. doi:10.1016/S0012-821X(98)00267-2

Lee, C.T.A., Leeman, W.P., Canil, D., Li, Z.X.A., 2005. Similar V/Sc systematics in MORB and arc basalts: Implications for the oxygen fugacities of their mantle source regions. J. Petrol. 46, 2313–2336.

Liu, L., 1987. Effects of H_2O on the phase behaviour of the forsterite-enstatite system at high pressures and temperatures and implications for the Earth. Phys. Earth Planet. Inter. 49, 142–167. doi:10.1016/0031-9201(87)90138-5

Liu, L.-G., Lin, C.C., Mernagh, T.P., Irifune, T., 1997a. Raman spectra of phase a at various pressures and temperatures. J. Phys. Chem. Solids 58, 2023–2030. doi:10.1016/S0022-3697(97)00121-2

Liu, L.-G., Mernagh, T.P., Lin, C.C., Irifune, T., 1997b. EPSL Raman spectra of phase E at various pressures and temperatures with geophysical implications. Earth Planet. Sci. Lett. 149, 57–65.

López Sánchez-Vizcaíno, V., Trommsdorff, V., Gómez-Pugnaire, M.T., Garrido, C.J., Müntener, O., Connolly, J.A.D., 2005. Petrology of titanian clinohumite and olivine at the high-pressure breakdown of antigorite serpentinite to chlorite harzburgite (Almirez Massif, S. Spain). Contrib. to Mineral. Petrol. 149, 627–646. doi:10.1007/s00410-005-0678-3

Luth, R.W., 2003. Mantle Volatiles—Distribution and Consequences, in: Treatise on Geochemistry. Elsevier, pp. 319–361. doi:10.1016/B0-08-043751-6/02124-1

Luth, R.W., 1995. Is phase A relevant to the Earth's mantle? Geochim. Cosmochim. Acta 59, 679–682. doi:10.1016/0016-7037(95)00319-U

M

Magni, V., Bouilhol, P., van Hunen, J., 2014. Deep water recycling through time. Geochemistry, Geophys. Geosystems 15, 4203–4216. doi:10.1002/2014GC005525

Mallmann, G., O'Neill, H.S.C., 2009. The Crystal/Melt Partitioning of V during Mantle Melting as a Function of Oxygen Fugacity Compared with some other Elements (Al, P, Ca, Sc, Ti, Cr, Fe, Ga, Y, Zr and Nb). J. Petrol. 50, 1765–1794. doi:10.1093/petrology/egp053

Marcaillou, C., Muñoz, M., Vidal, O., Parra, T., Harfouche, M., 2011. Mineralogical evidence for H2 degassing during serpentinization at 300°C/300bar. Earth Planet. Sci. Lett. 303, 281–290. doi:10.1016/j.epsl.2011.01.006

McKenzie, D.P., 1969. Speculations on the Consequences and Causes of Plate Motions. Geophys. J. Int. 18, 1–32. doi:10.1111/j.1365-246X.1969.tb00259.x

Meissner, E., Chakraborty, S., Seifert F., Sharp, T.G. (1997). Analytische transmissions Elektronenmikroskopie (ATEM) zur Bestimmung von Mg-Fe Interdiffusionskoeffizienten in olivin. Berichte der Deutschen Mineralogischen Gesellschaft, Beih. zur European Journal of Mineralogy 9

Mellini, M., Trommsdorff, V., Compagnoni, R., 1987. Antigorite polysomatism: behaviour during progressive metamorphism. Contrib. to Mineral. Petrol. 97, 147–155. doi:10.1007/BF00371235

Merkulova, M., Muñoz, M., Vidal, O., Brunet, F., 2016. Role of iron content on serpentinite dehydration depth in subduction zones: Experiments and thermodynamic modeling. doi:10.1016/j.lithos.2016.09.007

Mevel, C., 2003. Serpentinization of abyssal peridotites at mid-ocean ridges. Geomaterials.

Mibe, K., Fujii, T., Yasuda, A., 2002. Composition of aqueous fluid coexisting with mantle minerals at high pressure and its bearing on the differentiation of the Earth's mantle. Geochim. Cosmochim. Acta 66, 2273–2285. doi:10.1016/S0016-7037(02)00856-6

Michael, P., 1995. Regionally distinctive sources of depleted MORB: Evidence from trace elements and H2O. Earth Planet. Sci. Lett. 131, 301–320. doi:10.1016/0012-821X(95)00023-6

Millhollen, G.L., Irving, A.J., Wyllie, P.J., 1974. Melting Interval of Peridotite with 5.7 per Cent Water to 30 Kilobars. J. Geol. 82, 575–587. doi:10.1086/628007

Mookherjee, M., Stixrude, L., 2009. Structure and elasticity of serpentine at high-pressure. Earth Planet. Sci. Lett. 279, 11–19. doi:10.1016/j.epsl.2008.12.018

Morten, L. and Puga, E., 1984. Blades of olivines and ortho- dissolved lithium in the oceans. Geochim. Cosmochim. pyroxenes in ultramafic rocks from the Cerro del Almirez, Acta, 48: 859-872. Sierra Nevada Complex, Spain: relics of quench-textured Strong, D.F. and Dostal, J., 1980. Dyna. Neues Jahrb. Miner. Monatsh. 5:211-218.

Muller, M.R., Robinson, C.J., Minshull, T.A., White, R.S., Bickle, M.J., 1997. Thin crust beneath ocean drilling program borehole 735B at the Southwest Indian Ridge? Earth Planet. Sci. Lett. 148, 93–107. doi:10.1016/S0012-821X(97)00030-7

Mysen, B.O., Wheeler, K., 2000. Alkali aluminosilicate-saturated aqueous fluids in the earth's upper mantle. Geochim. Cosmochim. Acta 64, 4243–4256. doi:10.1016/S0016-7037(00)00498-1

N

Nichols, A.R.L., Carroll, M.R., Höskuldsson, Á., 2002. Is the Iceland hot spot also wet? Evidence from the water contents of undegassed submarine and subglacial pillow basalts. Earth Planet. Sci. Lett. 202, 77–87. doi:10.1016/S0012-821X(02)00758-6

Niida, K., Green, D.H., 1999. Stability and chemical composition of pargasitic amphibole in MORB pyrolite under upper mantle conditions. Contrib. to Mineral. Petrol. 135, 18–40. doi:10.1007/s004100050495

Nimis, P., Goncharov, A., Ionov, D.A., McCammon, C., 2015. Fe3+ partitioning systematics between orthopyroxene and garnet in mantle peridotite xenoliths and implications for thermobarometry of oxidized and reduced mantle rocks. Contrib. to Mineral. Petrol. 169,

6. doi:10.1007/s00410-014-1101-8

Nishi, M., Irifune, T., Tsuchiya, J., Tange, Y., Nishihara, Y., Fujino, K., Higo, Y., 2014. Stability of hydrous silicate at high pressures and water transport to the deep lower mantle. Nat. Geosci. 7, 224–227. doi:10.1038/ngeo2074

O

O'Hanley, D.S., 1996. Serpentinites : records of tectonic and petrological history. Oxford University Press.

Ohtani, E., Shibata, T., Kubo, T., Kato, T., 1995. Stability of hydrous phases in the transition zone and the upper most part of the lower mantle. Geophys. Res. Lett. 22, 2553–2556. doi:10.1029/95GL02338

Omori, S., Komabayashi, T., Maruyama, S., 2000. Intraslab seismic zone morphology and devolatilization phase equilibria of the subducting slab. Eos, Trans. Am. Geophys. Union.

Omori, S., Kamiya, S., Maruyama, S., Zhao, D., 2002. Morphology of the Intraslab Seismic Zone and Devolatilization Phase Equilibria of the Subducting Slab Peridotite 76.

Omori, S., Komabayashi, T., Maruyama, S., 2004. Dehydration and earthquakes in the subducting slab: empirical link in intermediate and deep seismic zones. Phys. Earth Planet. Inter. 146, 297–311. doi:10.1016/j.pepi.2003.08.014

P

Padrón-Navarta, J.A., Hermann, J., Garrido, C.J., López Sánchez-Vizcaíno, V., Gómez-Pugnaire, M.T., 2009. An experimental investigation of antigorite dehydration in natural silica-enriched serpentinite. Contrib. to Mineral. Petrol. 159, 25–42. doi:10.1007/s00410-009-0414-5

Padrón-Navarta, J.A., Lopez Sanchez-Vizcaino, V., Garrido, C.J., Gomez-Pugnaire, M.T., 2011. Metamorphic Record of High-pressure Dehydration of Antigorite Serpentinite to Chlorite Harzburgite in a Subduction Setting (Cerro del Almirez, Nevado-Filabride Complex, Southern Spain). J. Petrol. 52, 2047–2078. doi:10.1093/petrology/egr039

Padrón-Navarta, J.A., Sánchez-Vizcaíno, V.L., Hermann, J., Connolly, J.A.D., Garrido, C.J., Gómez-Pugnaire, M.T., Marchesi, C., 2013. Tschermak's substitution in antigorite and consequences for phase relations and water liberation in high-grade serpentinites. Lithos 178, 186–196. doi:10.1016/j.lithos.2013.02.001

Padrón-Navarta, J.A., Tommasi, A., Garrido, C.J., Sanchez-Vizcaino, V.L., Gomez-Pugnaire, M.T., Jabaloy, A., Vauchez, A., 2010. Fluid transfer into the wedge controlled by high-pressure hydrofracturing in the cold top-slab mantle. Earth Planet. Sci. Lett. 297, 271–286.

doi:10.1016/j.epsl.2010.06.029

Pamato, M.G., Myhill, R., Boffa Ballaran, T., Frost, D.J., Heidelbach, F., Miyajima, N., 2014. Lower-mantle water reservoir implied by the extreme stability of a hydrous aluminosilicate. Nat. Geosci. 8, 75–79. doi:10.1038/ngeo2306

Parkinson, I.J., Arculus, R.J., 1999. The redox state of subduction zones: insights from arc-peridotites. Chem. Geol. 160, 409–423. doi:10.1016/S0009-2541(99)00110-2

Pawley, A., 2003. Chlorite stability in mantle peridotite: the reaction clinochlore+enstatite=forsterite+pyrope+H2O. Contrib. to Mineral. Petrol. 144, 449–456. doi:10.1007/s00410-002-0409-y

Pawley, A.R., 1994. The pressure and temperature stability limits of lawsonite: implications for H2O recycling in subduction zones. Contrib. to Mineral. Petrol. 118, 99–108. doi:10.1007/BF00310614

Pawley, A.R., Redfern, S.A.T., Wood, B.J., 1995. Thermal expansivities and compressibilities of hydrous phases in the system MgO-SiO_2 -H_2O: talc, phase A and 10-Å phase. Contrib. to Mineral. Petrol. 122, 301–307. doi:10.1007/s004100050129

Peacock, S., 1996. Thermal and petrologic structure of subduction zones. AGU 96, 119–133.

Peacock, S.A., 1990. Fluid processes in subduction zones. Science (80). 248, 329–337.

Peacock, S.M., 2001. Are the lower planes of double seismic zones caused by serpentine dehydration in subducting oceanic mantle? Geology 29, 299–302. doi:10.1130/0091-7613(2001)029<0299:ATLPOD>2.0.CO;2

Peacock, S.M., Rushmer, T., Thompson, A.B., 1994. Partial melting of subducting oceanic crust. Earth Planet. Sci. Lett. 121, 227–244. doi:10.1016/0012-821X(94)90042-6

Peacock, S.M., 1993. Large-scale hydration of the lithosphere above subducting slabs. Chem. Geol. 108, 49–59. doi:10.1016/0009-2541(93)90317-C

Peacock, Wang, 1999. Seismic consequences of warm versus cool subduction metamorphism: examples from southwest and northeast japan. Science 286, 937–9.

Pearson, D.G., Brenker, F.E., Nestola, F., McNeill, J., Nasdala, L., Hutchison, M.T., Matveev, S., Mather, K., Silversmit, G., Schmitz, S., Vekemans, B., Vincze, L., 2014. Hydrous mantle transition zone indicated by ringwoodite included within diamond. Nature 507, 221–4. doi:10.1038/nature13080

Perrillat, J.-P., Daniel, I., Koga, K.T., Reynard, B., Cardon, H., Crichton, W.A., 2005. Kinetics of antigorite dehydration: A real-time X-ray diffraction study, Earth and Planetary Science Letters. doi:10.1016/j.epsl.2005.06.006

Plank, T., Langmuir, C.H., 1998. The chemical composition of subducting sediment and its consequences for the crust and mantle. Chem. Geol. 145, 325–394.

Poli., S., Schmidt, W., 1995. H2O transport and release in subduction zones: Experimental constraints on basaltic and andesitic systems. J. Geophys. Res. 100, 22.299-22.314.

R

Ranero, C.R., Morgan, J.P., McIntosh, K., Reichert, C., 2003. Bending-related faulting and mantle serpentinization at the Middle America trench. Nature 425, 367–373.

Reynard, B., Nakajima, J., Kawakatsu, H., 2010. Earthquakes and plastic deformation of anhydrous slab mantle in double Wadati-Benioff zones. Geophys. Res. Lett. 37. doi:10.1029/2010GL045494>

Ringwood, A.E., Major, A., 1967. High-pressure reconnaissance investigations in the system Mg2SiO4 - MgO - H2O. Earth Planet. Sci. Lett. 2, 130–133. doi:10.1016/0012-821X(67)90114-8

Rüpke, L., Phipps Morgan, J., Eaby Dixon, J., 2006. Implications of Subduction Rehydration for Earth's Deep Water Cycle. doi:10.1029/168GM20

Rüpke, L.H., Morgan, J.P., Hort, M., Connolly, J.A.D., 2004. Serpentine and the subduction zone water cycle. Earth Planet. Sci. Lett. 223, 17–34. doi:10.1016/j.epsl.2004.04.018

S

Savov, I.P., Ryan, J.G., D'Antonio, M., Fryer, P., 2007. Shallow slab fluid release across and along the Mariana arc-basin system: Insights from geochemistry of serpentinized peridotites from the Mariana fore arc. J. Geophys. Res. 112, B09205. doi:10.1029/2006JB004749

Scambelluri, M., Bottazzi, P., Trommsdorff, V., Vannucci, R., Hermann, J., Gòmez-Pugnaire, M.T., Lòpez-Sànchez Vizcaìno, V., 2001. Incompatible element-rich fluids released by antigorite breakdown in deeply subducted mantle. Earth Planet. Sci. Lett. 192, 457–470. doi:10.1016/S0012-821X(01)00457-5

Scambelluri, M., Müntener, O., Hermann, J., Piccardo, G.B., Trommsdorff, V., 1995. Subduction of water into the mantle: History of an Alpine peridotite. Geology 23, 459. doi:10.1130/0091-7613(1995)

Scambelluri, M., Tonarini, S., 2012. Boron isotope evidence for shallow fluid transfer across subduction zones by serpentinized mantle. Geology 40, 907–910. doi:10.1130/G33233.1

Schmidt, M.W., Poli, S., 2014. Devolatilization During Subduction, in: Treatise on Geochemistry. Elsevier, pp. 669–701. doi:10.1016/B978-0-08-095975-7.00321-1

Schmidt, M.W., Poli, S., 1998. Experimentally based water budgets for dehydrating slabs and consequences for arc magma generation. Earth Planet. Sci. Lett. 163, 361–379. doi:10.1016/S0012-821X(98)00142-3

Schmidt, M.W., 1996. Experimental Constraints on Recycling of Potassium from Subducted Oceanic Crust. Science (80-.). 272.

Schmidt, M.W., Poli, S., 1994. The stability of lawsonite and zoisite at high pressures: Experiments in CASH to 92 kbar and implications for the presence of hydrous phases in subducted lithosphere. Earth Planet. Sci. Lett. 124, 105–118. doi:10.1016/0012-821X(94)00080-8

Schneider, M.E., Eggler, D.H., 1986. Fluids in equilibrium with peridotite minerals: Implications for mantle metasomatism. Geochim. Cosmochim. Acta 50, 711–724. doi:10.1016/0016-7037(86)90347-9

Schwartz, S., Guillot, S., Reynard, B., Lafay, R., Debret, B., Nicollet, C., Lanari, P., Auzende, A.L., 2013. Pressure–temperature estimates of the lizardite/antigorite transition in high pressure serpentinites. Lithos 178, 197–210. doi:10.1016/j.lithos.2012.11.023

Spear, F.S., 1993. Metamorphic phase equilibria and pressure-temperature time path, Mineralogi. ed.

Stalder, R., Ulmer, P., 2001a. Phase relations of a serpentine composition between 5 and 14 GPa: significance of clinohumite and phase E as water carriers into the transition zone. Contrib. to Mineral. Petrol. 140, 670–679. doi:10.1007/s004100000208

Stalder, R., Ulmer, P., 2001b. Phase relations of a serpentine composition between 5 and 14 GPa: significance of clinohumite and phase E as water carriers into the transition zone. Contrib. to Mineral. Petrol. 140, 670–679. doi:10.1007/s004100000208

Stalder, R., Ulmer, P., Thompson, A., Günther, D., 2001. High pressure fluids in the system $MgO–SiO_2–H_2O$ under upper mantle conditions. Contrib. to Mineral. Petrol. 140, 607–618. doi:10.1007/s004100000212

Stein, S., Stein, C.A., 1996. Thermo-Mechanical Evolution of Oceanic Lithosphere: Implications for the Subduction Process and Deep Earthquakes. pp. 1–17. doi:10.1029/GM096p0001

Stolper, E., Newman, S., 1994. The role of water in the petrogenesis of Mariana trough magmas. Earth Planet. Sci. Lett. 121, 293–325. doi:10.1016/0012-821X(94)90074-4

Syracuse, E.M., Abers, G.A., 2006. Global compilation of variations in slab depth beneath arc volcanoes and implications. Geochemistry, Geophys. Geosystems 7, n/a-n/a. doi:10.1029/2005GC001045

Syracuse, E.M., van Keken, P.E., Abers, G.A., 2010. The global range of subduction zone thermal models. Phys. Earth Planet. Inter. 183, 73–90. doi:10.1016/j.pepi.2010.02.004

T

Tatsumi, Y., 1986. Formation of the volcanic front in subduction zones. Geophys. Res. Lett. 13, 717–720. doi:10.1029/GL013i008p00717

Taylor, W.R., Green, D.H., 1988. Measurement of reduced peridotite-C-O-Hsolidus and implicationsfor redox melting of the mantle. Nature 332, 349–352. doi:10.1038/332349a0

Tenner, T.J., Hirschmann, M.M., Humayun, M., 2012. The effect of H 2 O on partial melting of garnet peridotite at 3.5 GPa. Geochemistry, Geophys. Geosystems 13, n/a-n/a. doi:10.1029/2011GC003942

Trommsdorff, V., and Evans, B. W. (1980) Titanium hydroxyl c1inohumite: Formation and breakdown in antigorite rocks (Malenco, Italy). Contrib. Mineral. Petrol. 72,229-242.

Trommsdorff, V., Sánchez-Vizcaíno, V.L., Gómez-Pugnaire, M.T., Müntener, O., 1998. High pressure breakdown of antigorite to spinifex-textured olivine and orthopyroxene, SE Spain. Contrib. to Mineral. Petrol. 132, 139–148. doi:10.1007/s004100050412

Tumiati, S., Godard, G., Martin, S., Malaspina, N., Poli, S., 2015. Ultra-oxidized rocks in subduction mélanges? Decoupling between oxygen fugacity and oxygen availability in a Mn-rich metasomatic environment. Lithos 226, 116–130. doi:10.1016/j.lithos.2014.12.008

U

Uehara, S., Shirozu, H., 1985. Variations in chemical composition and structural properties of antigorites. Mineral. J. 12, 299–318. doi:10.2465/minerj.12.299

Ulmer, P., 2001. Partial melting in the mantle wedge - the role of H_2O in the genesis of mantle-derived arc-related magmas. Phys. Earth Planet. Inter. 127, 215–232. doi:http://dx.doi.org/10.1016/S0031-9201(01)00229-1

Ulmer, P., Luth, R.W., 1991. The graphite-COH fluid equilibrium in P, T, fO_2 space. Contrib. to Mineral. Petrol. 106, 265–272. doi:10.1007/BF00324556

Ulmer, P., Trommsdorff, V., 1995. Serpentine stability to mantle depths and subduction-related magmatism. Science 268, 858–861. doi:10.1126/science.268.5212.858

V

van Keken, P.E., 2003. The structure and dynamics of the mantle wedge. Earth Planet. Sci. Lett. 215, 323–338. doi:10.1016/S0012-821X(03)00460-6

van Keken, P.E., Hacker, B.R., Syracuse, E.M., Abers, G.A., 2011. Subduction factory: 4. Depth-dependent flux of H $_2$ O from subducting slabs worldwide. J. Geophys. Res. 116, B01401. doi:10.1029/2010JB007922

van Keken, P.E., Kiefer, B., Peacock, S.M., 2002. High-resolution models of subduction zones:

Implications for mineral dehydration reactions and the transport of water into the deep mantle. Geochemistry, Geophys. Geosystems 3, 1 of 20-20 of 20. doi:10.1029/2001GC000256

von Seckendorff, V., O'Neill, H.S.C., 1993. An experimental study of Fe-Mg partitioning between olivine and orthopyroxene at 1173, 1273 and 1423 K and 1.6 GPa. Contrib. to Mineral. Petrol. 113, 196–207. doi:10.1007/BF00283228

W

Wallace, P.J., 2005. Volatiles in subduction zone magmas: concentrations and fluxes based on melt inclusion and volcanic gas data. J. Volcanol. Geotherm. Res. 140, 217–240. doi:10.1016/j.jvolgeores.2004.07.023

Wicks, F.J., Whittaker, E.J.W., 1975. A reappraisal of the structures of the serpentine minerals. Can. Mineral. 13, 227–243.

Wunder, B., and Schreyer, W. (1992) Metastability of the IO-A phase in the system MgO-Si02-H20 (MSH): What about hydrous MSH phases in subduction zones? Journal of Petrology, 33, 877-889.

Wunder, B., 1998. Equilibrium experiments in the system $MgO-SiO_2-H_2O$ (MSH): stability fields of clinohumite-OH [$Mg_9Si_4O_{16}(OH)$], chondrodite-OH [$Mg_5Si_2O_8(OH)_2$] and phase A ($Mg_7Si_2O_8(OH)_6$). Contrib. to Mineral. Petrol. 132, 111–120. doi:10.1007/s004100050410

Wunder, B., Gottschalk, M., 2002. Fe-Mg solid solution of sursassite, $(Fe,Mg)_4(Mg,Al,Fe)_2Al_4[Si_6O_{21}/(OH)_7]$. Eur. J. Mineral. 14, 575–580. doi:10.1127/0935-1221/2002/0014-0575

Wunder, B., Schreyer, W., 1997. Antigorite: High-pressure stability in the system $MgO-SiO_2-H_2O$ (MSH). Lithos 41, 213–227. doi:10.1016/S0024-4937(97)82013-0

Wunder, B., Wirth, R., Gottschalk, M., 2001. Antigorite: Pressure and temperature dependence of polysomatism and water content. Eur. J. Mineral. 13, 485–495. doi:10.1127/0935-1221/2001/0013-0485

Y

Yamamoto, K., Akimoto, S., 1977. The system $MgO-SiO_2-H_2O$ at high pressures and temperatures; stability field for hydroxyl-chondrodite, hydroxyl-clinohumite and 10A -phase. Am. J. Sci. 277, 288–312. doi:10.2475/ajs.277.3.288

Yamamoto, K., Akimoto, S.-I., 1974. High pressure and high temperature investigations in the system $MgO-SiO_2-H_2O$. J. Solid State Chem. 9, 187–195. doi:10.1016/0022-4596(74)90073-5

Z

ZHANGR. Y., LIOU J. G., and CONG B. L. (1995) Talc-, magnesite-, and Ti-clinohumite-bearing ultrahigh pressure meta-mafic and ultramafic complex in the Dabie Mountains, China. 1. Petrol. 36, IOll-1037.

Zhang, J., Li, B., Utsumi, W., Liebermann, R., 1996. In situ X-ray observations of the coesite-stishovite transition: reversed phase boundary and kinetics. Phys. Chem. Miner. 23, 1–10. doi:10.1007/BF00202987

Electron backscattered diffraction (EBSD) data for phase E identification

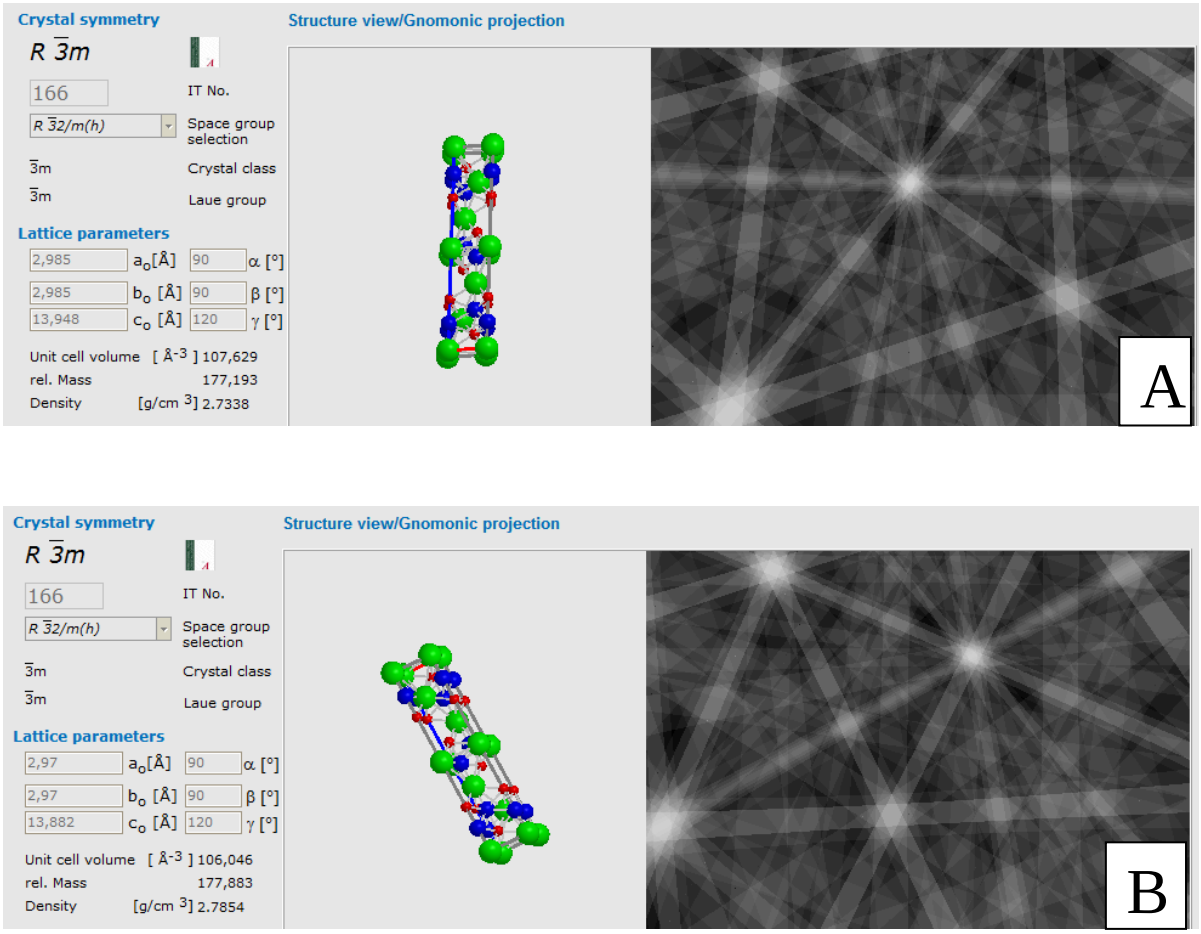

Figure S01. Kikuchi lines and view of phase E structure for two different orientations

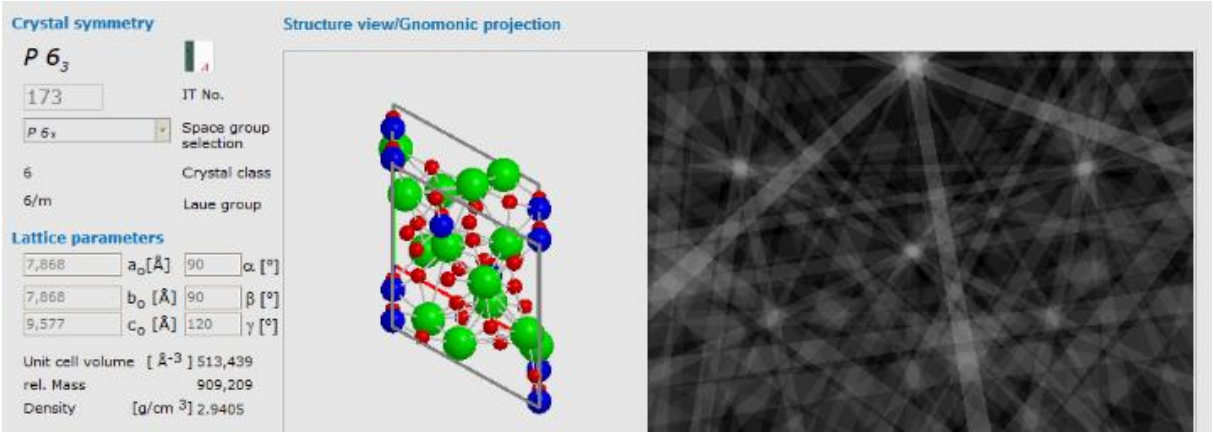

Figure S2. Kikuchi lines and view of phase A structure

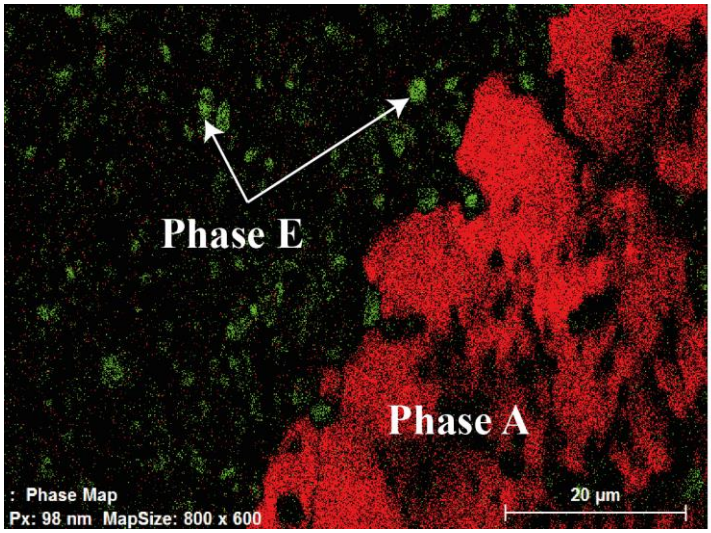

Kikuchi lines forming the diffraction pattern (Phase E)

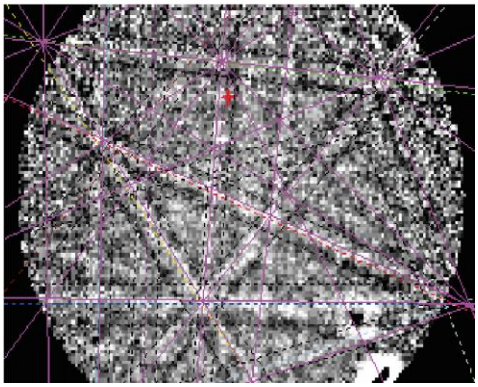

Figure S3.. Map of the region of the sample M471 used for EBSD analysis. Phase A and phase E were identified from fitting diffraction patterns obtained on this sample with the database patterns, with a priori on the nature of the mineral from combined EPMA. Unlike the rest of maps presented in this thesis, this map is not based on chemical data but was produced based on the diffraction patterns identified.

Table S-1. List of minerals of interest for this thesis.

Mineral	Formula	H_2O wt%
clinohumite-OH	$Mg_9Si_40_{16}(OH)_2$	**2.9**
Antigorite	$Mg_{48}Si_{34}O_{85}(OH)_{62}$	**12.3**
Brucite	$Mg(OH)_2$	**30.9**
Phase A	$Mg_7Si_2O_8(OH)_6$	**11.8**
PhaseE	$Mg_{2.3}Si_{1.3}H_{2.4}O_6$	**11.4**
Forsterite	Mg_2SiO_4	
Garnet	$(Fe,Mg)_3Al_2Si_3O_{12}$	
Enstatite	MgSiO3	
Humite-OH	$Mg_7Si_3O_{12}(OH)_2$	**3.75**
10Å-phase	$Mg_3Si_4O_{10}(OH)_2.n\,H_2O$	**7.6-13**
Al-10Å-phase	$Mg_2Si3Al_2O_{10}(OH)_2$	
Al-23Å-phase	$Mg_{11}Al_2Si4O_{16}(OH)_{12}$	**12.1**
23Å-phase	$Mg_{12}Si_5O_{16}(OH)_{12}$	**12.1**
3.65Å-phase	$Mg_{1.4}Si1.3\square_{1.3}(OH)_8$	
Serpentine	$Mg_3Si_2O_5(OH)_4$	**13**
Talc	$Mg_3Si_4O_{10}(OH)_2$	**4.7**
Mg-sursassite	$Mg_5Al_5Si_6O_{21}(OH)_7$	**7**
HAPY	$Mg_{2.1}Al_{0.9}(OH)_2Al_{0.9}Si_{1.1}O_6$	**7**
Cr-HAPY	$Mg_{2.1}Al_{0.9}(OH)_2Cr_{0.9}Si_{1.1}O_6$	**7**
chondrodite	$(Mg,Fe)_5^{2+}Si_2O_8(OH)_2$	**5.3**
11.5A	$Mg_{6.3}Si_{2.4}Al_{1.2.}$	**14-15**